



UNIVERSITY OF THE  
WITWATERSRAND,  
JOHANNESBURG

**Failure of Pump Systems Operating in Highly Corrosive  
Mine Water at Otjihase Mine**

Doctor of Philosophy

Silas Ithete Hango

Student Number: 609011

A thesis submitted to the Faculty of Engineering and the Built  
Environment, University of the Witwatersrand, Johannesburg,  
in fulfilment of the requirements for the degree of  
Doctor of Philosophy

Johannesburg, March 2018

## DECLARATION

I declare that this thesis is my own, unaided work. It is being submitted for the Degree of Doctor of Philosophy to the University of the Witwatersrand, Johannesburg. It has not been submitted before for any degree or examination to any other University. All cited sources are indicated and acknowledged by means of a list of references, and any help from others has been acknowledged.



Silas Ithete Hango

3 March 2018

## ABSTRACT

In the Namibian Otjihase underground mine, water is pumped from natural underground reservoirs to the surface using mild steel pumps that have cast iron valves and shaft sleeves coated with a Ni-Cr-Fe alloy. As these components failed very frequently in the highly corrosive mine water environment, it became necessary to provide recommendations for alternative pump materials.

The Ni-Cr-Fe coated, carbon steel shaft sleeves were mechanically worn by abrasion in contact with debris trapped in packing glands. The highly corrosive mine water contained solid soil particles, which contributed to internal erosion-corrosion of the pump components. Once the protective coating was breached, the exposed steel corroded rapidly when reacting with the corrosive mine water, resulting in leakages.

The main objective of this work was therefore to characterise the steel and cast iron components used in the pump system, determine methods to improve the tribocorrosion resistance of the pump components and recommend a hardfacing material with improved performance in the tribocorrosive mine environment.

To simulate and study the synergistic effect of electrochemical and mechanical interaction between the pump components and highly corrosive mine water, the hardness and electrochemical response in synthetic mine water of the following proposed bulk materials were tested: Hastelloy G30, ULTIMET, Stellite 6B and ToughMet 3. Hastelloy G30 demonstrated good corrosion resistance, but had low hardness and poor abrasion resistance. ToughMet 3 had high hardness, but low corrosion resistance. As ULTIMET and Stellite 6B both had high hardness and good corrosion resistance, they were selected for further investigation to assess sliding abrasive wear and tribocorrosion behaviour in synthetic mine water.

The possibility of enhancing the corrosion resistance of ULTIMET and Stellite 6 (not 6B) alloys as protective coatings by adding minor amounts of ruthenium was investigated. ULTIMET and Stellite 6 powders were each mixed with nominal 0.3 wt% Ru and nominal 0.6 wt% Ru additions. The powders with no Ru, nominal 0.3 wt% Ru and nominal 0.6 wt% Ru were then thermally sprayed by the high velocity oxy-fuel flame (HVOF) process onto a carbon steel substrate, and compared to a Cr<sub>2</sub>O<sub>3</sub> coated steel as a benchmark. The powders and the coatings were characterised using optical and scanning electron microscopy with energy dispersive X-ray spectroscopy, and X-ray diffraction.

Hardness, sliding abrasive wear, and corrosion and tribocorrosion behaviour of the coatings and the substrate in synthetic mine water were then determined.

Comparison of the hardness showed that the nominal 0.3 wt% Ru ULTIMET coating had higher hardness than the same coatings with no Ru and nominal 0.6 wt% Ru, the nominal 0.6 wt% Ru Stellite 6 coating had the highest hardness and overall, the Stellite 6 coatings had higher hardness values than both ULTIMET and Cr<sub>2</sub>O<sub>3</sub> coatings.

At pH 6, the ULTIMET and Stellite 6 coatings with and without Ru additions had low corrosion current densities and consequently low corrosion rates in synthetic mine water. For the ULTIMET coatings, the corrosion rates decreased as the Ru content increased. The Stellite 6 coating had slightly lower corrosion current densities and corrosion rates than ULTIMET under all tested conditions.

Stellite 6 coatings had lower abrasive wear rates at the tested loads than the other materials. The lowest abrasive wear rates were recorded with additions of nominal 0.3 wt% Ru (5 N), and nominal 0.6 wt% Ru (10 N).

As expected, tribocorrosive wear rates increased with increasing load for all alloys. Ruthenium additions to ULTIMET and Stellite 6 coatings decreased the tribocorrosive wear rate. The best tribocorrosion resistance was achieved by the Stellite 6 coatings.

Stellite 6B bulk samples and Stellite 6 coatings with Ru had higher hardnesses, lower corrosion rates, lower wear rates and lower tribocorrosion rates than the carbon steel substrate, Cr<sub>2</sub>O<sub>3</sub> coating, and ULTIMET bulk material and coatings. Stellite 6 coating with nominal 0.6 wt% Ru exhibited lower corrosion rates at pH 6 and 3 than the ULTIMET coating. Therefore, the Stellite 6 coating were recommended for use in pump shaft sleeves and the Stellite 6B bulk alloy in valves at Otjihase Underground Mine.

The cost saving for using the proposed alternative materials was calculated as US\$ 8 546.68 (R 128 200.20) per year. This is a major economic incentive for Otjihase Underground Mine.



## **DEDICATION**

To the Almighty God and the most important people in my life: brothers and sisters, family, relatives and friends.

In memory of my father and mother

**Wilbard Amunyela gwaHango yaShoombe**

**and**

**Helena Nduuviteko Amadhila-Shoombe**

They brought me up through teaching of discipline, respect of other people, men's work at home, and made me the person I am today. They had always been there when I needed them. I will forever be thankful to them for being my parents.

*Tate na Meme aaholike, vululukweni nombili!*

## ACKNOWLEDGEMENTS

I thank the Almighty God for his strength and love throughout the course of the work. I would like to thank the following people and institutions for the assistance they gave:

- My supervisors, Prof. Lesley A. Cornish, Dr Lesley H. Chown, Dr Josias W. van der Merwe (University of the Witwatersrand) and Prof. Frank P.L. Kavishe (University of Namibia) for guidance and encouragement. On top of these, I thank you for your valuable and effective supervision, filled with constructive thoughts, dedication and quality criticisms. You were always accessible and willing to provide input.
- African Materials Science and Engineering Network (AMSEN) for the bursary to undertake the research at Wits.
- The DST-NRF Centre of Excellence in Strong Materials for support and excellent administration of the AMSEN bursary. The Financial Aid and Scholarships Office of the University of the Witwatersrand is also acknowledged for its financial support through a Postgraduate Merit Award.
- Members of staff of the DST-NRF Centre of Excellence in Strong Materials Secretariat: Mrs Casey Sparkes, Mrs Marina Labauschagne, Mrs Jacqueline Jacobs and Mrs Moira Messenger – many thanks, may God bless you all.
- Otjihase Mine, Namibia, for the research opportunity. Mr Craig Thomas, Mr Odilon Ilunga and Mr Raymond Hulbert for allowing me the opportunity and the topic of research at Otjihase Mine, Namibia. I would like to thank everyone at the mine who directly or indirectly helped me during the site visits and enquiries while I was at Wits, especially Mrs Medried Muyongo.
- Multi Alloys, South Africa, represented by Mr Ken Perel for the free supply of the test samples (Hastelloy G30, ULTIMET, Stellite 6B and ToughMet 3).
- HAYNES International, USA, represented by Dr Paul Minning for the free supply of test samples (Hastelloy G30 and ULTIMET).
- Weartech Pty (Ltd) represented by Mr Adam Wintle and Fe Powder Supplies (Pty) Ltd represented by Mr Ray McCullough for the free supply of powders for spray coating samples (ULTIMET and Stellite 6).
- Thermaspray (Pty) Ltd, Olifantsfontein, South Africa, for allowing me to use the HVOF facilities, and also for the free supply of the Cr<sub>2</sub>O<sub>3</sub> and NiCrAlY coating powders. Dr Jan Lourens, Mr Paul Young, Mr Ruemain Govender and Mr George Ntloshana – thank you for the assistance with the thermal spray coating of the samples.

- Mintek, Randburg, South Africa, for allowing me access to their corrosion laboratory facilities. Mrs Melanie Smit and her team for facilitating my work at Mintek laboratories, and for constructive explanation and guidance.
- Tswane University of Technology, Pretoria, for tribocorrosion, especially Mr Isaac Makena for assisting with the measurements.
- Mr Brayner Nelwalani for SEM imaging in the School of Chemical and Metallurgical Engineering, and for abrasive wear measurements, Wits University.
- All the postgraduate students in RW418 at Wits, for their friendliness and helpfulness. Special thanks go to Mr Desmond Klenam, Mr Muziwethlathla Masikane, Dr Rodney Genga, Dr Philip Oladijo, Ms Boitshoko Modigwane, Dr Enoch Ogunmuyiwa, Dr Abdul Jimoh, Ms Adefunke Fabuyide, Ms Dineo Lioma, Ms Erika Erasmus, Mr Frans Shafuda and Ms Fortunate Moyo for sharing of good ideas, advises and contributions to the success of this work. You guys were my 'lubricants and corrosion inhibitors' during my research, else I would have been 'worn and corroded'.
- Prof. Dave Billing and Dr Stuart Miller for their assistance with the XRD work: metallic samples.
- Mr. Louis Coetzee, SGS South Africa (Pty) Ltd, Johannesburg for their assistance with XRD work: powders.
- The technical and support staff members of the School of Chemical and Metallurgical Engineering and the Faculty of Engineering and the Built Environment, University of the Witwatersrand, for their assistance during the research period, particularly Mr Shadrack Moqabulane, Mr Rhoderick McRae-Samuel, Mr Theo Prassinios, Mr Phatu Sikhware, Mr Donald Mahole and Mr Zoe Ilunga for their assistance with workshop work.
- My profound gratitude and appreciation goes to my beloved wife, Mrs Magano Mbute Kanime-Hango, for love, understanding, support, and endurance throughout the period of study. I promise to continue to love you more.
- Mr Andreas Tangeni Ndapuka for advice and encouragement before and throughout the duration of research.
- The University of Namibia, and the Faculty of Engineering and Information Technology academic and technical staff members.
- And lastly, but not least, siblings, relatives and friends for their love and care. Prayers and support from Ms Martha Amwaama, Johanna Niimpungu (Junior) Kadhila, Mr Andreas Elombo and Mr Junias Kalumbu are not forgotten. The following families are also acknowledged (Mr and Mrs): Kadhila, Hango, Iigonda, Ndazapo, Amadhila, Shigwedha (Senior), and Amwaama (Senior) for their prayers, love, trust and care.

# TABLE OF CONTENTS

<b>CHAPTER 1: INTRODUCTION.....</b>	<b>1</b>
1.1 Orientation.....	1
1.2 Problem statement.....	3
1.3 Objectives.....	4
<b>CHAPTER 2: LITERATURE REVIEW .....</b>	<b>6</b>
2.1 Introduction .....	6
2.2 Common forms of corrosion.....	6
2.3 Corrosion reactions.....	8
2.4 Corrosion measurements.....	9
2.4.1 Potentiodynamic polarisation.....	9
2.4.2 Polarisation resistance and corrosion rate .....	11
2.5 Corrosion behaviour of mild steel and cast iron.....	13
2.6 Corrosion behaviour of cobalt and cobalt alloys .....	15
2.7 Corrosion behaviour of chromium oxide .....	16
2.8 Corrosion in mine environments .....	17
2.9 Corrosion protection methods used in mines .....	24
2.10 Ruthenium as an alloying element.....	28
2.11 Friction and wear .....	29
2.11.1 Mechanism of friction .....	29
2.11.2 Mechanisms of wear .....	30
2.11.3 Wear resistance of cobalt-based hardfacing and chromium oxide coatings.....	32
2.12 Fundamentals of tribocorrosion .....	33
2.12.1 Mechanism of tribocorrosion .....	33
2.12.2 Measurement of tribocorrosion .....	34
2.13 Basics of thermal spray coating .....	36
2.13.1 Thermal spray coating techniques.....	36
2.13.2 The HVOF thermal spray process.....	37
2.13.3 Plasma spray process .....	37
2.14 Study approach .....	38
<b>CHAPTER 3: EXPERIMENTAL PROCEDURE .....</b>	<b>39</b>
3.1 Introduction .....	39
3.2 Materials .....	39

3.2.1 Materials for bulk studies .....	39
3.2.2 Materials for spray-coating studies .....	40
3.3 Metallographic preparation .....	42
3.4 Microscopy and hardness tests.....	43
3.5 XRD analysis .....	43
3.6 Analysis of synthetic and Otjihase mine water .....	43
3.7 Corrosion measurements.....	44
3.7.1 Cyclic potentiodynamic polarisation measurements.....	44
3.7.2 Tribocorrosion tests .....	46
3.8 Abrasive wear measurements .....	47
<b>CHAPTER 4: EXAMINATION OF CORRODED PUMP COMPONENTS AND THE CORROSION MEDIUM TAKEN FROM OTJIHASE UNDERGROUND MINE .....</b>	<b>49</b>
4.1 Introduction .....	49
4.2 Surface morphology of samples.....	49
4.3 Spectrographic analysis of samples .....	55
4.4 Optical metallography.....	55
4.5 Hardness of the samples .....	58
4.6 Analysis of the mine water.....	58
4.6.1 Sulphate, nitrite, chloride, turbidity, conductivity, total dissolved solids and pH tests ..	58
4.6.2 Chemical composition of the mine water.....	59
4.7 Corrosion results .....	63
4.7.1 Cyclic potentiodynamic polarisation measurements.....	63
4.8 Morphologies and compositions of the samples after corrosion tests .....	66
4.9 Identification of substitute alloys (bulk materials) .....	72
4.10 Summary .....	72
<b>CHAPTER 5: PROPERTIES OF THE ALTERNATIVE BULK ALLOYS .....</b>	<b>74</b>
5.1 Introduction .....	74
5.2 Microstructures.....	74
5.3 Hardness and grain size values .....	78
5.4 Chemical compositions of synthetic and acidified mine water before and after corrosion testing .....	79
5.5 Cyclic potentiodynamic polarisation measurements.....	80
5.5.1 Cyclic potentiodynamic polarisation curves .....	80
5.5.2 Morphologies and compositions of the samples after corrosion tests .....	84

5.6 Friction and sliding wear results .....	94
5.7 Summary .....	98
<b>CHAPTER 6: RESULTS FROM THE SPRAY-COATED MATERIALS .....</b>	<b>99</b>
6.1 Introduction .....	99
6.2. Powder characterisation .....	99
6.2.1 Particle sizes of the powders .....	99
6.2.2 Surface morphology of the powders .....	100
6.2.3 Energy dispersive X-ray and X-ray diffraction analysis of the powders.....	104
6.3 Characterisation of the coatings .....	108
6.3.1 Surface morphology of the coatings .....	108
6.3.2 Energy dispersive X-ray and X-ray diffraction results of the coatings .....	108
6.3.3 Hardness values .....	115
6.4 Corrosion results .....	115
6.4.1 Open circuit corrosion potential results .....	115
6.4.2 Cyclic potentiodynamic polarisation curves .....	118
6.4.3 SEM-EDX results after cyclic potentiodynamic polarisation .....	127
6.5 Friction and sliding wear characteristics.....	139
6.5.1 Coefficients of friction, penetration depths and wear rates .....	139
6.5.2 Wear mechanisms in sliding wear .....	142
6.6 Tribocorrosion results in synthetic mine water .....	151
6.6.1 Tribocorrosion open circuit potential results .....	151
6.6.2 Tribocorrosion potentiodynamic polarisation curves.....	151
6.6.3 SEM-EDX results after tribocorrosion potentiodynamic polarisation.....	155
6.7 Tribocorrosion potentiodynamic polarisation curves in acid mine water from Otjihase Mine .....	160
6.8 Summary .....	160
<b>CHAPTER 7: DISCUSSION: COMPARISON OF THE PROPERTIES OF THE SUBSTITUTE ALLOYS AND THE CURRENT MATERIALS .....</b>	<b>161</b>
7.1 Introduction .....	161
7.2 Corrosion at the Otjihase Underground Mine .....	161
7.3 Approaches for reducing corrosion and wear in mines .....	162
7.4 Mine environment .....	163
7.5. Microstructures.....	164
7.5.1 Analytical techniques .....	164
7.5.2 Bulk samples .....	164
7.5.3 Coatings.....	165
7.5.4 Comparison of the bulk samples and the coatings .....	165

7.6 Hardness of the bulk samples and the coatings .....	167
7.7 Corrosion results .....	168
7.7.1 Bulk alloys .....	168
7.7.2 Coatings.....	170
7.7.3 Comparison of the bulk samples and the coatings .....	173
7.8 Abrasive wear results.....	173
7.8.1 Bulk alloys .....	173
<b>7.8.2 Coatings</b> .....	175
<b>7.8.3 Comparison of the bulk samples and the coatings</b> .....	181
<b>7.9 Tribocorrosion results</b> .....	181
<b>7.10 Proposed alloys for pump system at Otjihase Mine</b> .....	183
7.11 Cost comparison between current pump materials and the proposed alternative pump materials.....	183
<b>CHAPTER 8: CONCLUSIONS AND RECOMMENDATIONS .....</b>	<b>193</b>
8.1 Conclusions .....	193
8.1.1 Failure of Otjihase Underground Mine pump systems.....	193
8.1.2 Comparison of the targeted substitute alloys (bulk materials) .....	193
8.1.3 Comparison of the spray-coatings .....	194
8.2 Recommendations to Otjihase Underground Mine.....	195
8.3 Recommendations for further study .....	195
<b>REFERENCES.....</b>	<b>196</b>
<b>APPENDIX A: Optical and SEM micrographs of as-received: A<sub>1</sub>) Stellite 6B, and A<sub>2</sub>) Hastelloy G30. ....</b>	<b>206</b>
<b>APPENDIX B: OCP of ULTIMET and Stellite 6 coatings, Cr<sub>2</sub>O<sub>3</sub> coating and mild steel substrate in synthetic mine water .....</b>	<b>208</b>
<b>APPENDIX C: AWARD .....</b>	<b>213</b>
<b>APPENDIX D: PUBLICATIONS AND PRESENTATIONS .....</b>	<b>213</b>

# LIST OF FIGURES

<b>Figure 2.1.</b> Elements of an electrochemical corrosion process. <sup>6</sup> .....	8
<b>Figure 2.2.</b> Theoretical potentiodynamic polarisation plots of an active-passive metal: a) cathodic, and b) anodic polarisation plots. <sup>33</sup> .....	10
<b>Figure 2.3.</b> Schematic diagram of typical cyclic potentiodynamic polarisation curve. <sup>35</sup> .....	11
<b>Figure 2.4.</b> Hypothetical linear polarisation plot. <sup>38</sup> .....	12
<b>Figure 2.5.</b> Relationship between erosion-corrosion wear rate and H <sub>2</sub> SO <sub>4</sub> concentration for: a) laser clad coating, and b) 420 stainless steel. <sup>68</sup> .....	26
<b>Figure 2.6.</b> Schematic diagram of the progress of tribocorrosion. <sup>110</sup> .....	34
<b>Figure 2.7.</b> Variation of OCP of an AISI 316 stainless steel sample in 0.5M H <sub>2</sub> SO <sub>4</sub> before (Areas 1 and 2), during (Area 3), and after loading (Area 4) against a corundum ball at 10 N load. <sup>124</sup> .....	35
<b>Figure 2.8.</b> Schematic diagram of a HVOF combustion chamber. <sup>137</sup> .....	37
<b>Figure 2.9.</b> Schematic diagram of a plasma spraying chamber. <sup>137</sup> .....	38
<b>Figure 3.1.</b> Electrochemical corrosion cell, showing the electrode and the Luggin capillary.....	45
<b>Figure 3.2.</b> Schematic diagram of tribocorrosion cell and test set-up.....	46
<b>Figure 3.3.</b> Examples of measurements of the diameters of the wear tracks on the samples. ....	48
<b>Figure 4.1.</b> Pump components at Otjihase Underground Mine, showing: a) corroded pump and little leakage of mine water, and b) leakage from the stuffing box. ....	50
<b>Figure 4.2.</b> Graphite filament packing gland which wears the shaft sleeves. ....	51
<b>Figure 4.3.</b> Photograph of whole corroded shaft sleeve and the selected parts from Sections 3 and 4 from a pump at Otjihase Mine, Namibia.....	51
<b>Figure 4.4.</b> Micrographs of shaft sleeve sections showing: a) coating partially removed by wear (W), pitting (P), general corrosion of the substrate (G), and b) attacked substrate after coating removal during service. ....	51
<b>Figure 4.5.</b> Optical micrographs of a shaft sleeve cross-section showing: a) substrate and coating on unattacked region. b) substrate of attacked region after coating removal during service. ....	52
<b>Figure 4.6.</b> Photograph of a corroded cast iron valve from a pump at Otjihase Mine, Namibia. ....	52
<b>Figure 4.7.</b> SEM In-Lens image of shaft sleeve, showing pits (P) and cracks (C) in substrate attacked region. (Numbers give EDX analysis positions) .....	53
<b>Figure 4.8.</b> SEM-SE image of the cast iron valve, showing pits, cracks and globular corrosion products. (Numbers refer to EDX analysis positions.).....	53
<b>Figure 4.9.</b> Macrograph of the shaft sleeve from Otjihase Mine, showing pits, and the removal of the protective film by abrasion on the Ni-Cr-Fe coating. ....	54
<b>Figure 4.10.</b> Optical micrographs of a corroded shaft sleeve substrate from an unattacked region, showing: a) ferrite (light) and pearlite (dark), and b) pearlite resolved showing ferrite and cementite alternating layers (arrow). ....	56



<b>Figure 4.11.</b> Optical micrograph of a corroded shaft sleeve coating from an unattacked region, showing Ni-Cr-Fe matrix (light brown) and Ni-rich regions (light), with carbides of Cr and Mo (dark).....	57
<b>Figure 4.12.</b> Optical micrograph of a corroded cast iron valve cross-section, showing the depth of corrosion (~250 $\mu\text{m}$ ) on the top exposed surface and the unattacked region underneath. Graphite nodules (N) and flakes (F) appear light in the attacked region, and dark in the unattacked region.....	57
<b>Figure 4.13.</b> Chemical analysis of mine water from Kuruma pump, Otjihase Mine, Namibia, for April-October 2012 and January 2013. ....	60
<b>Figure 4.14.</b> Chemical analysis of mine water from Satellite pump, Otjihase Mine, Namibia, for April-October 2012. ....	61
<b>Figure 4.15.</b> Chemical analysis of mine water from Conveyor No. 6 pump, Otjihase Mine, Namibia, for April-October 2012 and January 2013. ....	62
<b>Figure 4.16.</b> Cyclic potentiodynamic polarisation curves of Ni-Cr-Fe coating, mildsteel and cast iron samples from Otjihase Mine in synthetic mine water at ambient temperature at pH: a) 6, b) 3, and c).....	65
<b>Figure 4.17.</b> SEM-SE micrographs of the Ni-Cr-Fe, mild steel and cast iron sample surfaces after cyclic potentiodynamic polarisation in synthetic mine water at pH 6, showing general and pitting corrosion on the surfaces. ....	67
<b>Figure 4.18.</b> SEM-SE micrographs of the Ni-Cr-Fe, mild steel and cast iron sample surfaces after cyclic potentiodynamic polarisation in acidified synthetic mine water at pH 3, showing general and pitting corrosion on the surfaces.....	68
<b>Figure 4.19.</b> SEM-SE micrographs of the Ni-Cr-Fe, mild steel and cast iron sample surfaces after cyclic potentiodynamic polarisation in acidified synthetic mine water at pH 1, showing general and pitting corrosion on the surfaces.....	69
<b>Figure 5.1.</b> SEM-BSE micrograph of as-received ULTIMET, showing equiaxed (dark, D and light, L) and twins in the $\gamma$ grains (T), and a thin grain boundary layer. ....	75
<b>Figure 5.2.</b> SEM-BSE micrograph of as-received Stellite 6B, showing equiaxed (light, L) grains and twins in the $\gamma$ grains (arrows) in the matrix, with $\text{Cr}_7\text{C}_3$ (dark, D) at the grain boundaries.....	75
<b>Figure 5.3.</b> SEM-BSE micrograph of as-received ToughMet 3, showing large and irregular single-phase grains. ....	76
<b>Figure 5.4.</b> Optical micrographs of as-received Hastelloy G30, showing equiaxed grains. ....	76
<b>Figure 5.5.</b> Cyclic potentiodynamic polarisation curves of ULTIMET, Stellite 6B, ToughMet 3 and Hastelloy G30 samples at ambient temperature in synthetic mine water at pH: a) 6, b) 3, and c) 1 (no Hastelloy G30).....	83
<b>Figure 5.6.</b> Cyclic potentiodynamic polarisation. Photographs of: a) ULTIMET and Stellite 6B (solution turned yellow), b) ToughMet 3 (solution turned blue), and c) ToughMet 3 sample: thick surface layer (arrows) and rust in the corrosion test cell. ....	84
<b>Figure 5.7.</b> SEM-SE micrographs of the CuCl-Cu <sub>2</sub> O thick layer on the surface of the ToughMet 3 sample at: a) low, and b) high magnifications.....	85
<b>Figure 5.8.</b> Optical micrographs of ULTIMET, Stellite 6B and ToughMet 3 samples after cyclic potentiodynamic polarisation in synthetic mine water at pH 6, 3 and 1.....	87

<b>Figure 5.9.</b> SEM-SE micrographs of the ULTIMET sample surface after cyclic potentiodynamic polarisation in synthetic mine water at pH 6, at: a) low, and b) high magnification, showing slight pitting and intergranular corrosion, and corrosion products.....	88
<b>Figure 5.10.</b> SEM-SE micrographs of Stellite 6B sample surface after cyclic potentiodynamic polarisation in synthetic mine water at pH 6, showing intergranular corrosion, oxides on the surface and carbides in pits. a) low, and b) high magnification. ....	88
<b>Figure 5.11.</b> SEM-SE micrographs of the ToughMet 3 sample surface after cyclic potentiodynamic polarisation in synthetic mine water at pH 6, showing pitting, general and selective corrosion with a thick CuCl-Cu <sub>2</sub> O layer on the surface. a) low, and b) high magnification. ....	89
<b>Figure 5.12.</b> SEM-SE micrographs of the ULTIMET sample surface after corrosion in acidified synthetic mine water at pH 3, at: a) low, and b) high magnification, showing shallow pits.....	90
<b>Figure 5.13.</b> SEM-SE micrographs of Stellite 6B surface after cyclic potentiodynamic polarisation (acidified synthetic mine water, pH 3). a) low, and b) high magnification, showing intergranular corrosion, oxides on the surface and carbides in pits.....	90
<b>Figure 5.14.</b> SEM-SE micrographs of ToughMet 3 after cyclic potentiodynamic polarisation (acidified synthetic mine water, pH 3). a) low, and b) high magnification, showing pitting, general and selective corrosion.....	91
<b>Figure 5.15.</b> SEM-SE micrographs of the ULTIMET sample surface after cyclic potentiodynamic polarisation in acidified synthetic mine water at pH 1, at: a) low, and b) high magnification showing pitting, and slight intergranular corrosion.....	92
<b>Figure 5.16.</b> SEM-SE micrographs of the Stellite 6B sample surface after cyclic potentiodynamic polarisation in acidified synthetic mine water at pH 1, at: a) low, and b) high magnification, showing general and intergranular corrosion, oxides on the surface and carbides in pits. ....	92
<b>Figure 5.17.</b> SEM-SE micrographs of the ToughMet 3 sample surface after cyclic potentiodynamic polarisation in acidified synthetic mine water at pH 1, at: a) low, and b) high magnification, showing severe general and selective corrosion on the grains.....	93
<b>Figure 5.18.</b> Friction behaviour of ULTIMET and Stellite 6B alloys against 100Cr steel balls at: a)5 N, and b) 10 N.....	95
<b>Figure 5.19.</b> Stereo microscope macrographs of: a) ULTIMET, and b) Stellite 6B after ball-on-disc sliding wear at room temperature. ....	96
<b>Figure 5.20.</b> SEM-SE micrographs of: a) and c) ULTIMET, and b) and d) Stellite 6B after ball-on-disc sliding wear at 5 N and 10 N, showing wider wear tracks of ULTIMET than Stellite 6B at both loads. ....	96
<b>Figure 5.21.</b> SEM-SE micrographs after ball-on-disc sliding wear of: (a) ULTIMET, showing fairly long continuous furrows, and flattered and delaminated particles on the furrows, and (b) Stellite 6B, showing much debris collected in the grooves.....	97
<b>Figure 5.22.</b> SEM-SE micrographs of: a) and c) ULTIMET, showing tearing, slip bands and slip steps on the surface near the wear track, and b) and d) SEM-BSE image: Stellite	

6B, showing debris in the grooves, and the matrix phase ploughed out, leaving carbides on the surface. ....	97
<b>Figure 6.1.</b> Particle size analysis of ULTIMET powders. ....	101
<b>Figure 6.2.</b> Particle size analysis of Stellite 6 powders. ....	101
<b>Figure 6.3.</b> Particle size analysis of Cr <sub>2</sub> O <sub>3</sub> powders. ....	101
<b>Figure 6.4.</b> Particle size analysis of NiCrAlY powders. ....	101
<b>Figure 6.5.</b> Particle size analysis of ruthenium powders. ....	101
<b>Figure 6.6.</b> SEM-BSE micrographs showing the morphologies of ULTIMET powders, with a) and b) no Ru, c) and d) nominal 0.3 wt% Ru, and e) and f) nominal 0.6 wt% Ru, showing spherical particles with surface dendrites, and their smallest particles enclosed in ruthenium powder after mixing. ....	102
<b>Figure 6.7.</b> SEM-BSE micrographs showing the morphologies of Stellite 6 powders: a) and b) with 0 wt% Ru, c) and d) with nominal 0.3 wt% Ru, and e) and f) with nominal 0.6 wt% Ru, showing spherical particles with dendrites. ....	103
<b>Figure 6.8.</b> SEM micrographs showing the morphologies of: a) and b) Cr <sub>2</sub> O <sub>3</sub> , c) and d) NiCrAlY, and e) and f) ruthenium powders. ....	104
<b>Figure 6.9.</b> XRD patterns of the ULTIMET powders with no Ru, 0.3 and 0.6 wt% Ru. ....	106
<b>Figure 6.10.</b> XRD patterns of the Stellite 6 powders with no Ru, 0.3 and 0.6 wt% Ru. ....	106
<b>Figure 6.11.</b> XRD pattern of the Cr <sub>2</sub> O <sub>3</sub> powder. ....	107
<b>Figure 6.12.</b> XRD pattern of NiCrAlY bond coating powder. ....	107
<b>Figure 6.13.</b> SEM-SE micrographs showing the morphologies of ULTIMET coatings, with: a) and b) no Ru, c) and d) nominal 0.3 wt% Ru, and e) and f) nominal 0.6 wt% Ru, showing equiaxed dendrites surrounded by a network of interdendritic carbides. ....	109
<b>Figure 6.14.</b> SEM-SE micrographs showing morphologies of Stellite 6 coatings, with: a) showing the sprayed particles outlined, b) no Ru, c) and d) nominal 0.3 wt% Ru, and e) and f) nominal 0.6 wt% Ru, showing circular particles with equiaxed dendrites surrounded by a network of interdendritic carbides. ....	110
<b>Figure 6.15.</b> SEM-BSE micrographs showing the morphologies of: a) Cr <sub>2</sub> O <sub>3</sub> top coating and NiCrAlY bond coating, showing cracking parallel to the substrate, and b) Cr <sub>2</sub> O <sub>3</sub> top coating at higher magnifications, showing dendrites. ....	111
<b>Figure 6.16.</b> XRD pattern of the ULTIMET coatings with: a) no, b) nominal 0.3 wt% Ru and c) nominal 0.6 wt% Ru. ....	112
<b>Figure 6.17.</b> XRD pattern of Stellite 6 coatings with: a) no, b) nominal 0.3 wt% Ru and c) nominal 0.6 wt% Ru. ....	113
<b>Figure 6.18.</b> XRD pattern of Cr <sub>2</sub> O <sub>3</sub> coating. ....	114
<b>Figure 6.19.</b> XRD pattern of mild steel substrate. ....	114
<b>Figure 6.20.</b> Effect of Ru addition on OCP of ULTIMET coatings at various pH. ....	116
<b>Figure 6.21.</b> Effect of Ru addition on OCP of Stellite 6 coatings at various pH. ....	116
<b>Figure 6.22.</b> Effect of pH on OCP of ULTIMET and Stellite 6 coatings with no Ru, and Cr <sub>2</sub> O <sub>3</sub> coatings and mild steel substrate. ....	117

<b>Figure 6.23.</b> Effect of pH on OCP of ULTIMET and Stellite 6 coatings with nominal 0.3 wt% Ru, and Cr <sub>2</sub> O <sub>3</sub> coatings and mild steel substrate. ....	117
<b>Figure 6.24.</b> Effect of pH on OCP of ULTIMET and Stellite 6 coatings with nominal 0.6 wt% Ru, and Cr <sub>2</sub> O <sub>3</sub> coatings and mild steel substrate. ....	117
<b>Figure 6.25.</b> Cyclic potentiodynamic polarisation curves at ambient temperature of ULTIMET coatings with no Ru in synthetic mine water at pH 6, 3 and 1.....	118
<b>Figure 6.26.</b> Cyclic potentiodynamic polarisation curves at ambient temperature of ULTIMET coatings with nominal 0.3 wt% Ru in synthetic mine water at pH 6, 3 and 1.....	119
<b>Figure 6.27.</b> Cyclic potentiodynamic polarisation curves at ambient temperature of ULTIMET coatings with nominal 0.6 wt% Ru in synthetic mine water at pH 6, 3 and 1.....	119
<b>Figure 6.28.</b> Corrosion rate at ambient temperature of ULTIMET coatings with no Ru, nominal 0.3 wt% Ru and nominal 0.6 wt% Ru in synthetic mine water at pH 6, 3 and 1.....	120
<b>Figure 6.29.</b> Effect of ruthenium addition on corrosion rate of ULTIMET coatings with no Ru, nominal 0.3 wt% Ru and nominal 0.6 wt% Ru in synthetic mine water at ambient temperature and pH 6, 3 and 1.....	120
<b>Figure 6.30.</b> Cyclic potentiodynamic polarisation curves at ambient temperature of Stellite 6 coatings with no Ru in synthetic mine water at pH 6, 3 and 1.....	122
<b>Figure 6.31.</b> Cyclic potentiodynamic polarisation curves, at ambient temperature of Stellite 6 coatings with nominal 0.3 wt% Ru in synthetic mine water at pH 6, 3 and 1.....	122
<b>Figure 6.32.</b> Cyclic potentiodynamic polarisation curves at ambient temperature of Stellite 6 coatings with nominal 0.6 wt% Ru in synthetic mine water at pH 6, 3 and 1.....	122
<b>Figure 6.33.</b> Corrosion rate at ambient temperature of Stellite 6 coatings with no Ru, nominal 0.3 wt% Ru and nominal 0.6 wt% Ru in synthetic mine water at pH 6, 3 and 1. ....	123
<b>Figure 6.34.</b> Effect of ruthenium additions on corrosion rate at ambient temperature of Stellite 6 coatings with no Ru, nominal 0.3 wt% Ru and nominal 0.6 wt% Ru in synthetic mine water at pH 6, 3 and 1. ....	123
<b>Figure 6.35.</b> Cyclic potentiodynamic polarisation curves at ambient temperature of Cr <sub>2</sub> O <sub>3</sub> coatings in synthetic mine water at pH 6, 3 and 1. ....	125
<b>Figure 6.36.</b> Corrosion rate at ambient temperature of Cr <sub>2</sub> O <sub>3</sub> and mild steel in synthetic mine water at pH 6, 3 and 1. ....	125
<b>Figure 6.37.</b> Cyclic potentiodynamic polarisation curves at ambient temperature of the mild steel substrates in synthetic mine water at pH 6, 3 and 1. ....	126
<b>Figure 6.38.</b> SEM-SE surface micrographs of the ULTIMET coating without Ru after cyclic potentiodynamic polarisation in synthetic mine water at ambient temperature and pH 6, 3 and 1, showing general corrosion, corrosion products on the surfaces and degradation at particle boundaries.....	129
<b>Figure 6.39.</b> SEM-SE surface micrographs of the ULTIMET coatings with nominal 0.3 wt% Ru after cyclic potentiodynamic polarisation in synthetic mine water at pH 6, 3 and 1, at ambient temperature, showing general corrosion, corrosion products on the surfaces and degradation at particle boundaries, with undissolved Ru particles (light) at all pH. ....	130
<b>Figure 6.40.</b> SEM-SE surface micrographs of the ULTIMET coatings with nominal 0.6 wt% Ru after cyclic potentiodynamic polarisation in synthetic mine water at pH 6, 3	

and 1, at ambient temperature, showing general corrosion, corrosion products on the surfaces and degradation at particle boundaries, with undissolved Ru particles (light) at all pH. ....	131
<b>Figure 6.41.</b> SEM-SE surface micrographs of the Stellite 6 coatings without Ru after cyclic potentiodynamic polarisation in synthetic mine water at pH 6, 3 and 1, at ambient temperature, showing general corrosion, corrosion products and degradation at particle boundaries, and boundary corrosion between main particles. ....	132
<b>Figure 6.42.</b> SEM-SE surface micrographs of the Stellite 6 coatings with nominal 0.3 wt% Ru after cyclic potentiodynamic polarisation in synthetic mine water at pH 6, 3 and 1, at ambient temperature, showing general corrosion, corrosion products and degradation at particle boundaries, with undissolved Ru particles (light) at all pH. ....	133
<b>Figure 6.43.</b> SEM-SE surface micrographs of the Stellite 6 coatings with nominal 0.6 wt% Ru after cyclic potentiodynamic polarisation in synthetic mine water at pH 6, 3 and 1, at ambient temperature, showing general corrosion, corrosion products and degradation at particle boundaries, with undissolved Ru particles (light) at all pH. ....	134
<b>Figure 6.44.</b> SEM-SE surface micrographs of Cr <sub>2</sub> O <sub>3</sub> coatings after cyclic potentiodynamic polarisation in synthetic mine water at pH 6, 3 and 1, at ambient temperature showing general corrosion and corrosion products in pits. ....	135
<b>Figure 6.45.</b> SEM-SE surface micrographs of mild steel substrate after cyclic potentiodynamic polarisation in synthetic mine water at pH 6, 3 and 1, at ambient temperature showing general corrosion and corrosion products on entire surface. ....	136
<b>Figure 6.46.</b> Friction behaviour of ULTIMET and Stellite 6 coatings without Ru, Cr <sub>2</sub> O <sub>3</sub> coating, and mild steel against 100Cr steel balls at 5N, showing Stellite 6 had the highest coefficient of friction at 200 m. ....	140
<b>Figure 6.47.</b> Friction behaviour of ULTIMET and Stellite 6 coatings without Ru, Cr <sub>2</sub> O <sub>3</sub> coating and mild steel substrate against 100Cr steel balls at 10N, showing Cr <sub>2</sub> O <sub>3</sub> had the highest coefficient of friction at steady state, at 200 m. ....	140
<b>Figure 6.48.</b> Friction behaviour of ULTIMET and Stellite 6 coatings with nominal 0.3 wt% Ru against 100Cr steel balls at 5N, showing Stellite 6 had a higher coefficient of friction at 200 m. ....	141
<b>Figure 6.49.</b> Friction behaviour of ULTIMET and Stellite 6 coatings with nominal 0.3 wt% Ru against 100Cr steel balls at 10N, showing Stellite 6 had a higher coefficient of friction at 200 m. ....	141
<b>Figure 6.50.</b> Friction behaviour of ULTIMET and Stellite 6 coatings with nominal 0.6 wt% Ru against 100Cr steel balls at 5N, showing Stellite 6 had a higher coefficient of friction at 200 m. ....	141
<b>Figure 6.51.</b> Friction behaviour of ULTIMET and Stellite 6 coatings with nominal 0.6 wt% Ru against 100Cr steel balls at 10N, showing Stellite 6 had a higher coefficient of friction at 200 m. ....	142
<b>Figure 6.52.</b> SEM-SE micrographs of ULTIMET coatings with no Ru, nominal 0.3 wt% Ru and nominal 0.6 wt% Ru after ball-on-disc sliding wear at 5N, showing wide wear tracks and damage with debris in pits. ....	144

<b>Figure 6.53.</b> SEM-SE micrographs of ULTIMET coatings with no Ru, nominal 0.3 wt% Ru and nominal 0.6 wt% Ru after ball-on-disc sliding wear at 10N, showing wide wear tracks and damage with debris in pits.....	145
<b>Figure 6.54.</b> SEM-SE micrographs of Stellite 6 coatings with no Ru, nominal 0.3 wt% Ru and nominal 0.6 wt% Ru after ball-on-disc sliding wear at 5N, showing wide wear tracks and damage with debris on the surface. ....	146
<b>Figure 6.55.</b> SEM-SE micrographs of Stellite 6 coatings with no Ru, nominal 0.3 wt% Ru and nominal 0.6 wt% Ru after ball-on-disc sliding wear at 10N, showing wide wear tracks and damage with debris on the surface. ....	147
<b>Figure 6.56.</b> SEM-SE micrographs of Cr <sub>2</sub> O <sub>3</sub> coatings after ball-on-disc sliding wear at 5N and 10N, showing wide wear tracks and damage with debris in pits. ....	148
<b>Figure 6.57.</b> SEM-SE micrographs of mild steel substrates after ball-on-disc sliding wear at 5N and 10N, showing wide wear tracks and damage with debris in pits. ....	148
<b>Figure 6.58.</b> Tribocorrosion potentiodynamic polarisation curves of ULTIMET coatings without Ru in synthetic mine water under loads of 5N and 10N.....	152
<b>Figure 6.59.</b> Tribocorrosion potentiodynamic polarisation curves of ULTIMET coatings with nominal 0.6 wt% Ru in synthetic mine water under loads of 5N and 10N at ambient temperature.....	152
<b>Figure 6.60.</b> Tribocorrosion potentiodynamic polarisation curves of Stellite 6 coatings without Ru in synthetic mine water under loads of 5N and 10N at ambient temperature. ....	153
<b>Figure 6.61.</b> Tribocorrosion potentiodynamic polarisation curves of Stellite 6 coatings with nominal 0.6 wt% Ru in synthetic mine water under loads of 5N and 10N at ambient temperature.....	153
<b>Figure 6.62.</b> Tribocorrosion potentiodynamic polarisation curves of Cr <sub>2</sub> O <sub>3</sub> coatings on mild steel in synthetic mine water under loads of 5N and 10N at ambient temperature. ....	154
<b>Figure 6.63.</b> Tribocorrosion potentiodynamic polarisation curves of mild steel substrates in synthetic mine water under loads of 5N and 10N at ambient temperature. ....	154
<b>Figure 6.64.</b> Example of tribocorrosion scar on a sample after reciprocating ball-on-disc at 5N or 10N.....	156
<b>Figure 6.65.</b> SEM-SE micrographs of ULTIMET coatings with no Ru and nominal 0.6 wt% Ru after reciprocating ball-on-disc at 5N and 10N, showing damage on wear tracks and debris in furrows.....	157
<b>Figure 6.66.</b> SEM-SE micrographs of Stellite 6 coatings (no Ru and nominal 0.6 wt% Ru) after reciprocating ball-on-disc at 5N and 10N:-wear track damage and debris in furrows. ....	157
<b>Figure 6.67.</b> SEM-SE micrographs of Cr <sub>2</sub> O <sub>3</sub> coatings and mild steel substrate after reciprocating ball-on-disc at 5N and 10N, showing wear track damage, debris and cracks (arrows). ....	158
<b>Figure 7.1.</b> Relationship between coefficient of friction and penetration depth of 0, nominal 0.3 wt% Ru and nominal 0.6 wt% Ru ULTIMET and Stellite 6, Cr <sub>2</sub> O <sub>3</sub> coatings and mild steel at 5 N.....	177

<b>Figure 7.2.</b> Relationship between coefficient of friction and penetration depth of 0, nominal 0.3 wt% Ru and nominal 0.6 wt% Ru ULTIMET and Stellite 6, Cr <sub>2</sub> O <sub>3</sub> coatings and mild steel at 10 N.....	178
<b>Figure 7.3.</b> Relationship between coefficient of friction and wear rate of 0, nominal 0.3 wt% Ru and nominal 0.6 wt% Ru ULTIMET and Stellite 6, Cr <sub>2</sub> O <sub>3</sub> coatings and mild steel at 5 N.....	178
<b>Figure 7.4.</b> Relationship between coefficient of friction and wear rate of 0, nominal 0.3 wt% Ru and nominal 0.6 wt% Ru ULTIMET and Stellite 6, Cr <sub>2</sub> O <sub>3</sub> coatings and mild steel at 10 N.....	179
<b>Figure 7.5.</b> Relationship between hardness and wear rate of 0, nominal 0.3 wt% Ru and nominal 0.6 wt% Ru ULTIMET and Stellite 6, Cr <sub>2</sub> O <sub>3</sub> coatings and mild steel at 5 N. ....	180
<b>Figure 7.6.</b> Relationship between hardness and wear rate of 0, nominal 0.3 wt% Ru and nominal 0.6 wt% Ru ULTIMET and Stellite 6, Cr <sub>2</sub> O <sub>3</sub> coatings and mild steel at 10 N. ....	180
<b>Figure 7.7.</b> Cost comparison of alloys due to corrosion in synthetic mine water at pH 6, 3 and 1.....	187
<b>Figure 7.8.</b> Prediction of life comparison of alloys due to corrosion in synthetic mine water at pH 6, 3 and 1.....	187
<b>Figure 7.9.</b> Cost comparison of coatings with no Ru, nominal 0.3 wt% Ru and nominal 0.6 wt% Ru and Ni-Cr-Fe coating due to corrosion in synthetic mine water at pH 6, 3 and 1.....	188
<b>Figure 7.10.</b> Prediction of life comparison of coatings due to corrosion in synthetic mine water at pH 6, 3 and 1. ....	189
<b>Figure 7.11.</b> Cost comparison of coatings with no Ru, nominal 0.3 wt% Ru and nominal 0.6 wt% Ru and Ni-Cr-Fe coating due to tribocorrosion in synthetic mine water at pH 6. ....	190
<b>Figure 7.12.</b> Prediction of life comparison of coatings due to tribocorrosion in synthetic mine water at pH 6.....	191

# LIST OF TABLES

<b>Table 2.1.</b> Summary of the survey on failure of pump components in material-handling systems in the mining and mineral-processing industry, July 1986. <sup>72</sup> .....	18
<b>Table 2.2.</b> Analysis of acid mine water from 4 anthracite mines in Pennsylvania, USA, January 1953-January 1954. <sup>73</sup> .....	19
<b>Table 2.3.</b> Corrosion rates (mm·y <sup>-1</sup> ) of specimens in acid mine water from different anthracite mines in Pennsylvania, USA, January 1953-January 1954. <sup>73</sup> .....	20
<b>Table 2.4.</b> Summary of immersion tests in acid mine water of stainless steel specimens and their surface appearances. <sup>73</sup> .....	23
<b>Table 2.5.</b> Composition of 30CrMnMoTi alloy (wt%). <sup>82</sup> .....	27
<b>Table 3.1.</b> Typical chemical compositions of the test materials (wt%). <sup>121, 138, 139</sup> .....	40
<b>Table 3.2.</b> Chemical composition of ULTIMET, Stellite 6 and Cr <sub>2</sub> O <sub>3</sub> commercial alloy powders and ASTM A516 Grade 70 mild steel substrate. <sup>121, 138, 139</sup> .....	42
<b>Table 3.3.</b> Operating parameters of the HVOF and plasma spraying processes. ....	42
<b>Table 3.4.</b> Composition of synthetic mine water solution used in the tests. <sup>142</sup> .....	45
<b>Table 4.1.</b> EDX analysis of pits on a mild steel substrate of the areas of the shaft sleeve shown in Figure 4.7. ....	54
<b>Table 4.2.</b> EDX analysis of areas given in Figure 4.8 on the cast iron valve surface. ....	54
<b>Table 4.3.</b> Optical emission spectrographic analysis of the mild steel substrate, Ni-Cr-Fe coating and cast iron valve. ....	55
<b>Table 4.4.</b> Hardness values of mild steel, Ni-Cr-Fe and cast iron samples. ....	58
<b>Table 4.5.</b> Turbidity, conductivity, TDS and pH test results of mine water from Kuruma, Satellite and Conveyor No. 6 pumps, 30-10-2013.....	58
<b>Table 4.6.</b> Cyclic potentiodynamic polarisation test results of Ni-Cr-Fe coating, mild steel and cast iron from Otjihase Mine in synthetic mine water at ambient temperature, pH 6, 3 and 1.....	66
<b>Table 4.7.</b> EDX analyses of the Ni-Cr-Fe sleeve coating surface of Figures 4.17-4.19 after cyclic potentiodynamic polarisation in synthetic mine water at pH 6, 3 and 1.....	70
<b>Table 4.8.</b> EDX analyses of the mild steel substrate surface of Figures 4.17-4.19 after cyclic potentiodynamic polarisation in synthetic mine water at pH 6, 3 and 1.....	70
<b>Table 4.9.</b> EDX analysis of the cast iron sample surface of Figures 4.17-4.19 after cyclic potentiodynamic polarisation in synthetic mine water at pH 6, 3 and 1.....	71
<b>Table 5.1.</b> EDX analysis (wt%) of ULTIMET (Figure 5.1) before cyclic potentiodynamic polarisation measurements.....	77
<b>Table 5.2.</b> EDX analysis (wt%) of Stellite 6B (Figure 5.2) before cyclic potentiodynamic polarisation measurements.....	77
<b>Table 5.3.</b> EDX analysis (wt%) of ToughMet 3 (Figure 5.3) before cyclic potentiodynamic polarisation measurements.....	78



<b>Table 5.4.</b> EDX analysis (wt%) of Hastelloy G30 (Figure A <sub>2</sub> ) before cyclic potentiodynamic polarisation measurements.....	78
<b>Table 5.5.</b> Microhardness and grain sizes of ULTIMET, Stellite 6B, ToughMet 3 and Hastelloy G30. ....	79
<b>Table 5.6.</b> Properties of synthetic and acidified synthetic mine water for corrosion testing. ....	79
<b>Table 5.7.</b> Inductively coupled plasma mass spectrometry (ICP-MS) results of the test solutions after cyclic potentiodynamic polarisation in synthetic mine water at pH 1. ....	80
<b>Table 5.8.</b> Inductively coupled plasma optical emission spectrometry (ICP-OES) results of the test solutions after cyclic potentiodynamic polarisation in synthetic mine water at pH 1. ....	80
<b>Table 5.9.</b> Ion chromatography results of the test solutions after cyclic potentiodynamic polarisation in synthetic mine water at pH 1. ....	80
<b>Table 5.10.</b> Cyclic potentiodynamic polarisation test results of ULTIMET, Stellite 6B, ToughMet 3 and Hastelloy G30 alloys in synthetic and acidified synthetic mine water. ....	82
<b>Table 5.11.</b> EDX analysis of the CuCl-Cu <sub>2</sub> O thick layer on the surface of the ToughMet 3 sample after cyclic potentiodynamic polarisation in synthetic mine water. ....	85
<b>Table 5.12.</b> EDX analysis of the ULTIMET sample surface of Figure 5.9 after cyclic potentiodynamic polarisation in synthetic mine water at pH 6.....	88
<b>Table 5.13.</b> EDX analysis of the Stellite 6B sample surface of Figure 5.10 after cyclic potentiodynamic polarisation in synthetic mine water at pH 6.....	89
<b>Table 5.14.</b> EDX analysis of the ToughMet 3 sample surface of Figure 5.11 after cyclic potentiodynamic polarisation in synthetic mine water at pH 6.....	89
<b>Table 5.15.</b> EDX analysis of the ULTIMET sample surfaces of Figure 5.12 after cyclic potentiodynamic polarisation in acidified synthetic mine water at pH 3.....	90
<b>Table 5.16.</b> EDX analysis of the Stellite 6B sample surfaces of Figure 5.13 after cyclic potentiodynamic polarisation in acidified synthetic mine water at pH 3.....	91
<b>Table 5.17.</b> EDX analysis (wt%) of the ToughMet 3 sample surfaces of Figure 5.14 after cyclic potentiodynamic polarisation in acidified synthetic mine water at pH 3.....	91
<b>Table 5.18.</b> EDX analysis of the ULTIMET sample surfaces of Figure 5.15 after cyclic potentiodynamic polarisation in acidified synthetic mine water at pH 1.....	92
<b>Table 5.19.</b> EDX analysis of the Stellite 6B sample surfaces of Figure 5.16 after cyclic potentiodynamic polarisation in acidified synthetic mine water at pH 1.....	93
<b>Table 5.20.</b> EDX analysis of the ToughMet 3 sample surfaces of Figure 5.17 after cyclic potentiodynamic polarisation in acidified synthetic mine water at pH 1.....	93
<b>Table 5.21.</b> EDX analysis of the ULTIMET and Stellite 6B sample surfaces of Figures 5.20 a) and b), 5.21 a), and 5.22 a) and b) after ball-on-disc sliding wear at 5N. ....	98
<b>Table 6.1.</b> Particle sizes and distributions of the powders (by Malvern particle size analysis) in Figures 6.1-6.5. ....	100
<b>Table 6.2.</b> EDX analysis of the powders for coating.....	105

<b>Table 6.3.</b> EDX analysis of the coatings before tests. ....	111
<b>Table 6.4.</b> Hardnesses (HV <sub>2</sub> ) of ULTIMET, Stellite 6, Cr <sub>2</sub> O <sub>3</sub> coatings and mild steel substrate. ....	115
<b>Table 6.5.</b> Cyclic potentiodynamic polarisation results at ambient temperature of ULTIMET coatings with no Ru, nominal 0.3 wt% Ru and nominal 0.6 wt% Ru in synthetic mine water (pH 6, 3 and 1). ....	121
<b>Table 6.6.</b> Cyclic potentiodynamic polarisation results of Stellite 6 coatings with no Ru, nominal 0.3 wt% Ru and nominal 0.6 wt% Ru in synthetic mine water at pH 6, 3 and 1, at ambient temperature. ....	124
<b>Table 6.7.</b> Cyclic potentiodynamic polarisation results at ambient temperature of Cr <sub>2</sub> O <sub>3</sub> coatings in synthetic mine water at pH 6, 3 and 1. ....	126
<b>Table 6.8.</b> Cyclic potentiodynamic polarisation results at ambient temperature of the mild steel substrates in synthetic mine water at pH 6, 3 and 1. ....	127
<b>Table 6.9.</b> EDX analysis (wt%) of the ULTIMET sample surface of Figures 6.38-6.40 after cyclic potentiodynamic polarisation in synthetic mine water at pH 6, 3 and 1, at ambient temperature. ....	137
<b>Table 6.10.</b> EDX analysis (wt%) of the Stellite 6 coating surfaces of Figures 6.41-6.43 after cyclic potentiodynamic polarisation in synthetic mine water at pH 6, 3 and 1, at ambient temperature. ....	138
<b>Table 6.11.</b> EDX analysis (wt%) of Cr <sub>2</sub> O <sub>3</sub> coating surfaces of Figure 6.44 after cyclic potentiodynamic polarisation in synthetic mine water at pH 6, 3 and 1, at ambient temperature. ....	138
<b>Table 6.12.</b> EDX analysis (wt%) of mild steel substrate surfaces of Figure 6.45 after cyclic potentiodynamic polarisation in synthetic mine water at pH 6, 3 and 1, at ambient temperature. ....	139
<b>Table 6.13.</b> Coefficients of friction, forces of friction, maximum penetration depths (Pd <sub>max</sub> ) and wear rates of ULTIMET and Stellite 6 coatings with no Ru, nominal 0.3 and nominal 0.6 wt% Ru, Cr <sub>2</sub> O <sub>3</sub> coatings and mild steel substrates at 5N. ....	142
<b>Table 6.14.</b> Coefficients of friction, forces of friction, maximum penetration depths (Pd <sub>max</sub> ) and wear rates of ULTIMET and Stellite 6 coatings with no Ru, nominal 0.3 wt% Ru and nominal 0.6 wt% Ru, Cr <sub>2</sub> O <sub>3</sub> coatings and mild steel substrates at 10N. ....	143
<b>Table 6.15.</b> EDX analysis of the ULTIMET coatings without Ru of Figures 6.52 and 6.53 after ball-on-disc sliding wear at 5N and 10N. ....	149
<b>Table 6.16.</b> EDX analysis of the ULTIMET coatings with nominal 0.3 wt% Ru of Figures 6.52 and 6.53 after ball-on-disc sliding wear at 5N and 10N. ....	149
<b>Table 6.17.</b> EDX analysis of the ULTIMET coatings with nominal 0.6 wt% Ru of Figures 6.52 and 6.53 after ball-on-disc sliding wear at 5N and 10N. ....	149
<b>Table 6.18.</b> EDX analysis of the Stellite 6 coatings with no Ru (Figures 6.54 and 6.55) after ball-on-disc sliding wear at 5N and 10N. ....	150
<b>Table 6.19.</b> EDX analysis of the Stellite 6 coatings with nominal 0.3 wt% Ru (Figures 6.54 and 6.55) after ball-on-disc sliding wear at 5N and 10N. ....	150
<b>Table 6.20.</b> EDX analysis of the Stellite 6 coatings with nominal 0.6 wt% Ru (Figures 6.54 and 6.55) after ball-on-disc sliding wear at 5N and 10N. ....	150
<b>Table 6.21.</b> EDX analysis of the Cr <sub>2</sub> O <sub>3</sub> coatings (Figure 6.56) after ball-on-disc sliding wear at 5N and 10N. ....	151

<b>Table 6.22.</b> EDX analysis of mild steel substrates (Figure 6.57) after ball-on-disc sliding wear at 5N and 10N.....	151
<b>Table 6.23.</b> Tribocorrosion potentiodynamic polarisation results of ULTIMET and Stellite 6 coatings with no Ru and nominal 0.6 wt% Ru, Cr <sub>2</sub> O <sub>3</sub> coatings and steel substrates under loads of 5N and 10N in synthetic mine water.....	155
<b>Table 6.24.</b> EDX analysis of ULTIMET coatings with no Ru and nominal 0.6 wt% Ru of Figure 6.65 after reciprocating ball-on-disc at 5N and 10N in synthetic mine water at room temperature.....	158
<b>Table 6.25.</b> EDX analysis of Stellite 6 coatings with no Ru and nominal 0.6 wt% Ru of Figure 6.66 after reciprocating ball-on-disc at 5N and 10N in synthetic mine water at room temperature.....	159
<b>Table 6.26.</b> EDX analysis of Cr <sub>2</sub> O <sub>3</sub> coatings of Figure 6.67 after reciprocating ball-on-disc at 5N and 10N in synthetic mine water at room temperature.....	159
<b>Table 6.27.</b> EDX analysis of mild steel substrates of Figure 6.67 after reciprocating ball-on-disc at 5N and 10N in synthetic mine water at room temperature. ....	159
<b>Table 7.1.</b> Grain sizes and carbide fraction of the bulk alloys, average powder sizes, and globular and ruthenium particle sizes of the coatings. ....	166
<b>Table 7.2.</b> Hardness measurements of the coatings and the bulk samples. ....	168
<b>Table 7.3.</b> Cost of alloys as provided by WEARTECH Pty (Ltd), November 2014.....	183
<b>Table 7.4.</b> Cost and predicted life of materials due to corrosion in synthetic mine water at pH 6, 3 and 1. ....	184
<b>Table 7.5.</b> Cost and predicted life of materials due to tribocorrosion in synthetic mine water at pH 6. ....	185

## LIST OF ABBREVIATIONS AND SYMBOLS

AAS	Atomic absorption spectroscopy
ASTM	American Society for Testing and Materials
B	Stern Geary coefficient
CR	Corrosion Rate
EIS	Electrochemical impedance spectroscopy
$E_{bd}$	Breakdown potential
$E_{corr}$	Corrosion potential
$E_{rp}$	Repassivation potential
$E_{prot}$	Protection potential
$E_{trans}$	Transpassive potential
$E_{pit}$	Pitting potential
$\Delta E$	Change in potential
$\Delta t$	Change in time
EDX	Energy dispersive X-ray spectroscopy
$E_w$	Equivalent weight
FESEM	Field emission scanning electron microscopy
fcc	Face centred cubic
hcp	Hexagonal close packed
HV	Vickers Hardness
$i_{corr}$	Corrosion current density
ICP-MS	Inductively coupled plasma mass spectrometry
ICP-OES	Inductively coupled plasma optical emission spectroscopy
ipy	Inches per year
LPR	Linear polarisation resistance
mA	milliampere
mV	millivolt
OCP	Open circuit potential
PDP	Potentiodynamic polarisation
PGM	Platinum group metals
pH	Power of hydrogen
PTA	Plasma transferred arc
$R_p$	Polarisation resistance
SEM	Scanning electron microscopy
SSC	Stress corrosion cracking
TDS	Total dissolved solids
TEM	Transmission electron microscopy

UNS	Unified numbering system
XRD	X-ray diffraction
$\beta_a$	Anodic Tafel slope
$\beta_c$	Cathodic Tafel slope
$\rho$	Density
$\mu$	Coefficient of friction
$\mu_s$	Static coefficient of friction
$\mu_k$	Kinetic coefficient of friction
$\mu_{OCP}$	Coefficient of friction during open circuit potential measurement
$\mu_P$	Coefficient of friction during potentiodynamic polarisation
$\Omega.m$	Ohm-meter

# CHAPTER 1: INTRODUCTION

---

## 1.1 Orientation

Steel shaft sleeves, valves and casings are used in water pump systems at copper mines such as Otjihase Underground Mine in Namibia, which continually pump water from underground reservoirs to the surface to prevent flooding of the mine. These components experience very high degradation rates due to the synergic effects of electrochemical corrosion from the highly corrosive mine water and erosion due to the mechanical interaction between the pump components and solid particles in the mine water. As a result, the pumping systems regularly break down, leading to unacceptably frequent maintenance, down-time and replacement of parts.

Otjihase Mine is a copper underground mine with a massive sulphide deposit. The ore that is mined has a high concentration of copper (~1.6 wt%) with zinc, lead, silver and gold as by-products.<sup>1, 2</sup> The mine is situated 18 km north-east of the Namibian capital, Windhoek, and operated by Weatherly International plc., which took over from the Ongopolo Mining and Processing Limited in 2008, and was renamed Weatherly Mining Namibia Limited. The mining activities are currently taking place at a depth of 800 m from the surface.

During mining and ore processing activities at Otjihase Mine, stream sediments, sumps and surface water are usually contaminated by waste rocks and tailings.<sup>1</sup> The main source of contamination of mine water is tailings dump.<sup>1</sup> The seepage from the tailings dump consists of pyrite ( $\text{FeS}_2$ ), which forms acid mine water when it comes in contact with oxygen, making the mine water acidic and corrosive.

All metallic materials in the mine are subjected to a corrosive environment. Some materials are directly in contact with the aqueous environment, while others are only in contact with the mine atmosphere. The mine water that is pumped out contains copper ions, alkaline earth elements, rare earth elements, sulphates, nitrates and an acidic pH, which varies seasonally, as well as a high electrical conductivity and high total dissolved solids (TDS). The atmosphere contains nitrogen, oxygen, water vapour, chlorine, and other gases.

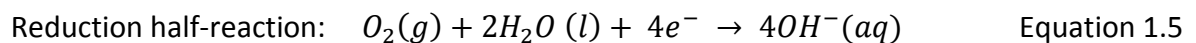
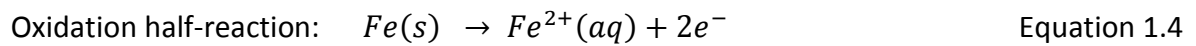
During mine operation, diesel engines running underground release sulphur dioxide ( $\text{SO}_2$ ), oxygen, water vapour, chlorine among others. In the presence of air,  $\text{SO}_2$  reacts with

oxygen to form  $SO_3$  (Equation 1.1<sup>3</sup>), which dissolves in water to form  $H_2SO_4$  (Equation 1.2<sup>4</sup>). Chlorine and hydrogen ions react to form HCl (Equation 1.3<sup>5</sup>):

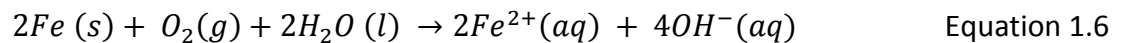


These acids (Equations 1.2 and 1.3) may cause the mine water (dilute slurry) to be acidic and highly corrosive to mine hardware, affecting the performance of pump systems in the mine.

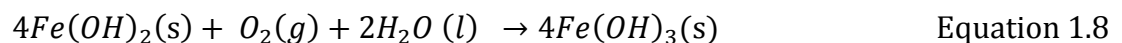
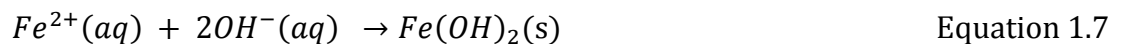
During the corrosion process, iron is oxidised to iron (II) ions ( $Fe^{2+}$ ), and oxygen from the air in the mine is reduced to hydroxide ions ( $OH^-$ ). This is best described by oxidation-reduction half-reactions (Equations 1.4 and 1.5<sup>5</sup>):



Combination of Equations 1.5 and 1.6 gives the overall reaction of iron, oxygen, and water (Equation 1.6<sup>6,7</sup>):

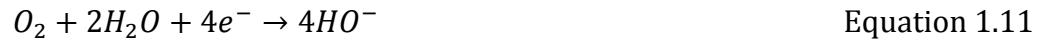


$Fe^{2+}$  and  $OH^-$  ions in Equation 1.6<sup>6,7</sup> may combine to form solid iron(II) hydroxide,  $Fe(OH)_2$  (Equation 1.7<sup>5</sup>), which further reacts with oxygen and water to form iron(III) hydroxide known as rust (Equation 1.8<sup>6</sup>):



Under static, purely corrosive conditions, a surface oxide layer/film will form as protection against corrosion on steel components. However, pump components at Otjihase Underground Mine operate in a tribocorrosive environment at the following water pump stations: Kuruma, North, Satellite, 22 BOOC and Conveyor 6. With added abrasion or erosion, the oxide layer is removed from the wear track area, exposing fresh surfaces to the aqueous environment.<sup>8, 9</sup> The exposed surface undergoes anodic

dissolution and forms a passive oxide film on the surface (Equations 1.9 and 1.10<sup>3</sup>), generating electrons which are consumed by the cathodic reaction (Equation 1.11<sup>3</sup>).



When the pump operates, its shaft sleeve, made of coated steel, often experiences wear by debris trapped in the packing gland, and once the coating is removed, corrosion from slurry further accelerates tribocorrosion. The passive film regrows, and partial anodic current flows from the worn area which modifies the electrochemical state of the sample.<sup>10</sup>

This research focussed on the tribocorrosion of the steel pump systems at the Otjihase Mine. Shaft sleeves and valves were identified for study, since they experience degradation at a very high rate. The degradation causes reduction in the component thicknesses, leading to reduced mechanical strength and structural failure, mechanical damage to sleeves and valves, and leakage of pipes due to tribocorrosion.<sup>11, 12</sup> Due to the mining conditions, these components experience tribocorrosion, and fail more often than the rest of the pump components, and this affects the mining activities. Due to the high corrosion rate, the mine spends much money on the maintenance and replacement of these pump systems. The cost of a pump at Otjihase Mine is ~US\$ 700 (~R 10 500), and components such as the coated shafts and shaft sleeves cost ~US\$ 290 (~R4 350) each. As the replacement of these components may be done every 6 weeks, the cost of the shafts and shaft sleeves amount to US\$ 4 100 (~R 61 500) per 6 weeks, excluding labour, maintenance and down-time, or ~US\$ 210 000 (~R 3.2 million) per annum.

The aim of this research was to address this specific corrosion problem in this type of mining environment. This work included:

- Determining the suitable alloys from which to manufacture the pumps.
- Identifying other materials to be used as coatings of the pump components.
- Determining whether these materials are available in bulk, are cost-effective, have reasonable production processes, and are readily available in Southern Africa.



## **1.2 Problem statement**

No previous field study had been done on corrosion of pump systems in Otjihase Mine, despite the large deleterious effects of this major problem. Many researchers have worked on the effect of corrosion on copper-containing steels<sup>13-18</sup>, but not on the corrosion behaviour of steels in a solution of dissolved copper and mine water. Thus, in this work, the effect of this aqueous solution on steel shaft sleeves and valves at the mine was examined. Alternative materials which may withstand exposure to very corrosive conditions, combined with frictional wear, were explored.

As a solution to this industrial problem, coating of the pump components, such as shaft sleeves and valves, was suggested. Coatings have been developed to protect the base material against corrosion and wear due to the chemical and mechanical interactions with the aggressive environment.

This work may provide solutions in terms of tribocorrosion protection in the mine environment. It also adds knowledge to the tribocorrosion mechanisms of the steels used in the shaft sleeves and valves, in a specific mining environment. It further advises on possible preventative methods, which may benefit other industries with similar tribocorrosion problems.

## **1.3 Objectives**

The main objective of this study was to understand why so much corrosion was occurring in the Otjihase Mine, and then attempt to mitigate it by the identification of suitable materials to substitute those currently in use. This was achieved through the following specific objectives:

1. To conduct a systematic investigation of the corrosion behaviour of mild steel and cast iron components used in the pumps operating in highly corrosive mine water at Otjihase Underground Mine.
2. To determine the compositions and structure of the steel and cast iron pump components currently being used at Otjihase Underground Mine, Namibia.
3. To identify suitable replacement materials for the pump components, and test them in bulk form initially to ascertain whether they would be suitable.
4. To investigate the corrosion behaviour in synthetic mine water of hardfacing alloys (once they had shown that they would be suitable), coated onto steels.
5. To investigate the abrasive wear behaviour of hardfacing alloys, coated onto steels.

6. To investigate the combined corrosive-abrasive wear performance in synthetic mine water of hardfacing alloys, coated onto steels.
7. To determine methods to improve the tribocorrosion resistance of steel pump components, and recommend a hardfacing material with improved performance in the tribocorrosive mine environment.
8. To establish the cost savings arising from the use of the recommended new material for the pump systems at the mine.

## CHAPTER 2: LITERATURE REVIEW

---

### 2.1 Introduction

This chapter is a survey of the literature, and gives the necessary background on the corrosion of metallic alloys in environments with different pH values, including aggressive mine water, as well as the possible corrosion preventative methods. It gives a brief account of the corrosion mechanisms of steels, cobalt-based coatings and chromium oxide coatings. The chapter also gives a background on friction and wear mechanisms, and describes the wear resistance of cobalt-based and chromium oxide coatings, as well as the effect of ruthenium additions to the cobalt-based coatings and their reaction in tribocorrosive environments.

### 2.2 Common forms of corrosion

Corrosion is the progressive surface wastage that occurs when metals are exposed to reactive environments.<sup>7, 19</sup> It is one of the most serious engineering problems and its study has increased in recent years. Corrosion is a major cause of material failure in buildings, mines, power plants, as well as in transport locomotives. The corrosion of steels in aggressive media is a common problem and much research has been carried out.<sup>7, 20</sup> Corrosion may appear in the form of uniform, galvanic, crevice, pitting, intergranular, erosion, stress corrosion cracking or tribocorrosion.<sup>7, 11</sup>

General or uniform corrosion is the name given to the corrosion process dominated by uniform thinning, which proceeds without appreciable localised attack.<sup>21</sup> Two theoretical basic stages of the uniform corrosion mechanism are: (a) the initial stage, in which the primary surface of the metal is attacked by chemical solutions, (b) corrosion nucleates and propagates on the surface area of the metal, causing uniform corrosion. After uniform corrosion, the repassivation of the protective film cannot take place, therefore anodic and cathodic sites become virtually indistinguishable.

Galvanic corrosion is caused by dissimilar metals when electrically connected in an electrolyte. This can be used for protection where one metal (the less noble) is sacrificed to protect the other (the more noble).<sup>5, 22</sup> The less resistant metal corrodes (becomes anodic), and the more resistant becomes cathodic, where less or negligible corrosion occurs.

Kruger and Rhyne<sup>23</sup> defined pitting corrosion as a form of localised attack which produces penetration into a metal object at sites called pits. Initiation of pitting corrosion

involves the chemical breakdown of a protective or passive film on a metal or alloy surface by aggressive species such as chlorides or sulphates.<sup>6,5</sup>

Crevice corrosion is a localised type of corrosion occurring within or adjacent to narrow gaps or openings formed by two metals or a metal and non-metallic material contact, where a small volume of a stagnant solution is present.<sup>6,5</sup> The parts that may experience crevice corrosion include gaskets, valve seats, rivet- and bolt-heads.

Schweitzer<sup>5</sup> defined intergranular corrosion as a specialized type of attack that occurs at the grain boundaries in a metal, with only little or no attack observed on the main body of the grain. In stainless steels, the mechanism is explained by the chromium depletion theory,<sup>24-26</sup> in which carbon diffuses to grain boundaries and reacts with chromium to form chromium carbides. If this has occurred, the regions near grain boundaries become less resistant to corrosion, because the chromium has been tied up in the carbides.

Erosion-corrosion occurs when deterioration is due to the combined action of chemical attack and mechanical abrasion or wear as a result of aqueous or gaseous corrodent flowing over the metal surface.<sup>24, 26</sup> Pipes, valves, casings and shaft sleeves commonly experience this form of corrosion.

Stress corrosion, often called stress corrosion cracking (SCC), is the failure of components subjected to aggressive environments in the presence of a static tensile stress.<sup>26, 27</sup> It usually initiates at points of stress concentration, and the cracks are often branched.

Major effects of corrosion are being reported every year and can cause social or economic effects.<sup>28</sup> Detrimental effects of corrosion on society involve safety, for example, sudden failure can cause fire, explosion, release of toxic products, and construction collapse; health issues, from pollution due to escaping product from corroded equipment or due to a corrosion product itself; depletion of natural resources, including metals and the fuels used to manufacture them and degradation of appearance.<sup>28</sup>

Economic consequences of corrosion may cause or require:<sup>5, 26, 28</sup>

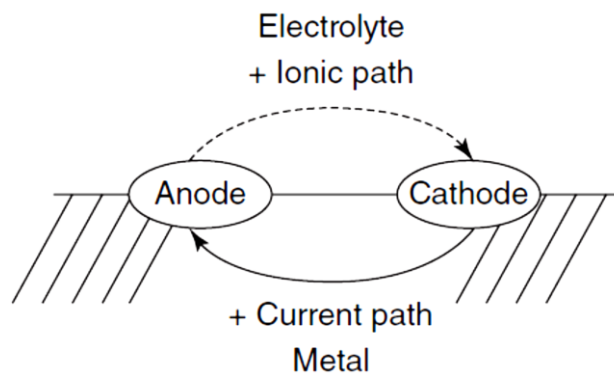
- Replacement of corroded equipment
- Overdesign to allow for corrosion
- Preventive maintenance, for example, painting
- Shutdown of equipment due to corrosion failure
- Contamination of a product

- Loss of efficiency, *e.g.* overdesign and corrosion products decrease the heat-transfer rate in heat exchangers
- Loss of valuable products, *e.g.* from a container that has perforated due to corrosion.

All of these factors increase costs: in Southern Africa, the direct cost of metal corrosion is ~US\$ 11 billion (~R154 billion) per annum, while in the U.S.A., the cost is ~US\$300 billion per year.<sup>11, 29</sup> Approximately one-third of these costs could be reduced by broader application of corrosion-resistant materials and the application of best corrosion-related technical practices.<sup>32</sup>

### 2.3 Corrosion reactions

Corrosion of metals and alloys in aqueous solutions or in any conducting medium, occurs by an electrochemical mechanism, whereby the electrochemical corrosion reaction requires four parts as shown in Figure 2.1<sup>6</sup>: anode (A), cathode (C), metallic conductor (M) and electrolytic conductor (E).



**Figure 2.1.** Elements of an electrochemical corrosion process.<sup>6</sup>

For electrochemical corrosion to occur, all four processes should take place simultaneously. At the anode (A), metallic ions leave the metal surface and go into solution, leaving electrons on the metal surface. In this way, the metal is oxidised (losing electrons) at the anode. There are two electrochemical corrosion reactions: anodic and cathodic. The anodic, or oxidation, reaction is a process where the anode metal M corrodes and goes into solution in the electrolyte as metal ions, Equation 2.1:<sup>7</sup>



where  $n$  = the number of electrons ( $e^{-}$ ) released by the metal.

Electrons migrate through the electrolytic conductor to the cathode, and the electrons left by the metal ions at the anode site are carried to the cathodic site by the metallic conductor (M).

The reaction that consumes the electrons produced at the anode is called the cathodic, or reduction reaction. The most commonly-occurring reduction reactions at the cathode are: hydrogen ion reduction (Equation 2.2) or oxygen reduction (Equation 2.3):<sup>6</sup>



When the metal is in contact with an aqueous or corrosive medium, the metal experiences a corrosion potential ( $E_{corr}$ ), where both anodic and cathodic currents present on its surface.<sup>5, 30</sup> These currents are equal in magnitude, therefore there is no net current to be measured at this potential. The rate of the anodic reaction at the corrosion potential defines the corrosion current density ( $i_{corr}$ ) which gives the corrosion rate of a metal. The interaction between anodic and cathodic reactions is defined by polarisation behaviour and determines the corrosion rate.

## 2.4 Corrosion measurements

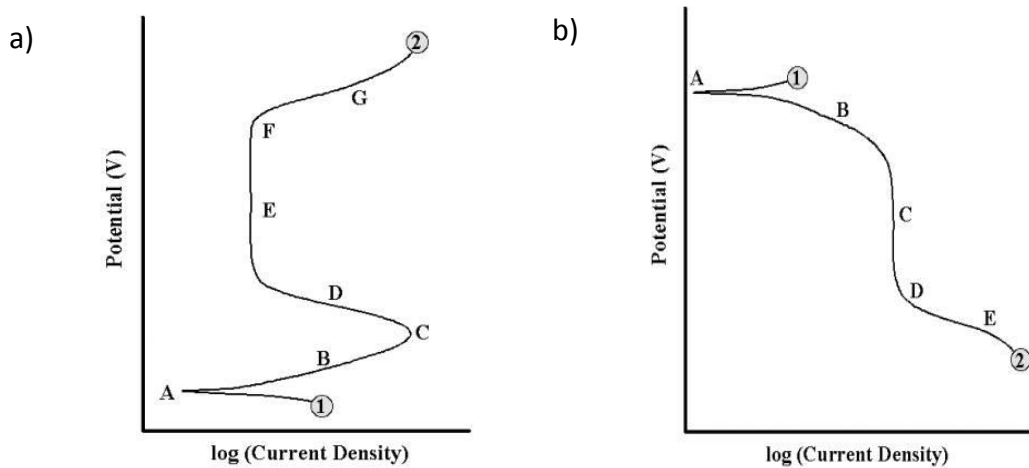
### 2.4.1 Potentiodynamic polarisation

Potentiodynamic polarisation is a technique where the potential of the electrode is varied at a selected rate by application of a current through the electrolyte.<sup>31</sup> It is a measure of polarisation characteristics by plotting the current response as a function of the applied potential.<sup>15</sup> Usually, the log current function is plotted against potential on a semi-log graph. This plot is termed a potentiodynamic polarisation plot, and its curve shows the corrosion behaviours of the working electrode in the test solution (electrolyte). These behaviours include information on corrosion rates, passivity, films, and pitting tendencies.

There are two scans during potentiodynamic polarisation: anodic and cathodic polarisation scans as illustrated in Figures 2.2 (a) and (b) respectively.<sup>32, 33</sup> In the anodic polarisation curve (Figure 2.2 a), the scan starts from Point 1 and progresses in the positive (potential) direction until termination at Point 2. The open circuit or rest potential is located at Point A. As the applied potential increases, the scan moves to Region B, which is the active region where metal oxidation is mainly taking place. Point C is known as the passivation potential. The current density decreases in Region D until a low, passive current density is achieved (Passive Region E). Once the potential reaches a

sufficiently positive value at Point F, called breakaway (*i.e.* the potential at which the surface film breaks down), the potential and the applied current increases in Region G.

In the schematic cathodic polarisation scan (Figure 2.2 b)<sup>33</sup>, the potential is varied from Point 1 in the negative direction to Point 2. The open circuit potential is located at Point A. Depending on the pH and dissolved oxygen concentration in the solution, Region B may represent the oxygen reduction reaction. The potential applied decreases further, resulting in no change in the rate of reaction, and hence the constant current at Region C. At Point D, the applied potential becomes sufficiently negative for another cathodic reaction to take place. As the potential increases, this cathodic reaction becomes dominant at Region E.



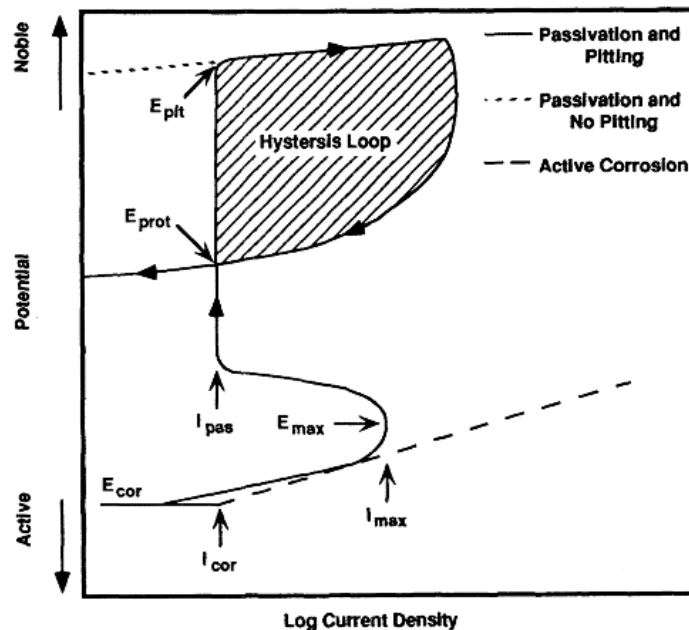
**Figure 2.2.** Theoretical potentiodynamic polarisation plots of an active-passive metal: a) cathodic, and b) anodic polarisation plots.<sup>33</sup>

The most useful electrochemical technique for localised corrosion susceptibility is cyclic potentiodynamic polarisation.<sup>34, 35</sup> The technique involves polarising the sample from its open circuit potential (or slightly below) anodically, until a predetermined current density is achieved. This current density is called the vertex current density. At this point, the potential is scanned back until the current reverses polarity. There are notable potentials on the curve, such as the transpassive or pitting ( $E_{trans}$  or  $E_{pit}$ ) potential, at which pits initiate, breakdown potential ( $E_{bd}$ ), at which the surface film breaks down, and repassivation potential ( $E_{rp}$ ), potential at which the reverse scan crosses the forward scan. This potential is also called protection potential ( $E_{prot}$ ). The values of  $E_{trans}$  and  $E_{rp}$  are important for engineering materials if they are accurately measured. A material will not undergo pitting if its potential is below  $E_{trans}$ , and a material will not experience localised corrosion if the potential is maintained below  $E_{rp}$ . The occurrence of hysteresis between the forward and reverse scans is an indication of pitting. If the hysteresis is very large, the

protection potential may be very close to the open circuit potential, indicating a high probability of pitting in that particular environment.<sup>35</sup>

A hysteresis loop is positive when the current density during the reverse scan is higher than that for the forward scan at any given potential. The area under this loop indicates the amount of localised corrosion incurred by the material.<sup>36</sup> A hysteresis loop is a negative loop or if there is no hysteresis when the current density during the reverse scan is lower than for the forward scan at any given potential, and the forward and reverse scans overlap. This indicates high resistance to localised corrosion, and very few small shallow pits have occurred.<sup>36, 37</sup> A schematic diagram of cyclic potentiodynamic polarisation curves, showing several types of behaviour is given in Figure 2.3.<sup>35</sup>

Although cyclic potentiodynamic polarisation is a good technique which gives useful parameters, often mass loss experiments are needed as well, especially in a case where long time data are needed.



**Figure 2.3.** Schematic diagram of typical cyclic potentiodynamic polarisation curve.<sup>35</sup>

#### 2.4.2 Polarisation resistance and corrosion rate

Polarisation resistance ( $R_p$ ), also called linear polarisation resistance, is the slope at the corrosion potential of a potential–current density curve (Figure 2.4).<sup>38</sup> It is the slope ( $\frac{dE}{di}$ ) obtained by scanning through a potential range of  $\pm 25$  mV that is very close to the



corrosion potential ( $E_{corr}$ ).  $R_p$  is inversely proportional to  $i_{corr}$  according to the Stern–Geary approximation in Equation 2.4:<sup>38</sup>

$$R_p = \frac{(\Delta E)}{(\Delta i)_{\Delta E \rightarrow 0}} = \frac{B}{i_{corr}} \quad \text{Equation 2.4}$$

where  $R_p$  = polarisation resistance,  $i_{corr}$  = corrosion current density,  $B$  = polarisation resistance constant that can be related to the anodic Tafel slope ( $\beta_a$ ) and cathodic Tafel slope ( $\beta_c$ ) in Equation 2.5:<sup>38</sup>

$$B = \frac{\beta_a |\beta_c|}{2.3(\beta_a + |\beta_c|)} \quad \text{Equation 2.5}$$

Equation 2.4 can be written in terms of  $i_{corr}$  as in Equation 2.6:<sup>38</sup>

$$i_{corr} = \frac{1}{(2.3R_p)} \left( \frac{\beta_a |\beta_c|}{\beta_a + |\beta_c|} \right) \quad \text{Equation 2.6}$$

The corrosion rate (CR) in  $\text{mm.y}^{-1}$  is calculated using Equation 2.7:<sup>38</sup>

$$\text{Corrosion rate (CR)} = \left( \frac{0.00327 E_w}{\rho} \right) i_{corr} \quad \text{Equation 2.7}$$

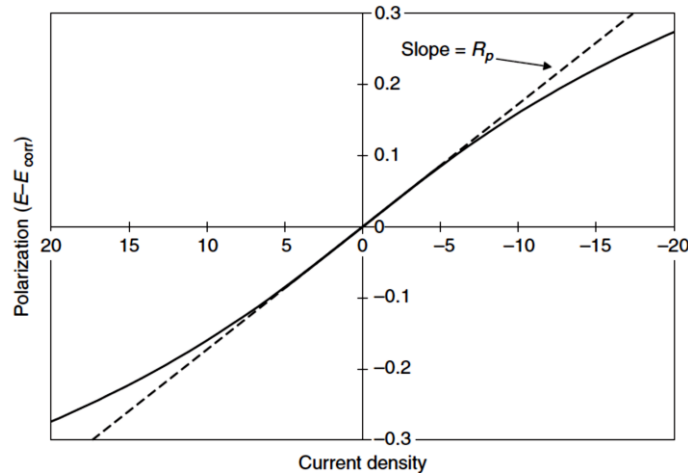
where  $E_w$  = equivalent weight of alloy (g) (Equation 2.8),  $\rho$  = density of alloy ( $\text{g.cm}^{-3}$ ) (Equation 2.9), and  $i_{corr}$  = corrosion current density ( $\mu\text{A.cm}^{-2}$ ).<sup>38</sup>

$$E_w = \frac{1}{\sum_{i=1}^n Q_i} = \frac{1}{\sum_{i=1}^n \frac{n_i f_i}{W_i}} \quad \text{Equation 2.8}$$

where  $Q_i$  = electron equivalent of the  $i^{\text{th}}$  element in the alloy (g),  $f_i$  = mass fraction of the  $i^{\text{th}}$  element in the alloy (g),  $W_i$  = atomic weight of the  $i^{\text{th}}$  element in the alloy, and  $n_i$  = valence of the  $i^{\text{th}}$  element of the alloy.

$$\rho = \frac{\sum_{i=1}^n \rho_i W_i}{100} \quad \text{Equation 2.9}$$

where  $\rho_i$  = actual density of the  $i^{\text{th}}$  element in the alloy and  $W_i$  = the weight of the  $i^{\text{th}}$  element.



**Figure 2.4.** Hypothetical linear polarisation plot.<sup>38</sup>

## 2.5 Corrosion behaviour of mild steel and cast iron

Mild steel is the most useful steel for many engineering applications, due to their low cost, good strength, hardness and machinability.<sup>39</sup> It can be welded into a limitless variety of shapes for use in cars, ships, pump systems and building materials. This steel is used in various service environments containing acids, alkalis and salt solutions, and so experience degradation.<sup>40, 41</sup> Cast iron is also a widely used material, especially for car parts, seawater-handling components, pumps for desalination and power plants and hydraulic machinery. Therefore, it is important to know the corrosion mechanisms of mild steel and cast iron and the preventative methods in different environments.

A review by Ibrahim *et al.*<sup>42</sup> on corrosion of carbon steel pipes and tanks by concentrated sulphuric acid (5, 6.5 and 9 mol.L<sup>-1</sup>) showed that when carbon steel came into contact with the sulphuric acid, the former was reduced to form H<sub>2</sub> and the iron oxidised with the formation of ferrous sulphate (FeSO<sub>4</sub>). The FeSO<sub>4</sub> adhered to the steel surface and formed a protective layer, which protected the metal from further attack by concentrated sulphuric acid.

Andijani and Turgoose<sup>43</sup> used polarisation resistance measurements to study the corrosion behaviour of carbon steel in deaerated 1M NaCl solution and artificial seawater. At low temperature (25°C) and neutral pH, corrosion rates were very low, and increased with decreased pH, and corrosion potential increased with a decreased in pH. Noor and Al-Moubaraki<sup>44</sup> also found similar behaviour in their study of the corrosion of mild steel in HCl solutions. After immersion in different concentrations of HCl (0.25-2.50 M), the mild steel showed general and pitting corrosion, especially at higher HCl concentrations.

Zhang *et al.*<sup>12</sup> performed fretting corrosion tests on steel wires in alkaline corrosion media on a fretting wear rig. They derived the interactive damage mechanisms of fretting wear and corrosion at different periods by studying the material loss and wear morphologies. The electrochemical results showed that a thin passive film was formed, and the corrosion rate was lowest after an immersion of 14 minutes. The corrosion products deposited on the wire surface were observed after 12 and 46 hours immersion, and the corrosion rates formed a plateau after fretting. The film was damaged by increased fretting cycles. These results showed that the interactive damage mechanism of steel wires was due to the combination of plastic deformation, abrasive wear and electrochemical corrosion.

Mennucci *et al.*<sup>45</sup> evaluated the effect of benzotriazole (BTAH), a well-known corrosion

inhibitor for copper, as a possible corrosion inhibitor for a carbon steel (CA-50), which is used as reinforcement in concrete. The improvement of the corrosion resistance due to BTAH addition was superior to that of nitrite of similar concentration, suggesting that BTAH is a potentially attractive alternative to nitrites for inhibiting corrosion of reinforcement steel in concrete.

Mobin *et al.*<sup>20, 46</sup> employed free corrosion potential and potentiodynamic polarisation measurements to study the effect of heavy metal ions, Cu and Ni, on the localised corrosion behaviour of a carbon steel (Fe-1.30Mn-0.14C-0.2Si, with 0.01 wt% of Cr, Ni, Cu, P and S each) under different conditions. In the aqueous medium containing high concentrations of Cu and Ni, a stable protective barrier was more likely to be formed, which lowered the corrosion rate, while in the presence of lower concentrations of the metal ions, the observed increase in corrosion rate was due to the occurrence of cathodic reactions and absence of a stable protective barrier. The corrosion potentials of carbon steel in distilled water and seawater were in the range of –650 to –750 mV and –700 to –800 mV vs SCE, respectively. However, no evidence of localised attack on carbon steel in the presence of different concentrations of heavy metal ions was shown, which could be a drawback of this research.

Corrosion mechanisms of cast iron involve thinning, pitting, and graphitic corrosion.<sup>47</sup> Corrosion of cast iron occurs in the same way as in steel where the metal lost to the solution, with graphitic and selective leaching of iron components from the iron-graphite matrix, and leave out graphite flakes.<sup>48</sup> This lowers the strength of a material, and leads to a material failure. However, the graphite flakes and the matrix are kept together by iron oxide corrosion products within the region called graphitised zone. Under low pressure, these iron oxide corrosion products are static, and under minor stresses, impact loads, or vibrations from auto traffic, they fracture and cause catastrophes or failure of materials if not a rehabilitation, repair or replacement of parts.<sup>49</sup> Sherif *et al.*<sup>41</sup> reported that corrosion of cast iron depends mainly on the percent of silicon in the alloy; the higher the silicon content, the higher the corrosion resistance. However, silicon additions are limited, and so the improvement from this method is also limited.

Cast iron experienced minor general corrosion and localised corrosion in aerated static, aerated water and 3.5% NaCl environment.<sup>50, 51</sup> The localised corrosion was more around the graphite flakes and it is more severe, which was due to the differences in the morphology of the graphite flakes and the microstructure of the samples. The electrochemical responses of cast iron in these environment showed that open circuit potential (OCP) in aerated tap water test became more positive, *i.e.* less anodic, while in

static test, it became less positive, *i.e.* more anodic. No OCP trends were noticed in the samples tested in 3.5% NaCl, and much iron dissolution was detected in the solution, which was promoted by chlorine in the solution. The iron ions in NaCl solution reacted with the oxygen and increased the corrosion process.

## 2.6 Corrosion behaviour of cobalt and cobalt alloys

Pure cobalt exists in two allotropes, a high temperature allotrope alpha ( $\alpha$ ) or gamma austenite ( $\gamma$ ) with an fcc crystal structure, and a low-temperature allotrope epsilon ( $\epsilon$ ) with a hcp crystal structure.<sup>52, 53</sup> The fcc is usually a light contrast phase which etches with difficulty, while the hcp structure etches more easily, and is darker.<sup>54</sup> The particular crystal structure affects the corrosion resistance in acidic and alkaline solutions:<sup>55, 56</sup> hcp cobalt oxidised at a faster rate than fcc cobalt at high temperatures. The structure would be stabilised by alloying elements, which would also affect the corrosion resistance. Cobalt corrodes actively in acid media and forms  $\text{Co}^{2+}$  and  $\text{Co}^{3+}$  oxides in alkaline media.

Frenk and Kurz<sup>57</sup> reported that if the carbon content was lower than  $\sim 2$  wt%, the alloys were hypo-eutectic with primary fcc (Co) dendrites surrounded by a network of eutectic carbides ( $\text{M}_7\text{C}_3$ , where M = metal, usually Cr or Mo). For higher carbon contents of  $\sim 2.5$  wt% C, alloys were hyper-eutectic and consisted of primary  $\text{M}_7\text{C}_3$  carbides in an interdendritic eutectic matrix. Obviously, the proportions and distribution of the different phases would affect the corrosion resistance.

Unlike iron- and nickel-based alloys, corrosion behaviour of cobalt and its alloys has been less well researched, because they are more specialised alloys and less used in industry. Corrosion behaviour of CoCrMo was studied by Contu *et al.*<sup>58</sup> in biomedical applications such as dental skeletal structures and orthopaedic implants in acidic, neutral and alkaline in serum and inorganic buffered environments. A corrosion-resistant film formed on the surface of the alloy, mainly consisting of a mixture of cobalt, chromium and molybdenum oxides in neutral and alkaline pH environments. When the alloy was subjected to mechanical loading, this film experienced wear and fracture, with scratches, dents and fretting due to friction between the alloy and the parts where it operated, resulting in exposure of the base alloy to the corrosive environment.<sup>58, 59</sup> Obviously, these solutions would be much less aggressive than in the Otjihase mine.

Badawy *et al.*<sup>60</sup> investigated the corrosion and passivation behaviour of cobalt in aqueous solutions at pH values of 1-13, and found that cobalt had an unstable native passive film consisting of CoO or  $\text{CoO}\cdot\text{H}_2\text{O}$  in acidic solutions. In neutral solutions, stabilisation of CoO

took place, while in basic solutions, the  $\text{CoO}\cdot\text{H}_2\text{O}$  passive film further oxidised to Co(III) compounds such as  $\text{CoOOH}$  and/or  $\text{Co}_3\text{O}_4$ . The formation of either  $\text{CoOOH}$  or  $\text{Co}_3\text{O}_4$  increases the stability of the passive film and they can be present as a second layer on the top of the native  $\text{CoO}$  passive film. This work is relevant to the current study for the acidic conditions only.

The study of corrosion of palladium-containing cobalt-chromium dental alloys (45Co-25Pd-20Cr-10Mo and 40Co-25Pd-21.4Cr-12.7Mo) in phosphate-buffered saline solutions by Sarantopoulos *et al.*<sup>61</sup> showed that an increase in open circuit potential resulted in increased nobility. However, the corrosion resistance of these alloys were poorer with a decrease in polarisation resistance and increase in corrosion current density. These alloys exhibited an increased susceptibility to pitting corrosion.

## 2.7 Corrosion behaviour of chromium oxide

Chromium oxide coatings have shown very good chemical inertness, mechanical strength and hardness characteristics.<sup>62, 63</sup> These coatings are used in applications for corrosion protection and wear resistance.<sup>64, 65</sup> However, there are problems with poor adhesion of the coatings on metal substrates, due to the differences in the coefficients of thermal expansion.<sup>63, 66</sup> Apart from this, coatings frequently exhibit pores or micro-cracks, which form paths between the corrosive environment and the substrate, leading to localised galvanic attack and corrosion of the base material.

Liu *et al.*<sup>62</sup> studied the corrosion and tribological behaviour of chromium oxide coatings (prepared by the glow-discharge plasma technique) and AISI 316L stainless steel substrate in 3.5% NaCl solution. They found that  $\text{Cr}_2\text{O}_3$  coatings exhibited better corrosion resistance than AISI 316L stainless steel, and mechanical properties test results showed that the  $\text{Cr}_2\text{O}_3$  coatings had high hardness, and adhered well to the steel substrates. The coating also displayed excellent wear resistance and low coefficient of friction under dry sliding wear test conditions.

In their studies on the corrosion behaviour of various  $\text{Cr}_2\text{O}_3$ -based ceramics in supercritical water-cooled reactor (SCWR) environments, Dong *et al.*<sup>67</sup> found that the coatings suffered degradation due to their porous morphologies, which increased the grain boundary attack and the oxygen concentration, causing the dissolution of  $\text{Cr}_2\text{O}_3$ .

## 2.8 Corrosion in mine environments

In underground mines,  $\text{SO}_4^-$ ,  $\text{Na}^+$ ,  $\text{Ca}^+$ ,  $\text{Mg}^{2+}$  and  $\text{Cl}^-$  ions in the water with different pH values, and  $\text{CH}_4$ ,  $\text{CO}$ ,  $\text{CO}_2$ ,  $\text{H}_2\text{S}$  and  $\text{SO}_2$  in the air as emissions from mine equipment, create corrosive environments.<sup>68-70</sup> The effect of these in the corrosive mine water may lead to leakage in pump components, high replacement rates and costly maintenance. Aggressive mine water often leads to corrosion of pipes, well screens, ponds, bridges, water intakes and pumps.<sup>71</sup> Corrosion attack on pump systems is a critical issue in mining, as well as in mineral processing industries. The most common forms of corrosion on mine pump systems are uniform attack, caused by sulphuric acid, and pitting and crevice corrosion, caused by the presence of chlorides.

Information on piping and pumping systems and the history of their performance were surveyed by Carter<sup>72</sup>, revealing the extent of the problems due to erosion and corrosion experienced within the mining industry. The survey was restricted to material-handling systems, which include pumps, valves, piping, bends, and other pipe fittings, and showed that failure was due to erosion and abrasion at bends and T-pieces. The erosive nature of the fast-flowing corrosive solutions greatly accelerated the rate of metal loss, and led to the formation of undercut pits. Incorrect material selection, poor maintenance, poor installation, faulty design and manufacture had exacerbated the premature failure of these systems. The summary of the survey is given in Table 2.1.<sup>72</sup>

From Table 2.1, the components which caused failures of pumps were the bearings, shafts, seals and balancing discs among others, followed by failure due to abrasion, incorrect operation and materials selection of pump components. The components with manufacturing defects and ingress of mud into clear water systems could also cause failure of pump components. The pump had only failed twice due to corrosion.

Ash *et al.*<sup>73</sup> reported the corrosive and erosive effect of acid mine waters on metals and alloys for pumping equipment and drainage facilities. The mine water was highly corrosive, and attacked pumping equipment and drainage facilities used to remove and control the water in underground mines. As shown in Table 2.2<sup>73</sup>, the mine water caused severe erosion corrosion at 25°C, and contained acidic components of  $\text{SO}_4^{2-}$  and  $\text{SO}_4^{3-}$ , with  $\text{CO}_3^{2-}$ , and  $\text{CO}_3^{3-}$  as alkaline components. Elements such as Fe, Cl, Al, Ca, Mg and Mn, and silica were dissolved solids, and the mine water had a specific resistance of 390-1040  $\Omega\cdot\text{m}$ . The specific resistance, a measure of the ability of the mine water to resist the flow of current, is important because it measures the transfer of charge through ions *i.e.* conductivity in a solution, which is necessary for corrosion to occur.<sup>7, 11, 74</sup> The

conductivity is often related to the potential for corrosion, and depends on the species in the solution.

Higher levels of carbonates tend to decrease the corrosion rate, while higher concentrations of the aggressive ions and sulphates to increase corrosion.<sup>73</sup> The pumping equipment and drainage facilities were protected from corrosion by lining them with wood staves, glass, and later with cement. Test coupons were suspended in sumps, pump discharges and flumes at four USA anthracite mines. Using immersion tests, stainless steels (Series 302, 303, 304, 316, 410, 416, 430, 446, 304L, Armco 17-4 PH and Armco 17-7 PH) were compared, and had adequate corrosion resistance to severely corrosive acid mine water as shown in Tables 2.2-2.4.<sup>73</sup>

Despite the corrosiveness of the environments, steels did not corrode apart from the 416 and 304L stainless steel, which had about 0.0025-0.0127 mm·y<sup>-1</sup> (Table 2.3). There were some pits and cracks observed on surfaces of the samples after exposure in the corrosive sumps (Table 2.4). Pits and cracks were also observed on the wrought and cast stainless steels, which also showed corrosion resistance in the acid mine water. Only 1020 and 502 with 5 wt% Cr steels showed high corrosion rates, and they dissolved in the solution during the first day of exposure.

**Table 2.1.** Summary of the survey on failure of pump components in material-handling systems in the mining and mineral-processing industry, July 1986.<sup>72</sup>

Cause of failure	Number of times
Manufacturing defects	3
Ingress of mud into clear-water systems	3
Incorrect operation	5
Incorrect choice of material	5
Failure of bearings, shafts, seals, balancing discs, etc.	11
Abrasive attack	6
Corrosive attack	2

**Table 2.2.** Analysis of acid mine water from 4 anthracite mines in Pennsylvania, USA, January 1953-January 1954. 73

Component		Mine								
		Marvine			Loree		Wamanie		Storrs	
		Sump 1	Sump 2	Sump 3	Sump 4	Sump 5	Sump 6	Sump 7	Sump 8	Sump 9
pH		5.9	3.4	3.5	3	3	2.9	2.9	3	3.1
(ppm)	Acid: SO <sub>4</sub> <sup>2-</sup>	0	196	147	450	397	33	335	274	225
	Acid: SO <sub>4</sub> <sup>3-</sup>	7	389	308	1 032	1 029	680	865	477	556
	Alkaline: CO <sub>3</sub> <sup>2-</sup>	18	-	-	-	-	-	-	-	-
	Total solids	955	2 000	1 830	2 066	2 580	2 684	2 820	1 971	1 830
	Suspended solids	52	14	13	0	0	79	83	11	10
	Dissolved solids	903	1 986	1 817	2 066	2 580	2 605	2 737	1 960	1 820
Filtered water (ppm)	Total iron	5.6	46	68	68	40	84	83	85	82
	Ferrous iron	1.5	0	0.5	0.5	0	0	0.5	0.5	0
	Sulphate	550	1 192	1 540	1 540	1 510	1 595	1 683	990	978
	Chloride	8	14	14	14	18	15	16	12	16
	Aluminium	2	50	58	58	83	28	35	6	38
	Calcium	131	200	155	155	166	168	195	126	120
	Magnesium	42	125	159	159	160	189	210	90	68
	Manganese	0.8	10	18	18	20	174	17	8	8
	Silica	5	23	31	31	30	15	18	24	21
Specific resistance, Ωm		1 040	530	565	440	444	410	390	600	560



**Table 2.3.** Corrosion rates (mm·y<sup>-1</sup>) of specimens in acid mine water from different anthracite mines in Pennsylvania, USA, January 1953-January 1954.

73

Mine	Item	Stainless steels						
		410	416	430	304L	Armco17-4PH	Armco17-7PH	
Marvine	Sump	Mass loss (mg)	0	2.5	0	0.5	3.5	1.5
		Exposure (h)	816	816	816	816	816	816
		Corrosion rate	0	0	0	0	0	0
		Appearance at 7.5x magn.	No attack	No attack	Two small pits	Incipient pits in weld	Few small pits	Incipient pits
	Discharge	Mass loss (mg)	0	3.5	0	0.5	3.5	0
		Exposure (h)	1 452	1 452	1 452	1 452	1 452	1 452
		Corrosion rate	0	0	0	0	0	0
		Appearance at 7.5x magn.	2 small etched areas	Incipient pits	One small pit	Small pits in weld	Edge cracked	Rust stain
	Flume	Mass loss (mg)	0	11.5	0	0	4.5	2
		Exposure (h)	1 593	159	1 593	1 593	1 593	1 593
		Corrosion rate	0	0.0025	0	0	0	0
		Appearance at 7.5x magn.	2 small etched areas	No attack	No attack	Scratched	Incipient pits	No attack

**Table 2.3. Continues...**

Mine	Item	Stainless steels						
		410	416	430	304L	Armco17-4PH	Armco17-7PH	
Loree	Sump	Mass loss (mg)	0	32.5	0	0	8.5	0
		Exposure (h)	2 184	2 184	2 184	2 184	2 184	2 184
		Corrosion rate	0	0.0025	0	0	0	0
		Appearance at 7.5x magn.	Many scratches	Small pits	Small pits	Incipient pits	1 small etched area +incipient pitting	One pit. Edge cracked
	Discharge	Mass loss (mg)	1	5	0	0.5	2.5	1
		Exposure (h)	1 866	1 866	1 866	1 866	2 184	1 866
		Corrosion rate	0	0	0	0	0	0
		Appearance at 7.5x magn.	Few incipient pits	One small pit	No attack	Long pit in weld. Pits in base metal	Edge cracked. Incipient pits	Edge crack. 4 small pits
Storrs	Sump	Mass loss (mg)	0	11.5	0	95	3	2.5
		Exposure (h)	1 485	1 485	1 485	1 485	1 485	1 485
		Corrosion rate	0	0.0025	0	0.0127	0	0
		Appearance at 7.5x magn.	Few incipient pits	No attack	No attack	Small pits in weld. Incipient pits in base metal	No attack	Few small pits

**Table 2.3. Continues...**

Mine	Item	Stainless steels						
		410	416	430	304L	Armco17-4PH	Armco17-7PH	
Wanamie	Discharge	Weight loss (mg)	0	4	0	0.5	2	1
		Exposure (h)	212	212	212	212	212	212
		Corrosion rate	0	0.0025	0	0	0	0
		Appearance at 7.5x magn.	One rusted area. Several pits	No attack	No attack	One pit in weld	Edge cracked. Incipient pits	One long pit. Several on back
	Flume	Mass loss (mg)	0	3.5	0	0	1.5	2
		Exposure (h)	212	22	212	212	212	212
		Corrosion rate	0	0.0025	0	0	0	0
		Appearance at 7.5x magn.	Incipient pitting	Incipient pitting	Few small pits	Incipient pitting in weld	Cracked edge Incipient pits	One area incipient pitting. Few small pits

**Table 2.4.** Summary of immersion tests in acid mine water of stainless steel specimens and their surface appearances.<sup>73</sup>

Material		Exposure (h)	Mass loss (mg)	Corrosion rate (mm·y <sup>-1</sup> )	Appearance at 7.5x magnification
Wrought stainless steels	302	3 710	0.1	0	Some etching in small localised areas near outer edge; many small shallow pits
	303	7 968	3.6	0	Nine spindles had no apparent attack during 11 months' testing
	304	504	0	0	Many small shallow pits underneath
	316	840	0	0	Few small, shallow pits
	410	3 834	0.1	0	Crevice corrosion more severe; fewer small shallow pits; machining marks - so no attack
	430	4 012	0	0	No crevice attack; fewer small shallow pits
	446	1 008	0	0	One side smoother; showed more shallow pits; no crevice corrosion
	Armco 17-4 PH	7 968	0	0	Three spindles had no apparent attack during 11 months' testing
	Armco 17-7 PH	840	0	0	No attack, except for very few, small shallow pits and no crevice corrosion
Cast stainless steels	CE30	720	0	0	Very few small shallow pits; concentric abrasion circles apparent; no crevice attack
	CF8M	888	0	0	Very few small shallow pits; no crevice attack
	HC	3 666	0	0	Very few small shallow pits; no crevice attack
	HC Special	720	0	0	Very few small shallow pits; no crevice attack
Steel (1020 casting)		432	508.3	45.2	Samples dissolved during first day of testing
5wt% Cr steel (502)		432	170.4	18.35	Samples dissolved during first day of testing; smoother surface

## 2.9 Corrosion protection methods used in mines

There have been many studies on, and possible protection methods against, corrosion in various mining environments. Lalvani *et al.*<sup>69</sup> analysed water in underground mines and coal preparation plants. Due to recycling of water with very high concentrations of chlorides, sulphates and low pH, costly corrosive attack on metals used in boilers, combustion devices, piping, and other hardware occurred. In contrast, high calcium and magnesium carbonate, and bicarbonate contents inhibit corrosion by forming a protective film on metallic surfaces. Several approaches had been identified which could alleviate this corrosion:<sup>69</sup>

- Changing the construction materials
- Cathodic protection
- Redesign of processes and equipment and
- Dechlorination of coal.

Zinc-doped composite silane films formed by one-step electrochemical deposition for corrosion protection of mild steel were studied by Wu *et al.*<sup>75</sup>. The cross-linked network of organosilane films provided the desired barrier and the doped zinc gave cathodic protection to the steel substrate by its sacrificial dissolution. The increase of the zinc ion concentration in the silane precursor resulted in a constant decrease in potential. Thus, the composite films exhibit improved corrosion performance in NaCl and H<sub>2</sub>SO<sub>4</sub> corrosive solutions and in the atmospheric environment.

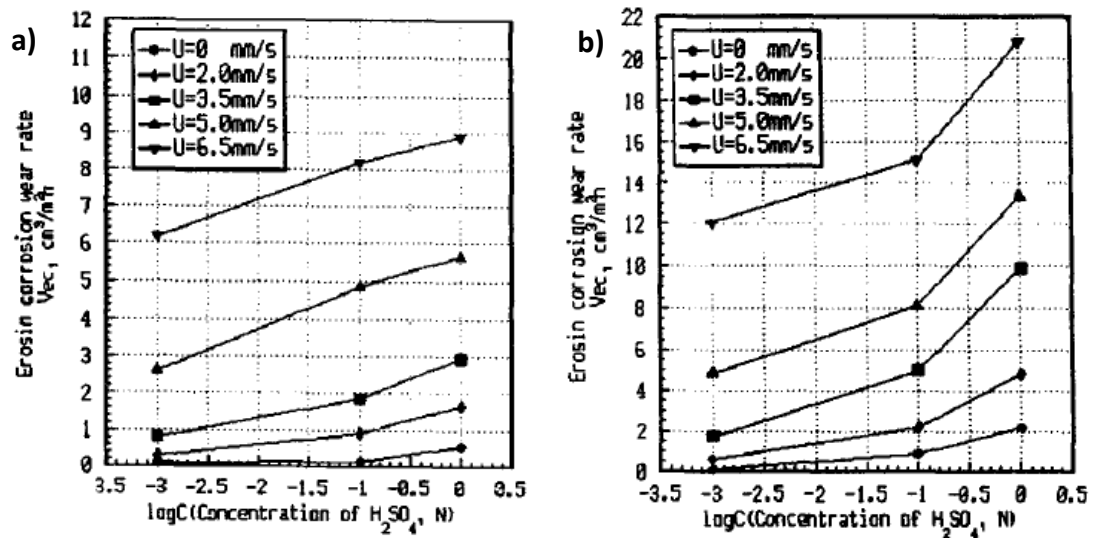
Stainless steel (316L SS) was protected from near neutral and alkaline corrosive solutions containing molybdate and nitrate by electrodeposition of polypyrrole, which is resistant to pitting corrosion in these solutions<sup>76</sup>. The corrosion behaviour of the coated electrodes was investigated in NaCl solutions by electrochemical techniques and scanning electron microscopy. The results showed that coating significantly reduced the pitting corrosion of the substrate.

Romero *et al.*<sup>77</sup> studied different inorganic oxide thin films of MgO, NiO and ZrO<sub>2</sub> as barrier coatings against the corrosion of galvanised steel. The chemical spray pyrolysis technique was used to deposit these thin films. The corrosion behaviour of the coatings was studied using potentiodynamic polarisation and amperometry. Good corrosion protection was found for the NiO coating on aluminised steel in both saline and acidic conditions, whereas the MgO coating only protected against corrosion in acidic conditions.

Austenite stainless steel coatings were deposited by high-velocity air-fuel (HVOF) thermal spray technology.<sup>78</sup> The HVOF system combusts a mixture of compressed air and fuel gas in the combustion chamber. These coatings are widely used for improving corrosion resistance on the surface of steels due to their low cost and high efficiency compared to atmospheric plasma sprayed (APS) and wire-arc sprayed (WAS) austenitic stainless steel coatings. The latter have relatively high amounts of porosity and oxides, since the high temperature particles readily react with oxygen in the atmosphere. The corrosion resistance of coatings formed by HVOF spraying, with and without sealing, was evaluated by salt spray tests for up to 500 h. No corrosion was observed on the sealed coatings.

Laser cladding is the melting and welding of a corrosion-resistant material onto the surface of the machine parts by applying a laser as the heat source,<sup>68</sup> and is a suitable technique to apply an erosion-corrosion resistant coating for many mining machine parts. Wang *et al.*<sup>68</sup> investigated laser clad nickel-based FZCr-60A (wt%: 0.84 C-3.62 B-15.57 Cr-4.33 Si-4.27 Fe-71.37 Ni) alloy layers on 1045 steel and 420 stainless steel, and found an exponential relationship between the H<sub>2</sub>SO<sub>4</sub> concentration and the erosion rate of the slurry (Figure 2.5).<sup>68</sup> Higher erosion-corrosion wear resistance were observed for the laser clad nickel-based FZCr-60A than 420 stainless steel at all erosion rates of slurry and H<sub>2</sub>SO<sub>4</sub> concentrations, making it reasonable to use high performance cladded coatings on plain carbon steel, instead of the high alloy steels used in underground mines.<sup>68</sup> This could be a good material and process to mitigate the corrosion problem at the Otjihase Underground Mine, but laser cladding is expensive, and thus unlikely to be used, although FZCr-60A would have similar costs to Ni-Cr-Fe, because the compositions are similar.

A system of sol-gel coatings and hybrid organic-inorganic coatings together with cerium molybdate nanocontainers loaded with corrosion inhibitor Mercapto-benzothiazole (MBT) was developed for the corrosion protection of hot dip galvanised (HDG) steel.<sup>79</sup> Thin oxide films were deposited on a substrate at lower temperatures than traditional ceramic methods, and provided protection against corrosion by creating an inert barrier between the metal surface and its environment.<sup>79</sup> The corrosion resistance of the coatings was studied using electrochemical impedance spectroscopy (EIS) in 0.5 M NaCl solution for 744 h (31 days). The coatings improved the corrosion protection, and the addition of nanocontainers with corrosion inhibitor improved the anticorrosive properties of the coatings compared to the coatings which had empty nanocontainers, or the coatings which had only the inhibitor.



**Figure 2.5.** Relationship between erosion-corrosion wear rate and H<sub>2</sub>SO<sub>4</sub> concentration for: a) laser clad coating, and b) 420 stainless steel.<sup>68</sup>

Phalaborwa Copper Mine, on the western border of the Kruger National Park, RSA, has had corrosion problems in its facilities.<sup>80</sup> Its environmental conditions are dry, dusty and appeared to be a typical Cl environment. The aggressiveness is caused by the acid and zirconia plants, which produce corrosive chemicals, including sulphuric acid. The mine uses the hot dip galvanising (HDG) method to stop corrosion by applying a hot dip galvanised powder coating duplex system, and then overcoating with an epoxy polyester powder.

Díaz *et al.*<sup>81</sup> used chemical vapour deposition (CVD) and physical vapour deposition (PVD) techniques, by low temperature atomic layer deposition (ALD) and filtered cathodic arc deposition (FCAD) to produce a 50 nm thick tantalum oxide nanocoating on a low alloy steel substrate. The film offered excellent mechanical properties and suitable corrosion protection of steels in corrosive sodium chloride aqueous solutions. The immersion tests in a neutral pH solution did not reveal significant coating degradation, except minor coating breakdown and/or pit growth for the ALD sample. However, in the more aggressive acid solution (pH 2), the resistance to localised corrosion was lower and pitting occurred faster in the ALD coating.

Using electrochemical polarisation neutral salt spray (NSS) measurements, Fang<sup>82</sup> investigated the growth process of the phosphate coating on a 30CrMnMoTi alloy steel (composition given in Table 2.5), fabricated by high temperature manganese phosphating. The corrosion potentials of the phosphated steel shifted positively about 480 mV from the uncoated steel in 3.5 wt% NaCl solution, and phosphating for 24 h improved the corrosion resistance of the 30CrMnMoTi alloy steel.

Peng *et al.*<sup>83</sup> used rare earth lanthanum salt and trimethoxy (vinyl) silane as chromate substitute for galvanised steel passivation, and compared it with zinc coated samples treated with chromate. The galvanised steel sample was immersed in a 0.1 mol.L<sup>-1</sup> La(NO<sub>3</sub>)<sub>3</sub> to form a rare earth film and 4 vol.% trimethoxy (vinyl) silane making a complex passive film. Another galvanised steel was immersed in 0.05 mol.L<sup>-1</sup> CrO<sub>3</sub> for comparison. The rare earth and silane gave excellent corrosion protection on the galvanised steel, which was more effective than Cr alone. This was due to the formation of a rare earth film on the zinc surface, which formed a surface barrier, blocking the cathodic sites and hindering the cathodic reactions.

Molybdates have been used as alternatives to hexavalent chromates in pitting corrosion prevention on mild steel, where molybdate ions adsorbed on the surface and formed a complex with the ferrous (Fe<sup>+2</sup>) ions.<sup>84</sup> In the presence of dissolved oxygen, the ferrous ions oxidised to ferric (Fe<sup>+3</sup>) ions, which formed an insoluble corrosion protective barrier of ferric molybdate, and protected the steels against chlorides and acid attack.

Kalendová *et al.*<sup>85</sup> studied the properties of organic coatings containing polyaniline (PANI), in combination with other anti-corrosive pigments such as zinc phosphate dihydrate (Zn<sub>3</sub>(PO<sub>4</sub>)<sub>2</sub>·2H<sub>2</sub>O), calcium metaborate (Ca<sub>3</sub>(BO<sub>3</sub>)<sub>2</sub>) and strontium chromate (SrCrO<sub>4</sub>), and PANI with zinc dust (>97% Zn). Epoxy coatings, an acidic aqueous Zn<sub>3</sub>(PO<sub>4</sub>)<sub>2</sub>·2H<sub>2</sub>O extract, a basic aqueous Ca<sub>3</sub>(BO<sub>3</sub>)<sub>2</sub> extract and a neutral aqueous SrCrO<sub>4</sub> extract were used in an atmosphere of 5 vol.% SO<sub>2</sub> and 10 vol.% NaCl. The accelerated corrosion test results revealed that PANI + Zn<sub>3</sub>(PO<sub>4</sub>)<sub>2</sub>·2H<sub>2</sub>O increased the corrosion resistance of the organic coatings. Both pigments had the same acidic pH of the aqueous extract, which may have led to very high corrosion resistance. However, excellent corrosion protection was provided by the PANI<sub>PVC=5%</sub> + Zn-dust in a SO<sub>2</sub> environment and in NCl.

**Table 2.5.** Composition of 30CrMnMoTi alloy (wt%).<sup>82</sup>

Mo	Ti	Ni	Cr	Cu	S	P	Mn	Si	C	Fe
0.27	0.08	0.06	1.16	0.060	0.02	0.02	0.77	0.33	0.33	Bal.

Epoxy varnish coatings were applied on cold rolled steel plate substrates, and exposed to an artificial weathering environment produced by fluorescent UV/condensation weathering equipment for different times.<sup>86</sup> The degradation of the epoxy varnish coating was studied by electrochemical impedance spectroscopy (EIS), scanning electron microscopy (SEM) and adhesion tests. The electrochemical behaviour of weathered



coatings was closely related to the formation and development of blisters on the surface, due to coating degradation.

The coating resistance decreased after 28 days of exposure, which indicated significant deterioration of the barrier properties. The soluble degradation products penetrated into the coating, along with water, to form osmotic cells, leading to the formation of blisters on the coating surface under the alternating wet and UV irradiation conditions. Small blisters were observed on coating surface after 21 days exposure. With increasing ageing time, blisters grew and subsequently ruptured. The spread of degraded areas caused the growth and development of blisters. With the loss of coating material and embrittlement of the coating, cracks appeared on the surface and the blisters broke, which resulted in significant deterioration of the coatings.

## 2.10 Ruthenium as an alloying element

Ruthenium is a noble metal of the platinum group metals (PGMs).<sup>87</sup> It is a hard, lustrous, white metal. Its melting point is  $\sim 2334$  °C, with a density of  $2.45 \text{ g.cm}^{-3}$ . Other PGMs are platinum, palladium, rhodium, iridium, and osmium. They occur together in nature and are produced from the same ore.<sup>88</sup> They are mined mainly in South Africa, Russia, and North America. PGMs are highly resistant to wear, tarnish and chemical attack and resist corrosion in aggressive environments.

Due to the above mentioned properties, PGMs are sometimes added to alloys, *e.g.* to Co-based alloys, to give improved mechanical and chemical properties. Ruthenium is used more than other PGMs, since it is the least expensive metal of the group, and it is readily available in South Africa<sup>89, 90</sup>, and may also be used as an effective hardener, producing alloys that are extremely corrosion- and wear- resistant.<sup>87</sup>

However, from a metallurgical point of view, in order to improve the corrosion resistance of Co–Cr alloys, the PGM additions should be uniformly distributed in the Co–Cr matrix.<sup>91</sup> The binary phase diagrams shows Au (a precious metal with similar solubility properties to the PGMs in Co) is not really soluble in Cr, but is slightly soluble in Co, while platinum is very soluble in Co, and but has limited solubility in Cr.<sup>91</sup> Ruthenium has a good solubility in the Co–Cr matrix compared to other PGMs and precious metals.<sup>92</sup> Thus, it is sometimes added to alloys to improve the corrosion resistance. This modification of an alloy by adding a small amount of a corrosion resistant PGM to it is known as cathodic modification.<sup>92</sup>

Potgieter *et al.*<sup>92</sup> studied the effect of additions of small quantities of Ru on the electrochemical behaviour of austenitic stainless steel in organic acids. They found that the corrosion potential of the samples alloyed with Ru moved to more positive potentials with increasing Ru, *i.e.* corrosion resistance of these samples increased with Ru additions.

Banda *et al.*<sup>90</sup> found that small additions of ruthenium up to 0.66 wt% Ru significantly improved the pitting potentials of the LDX2101 duplex stainless steel in aerated 3.56% NaCl aqueous solution. There was also no detrimental effect to the microstructure of the steel. In addition, Ru also lowered the current required to maintain the passive state of the steel. Ruthenium also increased the passive range of LDX2101 duplex stainless steel. Sherif *et al.*<sup>89</sup> also found similar results when they studied the effects of minor additions of ruthenium (up to 0.28 wt% Ru) on the passivation of duplex stainless steel in 2 M HCl solution. The presence of Ru in the steel showed a significant positive shift in the corrosion potential towards more noble values, and so the steel was protected from general and pitting corrosion in the solution tested.<sup>89</sup> This addition of Ru also caused a reduction in the corrosion rate of the steel.

Olaseinde<sup>93</sup> cathodically modified 2101 duplex stainless steel with Ru additions (up to 10 wt% Ru), and studied the modification effects in 0.5 M HCl, 0.5 M H<sub>2</sub>SO<sub>4</sub>, 1 M H<sub>2</sub>SO<sub>4</sub>, 3.5 M NaCl and 1 M H<sub>2</sub>SO<sub>4</sub> + 1% NaCl solutions. The results agreed with those of Potgieter *et al.*<sup>87, 92, 94, 95</sup>, Pirso *et al.*<sup>93</sup>, Karamiş *et al.*<sup>94</sup> and Sheriff *et al.*<sup>115</sup> Ruthenium additions increased the corrosion potential to more noble values in all the solutions. Spontaneous passivation was also observed with a wide range of passivity. The critical current density, the passive current density and the corrosion rate decreased with increasing ruthenium content. The hysteresis loops showed more resistance behaviour to pitting corrosion in 1 M H<sub>2</sub>SO<sub>4</sub> acid than in 3.5 M NaCl, although no pits were observed on the microstructures after corrosion.

## **2.11 Friction and wear**

### **2.11.1 Mechanism of friction**

Friction is the tangential resistance to motion, or impending motion, between two contacting solid bodies,<sup>96</sup> and is not a material property but rather a system response.<sup>97</sup> The resistive tangential force is called the friction force, and acts in the opposite direction to the direction of the motion. Friction can be understood using a ratio known as the coefficient of friction,  $\mu$ , a dimensionless quantity given by the ratio of two forces acting perpendicularly: the frictional force experienced,  $F$  (N), and the normal load on the

object,  $W$  (N) to the interface between the two bodies under relative motion or impending relative motion.<sup>98</sup> Thus:

$$\mu = \frac{F}{W} \quad \text{Equation 2.10}$$

There are two types of friction coefficients, the static coefficient of friction representing the friction opposing the onset of relative motion (impending motion), and the kinetic coefficient of friction representing the friction opposing the continuation of relative motion once that motion has started.<sup>98</sup> These coefficient of friction are defined in Equations 2.11 and 2.12:<sup>98</sup>

$$\mu_s = \frac{F_s}{W} \quad \text{Equation 2.11}$$

$$\mu_k = \frac{F_k}{W} \quad \text{Equation 2.12}$$

where:  $F_s$  = frictional force just sufficient to prevent the relative motion between two bodies,  $F_k$  = frictional force needed to maintain relative motion between two bodies, and  $W$  = force normal to the interface between the sliding bodies. The values for  $\mu_s$  and  $\mu_k$  for some materials are known and readily available.

### 2.11.2 Mechanisms of wear

Williams<sup>99</sup> defined wear as the progressive damage, involving material loss, which occurs on the surface of a component as a result of its motion relative to the advancement working parts. A wear mechanism was described by Petrica *et al.*<sup>100</sup> as scratching and grooving, combined with multiple indentations due to rolling or sliding hard particles. Wear arises from the friction forces created by the resultant interaction of the working part's surface roughness features.<sup>96</sup> The consequences of wear include the cost of replacement of parts and loss of production.

The definition of wear is generally based on loss of material, but it should be emphasised that damage due to material displacement on a given body, with no net change in weight or volume, may also constitute wear.<sup>97</sup> Wear is not a material property, it is a system response and is influenced by the operating conditions. The five main types of wear are: abrasive, adhesive, tribocorrosion (corrosive wear), sliding and erosion wear.<sup>56, 101, 102</sup>

Adhesion wear occurs when the interaction of asperities (*i.e.* the small peaks due to the roughness of the surfaces), after sticking together at only a few raised places on two opposed surfaces in motion, result in their fracture.<sup>74, 120</sup>

According to Gee<sup>101</sup>, abrasion wear occurs when hard particles from, or within, the worked material (rock, metal, ceramic) are dragged across the surface of the tool or wear part. Corrosive wear is the synergistic effect between chemical reaction at a surface and mechanical wear processes.<sup>74, 120</sup> Sliding wear (delamination wear) occurs when two solid surfaces slide over each other, with or without lubricant resulting in material transfer or loss from either surface, and erosive wear involves the removal of material from the surface of a component by the high-speed impact of a liquid or of a stream of hard particles carried in a flowing fluid.<sup>56, 101</sup>

Abrasive wear is a removal of materials due to scratching between two surfaces in relative motion, resulting in development of furrows or grooves on the soft material.<sup>56, 103</sup> Abrasion wear is categorised into two basic modes, namely, two-body abrasion wear, which occurs when a hard body slides over a soft surface, producing grooves due to ploughing and micro cutting of the softer material, and three-body abrasion wear, which occurs when a third body (an abrasive particle) enters the space between two parts in relative motion.<sup>94, 104, 105</sup>

The three terms used to describe the various types of abrasive wear in mining industry are<sup>106-108</sup>:

- Scratching abrasion: occurs by repeated scratching or scouring action of hard, sharp and small particles moving over the solid surface at varying velocities.
- Grinding abrasion: occurs when small abrasive particles are forced against a metal surface with enough force to fracture and be crushed generating sharp cutting edges.
- Gouging abrasion: occurs where abrasion is combined with strong impacts induced by large and heavy objects, which are forced with pressure against a solid surface, leaving prominent gouges and grooves.

These types of abrasive wear depend on hardness, microstructure and the work hardening properties of the material being abraded. Abrasive wear resistance of certain alloys often depends on carbide content; as the latter is increased, the wear rate is reduced.<sup>106, 109</sup>

Tribocorrosion (corrosive wear) involves mechanical and chemical or electrochemical interaction between bodies in relative motion<sup>110</sup>, so that corrosive wear occurs when two rubbing surfaces interact within a corrosive environment.<sup>56</sup> A metallic surface within a corrosive environment is often covered with a thick protective film which depends on its adherence to the substrate and ability to deform without cracking, and when locally worn, the exposed areas oxidise and reform the film.<sup>111</sup> This wear mode is confined to the

formation and removal of oxide films and is referred to as tribocorrosion or oxidative wear. However, not all coatings are protective in all environments. A schematic diagram of the process of tribocorrosion mechanisms is shown in Figure 2.6.<sup>110</sup>

### **2.11.3 Wear resistance of cobalt-based hardfacing and chromium oxide coatings**

Cobalt-based alloys such as Co-Cr-Mo and Co-Cr-W possess good wear resistance due to high carbon contents, similar to WC-Co based alloys.<sup>94, 112</sup> These wear-resistant cobalt-based alloys consist of  $\text{Cr}_7\text{C}_3$  hard particles dispersed in cobalt-chromium solid solution matrix<sup>113</sup>, e.g. Co-Cr-W/Mo. These carbides provide resistance to low-stress (or two-body) abrasion, which is encountered when surfaces are in relative motion with packed abrasives. Higher carbon content means higher resistance to low-stress abrasion, although carbide particle size also has a strong influence. In addition, cobalt alloys resist wear due to their ability to absorb energy through the fcc to hcp transformation and through twinning.<sup>114</sup>

Levy and Crook<sup>115</sup> investigated the erosion properties of various alloys for the chemical processing industries. They concluded that cobalt-based (Co-Cr-W-C and Co-Cr-W) alloys exhibited lower erosion rates than the austenitic stainless steels and Ni-Cr-Mo alloys. They suggested that this was due to low stacking fault energy, a fcc structure and or the tendency of the structure to transform from fcc to hcp under the action of mechanical stress.

The evaluation of the sliding wear resistance of cobalt-based and iron-based super alloys in a molten zinc bath was done by Zhang and Battiston<sup>116</sup>, using a submerged bearing test rig. Journal bearings with similar materials running against each other suffered severe wear and experienced heavy oscillation in coefficient of friction. However, this oscillation was from experimental anomalous behaviour. The coefficient of friction for all the materials tested was within the range 0.1-0.25, and there was no correlation between the coefficient of friction and the amount of wear a material experienced.

Cobalt-based and  $\text{Cr}_2\text{O}_3$  coatings are used in mining and other industries, due their unique properties, such as corrosion resistance, self-lubrication, wear resistance, good adhesion, strength and machinability.<sup>63, 95, 117, 118</sup> They are among the hardest engineering and industrial materials.<sup>63, 119</sup>

It would be expected that friction is independent of hardness as the coefficients of friction of all clean metals vary by less than a factor of two.<sup>120</sup> However, it is well known

that the coefficient of friction of hard substances, such as tungsten carbide, hard chromium, and hard steels, is less than that of softer metals.<sup>96, 120, 121</sup>

Cetinel *et al.*<sup>64</sup> studied the tribological behaviour of Cr<sub>2</sub>O<sub>3</sub> (as bearing materials) flame spray coated onto a AISI 304L steel substrate. The study was conducted under dry and acid environments (1% H<sub>2</sub>SO<sub>4</sub>) using a pin-on-plate tribometer configuration against the AISI 303 counter material for different loads. They found that in 1% H<sub>2</sub>SO<sub>4</sub>, the wear loss was less than in the dry condition, and the applied load level was more effective in the dry condition. The wear mechanisms revealed by SEM were generally characterised by local plastic deformation, cracks, pits, wear debris grooves, scratches and wear tracks.

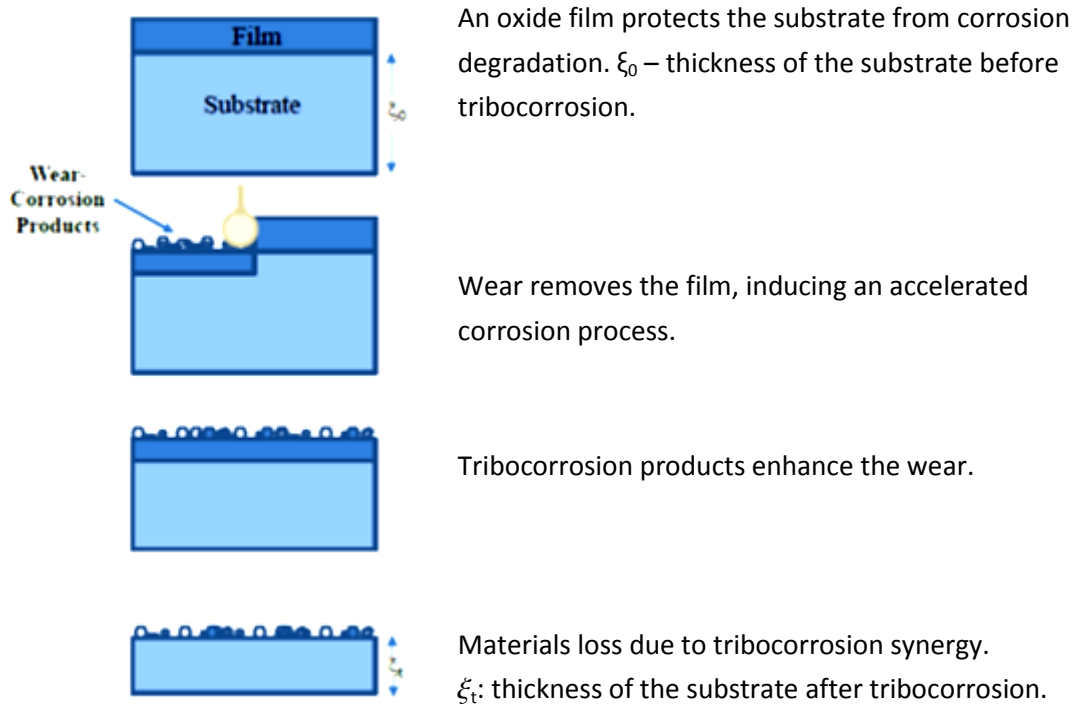
Similar wear mechanisms to those identified by Cetinel *et al.*<sup>64</sup> were also found by Ahn and Kwon<sup>122</sup> in their study of tribological behaviour of plasma-sprayed chromium oxide coatings on SS41 steel. The study was conducted using oscillating friction and wear tester in dry and lubricated conditions.

## **2.12 Fundamentals of tribocorrosion**

### **2.12.1 Mechanism of tribocorrosion**

Tribocorrosion can be defined as a process of simultaneous corrosion and wear taking place at contacting surfaces in relative motion with a synergy between wear and corrosion.<sup>9</sup> A schematic diagram of the progress of tribocorrosion is shown in Figure 2.6.<sup>110</sup> Tribocorrosion is also one of the major problems affecting the performance of equipment in many engineering fields.<sup>9</sup> Wear occurs on an area subjected to sliding, while corrosion occurs on the whole metal surface exposed to the corrosive environment. In mining components or medical implants, tribocorrosion often reduces the life-times of parts in contact.

Tribocorrosion may occur under a variety of conditions, such as sliding, fretting, rolling, impingement) in a corrosive medium.<sup>9</sup> Sliding is a reciprocating movement of two surfaces in contact. The surfaces contact may be two-body – when the surfaces of those contacting parts directly slide one over the other, or three-body contact when the sliding surfaces are separated by particles which are usually the wear debris. When a passive material is subjected to sliding conditions, worn surfaces are formed where the passive layer is removed, while the unworn areas remain passive.<sup>123</sup>



**Figure 2.6.** Schematic diagram of the progress of tribocorrosion.<sup>110</sup>

The tribocorrosion mechanism is based on a repetitive tearing off of the surface oxide after each contact, and eventually a removal of some of the underlying material.<sup>124</sup> During this action, oxide particles, the debris, are released from the contacting materials. Tribocorrosion products include grooves parallel to the direction of the sliding direction, smeared layers and severe delamination from the subsurface and crack growth.<sup>9</sup>

### 2.12.2 Measurement of tribocorrosion

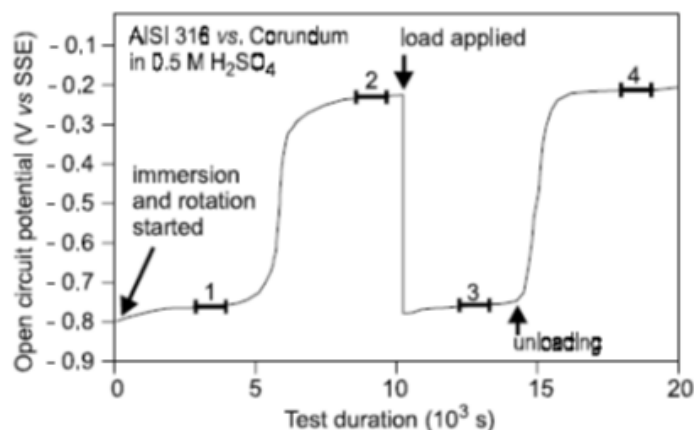
The interaction between mechanical and chemical factors leading to tribocorrosion is best understood using corrosion techniques. These are *in situ* tribological experiments that are carried out in aqueous ionic electrolytes under controlled electrochemical conditions.<sup>125</sup>

Open circuit potential (OCP) is a technique which records the potential of the working electrode relative to a reference electrode when no current is flowing in a tribocorrosion cell. This measurement of the potential of the metal (sample) in the test solution can be generated as a function of time.<sup>124, 125</sup> The measurement is performed with a potentiostat during the tribological test. Other techniques include the evaluation of galvanic cells, but the most relevant techniques for this study were the OCP and potentiodynamic measurements.

Ponthiaux et al.<sup>124</sup> used an OCP technique to study tribocorrosion processes of an AISI 316 stainless steel in aerated 0.5 M H<sub>2</sub>SO<sub>4</sub>, sliding against a corundum ball. The OCP was measured against a saturated calomel electrode during and after applying a 10 N load (Figure 2.7).<sup>124</sup>

Before starting the test, the sample was immersed in the solution, and OCP increased, indicating a stable passive surface state was achieved (Areas 1 and 2 in Figure 2.7). During loading, a sudden decrease of OCP took place (Area 3), and was close to the OCP at immersion. During unloading, the OCP increased back to the initial value (Area 4). This indicates that a passive state on the surface of the stainless steel was re-established in the wear track area.

Tribocorrosion wear mechanisms of a plasma carburised Stellite<sup>®</sup> 21 Co–Cr alloys were studied by Chen and Dong<sup>126</sup> using a reciprocating wear tests in 3.5% NaCl solution. The corrosion potentials of these materials were between 21.6 mV and 277 mV, and the materials exhibited strong passive behaviour. The transpassive region started around 600 mV and oxidation of Cr<sup>3+</sup> to Cr<sup>6+</sup> probably occurred under these conditions. Their EDX results indicated oxygen, sodium and chlorine in the wear track, as well as much ploughing, while BSE imaging showed worn carbides and the ploughed areas crossed through them, with cracks formed in the interface of the carbide/matrix. This work is relevant to the current study, which aims to solve corrosion and wear problems at the Otjihase Underground Mine.



**Figure 2.7.** Variation of OCP of an AISI 316 stainless steel sample in 0.5M H<sub>2</sub>SO<sub>4</sub> before (Areas 1 and 2), during (Area 3), and after loading (Area 4) against a corundum ball at 10 N load.<sup>124</sup>



## 2.13 Basics of thermal spray coating

### 2.13.1 Thermal spray coating techniques

Various technologies are used to deposit a coating on base materials include: electroplating, electroless plating and hot-dip galvanising, vapour deposition, thermal spray techniques, weld overlays.<sup>127-130</sup> The current research used coatings deposited by thermal spraying. The American Welding Society defined thermal spraying as a group of processes in which finely divided metallic or non-metallic materials are deposited in a molten or semi-molten condition on a prepared substrate to form a spray deposit (coating).<sup>128</sup> This includes processes that use the thermal energy generated by chemical (combustion) or electrical (plasma or arc) methods to melt, or soften, and accelerate fine particles or droplets to a substrate at a high speed.<sup>130</sup>

Thermal spraying processes include the techniques:<sup>129, 130</sup>

- Beam *e.g.* laser spraying
- Thermal spraying by liquid *e.g.* molten bath spraying
- Thermal spraying by gas *e.g.* flame, detonation, high velocity flame and cold gas spraying
- Thermal spraying by electric gas discharge *e.g.* arc and plasma spraying

Thermal spray coating is used to protect pump components against wear and corrosion due to its excellent erosion and abrasion resistance, high hardness and toughness.<sup>131</sup> Since the current research project needed coatings, thermal spraying was targeted, because it is an easy technique to coat pump components and other materials that may be subjected to wear operations and is widely used commercially.

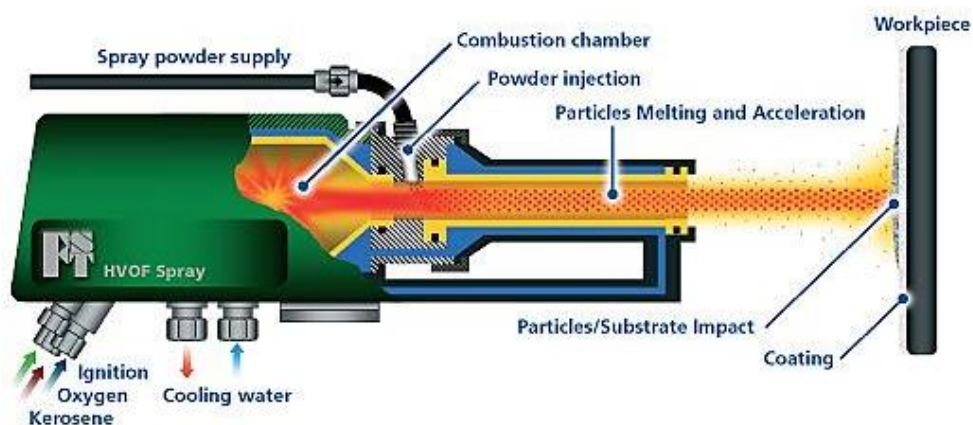
The most widely used thermal spray coating technique is high velocity oxy-fuel flame (HVOF) and plasma spraying. The HVOF method produces good microstructures compared to other spraying methods.<sup>132, 133</sup> These methods use powders with sizes ranging from negative to positive mesh size. The negative particle size means the particles pass through the sieve, and a positive particle size means particles are retained by the sieve.

HVOF spray coating has major applications in industries where protection against wear, friction and corrosion is needed<sup>102</sup>. In the mining industry, it is used for protection of slurry pump components.<sup>134</sup> The HVOF-sprayed coatings may have bond strengths of ~90 MPa, porosity lower than 1 %, and the coating thicknesses in the range 100–300 µm.<sup>135</sup>

Plasma spraying is also used to spray materials such as hardfacing coatings in mining and other industries, where a synergy of corrosion and wear is observed.<sup>131</sup> It offers a more economical alternative to high velocity oxygen fuel (HVOF) spraying.<sup>136</sup> Plasma-sprayed ceramics coatings may have bond strengths from 15-25 MPa, porosity from 1-7 %, and the coating thicknesses in the range 300 to 1500  $\mu\text{m}$ .<sup>145</sup> Prior to spray coating of ceramics, a bond coat is usually sprayed on the substrate. The most-used bond coat is NiCrAlY, which produces a dense, adherent bond between the substrate and the top coating.<sup>145</sup>

### 2.13.2 The HVOF thermal spray process

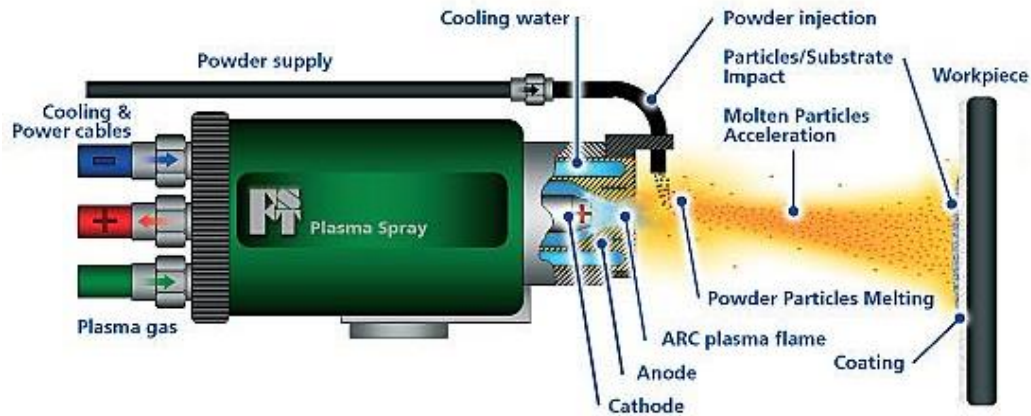
The HVOF process consists of fuel gas or liquid introduced into the combustion chamber, together with oxygen; the gas ignites at a high temperature and pressure,<sup>130, 135</sup> powder is introduced into the jet, and the exhaust gas is formed by a nozzle. The molten or semi-molten particles pass through the nozzle, and emerge at a high speed into the open atmosphere moving towards the substrate. The combustion chamber and nozzle are cooled by water. A schematic diagram of a HVOF set-up is shown Figure 2.8.<sup>137</sup>



**Figure 2.8.** Schematic diagram of a HVOF combustion chamber.<sup>137</sup>

### 2.13.3 Plasma spray process

Plasma spraying is carried out in an open atmosphere.<sup>98, 105</sup> A high-powered jet of ionized argon, helium and hydrogen (plasma) melt ceramic powders. The molten powder particles are then sprayed on to the substrate, cooled down rapidly and solidified, forming a very strong thermal spray coating on a substrate surface. A schematic diagram of a plasma spray is shown Figure 2.9.<sup>137</sup>



**Figure 2.9.** Schematic diagram of a plasma spraying chamber.<sup>137</sup>

## 2.14 Study approach

The literature review showed that different materials had been used in various environments, with various degrees of success. Some of the materials were too expensive to be used in the mine, *e.g.* the alloys with palladium. Information on the materials used in the mine was limited, and no reports were found on the target materials being used in the mine. Thus, studies of the corrosion and wear behaviour will fill a knowledge gap, and help to identify the best alloys for use in the mine. The potential of adding ruthenium to any targeted replacement material was identified, especially if the source was powder.

Some coating methods were also discussed, and because of the good properties chromium oxide was identified to be used as a benchmark.

Some of the experimental techniques used were described, and the relevant standards were identified.

# CHAPTER 3: EXPERIMENTAL PROCEDURE

---

## 3.1 Introduction

This chapter describes the materials, experimental procedures and equipment which were employed to investigate the corrosion behaviour of the materials of the pump components at Otjihase Underground Mine, and the corrosion and wear properties of candidate alloys which are being considered as replacements for the materials currently being used for the pump components (shaft sleeve and valve). These procedures include:

- Characterisation of the failed pump components, including corrosion tests,
- Corrosion, wear and tribocorrosion testing of the materials for replacement of the currently failed pump components at Otjihase Underground Mine, in bulk form, to ascertain their suitability.
- Thermal spray deposition of coatings on mild steel substrate, including with different ruthenium contents, and
- Corrosion, wear and tribocorrosion testing of the coated samples for replacement of the currently failed pump components at Otjihase Underground Mine.

The components collected from the mine were tested for corrosion. The shaft sleeve samples were cylindrical, making it hard to cut standard pieces for wear and tribocorrosion testing. Thus, wear and tribocorrosion tests were not performed for comparison with the proposed materials.

## 3.2 Materials

### 3.2.1 Materials for bulk studies

The materials used for preliminary study were as-cast ULTIMET<sup>®</sup>, ToughMet<sup>®</sup>3, Hastelloy<sup>®</sup>G30 (supplied by Multi Alloys South Africa and HAYNES Int. USA) and Stellite<sup>®</sup>6B (supplied by Multi Alloys South Africa and Kennametal Stellite, Koblenz, Germany). The chemical compositions of these alloys are given in Table 3.1. Samples from Otjihase Underground Mine pump systems, such as: a mild steel shaft sleeve with a nickel-chromium coating (INCONEL Alloy 600) and a cast iron valve were also collected for optical emission spectrometry (OES) characterisation at Scrooby's Laboratory Service cc., Johannesburg, and for failure analysis. Samples were photographed using a Nikon COOLPIX L310 camera, and a Nikon SMZ 745T stereo microscope.

A516 G70 mild steel substrate for all the coatings was supplied by MACSTEEL Service Centres (Pty) Ltd, SA, and 99.9% Ruthenium powder with mesh size of -100 was supplied by Johnson Matthey (Pty) Ltd, SA. All the powders, except ruthenium, are standard for use in commercial thermal spray coatings.

**Table 3.1.** Typical chemical compositions of the test materials (wt%).<sup>121, 138, 139</sup>

Element	Composition (wt%)			
	Hastelloy G30 <sup>117</sup>	ULTIMET <sup>141</sup>	Stellite 6B <sup>140</sup>	ToughMet 3 <sup>117</sup>
Ni	Balance	9.00	2.60	15.00
Co	5.00	Balance	Balance	-
Cr	28.00–31.50	25.00	28.80	-
Mo	4.00–6.00	5	1.50	-
W	1.50–4.00	2	4.50	-
Mn	1.50	0.80	1.00	-
Fe	13.00–17.00	3.00	2.50	-
Si	0.80	0.30	1.30	-
Sn	-	-	-	8
C	0.03	0.05	1.20	-
Cu	1.00–2.40	-	-	Balance
Nb	-	0.01	-	-
N	-	0.08	-	-
P	0.04	-	-	-
S	0.02	-	-	-
Nb+Ta	0.30–1.50	-	-	-

### 3.2.2 Materials for spray-coating studies

ULTIMET and Stellite 6 alloy powders were supplied by WEARTECH (Pty) Ltd and FE Powder Supplies (Pty) Ltd, SA, and Cr<sub>2</sub>O<sub>3</sub> powders were supplied by Thermal Spray (Pty) Ltd, Olifantsfontein, SA. Thermal spraying was chosen as the method of depositing the coating, because the technique was easily accessible, and although the quality of the coatings might not be optimal, at least some results for comparisons would be obtained.

The particle sizes and distribution of the powders were determined by a MS 200 Malvern Mastersizer<sup>®</sup> analyser, using laser diffraction to measure the size of particles with water as dispersant. The technique measures the intensity of light scattered when a laser beam passes through the dispersed particulate samples.<sup>140</sup> This intensity was then analysed using Malvern Mastersizer<sup>®</sup> software to calculate the size of the particles that created the scattering pattern. The powders were also placed on to aluminium sample holders using

conductive double-sided carbon tape to examine their sizes and morphologies using SEM-EDX analysis.

The ULTIMET and Stellite 6 powders were each mixed with Ru additions at Wits University using a TURBULA<sup>®</sup> T2F Shaker Mixer. The quantity of 1.5 g of Ru was added to 498.5 g of ULTIMET or Stellite 6 powders to provide 0.3 wt% Ru addition to the ULTIMET or Stellite 6, while 3 g Ru was added to 497 g of ULTIMET or Stellite 6 powders to provide 0.6 wt% Ru. The 0.3 and 0.6 wt% Ru compositions were chosen for comparison with no Ru composition, and ensure that there was no deleterious effect by Ru on the electrochemical and mechanical properties. These amounts were deliberately kept small, because ruthenium is expensive, although effective in small amounts. The higher addition was double that of the smaller one, and the gap was thought to be sufficient to distinguish between their different effects. A mass of 500 g for each coating were placed in a 500 mL closed plastic container, and mixed at 97 rpm in a cylindrical mixing chamber subjected to translational and rotational motion. The container was held in place by twisted rubber rings. Alumina balls with diameters of 6-12 mm were used to homogenise mixing.

Prior to coating, the substrates were pre-treated by removing any rust or corrosion products using acetone before being grit-blasted with 20 grit abrasive to ensure good adhesion of the coating layer to the substrate.

The surfaces of the substrates were pre-heated before coating. Samples of 12 mm thick ASTM A516 Grade 70 steel were high velocity oxygen fuel (HVOF) spray coated with a commercial alloy of CoCrNiW (ULTIMET), CoCrNiMo (Stellite 6), and plasma sprayed with chromium oxide ( $\text{Cr}_2\text{O}_3$ ) powders at Thermal Spray (Pty) Ltd, Olifantsfontein, SA. The spraying was done using a FANUC<sup>®</sup> System R-J3iB connected to a FANUC robot R-200 iA 16SF for ULTIMET and Stellite 6, and a SULZER METCO 9MC Plasma Control Unit for  $\text{Cr}_2\text{O}_3$  connected to a FANUC System R-J robot S-700. A NiCrAlY powder (22.0 Ni, 10.0 Cr, 1.0 Al, Y in wt%) was used as an undercoat (bond coat) on the substrate prior to  $\text{Cr}_2\text{O}_3$  plasma coating. The powder and steel compositions, and the operation parameters used are given in Tables 3.2 and 3.3.

Chromium oxide was used as a benchmark because it exhibits very good chemical inertness and hardness<sup>57, 67</sup>, and is widely used in corrosion protection and wear resistance applications. As  $\text{Cr}_2\text{O}_3$  is difficult to corrode, plastically deform or be ploughed during both wet and dry sliding wear processes<sup>57</sup>, it was used as a benchmark for this study.

### 3.3 Metallographic preparation

Samples from the pump components were collected from Otjihase Underground Mine, and cut at Wits using an ATM<sup>®</sup> Brillant 200 cutting machine for metallographic characterisation. All other samples used in this study were also cut by this method.

To study the microstructures, and for smooth surfaces for hardness testing, XRD analysis, electrochemical, tribocorrosion and abrasive wear measurements, the pump components, as-cast and as-sprayed coating samples were hot mounted in PolyFast<sup>®</sup>/MultiFast<sup>®</sup> resin and successively wet ground using 80, 120, 220, 1200 papers and 9 µm diamond suspension. Finally, the wet ground samples were polished on polishing cloths using 6, 3 and 1 µm diamond suspension for optical microscopy and SEM-EDX analysis.

**Table 3.2.** Chemical composition of ULTIMET, Stellite 6 and Cr<sub>2</sub>O<sub>3</sub> commercial alloy powders and ASTM A516 Grade 70 mild steel substrate.<sup>121, 138, 139</sup>

Sample	Element (wt%)													
	Co	C	Cr	Si	W	Fe	Ni	Mn	Mo	B	P	S	N	O
ULTIMET	Bal.	0.1	25.6	0.4	2.1	3.2	9.5	0.7	5.2	<0.1	<0.1	<0.1	0.1	0.1
Stellite 6	Bal.	1.1	30.3	1.3	4.8	2.3	2.5	0.4	0.2	0.4	0.1	0.1	-	-
Cr <sub>2</sub> O <sub>3</sub>	-	-	98.2	-	-	-	-	-	-	-	-	-	-	1.8
Mild steel	-	0.2	-	0.3	-	Bal.	-	1.1	-	-	-	-	-	-

**Table 3.3.** Operating parameters of the HVOF and plasma spraying processes.

Parameter	HVOF	Plasma spray
Spraying distance (mm)	380	100
N <sub>2</sub> flow rate, as powder carrier (m <sup>3</sup> .h <sup>-1</sup> )	52	0.8-0.9
H <sub>2</sub> : NiCrAlY; Cr <sub>2</sub> O <sub>3</sub> (m <sup>3</sup> .h <sup>-1</sup> )	-	11, 15
Ar: NiCrAlY; Cr <sub>2</sub> O <sub>3</sub> (m <sup>3</sup> .h <sup>-1</sup> )	-	40, 50
O <sub>2</sub> flow rate (m <sup>3</sup> .h <sup>-1</sup> )	56.6	-
Mesh size (µm)	-66.23 to +22	-35 to +15
Powder feed rate (g.s <sup>-1</sup> )	2.5	3.2
Substrate preheating temperature (°C)	47	138

The Hastelloy G30, ULTIMET and Stellite 6 specimens were etched electrolytically in 100 mL HCl and 5 mL H<sub>2</sub>O<sub>2</sub> (30%). Each sample was immersed and a 10 V DC was applied on its surface for 5 seconds. INCONEL Alloy 600 was etched in equal parts of HCl, HNO<sub>3</sub> and acetic acid, swabbing for 1 minute at room temperature. For ToughMet 3, a mixture of 5 g Fe(NO<sub>3</sub>)<sub>3</sub>, 25 mL HCl and 70 mL water etchant was used, swabbing for 3 minutes at

room temperature. The microstructure for Cr<sub>2</sub>O<sub>3</sub> coating was sufficiently revealed without etching.

### **3.4 Microscopy and hardness tests**

To examine the microstructures of the samples, a Zeiss Sigma field emission scanning electron microscope with EDX, using secondary electron (SE) and backscattered electron (BSE) modes, and optical microscope, Leica CTR6000, were used. The grain sizes of the bulk samples, the globular particle sizes of the coatings, and the carbide proportions were measured by the line intercept method, with at least 20 placements done on each<sup>141</sup>. Five EDX spot analyses were taken per phase, and the average was recorded.

Hardness tests were performed using a Vickers FM-700 microhardness tester, with 2 kg and 3 kg loads (on two different machines while one was broken). For statistical reproducibility, the tests were carried out 5 times, and the average and standard deviation were recorded.

### **3.5 XRD analysis**

The powder samples were loaded using the back loading technique for X-ray diffraction analysis before thermal spraying using a Panalytical X'pert Pro Diffractometer, employing Fe filtered Co-K $\alpha$  radiation, at angles  $2\theta = 0-120^\circ$ . Data interpretation was performed by means of Panalytical Highscore Plus analytical software, together with the PanICSD database.

Samples were prepared metallographically for X-ray diffraction analysis before and after corrosion measurements, one pair condition, as is normal practice. A BRUKER<sup>®</sup> D8 ADVANCE diffractometer was used at 40 kV and 40 mA, using molybdenum radiation with a wavelength of 0.7 Å. Diffractograms were recorded in a non-spinning regime for 5 hours, at angles  $2\theta = 15-100^\circ$ . Phase identification was done using Eva 3.2 software with an in-built database. The crystalline characteristics of the samples were determined by Rietveld refinement, to quantify the amounts of the phases.

### **3.6 Analysis of synthetic and Otjihase mine water**

The Otjihase Mine water was collected from three sumps (Kuruma, Satellite and Conveyor No. 6) and tested at the Chemistry Department, University of Namibia for sulphate, nitrite and chloride by ion chromatography, and conductivity and TDS using an EUTECH Cyber Scan Con1103K Con 11 meter, turbidity by EUTECH TN100 meter, trace elements by inductively coupled plasma optical emission spectroscopy (ICP-OES) and the pH was instantly measured at sumps by EUTECH Cyber Scan pH300 meter. These sumps were



chosen because the pump components at the sumps experience more degradation than at other sumps, *e.g.* the North and the 22 BOOC pumps.

Synthetic mine water (a manufactured solution representing the most aggressive water found in gold mines in South Africa<sup>142</sup>), after electrochemical tests, was tested for conductivity using an ORION STAR A212 conductivity meter; TDS, salinity, resistivity, pH using an ORION STAR A211 pH meter; cations ( $\text{Na}^+$ ,  $\text{Ca}^{2+}$  and  $\text{Mg}^{2+}$ ) and anions ( $\text{SO}_4^-$  and  $\text{Cl}^-$ ) using atomic absorption spectroscopy (AAS), and inductively coupled plasma optical emission spectroscopy (ICP-OES) at Mintek, Randburg, South Africa, and inductively coupled plasma mass spectrometry (ICP-MS) at the Department of Chemistry, Wits University.

### **3.7 Corrosion measurements**

The Ni-Cr-Fe coating, mild steel substrate and cast iron from the Otjihase Mine, and the ULTIMET, Stellite 6B, ToughMet 3 and Hatelloy G30 bulk alloys, as well as ULTIMET, Stellite 6 and  $\text{Cr}_2\text{O}_3$  coatings were tested for cyclic potentiodynamic polarisation, tribocorrosion (coatings only) testing in synthetic mine water solution of composition given in Table 3.4.<sup>142</sup> This was prepared by dissolving masses of salts in de-ionised water (pH 6), and acidified with 32% HCl to pH 3 and 1, which is comparable to the pH of the sumps in the Otjihase Underground Mine.

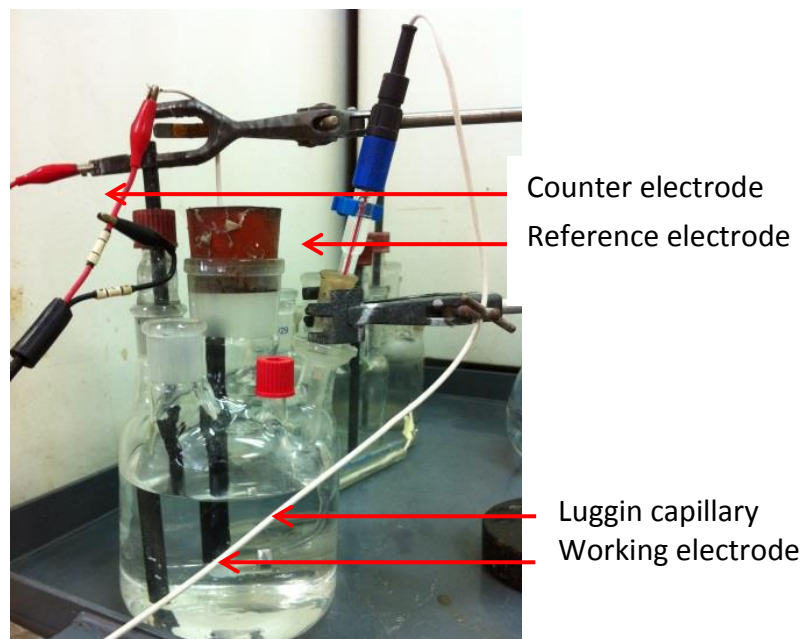
#### **3.7.1 Cyclic potentiodynamic polarisation measurements**

Cyclic polarisation measurements were performed to assess the passivity, pitting, and repassivation behaviours of the alloys in synthetic and acidified synthetic mine water. Every sample was ground to 9  $\mu\text{m}$  and connected to a copper wire by an aluminium tape before being cold-mounted in epoxy resin for 12 hours at room temperature. The exposed areas of the samples to the corrosive environment were measured, and each was aimed to be 1  $\text{cm}^2$ .

The electrochemical measurements were carried out in a corrosion cell with three electrodes (Figure 3.1): working electrode (sample), auxiliary (counter) electrode and reference electrode in accordance with ASTM Standards G5-94<sup>143</sup> and G102-89<sup>144</sup>. A graphite counter electrode and saturated calomel electrode (SCE) as reference were used. A Luggin capillary with a salt-bridge filled with a KCl solution was used to connect the reference electrode to the cell. To minimise errors due to ohmic drop, the end tip of the capillary tube was placed at about 2-3 mm from the working electrode.<sup>143, 145</sup>

Prior to each test, each sample was degreased and cleaned in ethanol. The counter electrode and the Luggin capillary were cleaned with de-ionised water before any test.

The tests were carried out in synthetic mine water (pH 6) (Table 3.4), and acidified synthetic mine water (pH 3 and 1 (except Hastelloy G30, due to insufficient samples for testing)) at ambient temperature ( $22.3 \pm 1.0^\circ\text{C}$ ). Cyclic potentiodynamic polarisation (CPDP) measurements using an Auto Tafel Potentiostat with Auto Tafel V1.79 and Auto LPR V2.7h software were performed at a scan rate of  $0.2 \text{ mV}\cdot\text{s}^{-1}$  from  $-250 \text{ mV}$  and reversed at  $1500 \text{ mV}$  versus the reference electrode potential after a 60 minute open circuit potential (OCP) scan, to stabilise at the potential applied at which a material may corrode. Linear polarisation resistance ( $R_p$ ), measured  $\pm 25 \text{ mV}$  relative to the corrosion potential ( $E_{\text{corr}}$ ), was used to calculate the corrosion rates of the samples. The corrosion current densities were calculated from values obtained from the polarisation resistance measurements. After polarisation, each sample was taken for optical and scanning electron microscopy to study the surface morphologies and films on the surface.



**Figure 3.1.** Electrochemical corrosion cell, showing the electrode and the Luggin capillary.

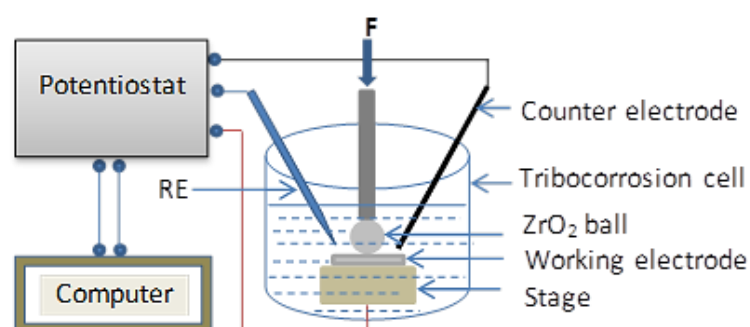
*Table 3.4. Composition of synthetic mine water solution used in the tests.*

Salt	Concentration ( $\text{mg}\cdot\text{L}^{-1}$ )
$\text{MgSO}_4$	198
$\text{Na}_2\text{SO}_4$	1215
$\text{CaCl}_2$	1038
$\text{NaCl}$	1379

### 3.7.2 Tribocorrosion tests

The tribocorrosion behaviour of two chromium-rich cobalt coatings with no Ru, 0.3 and 0.6 wt% Ru additions, Cr<sub>2</sub>O<sub>3</sub> coatings and a mild steel substrates as a function of load using a reciprocating ball-on-disk configuration in a synthetic mine water (pH 6) at 5 N and 10 N loads, was assessed.

Samples were cut into sizes of 20 x 20 x 3 mm, and wet ground to 9 µm, followed by cleaning with running water and then ethanol to prevent any oxidation on the surface. The exposed area of each sample to the test solutions was 1.54 cm<sup>2</sup>. The tribocorrosion behaviour of samples in synthetic mine water (pH 6) solutions were studied by open circuit potential (OCP) and potentiodynamic techniques, using a ball-on-disk reciprocating CETR UMT-2 Micro Tribometer and a three electrode electrochemical cell: working (sample), platinum wire auxiliary (counter) and silver-silver chloride (Ag/AgCl) reference electrodes. The potential of each sample was controlled using an UMT-2, Center for Tribology Inc. (CETR) potentiostat equipped with UMT software, and a 4 mm diameter zirconia oxide (ZrO<sub>2</sub>) ball was used as the counterpart. Figure 3.2 shows a schematic diagram of the experimental set-up.



**Figure 3.2.** Schematic diagram of tribocorrosion cell and test set-up.

Reciprocating sliding wear tests were carried out with 5 N and 10 N (maximum) normal loads, 1 Hz sliding frequency and 2 mm stroke length. The PVC test cell was filled with ~200 ml of the test solution for each test, and fresh solution was used for every test. All the tests were performed at room temperature ( $22.0 \pm 0.2^\circ\text{C}$ ), open to the air, and the scan rate was  $1 \text{ mV}\cdot\text{s}^{-1}$ .

First, each sample was immersed in a solution for 1 h in order to reach a stable potential. Next, potentiodynamic polarisation was performed (from -1 to 1.5 V) to characterise the electrochemical behaviour of the surface before undertaking the sliding wear test. Later, the ZrO<sub>2</sub> ball was loaded on the sample surface and the sliding test was initiated. During and after each sliding wear test, the OCP was continuously monitored. Finally,

potentiodynamic polarisation was performed to characterise the electrochemical behaviour of the surface after sliding. Coefficients of friction ( $\mu$ ) during OCP ( $\mu_{OCP}$ ) and potentiodynamic polarisation ( $\mu_p$ ) measurements were also obtained. After the test, the wear tracks were examined using a Leica CTR6000 optical microscope, and SEM with EDX, using secondary electron (SE) and back scattered electron (BSE) modes. The tribocorrosion rates were calculated from tribocorrosion current density as described in Section 2.4.2.

### 3.8 Abrasive wear measurements

Bulk ULTIMET and Stellite 6B commercial alloys, and as-sprayed coatings of ULTIMET, Stellite 6 and  $Cr_2O_3$  on mild steel substrates were tested for tribological responses at room temperature ( $23.2 \pm 0.1^\circ C$ ) under unlubricated conditions, and humidity of  $54.0 \pm 0.0\%$ . The mild steel substrate was also tested. The samples were ultrasonically cleaned in ethanol and dried before each test. The tests were performed using a CSM tribometer, using 6 mm diameter 100Cr steel balls. The test parameters were  $0.21 \text{ m}\cdot\text{s}^{-1}$  linear speed, 200 m sliding distance, and 5N and 10N applied loads were set in the CSM TriboX software for *in situ* measurement beforehand.

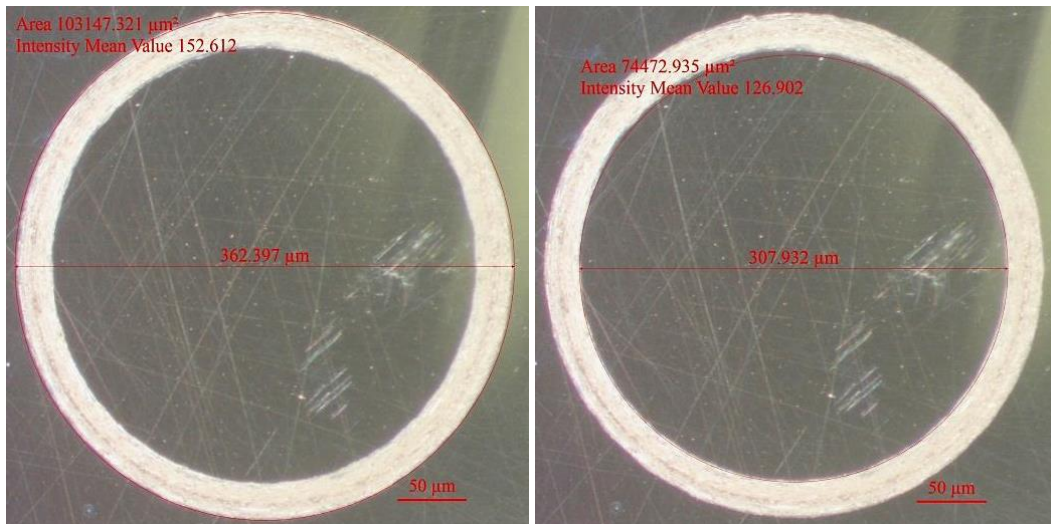
The wear tracks on the samples were measured, to obtain the worn volume of the samples and hence calculate the wear rate of samples. It was assumed that the wear track followed an elliptical path due to the elliptical Hertzian pressure profile that the ball exerts onto the sample<sup>133</sup>. The value of worn volume of the sample ( $V_s$ ) was obtained from the area of the wear track, by measuring five outer and inner diameters of the wear track per sample (an example is given in Figure 3.3) to obtain the outer and inner radii ( $R_2$  and  $R_1$ ), and the maximum penetration depth of the ball into the sample surface,  $Pd_{max}$ .  $V_s$  was calculated using Equation 3.1<sup>133</sup>:

$$V_s = \pi \times (R_2^2 - R_1^2) \times Pd_{max} \quad \text{Equation 3.1}$$

From Equation 3.1, the wear rate was calculated as:

$$k = \frac{V_s}{WS} \quad \text{Equation 3.2}$$

where:  $k$  = wear rate ( $\text{mm}^3(\text{N}\cdot\text{m})^{-1}$ ),  $V_s$  = volume of material lost ( $\text{mm}^3$ ),  $W$  = normal applied load (N), and  $S$  = sliding distance (m).



**Figure 3.3.** Examples of measurements of the diameters of the wear tracks on the samples.

# **CHAPTER 4: EXAMINATION OF CORRODED PUMP COMPONENTS AND THE CORROSION MEDIUM TAKEN FROM OTJIHASE UNDERGROUND MINE**

---

## **4.1 Introduction**

Pump systems operating in highly corrosive mine water at Otjihase Mine experience a high rate of replacement and high maintenance due to corrosion and wear of the pump components. When the pump operates (Figure 4.1), its shaft often experiences corrosion from slurry and wear from debris trapped in the packing gland (Figure 4.2), which further accelerates corrosion.<sup>146</sup> The pump components removed from the mine for investigation were the coated shaft sleeves, and cast iron valves. Their compositions were analysed by optical emission spectrometry (OES) to be mild steel substrates (AISI 1526 grade) with nickel-chromium-iron (Ni-Cr-Fe) coatings (INCONEL Alloy 600, UNS N06600 grade) for the shaft sleeves, and valves made from cast iron (UNS F32800, A536).

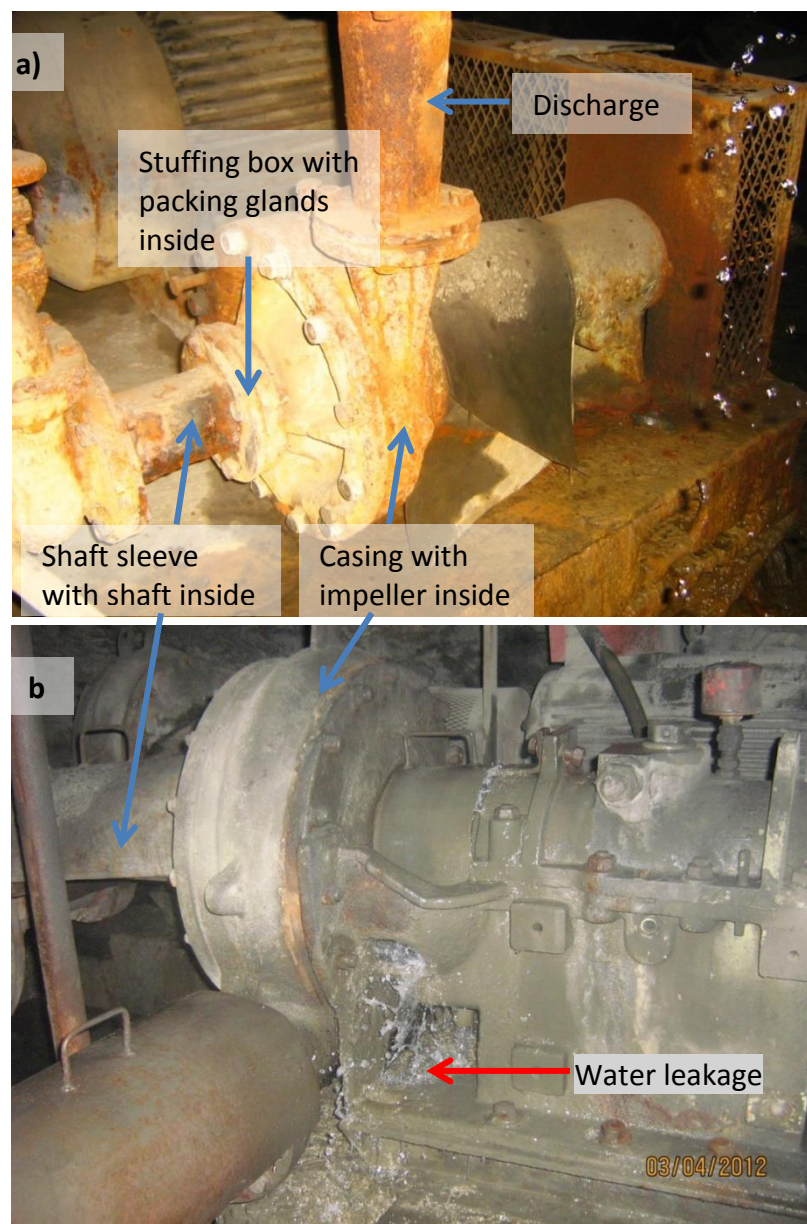
The surface morphology of the samples was studied using optical and scanning electron microscopy. Vickers hardness tests were performed to determine the hardnesses of the samples. The Otjihase Mine water was analysed for composition, as well as for turbidity, conductivity and total dissolved solids, and pH tests were also done. The results were used to suggest candidate alloys to substitute the alloys currently being used.

These samples were tested for corrosion resistance in synthetic mine water by cyclic potentiodynamic polarisation technique. The results were used to ascertain properties of the alternative alloys needed for replacement of the currently being used samples. Their surface morphologies after testing were also studied using SEM/EDX analysis. Due to their good chemical and mechanical properties, ULTIMET, Stellite 6B, ToughMet 3 and Hastelloy G30 bulk alloys were selected in order to mitigate the tribocorrosion problems at the Otjihase Underground Mine.

## **4.2 Surface morphology of samples**

The shaft sleeve was partitioned into six sections (Figure 4.3.), and the valve into three, to examine the corrosion products across the samples. An extra sample was cut from Section 4 of the sleeve (equivalent to Section 2) and ultrasonically cleaned in ethanol. Sections 1 and 6 were mostly not affected by corrosion, while Section 5 showed slight attack. Macrographs were taken in Sections 3 and 4, moving from unaffected to the corroded regions.

As shown in Figure 4.3, Sections 2 and 4 were similarly corroded, and Section 3 was heavily affected. The Ni-Cr-Fe shaft sleeve coating (INCONEL Alloy 600) of ~1000  $\mu\text{m}$  thick (measured by optical microscopy) was worn by debris trapped in packing gland and pitting (Figure 4.4 a)). Once the coating was damaged, the underlying mild steel of the shaft sleeve corroded quickly (Figure 4.4 b)). Figure 4.5 a) shows an optical micrograph of the shaft sleeve sample, showing the thickness of the coating on the substrate. Discontinuities at the interface and cross-section of the substrate after the coating was removed by wear and corrosion are shown in Figure 4.5 b). Figure 4.6 shows a cast iron valve which experienced severe uniform corrosion at Otjihase Underground Mine, Namibia.

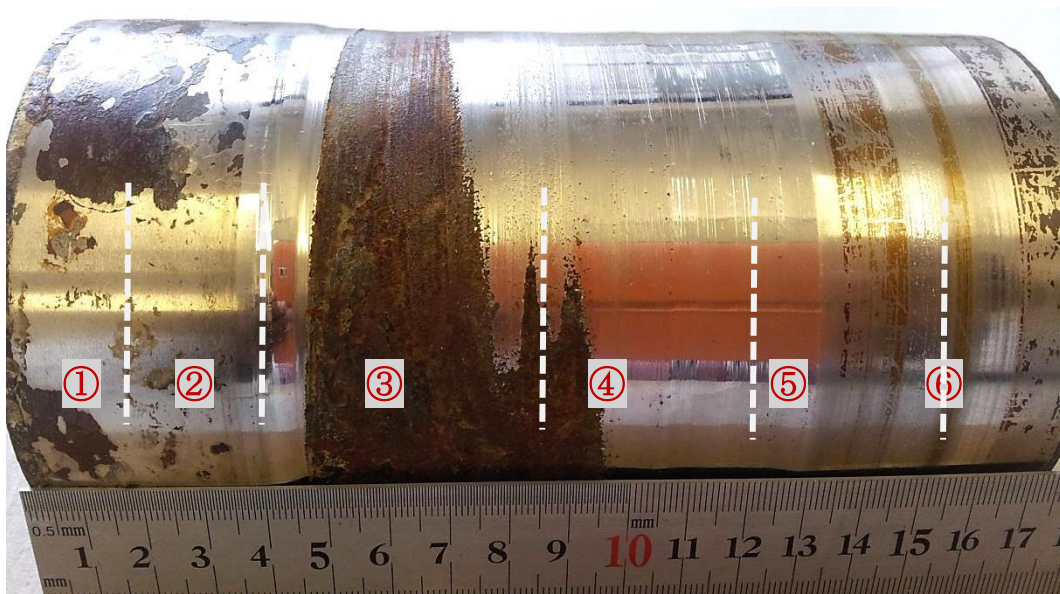


**Figure 4.1.** Pump components at Otjihase Underground Mine, showing: a) corroded pump and little leakage of mine water, and b) leakage from the stuffing box.

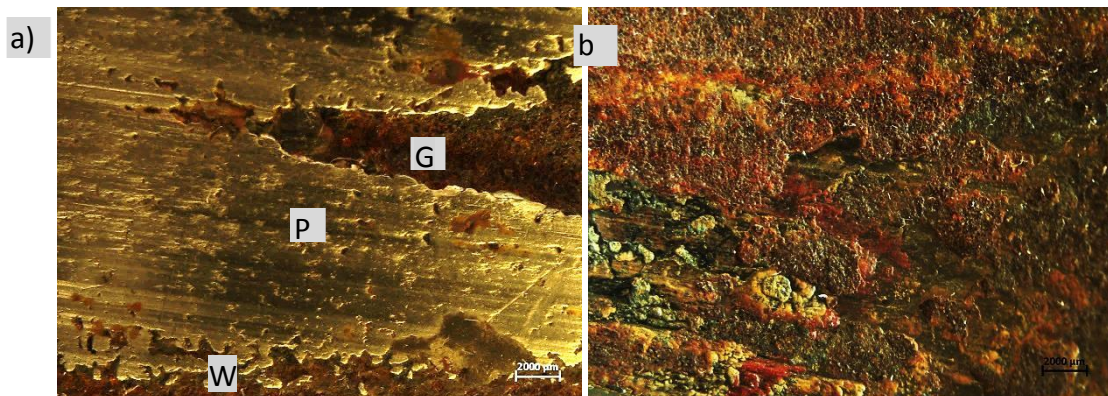




**Figure 4.2.** Graphite filament packing gland which wears the shaft sleeves.

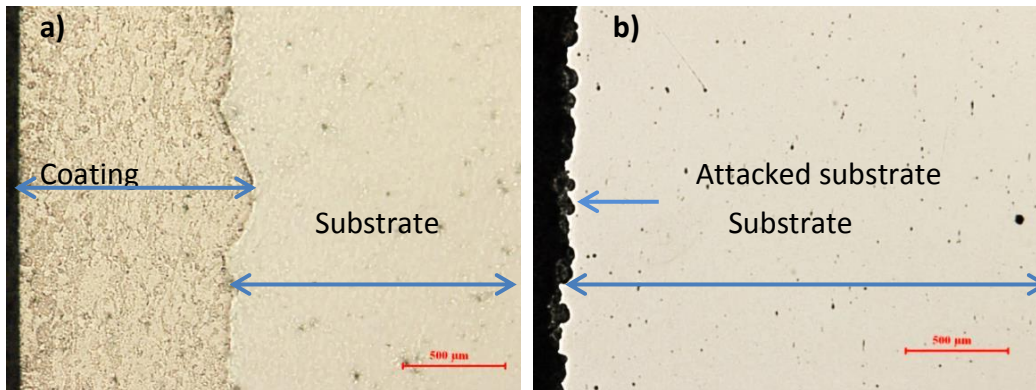


**Figure 4.3.** Photograph of whole corroded shaft sleeve and the selected parts from Sections 3 and 4 from a pump at Otjihase Mine, Namibia.



**Figure 4.4.** Micrographs of shaft sleeve sections showing: a) coating partially removed by wear (W), pitting (P), general corrosion of the substrate (G), and b) attacked substrate after coating removal during service.



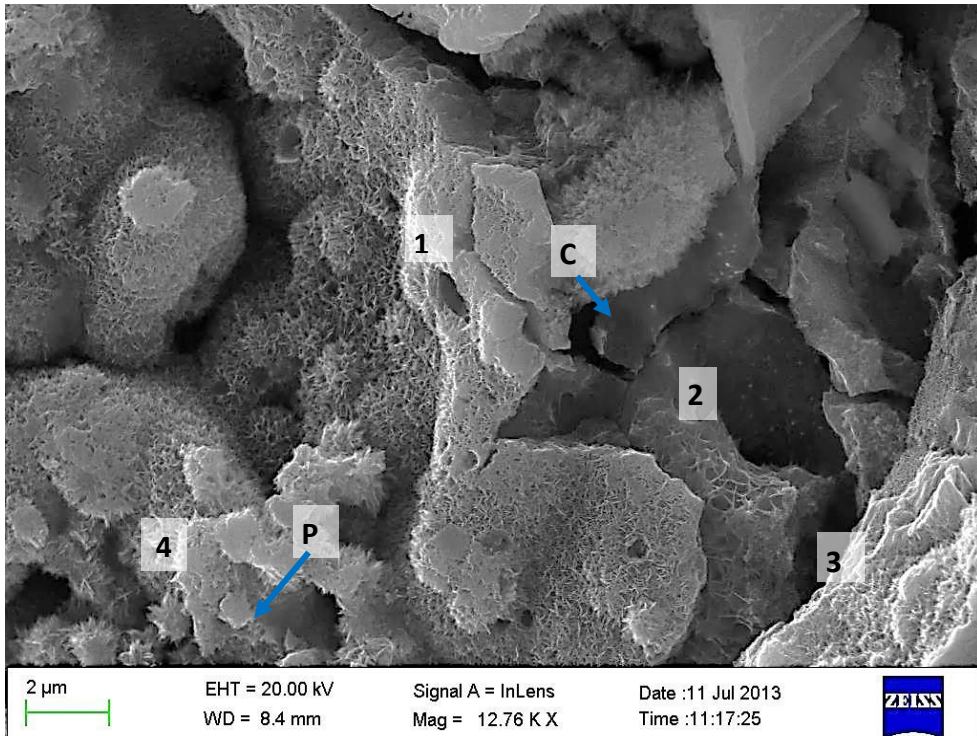


**Figure 4.5.** Optical micrographs of a shaft sleeve cross-section showing: a) substrate and coating on unattacked region. b) substrate of attacked region after coating removal during service.

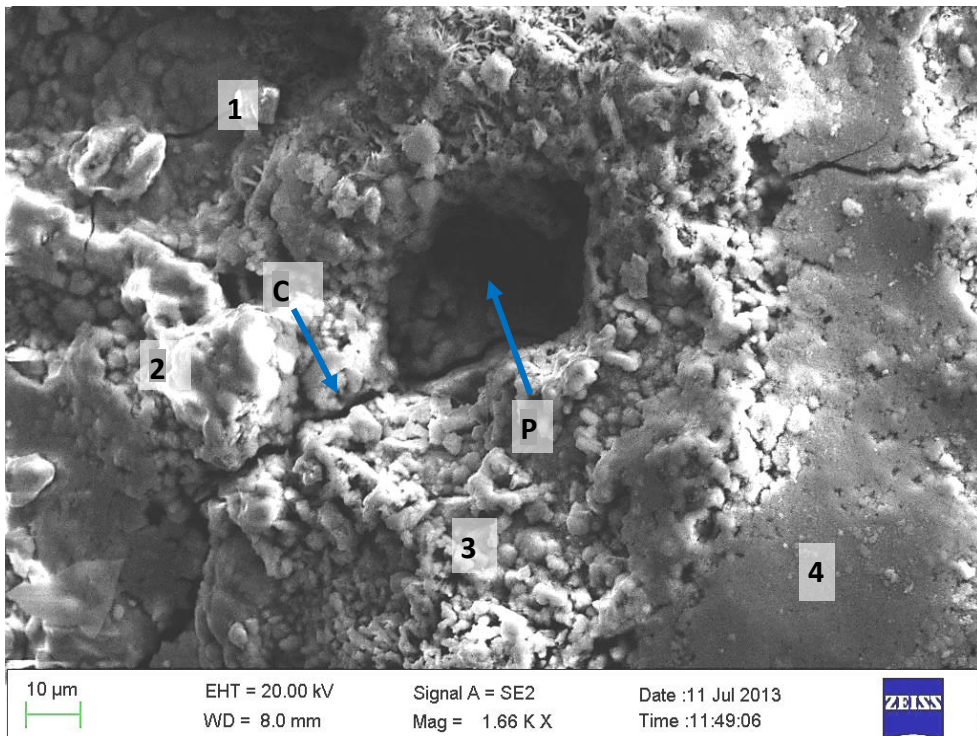


**Figure 4.6.** Photograph of a corroded cast iron valve from a pump at Otjihase Mine, Namibia.

SEM images of the attacked regions of the shaft sleeve and valve were taken (Figure 4.7: Areas 1-4 and Figure 4.8: Areas 1-4), showing irregular, cracked and non-productive oxide layer, with globular structures and pits. Figure 4.9 shows abrasion of the shaft sleeve coating, which removed the protective layer. EDX analyses were done in these areas and the results are given in Tables 4.1 and 4.2, showing B, Fe and O as the main elements present on the surfaces. The high boron content originated from the mine water which was being pumped. The alloy's original boron content was 0.2 wt%.



**Figure 4.7.** SEM In-Lens image of shaft sleeve, showing pits (P) and cracks (C) in substrate attacked region. (Numbers give EDX analysis positions)



**Figure 4.8.** SEM-SE image of the cast iron valve, showing pits, cracks and globular corrosion products. (Numbers refer to EDX analysis positions.)

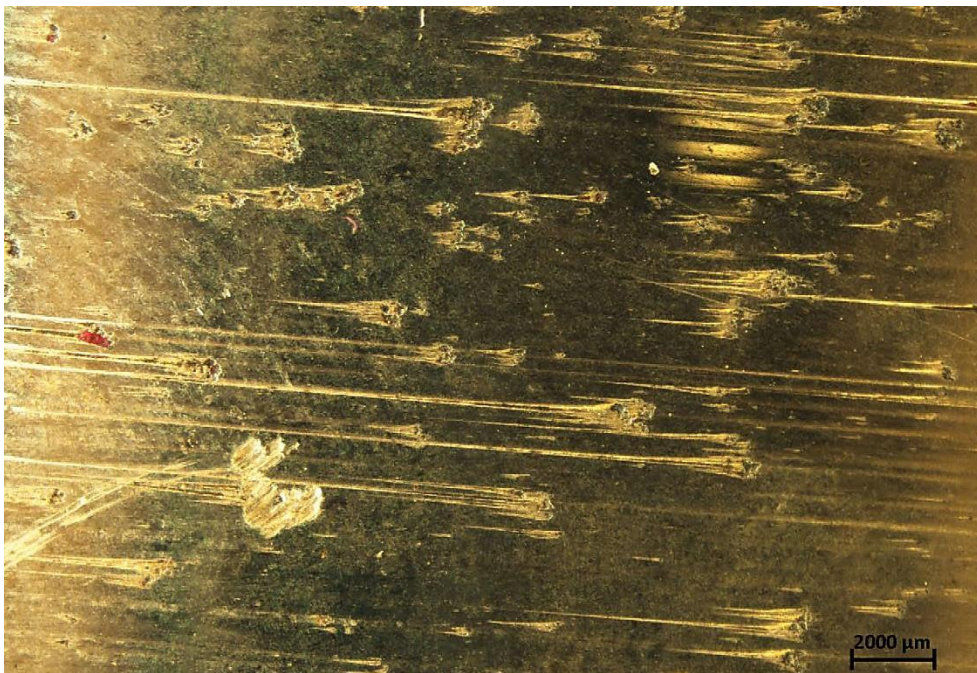


**Table 4.1.** EDX analysis of pits on a mild steel substrate of the areas of the shaft sleeve shown in Figure 4.7.

Element	Composition (wt%)			
	Area 1	Area 2	Area 3	Area 4
B	87.3	100.0	81.7	100.0
O	7.5	-	10.5	-
Mn	0.1	-	0.4	-
Fe	4.0	-	6.9	-
Co	0.2	-	-	-
Ni	0.5	-	0.5	-

**Table 4.2.** EDX analysis of areas given in Figure 4.8 on the cast iron valve surface.

Element	Composition (wt%)			
	Area 1	Area 2	Area 3	Area 4
B	54.0	35.9	39.8	21.8
O	1.6	27.6	20.6	37.3
Si	-	0.4	0.2	-
S	-	0.8	0.4	1.0
Mn	-	0.1	0.4	0.2
Fe	44.8	35.1	38.4	38.8
Co	-	0.5	0.6	0.4
Zn	-	0.1	-	0.6



**Figure 4.9.** Macrograph of the shaft sleeve from Otjihase Mine, showing pits, and the removal of the protective film by abrasion on the Ni-Cr-Fe coating.

### 4.3 Spectrographic analysis of samples

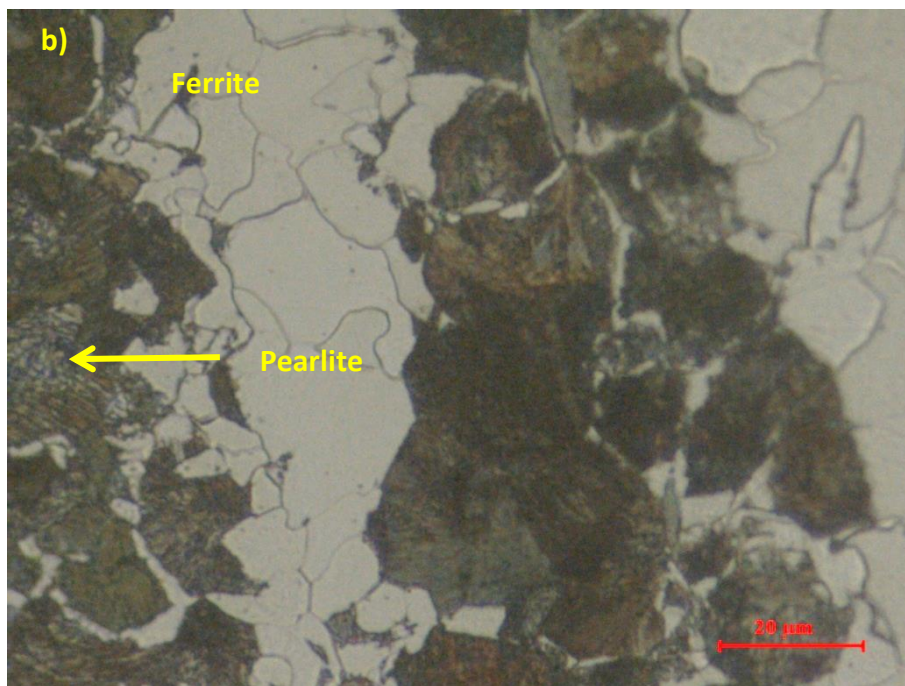
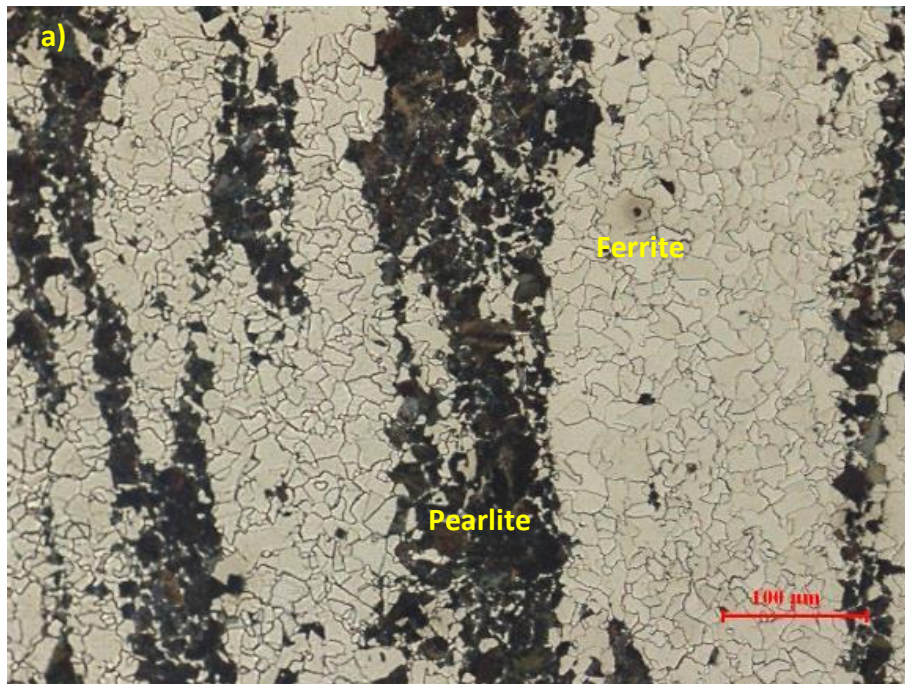
The spectrographic analysis results by optical emission spectrometry (OES) are given in Table 4.3. Iron and Mn were the major components in the mild steel sample, with Si, C, Cu and Cr as minor elements. The shaft sleeve coating contained Ni, Cr, Fe and Si and small amounts of C, Mn, Co and B. The cast iron valve had Fe, C and Si as more major constituents with traces of Mn, P and Ni.

### 4.4 Optical metallography

The optical micrographs show a banded ferrite-pearlite microstructure for the mild steel, with well-defined ferrite grain boundaries (Figure 4.10), and the pearlite was resolvable to show ferrite and cementite alternating layers (arrow in Figure 4.10 b). The shaft sleeve coating had irregular grains of Ni-Cr-Fe and Cr-rich phases, as well as carbide phase (Figure 4.11), confirmed by XRD analysis. The cast iron sample had a nodular graphite in a pearlite and ferrite matrix, with some graphite flakes (Figure 4.12). It is unusual to see so much flake graphite in this alloy, suggesting it was poor quality. Nodules and flakes were light in the corroded product region, and dark in the uncorroded region. Ferrite and graphite flakes were light in the corroded product region, and dark in the uncorroded region.

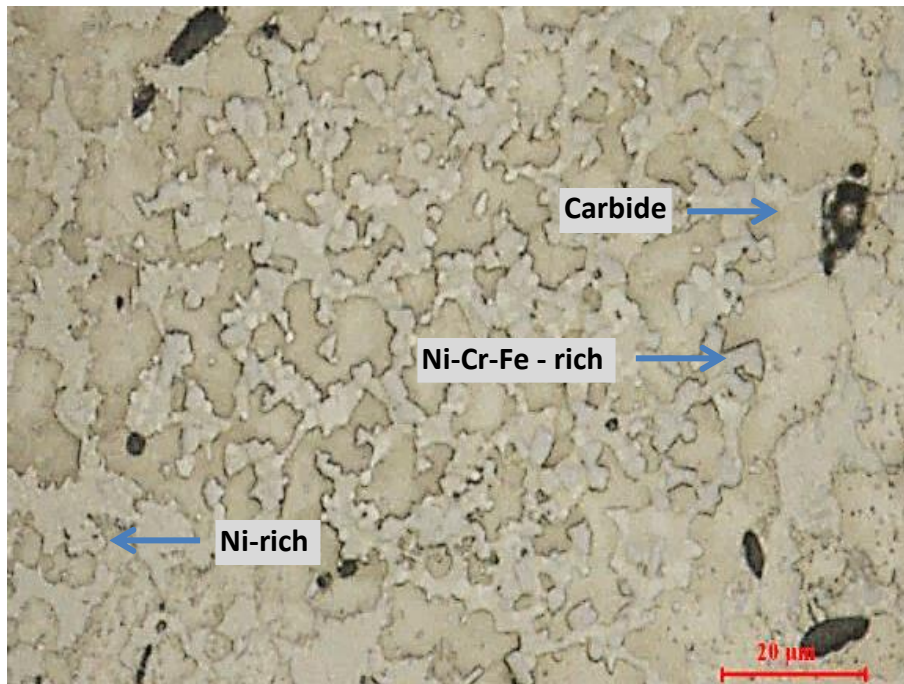
**Table 4.3.** Optical emission spectrographic analysis of the mild steel substrate, Ni-Cr-Fe coating and cast iron valve.

Element	Composition of alloys (wt%)		
	Mild steel	Ni-Cr-Fe	Cast iron
C	0.20	0.10	3.30
Mn	1.30	0.20	0.10
Sn	0.03	≤ 0.01	0.02
P	0.02	≤ 0.01	0.06
Si	0.30	4.50	2.20
Cr	0.14	16.60	0.02
Mo	≤ 0.01	0.04	≤ 0.01
Ni	0.04	74.10	0.10
Cu	0.20	≤ 0.01	0.02
Al	0.01	0.02	0.01
V	0.10	≤ 0.01	0.02
Nb	≤ 0.01	0.01	0.01
Ti	≤ 0.01	≤ 0.01	0.04
Co	0.01	0.30	0.02
Fe	97.70	4.00	94.10
B	0.01	0.20	0.00

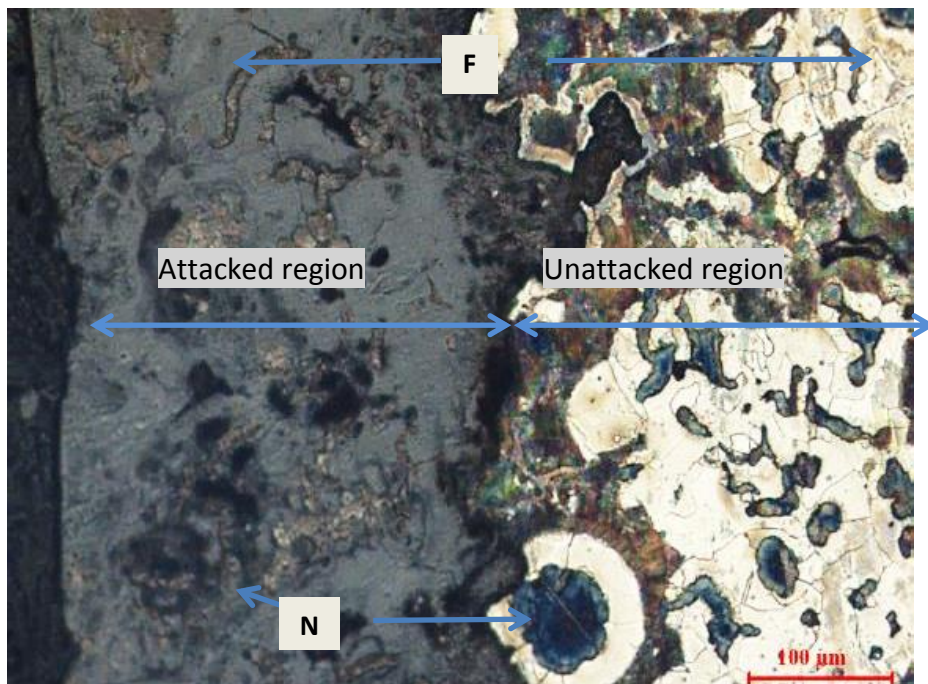


**Figure 4.10.** Optical micrographs of a corroded shaft sleeve substrate from an unattacked region, showing: a) ferrite (light) and pearlite (dark), and b) pearlite resolved showing ferrite and cementite alternating layers (arrow).





**Figure 4.11.** Optical micrograph of a corroded shaft sleeve coating from an unattacked region, showing Ni-Cr-Fe matrix (light brown) and Ni-rich regions (light), with carbides of Cr and Mo (dark).



**Figure 4.12.** Optical micrograph of a corroded cast iron valve cross-section, showing the depth of corrosion ( $\sim 250 \mu\text{m}$ ) on the top exposed surface and the unattacked region underneath. Graphite nodules (N) and flakes (F) appear light in the attacked region, and dark in the unattacked region.

## 4.5 Hardness of the samples

The hardness results for the mild steel substrate, Ni-Cr-Fe coating and cast iron valve samples of the pump from Otjihase Mine are given in Table 4.4. The shaft sleeve coating had the highest hardness, with the largest range. The cast iron was slightly harder than the mild steel substrate.

**Table 4.4.** Hardness values of mild steel, Ni-Cr-Fe and cast iron samples.

Sample	Vickers Hardness (HV <sub>2</sub> )
Mild steel substrate	160 ± 14
Ni-Cr-Fe coating	676 ± 58
Cast iron valve	168 ± 24

## 4.6 Analysis of the mine water

### 4.6.1 Sulphate, nitrite, chloride, turbidity, conductivity, total dissolved solids and pH tests

The results for the tests are shown in Table 4.5. The water samples from Kuruma and Satellite pumps could not show results of SO<sub>4</sub><sup>-</sup>, NO<sub>3</sub><sup>-</sup> and Cl<sup>-</sup>, because their concentrations were much below the detection limit of the equipment (0.001 mg.L<sup>-1</sup>). Conveyor 6 had very much higher concentrations of SO<sub>4</sub><sup>-</sup> than for Cl<sup>-</sup> and NO<sub>3</sub><sup>-</sup>. The high turbidity readings of Satellite pump show that there were more suspended particles than in the Kuruma and Conveyor No. 6 pumps. Conductivity and TDS were highest in Conveyor No.6, and lowest in Kuruma pump. Conveyor No. 6 had the lowest pH value, making it the most aggressive medium.

**Table 4.5.** Turbidity, conductivity, TDS and pH test results of mine water from Kuruma, Satellite and Conveyor No. 6 pumps, 30-10-2013.

	Kuruma	Satellite	Conveyor No. 6
Turbidity (NTU)	177.8 ± 4.0	209.6 ± 6.0	2.9 ± 1.0
Conductivity (mS)	3.3 ± 0.0	3.6 ± 1.0	11.8 ± 0.0
TDS (ppt)	1.6 ± 0.0	2.0±0.4	5.9 ± 0.0
pH	7.2 ± 0.0	6.9 ± 0.0	3.8 ± 0.0
SO <sub>4</sub> <sup>-</sup> (ppm)	-	-	3148
NO <sub>3</sub> <sup>-</sup> (ppm)	-	-	1.8
Cl <sup>-</sup> (ppm)	-	-	48

#### **4.6.2 Chemical composition of the mine water**

The composition of the mine water varies from season to season or even month to month, as shown by the chemical analysis provided by Otjihase Mine in Figures 4.13-4.15.

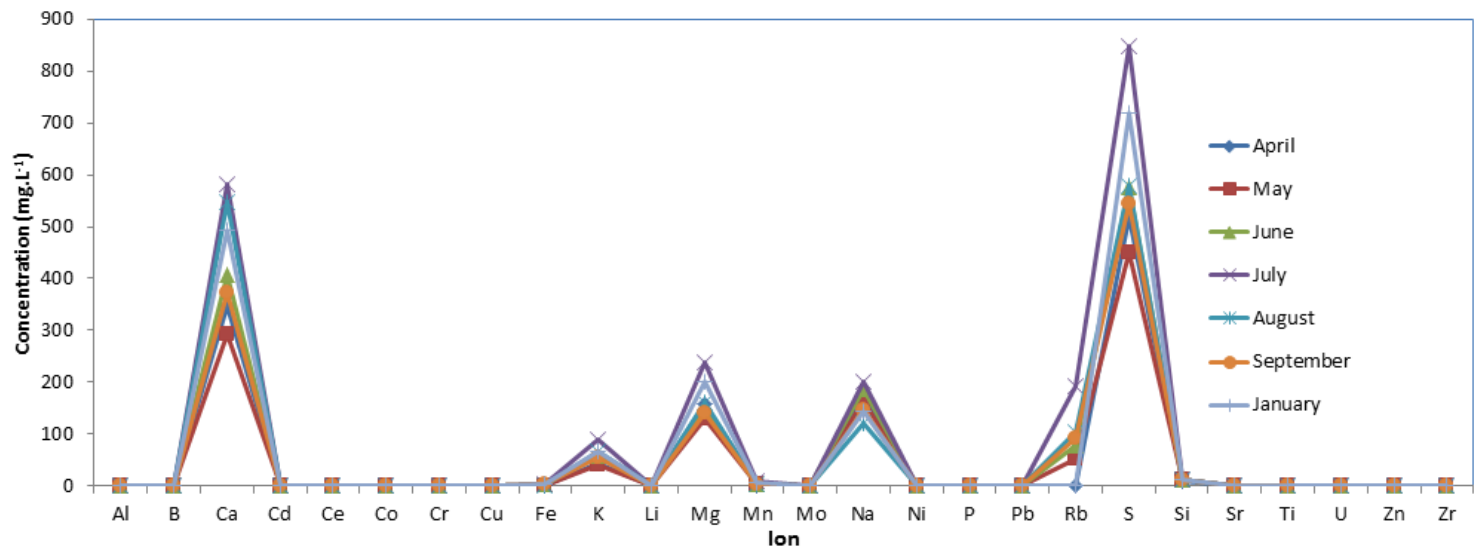
The highest concentrations of alkali metals were recorded in the Satellite pump in 2012. This included sodium in winter, potassium and rubidium in spring. Alkali earth metals such as calcium in spring and magnesium in winter were also recorded as the highest metals present in the mine water, as well as sulphur during spring. Sulphur is probably the most important component that would cause high corrosion rates with the formation of sulphuric acid.<sup>4</sup>

The rare earth metals: dysprosium, praseodymium, samarium and neodymium were detected at Conveyor No. 6 pump in spring of 2012. Transition metals, such as yttrium, were detected in winter, zinc was detected in spring, and zirconium was recorded in the summer of 2013.

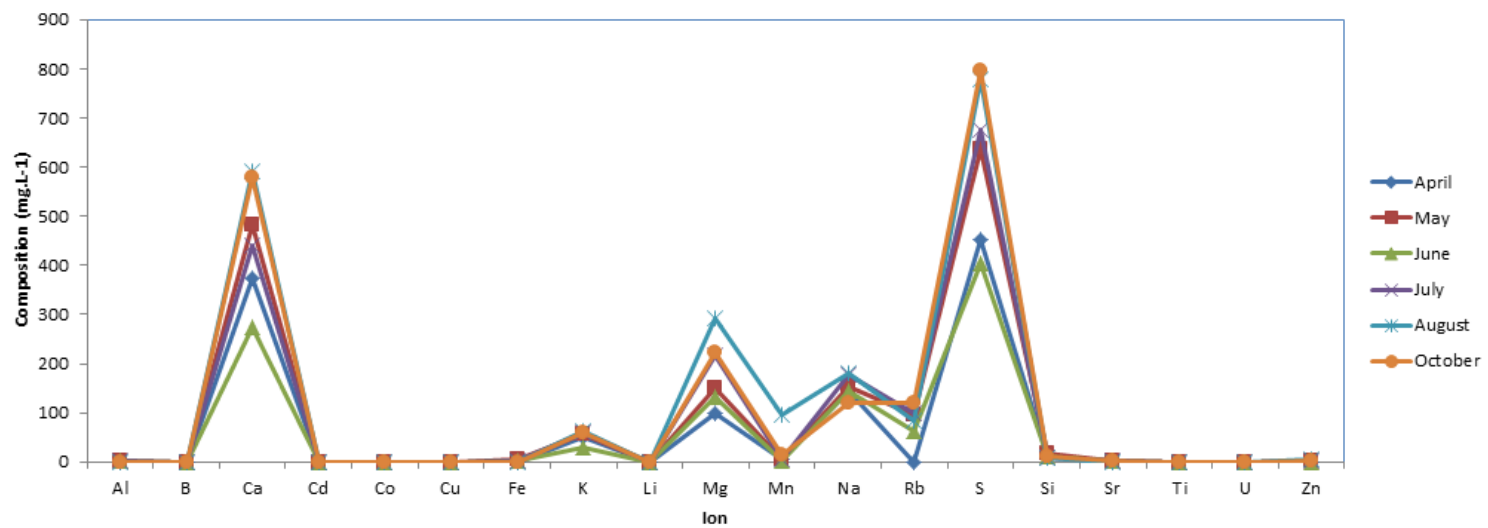
The highest concentrations of elements at Kuruma pump were similar to the Satellite pump, but were different in the winter of 2012, with a record of cadmium, molybdenum, nickel, phosphorus and zinc in the summer of 2013. Less Cu concentration was recorded at Kuruma and Satellite sumps at all seasons. In the summer of 2013, higher Cu concentration was recorded at Conveyor No. 6 pump. The overall analysis showed that the mine water flowing through Conveyor No. 6 pump contained more ions in spring than the other pumps.

From the information provided, it is suspected that the degradation of pump systems at the Otjihase Underground Mine is caused by a synergetic effect of abrasive wear of the coating on steel by debris trapped in the packing glands due to friction between their surfaces. This leads to deterioration of the coating by electrochemical reactions of mine water slurry which consists of TDS, chlorides and sulphates, which then react with the steels once the coating is removed by wear.

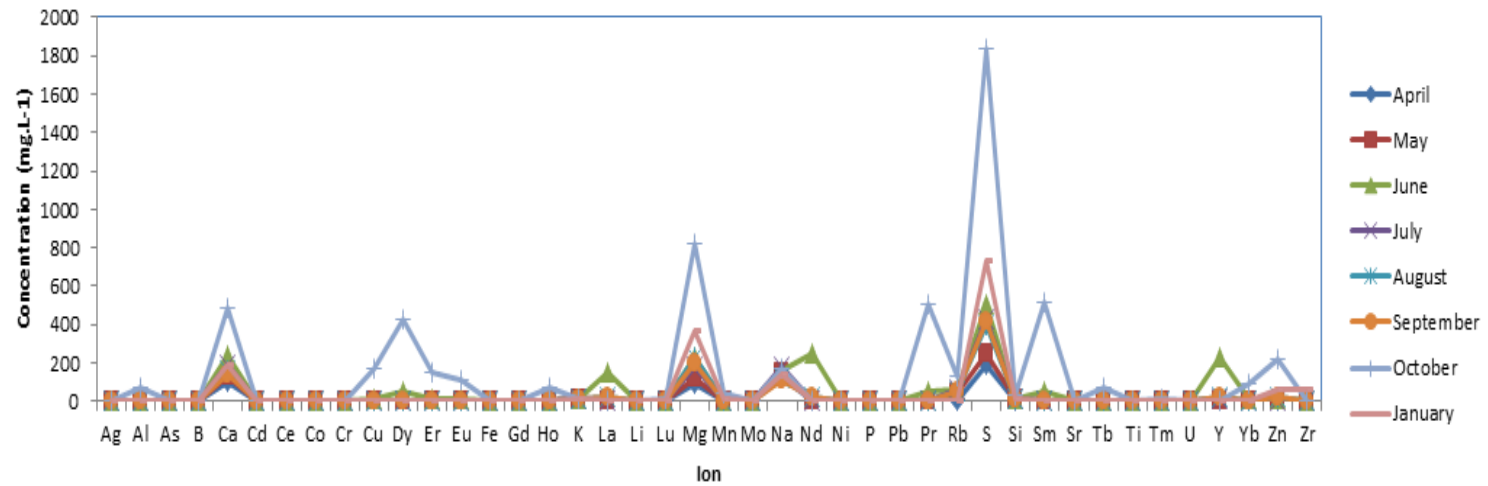




**Figure 4.13.** Chemical analysis of mine water from Kuruma pump, Otjihase Mine, Namibia, for April-October 2012 and January 2013.



**Figure 4.14.** Chemical analysis of mine water from Satellite pump, Otjihase Mine, Nambia, for April-October 2012.



**Figure 4.15.** Chemical analysis of mine water from Conveyor No. 6 pump, Otjihase Mine, Nambia, for April-October 2012 and January 2013.

## 4.7 Corrosion results

### 4.7.1 Cyclic potentiodynamic polarisation measurements

Figure 4.16 shows the potentiodynamic polarisation behaviour of the Ni-Cr-Fe coating, mild steel and cast iron samples from Otjihase Mine tested in synthetic mine water (pH 6), acidified synthetic mine water (pH 3 and 1). The results are given in Table 4.6.

#### ***pH 6 solution***

All samples showed typical current-potential potentiodynamic polarisation behaviours in the solution. The Ni-Cr-Fe coating had a low  $E_{\text{corr}}$  of -380 mV, but experienced pitting instantly after  $E_{\text{corr}}$  and crevice corrosion (Figure 4.16 a), with evidence of pseudo-passivation. Its protection potential (-377 mV) was almost equal to the corrosion potential. The mild steel substrate had corrosion potential (-463 mV) just below that of Ni-Cr-Fe coating, with no passivation behaviour with little evidence of pitting corrosion in the transpassive region as indicated by the small hysteresis. The protection potential (-758 mV) was far below the  $E_{\text{corr}}$ . Cast iron demonstrated evidence of oxide formation until the pitting potential of 174 mV, and showed transpassive behaviour. The corrosion rate of the cast iron was 0.0001 mmpy according to the Tafel extrapolation, which was lower than according to the polarisation resistance method. A large negative hysteresis was observed, and the protection potential (-760 mV) nearly coincided with the  $E_{\text{corr}}$ . The large negative hysteresis at high potential was an indication that the cast iron was more susceptible to pitting corrosion. Mild steel showed the highest corrosion current density and corrosion rate, followed by cast iron, whereas the Ni-Cr-Fe coating had a low corrosion current density and corrosion rate in the solution.

#### ***pH 3 solution***

At the pH of 3, the results of the potentiodynamic responses of the Ni-Cr-Fe coating, mild steel and cast iron samples from Otjihase Mine in acidified synthetic mine water (Figure 4.16 b)) showed slight differences from their responses in pH 6.

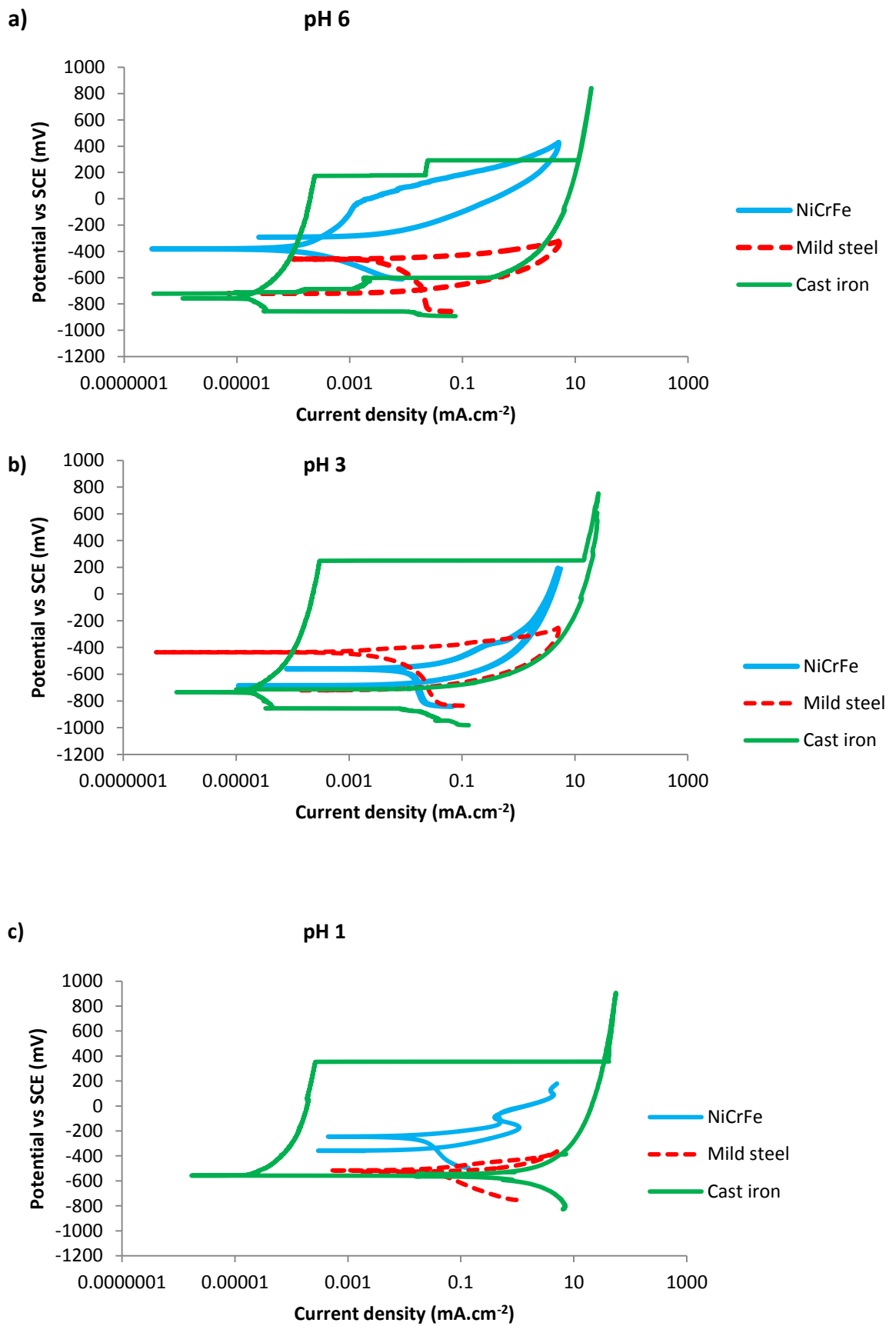
All samples showed typical current-potential potentiodynamic polarisation behaviours (Figure 4.16 b)). The Ni-Cr-Fe coating experienced pitting corrosion, shown by the breakdown (pitting) potential, although with a smaller hysteresis than at pH 6. There was no evidence of passivation of the Ni-Cr-Fe coating in this solution. The mild steel substrate showed no passivation behaviour, and little evidence of general corrosion as indicated by small hysteresis. Cast iron demonstrated spontaneous passivation, with a large negative hysteresis, indicating that it was susceptible to pitting corrosion. The

ranking of the corrosion potentials was: mild steel (-437 mV) > Ni-Cr-Fe (-562 mV) > cast iron (-734 mV).

The protection potential,  $E_{\text{prot}}$ , for both Ni-Cr-Fe and mild steel samples were below the corrosion potential, while cast iron was just above, indicating the very low pitting resistance or active corrosion of these two alloys, since there is little sign of passivity. The ranking of the protection potentials was: mild steel (-696 mV) > Ni-Cr-Fe (-701 mV) > cast iron (-749 mV). Cast iron (Table 4.6) had the highest corrosion current density and rate followed by Ni-Cr-Fe and then mild steel with the lowest corrosion density and rate. However, according to the Tafel extrapolation the corrosion rate of the cast iron was only 0.0004 mmpy.

### ***pH 1 solution***

All samples showed typical current-potential potentiodynamic polarisation behaviour (Figure 4.16 c)). The Ni-Cr-Fe coating exhibited pitting corrosion, although there was slight evidence of passivation. The mild steel showed no passivation behaviour with little evidence of crevice corrosion, indicated by limited hysteresis. Cast iron indicated spontaneous passivation by the large negative hysteresis, showing that the cast iron was susceptible to pitting corrosion. The ranking of the corrosion potentials was: Ni-Cr-Fe (-247 mV) > mild steel (-517 mV) > cast iron (-553 mV). The Ni-Cr-Fe sample had  $E_{\text{corr}} > E_{\text{prot}}$ , while mild steel and cast iron had  $E_{\text{prot}}$  coincided with  $E_{\text{corr}}$ . The ranking of the protection potentials was: cast iron (-553 mV) > mild steel (-517 mV) > Ni-Cr-Fe (-396 mV). Cast iron (Table 4.6) had the highest corrosion density and rate, followed by mild steel and then Ni-Cr-Fe with the lowest corrosion density and rate. Again, the corrosion rate of cast iron was only 0.045 mm.y<sup>-1</sup> according to the Tafel extrapolation.



**Figure 4.16.** Cyclic potentiodynamic polarisation curves of Ni-Cr-Fe coating, mildsteel and cast iron samples from Otjihase Mine in synthetic mine water at ambient temperature at pH: a) 6, b) 3, and c).

**Table 4.6.** Cyclic potentiodynamic polarisation test results of Ni-Cr-Fe coating, mild steel and cast iron from Otjihase Mine in synthetic mine water at ambient temperature, pH 6, 3 and 1.

Sample	pH	$E_{corr}$ (mV)	$i_{corr}$ ( $\mu\text{A}\cdot\text{cm}^{-2}$ )	Corrosion rate ( $\text{mm}\cdot\text{y}^{-1}$ )
Ni-Cr-Fe	6	-381	0.11	0.001
Mild steel		-463	19.70	0.220
Cast iron		-757	0.50	0.047
Ni-Cr-Fe	3	-562	12.60	0.120
Mild steel		-437	2.20	0.025
Cast iron		-734	29.70	0.350
Ni-Cr-Fe	1	-247	15.40	0.150
Mild steel		-517	41.90	0.480
Cast iron		-553	280.70	2.860

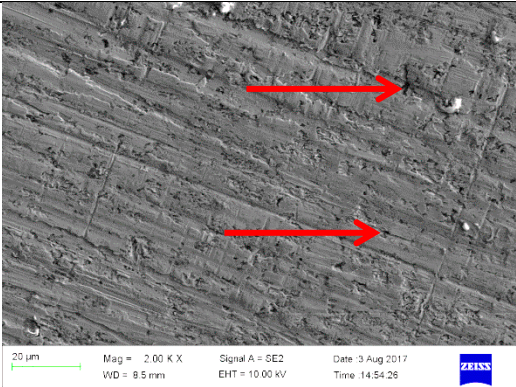
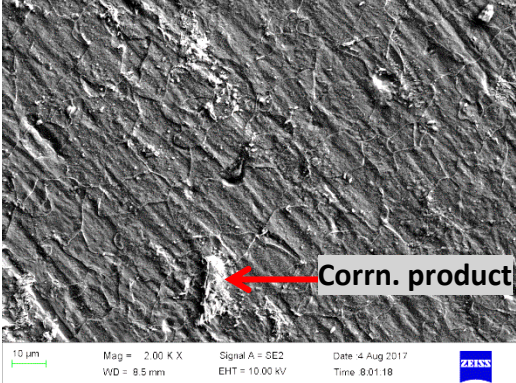
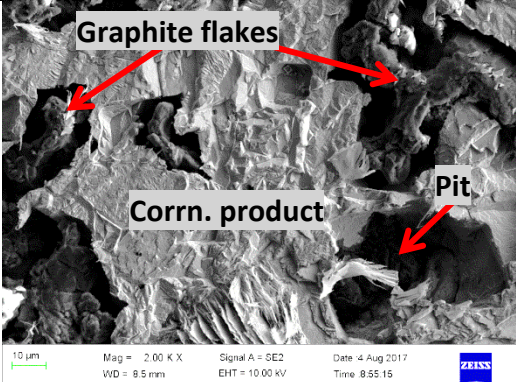
#### 4.8 Morphologies and compositions of the samples after corrosion tests

Figures 4.17-4.19 show SEM-SE micrographs of the surfaces of Ni-Cr-Fe coating, mild steel substrate and cast iron valve after cyclic potentiodynamic polarisation in synthetic (pH 6) and acidified synthetic mine water (pH 3 and 1). In all solutions, Ni-Cr-Fe coating experienced general and pitting corrosion with corrosion products on the surface (Figure 4.17). There were more corrosion products on the surface at pH 3 than at pH values of 1 and 6. The surface corrosion product at pH 6 (Table 4.8) consisted mainly of Ni, Cr, Fe and O, with small amounts of Si and S. The same elements were found in the corrosion products at pH values of 3 and 1, as well as Cl.

Mild steel experienced general corrosion pits with corrosion products on the surface at all pH values (Figures 4.17-4.19). Similar to the Ni-Cr-Fe coating, there were more corrosion products on the surface at pH 3 than at pH values of 1 and 6. The corrosion products consisted of Fe, O and Cu as the major elements, and Na, V, Si, Cl and S as minor elements at all pH values, with Mg detected at pH 6 and 3, and Ca detected at pH 3 only (Table 4.8). There were unacceptable large errors for the O and Fe analyses for mild steel sample, especially for pH values 6 and 3.

Cast iron had general corrosion with larger pits at pH 6 and 1 than at pH 3, and corrosion products on the surface, with graphite flakes exposed at pH 6 only (Figures 4.17-4.19). The major elements on the surface were Fe, O and Si at all pH values, and Cu at pH 1 only, with S, P and Cl as minor elements at all pH values, and Na at pH 1 only (Table 4.9).

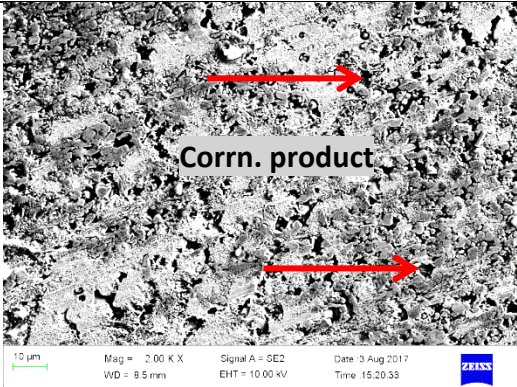
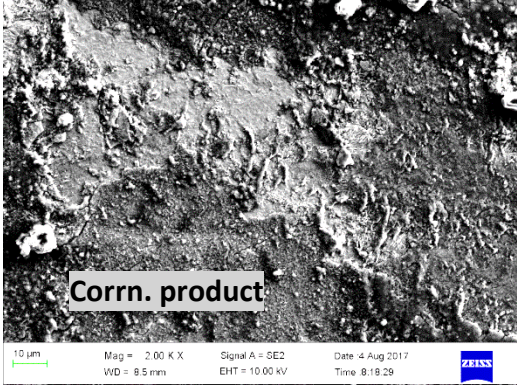
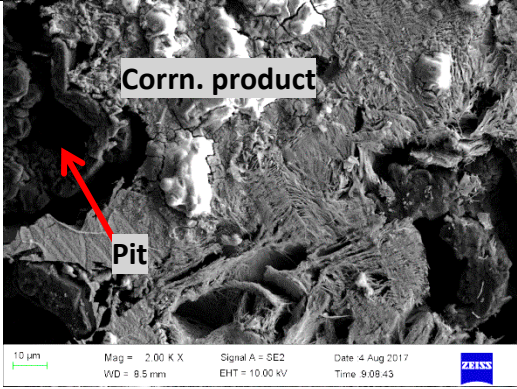
**pH 6 solution**

<p><b>Ni-Cr-Fe</b></p>	 <p>20 µm    Mag = 2.00 K X    Signal A = SE2    Date 3 Aug 2017 WD = 8.5 mm    EHT = 10.00 kV    Time 14:54:26    ZEISS</p>	<p>General corrosion with some small pits (arrows).</p>
<p><b>Mild steel</b></p>	 <p>10 µm    Mag = 2.00 K X    Signal A = SE2    Date 4 Aug 2017 WD = 8.5 mm    EHT = 10.00 kV    Time 8:01:18    ZEISS</p>	<p>General corrosion with corrosion products on the surface.</p>
<p><b>Cast iron</b></p>	 <p>10 µm    Mag = 2.00 K X    Signal A = SE2    Date 4 Aug 2017 WD = 8.5 mm    EHT = 10.00 kV    Time 8:55:15    ZEISS</p>	<p>General corrosion with large pits and corrosion products on the surface, with graphite flakes exposed.</p>

**Figure 4.17.** SEM-SE micrographs of the Ni-Cr-Fe, mild steel and cast iron sample surfaces after cyclic potentiodynamic polarisation in synthetic mine water at pH 6, showing general and pitting corrosion on the surfaces.

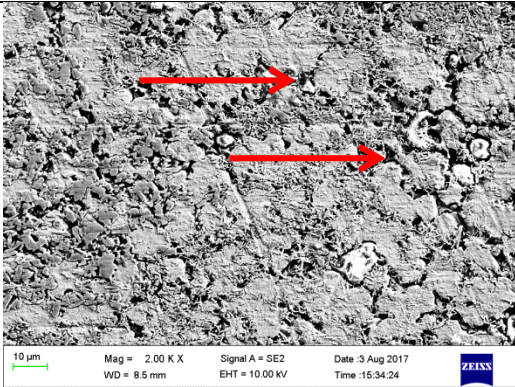

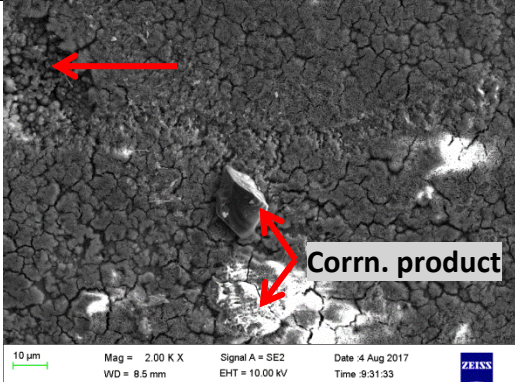


**pH 3 solution**

<p><b>Ni-Cr-Fe</b></p>	 <p>10 μm    Mag = 2.00 K X    Signal A = SE2    Date: 3 Aug 2017 WD = 8.5 mm    EHT = 10.00 kV    Time: 15:20:33    ZEISS</p>	<p>General and pitting corrosion (arrows) with corrosion products on the surface.</p>
<p><b>Mild steel</b></p>	 <p>10 μm    Mag = 2.00 K X    Signal A = SE2    Date: 4 Aug 2017 WD = 8.5 mm    EHT = 10.00 kV    Time: 8:19:29    ZEISS</p>	<p>General corrosion with corrosion products on the surface.</p>
<p><b>Cast iron</b></p>	 <p>10 μm    Mag = 2.00 K X    Signal A = SE2    Date: 4 Aug 2017 WD = 8.5 mm    EHT = 10.00 kV    Time: 9:08:43    ZEISS</p>	<p>General corrosion with large pits and corrosion products on the surface.</p>

**Figure 4.18.** SEM-SE micrographs of the Ni-Cr-Fe, mild steel and cast iron sample surfaces after cyclic potentiodynamic polarisation in acidified synthetic mine water at pH 3, showing general and pitting corrosion on the surfaces.

**pH 1 solution**

<p><b>Ni-Cr-Fe</b></p>	 <p>10 μm    Mag = 2.00 K X    Signal A = SE2    Date :3 Aug 2017 WD = 8.5 mm    EHT = 10.00 kV    Time :15:34:24    ZEISS</p>	<p>General and pitting corrosion (arrows) with corrosion products on the surface.</p>
<p><b>Mild steel</b></p>	 <p>10 μm    Mag = 2.00 K X    Signal A = SE2    Date :4 Aug 2017 WD = 8.5 mm    EHT = 10.00 kV    Time :8:39:57    ZEISS</p>	<p>General corrosion with corrosion products on the surface.</p>
<p><b>Cast iron</b></p>	 <p>10 μm    Mag = 2.00 K X    Signal A = SE2    Date :4 Aug 2017 WD = 8.5 mm    EHT = 10.00 kV    Time :9:31:33    ZEISS</p>	<p>General corrosion with a large pit (arrow) and corrosion products on the surface.</p>

**Figure 4.19.** SEM-SE micrographs of the Ni-Cr-Fe, mild steel and cast iron sample surfaces after cyclic potentiodynamic polarisation in acidified synthetic mine water at pH 1, showing general and pitting corrosion on the surfaces.

**Table 4.7.** EDX analyses of the Ni-Cr-Fe sleeve coating surface of Figures 4.17-4.19 after cyclic potentiodynamic polarisation in synthetic mine water at pH 6, 3 and 1.

Element (wt%)	pH 6		pH 3		pH 1	
	Overall	Corrosion product	Overall	Corrosion product	Overall	Corrosion product
O	6.7 ± 1.1	7.1 ± 1.2	5.7 ± 0.6	5.9 ± 0.7	4.2 ± 0.5	4.2 ± 0.6
Si	3.2 ± 0.1	3.3 ± 0.2	3.0 ± 0.1	2.9 ± 0.1	3.4 ± 0.1	3.3 ± 0.1
S	0.4 ± 0.2	0.5 ± 0.2	0.2 ± 0.0	0.2 ± 0.0	0.3 ± 0.0	0.2 ± 0.0
Cl	-	-	0.4 ± 0.2	0.4 ± 0.3	0.5 ± 0.1	0.4 ± 0.0
Cr	23.3 ± 2.0	23.1 ± 2.3	34.1 ± 1.0	34.3 ± 1.2	34.0 ± 2.0	34.0 ± 2.4
Fe	4.9 ± 0.1	4.7 ± 0.1	4.8 ± 0.5	5.1 ± 0.6	4.8 ± 1.0	5.4 ± 0.7
Ni	61.5 ± 1.3	61.3 ± 1.5	51.8 ± 0.8	51.2 ± 1.0	52.9 ± 2.0	52.6 ± 2.2

**Table 4.8.** EDX analyses of the mild steel substrate surface of Figures 4.17-4.19 after cyclic potentiodynamic polarisation in synthetic mine water at pH 6, 3 and 1.

Element (wt%)	pH 6		pH 3		pH 1	
	Overall	Corrosion product	Overall	Corrosion product	Overall	Corrosion product
O	9.4 ± 8.0	14.9 ± 9.0	24.5 ± 5.0	27.6 ± 5.0	21.9 ± 3.6	15.9 ± 2.8
Na	1.9 ± 0.5	1.6 ± 0.5	3.5 ± 2.0	4.0 ± 2.2	1.1 ± 0.5	1.7 ± 0.4
Mg	0.3 ± 0.1	0.3 ± 0.2	0.4 ± 0.1	0.4 ± 0.2	-	-
Si	0.5 ± 0.0	0.6 ± 0.1	1.5 ± 0.1	1.7 ± 0.5	0.7 ± 0.1	0.7 ± 0.1
S	0.2 ± 0.0	0.2 ± 0.0	0.8 ± 0.2	0.9 ± 0.2	0.2 ± 0.0	0.2 ± 0.1
Cl	0.2 ± 0.2	0.3 ± 0.2	1.1 ± 0.4	1.3 ± 0.5	0.2 ± 0.1	0.2 ± 0.0
Ca	-	-	1.2 ± 0.4	1.1 ± 0.5	-	-
V	1.0 ± 0.3	0.9 ± 0.4	0.6 ± 0.4	0.7 ± 0.5	0.3 ± 0.1	0.4 ± 0.1
Fe	83.5 ± 8.0	77.5 ± 8.0	62.9 ± 6.0	58.6 ± 6.8	74.0 ± 3.2	78.8 ± 3.2
Cu	3.1 ± 1.0	3.7 ± 1.2	3.5 ± 1.2	3.7 ± 1.3	1.6 ± 0.4	2.0 ± 0.4

**Table 4.9.** EDX analysis of the cast iron sample surface of Figures 4.17-4.19 after cyclic potentiodynamic polarisation in synthetic mine water at pH 6, 3 and 1.

Cast iron	pH 6		pH 3		pH 1	
	Overall	Corrosion product	Overall	Overall	Corrosion product	Overall
O	7.5 ± 0.5	7.5 ± 0.5	23.1 ± 2.0	24.1 ± 2.1	34.4 ± 0.8	34.8 ± 1.0
Na	-	-	-	-	0.7 ± 0.2	0.6 ± 0.2
Si	1.7 ± 0.1	1.7 ± 0.2	1.3 ± 0.0	1.3 ± 0.1	1.5 ± 0.1	1.5 ± 0.2
P	0.6 ± 0.0	0.5 ± 0.0	0.5 ± 0.1	0.5 ± 0.1	0.3 ± 0.1	0.3 ± 0.0
S	0.8 ± 0.2	0.6 ± 0.2	0.5 ± 0.1	0.5 ± 0.1	0.4 ± 0.1	0.3 ± 0.1
Cl	0.2 ± 0.2	0.3 ± 0.1	0.2 ± 0.1	0.2 ± 0.0	0.2 ± 0.1	0.2 ± 0.1
Fe	89.3 ± 0.6	89.4 ± 0.6	74.4 ± 2.0	73.5 ± 2.0	60.2 ± 1.0	60.0 ± 1.2
Cu	-	-	-	-	2.3 ± 0.4	2.3 ± 0.4

## 4.9 Identification of substitute alloys (bulk materials)

To recommend a material to substitute the current pump components operating in a tribocorrosive environment at the Otjihase Underground Mine, a few commercial bulk alloys were selected for testing: ULTIMET<sup>®</sup>, Stellite<sup>®</sup> 6B, Hastelloys<sup>®</sup> G30 and ToughMet<sup>®</sup> 3. They were selected due to their good electrochemical and mechanical properties.

ULTIMET<sup>®</sup> (UNS R31233) and Stellite<sup>®</sup> 6B (UNS R30006) are cobalt-chromium alloys, which offer excellent corrosion and wear resistance.<sup>141, 142</sup> Hastelloy<sup>®</sup> G30 (UNS N06030) is a nickel-based alloy suitable for handling phosphoric, sulphuric and nitric acids, while ToughMet<sup>®</sup> 3 (UNS C72800) is a copper-based alloy which is used in harsh environments, against mating surfaces, conditions with poor lubrication, because it has a good corrosion resistance.<sup>121</sup> These alloys may be hardfaced on low or mild steels to protect against mechanical and chemical attack.<sup>95</sup>

## 4.10 Summary

The Ni-Cr-Fe coating had irregular grains of Ni-Cr-Fe and Cr-rich phases, as well as carbide. Mild steel had a ferrite-pearlite structure, with well-defined grain boundaries and banded pearlite, with ferrite regions between. The cast iron sample had a nodular graphite in a pearlite and ferrite matrix, with some graphite flakes.

The hardness ranking of the samples was: Ni-Cr-Fe coating ( $676 \pm 58 \text{ HV}_2$ ) > Cast iron ( $168 \pm 24 \text{ HV}_2$ ) and > mild steel substrate ( $168 \pm 24 \text{ HV}_2$ ).

The Otjihase Mine water analysis in 2012 and in 2013 showed Conveyor No. 6 pump had high ion concentrations of alkali and alkaline earth elements, rare earth elements, chlorides, sulphates and nitrates, many more suspended particles, higher conductivity and salinity, and lower resistivity, higher alkalinity than the Kuruma, North, Satellite and 22 BOOC water pumps, explaining the higher corrosion.

The degradation of pump systems at the Otjihase Underground Mine was caused by a synergetic effect of chemical reactions of mine water slurry with reacting with the steels, and abrasion wear due to the friction between the debris trapped in packing glands and steel surfaces, leaving the underlying mild steel substrate suffered uniform corrosion.

The corrosion potential ranking of the samples at pH 6 was: cast iron (-757 mV) < mild steel (-463 mV) < Ni-Cr-Fe (-381 mV) and corrosion rate was: cast iron ( $0.047 \text{ mm.y}^{-1}$ ) >

mild steel ( $0.220 \text{ mm.y}^{-1}$ ) > Ni-Cr-Fe ( $0.001 \text{ mm.y}^{-1}$ ). At pH 3, corrosion potential ranking of the samples was: cast iron ( $-734 \text{ mV}$ ) < Ni-Cr-Fe ( $-562 \text{ mV}$ ) < mild steel ( $-437 \text{ mV}$ ) and corrosion rate was: cast iron ( $0.350 \text{ mm.y}^{-1}$ ) > Ni-Cr-Fe ( $0.120 \text{ mm.y}^{-1}$ ) > mild steel ( $0.025 \text{ mm.y}^{-1}$ ), and at pH 1, their corrosion potential ranking was: cast iron ( $-553 \text{ mV}$ ) < mild steel ( $-517 \text{ mV}$ ) < Ni-Cr-Fe ( $-247 \text{ mV}$ ) and corrosion rate was: cast iron ( $2.860 \text{ mm.y}^{-1}$ ) > mild steel ( $0.480 \text{ mm.y}^{-1}$ ) > Ni-Cr-Fe ( $0.150 \text{ mm.y}^{-1}$ ).

Ni-Cr-Fe experienced general and pitting corrosion. Mild steel showed general corrosion with some pits. Cast iron had general corrosion with larger pits at pH 6 and 1 than at pH 3.

The four selected commercial bulk alloys for testing were: ULTIMET<sup>®</sup>, Stellite<sup>®</sup> 6B, Hastelloys<sup>®</sup> G30 and ToughMet<sup>®</sup> 3 as potential replacements for the pump components currently being used at the Otjihase Underground Mine. They were selected for their good electrochemical and mechanical properties.

# CHAPTER 5: PROPERTIES OF THE ALTERNATIVE BULK ALLOYS

---

## 5.1 Introduction

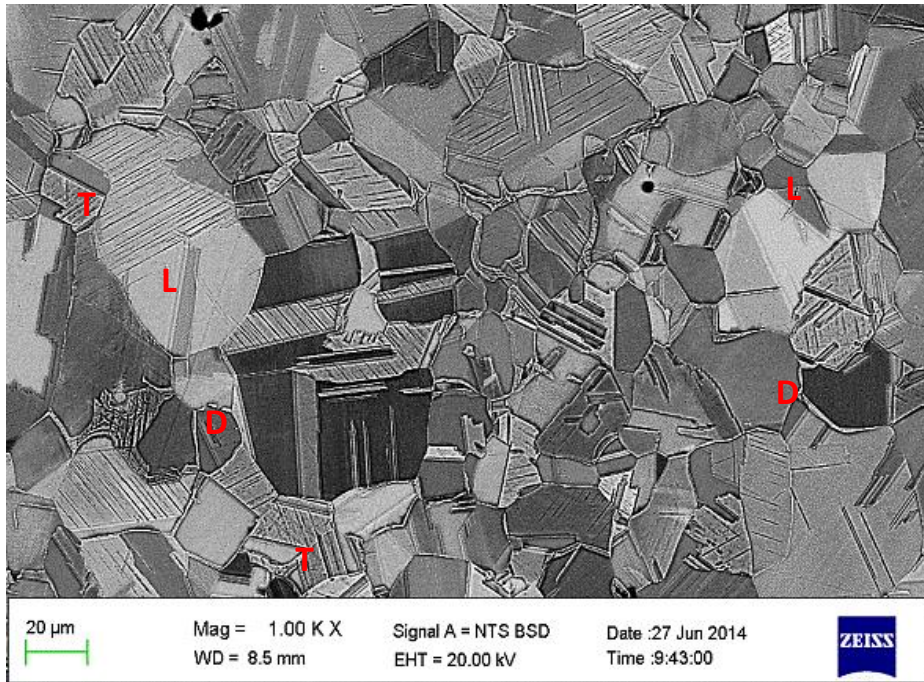
Two high chromium cobalt alloys (ULTIMET<sup>®</sup> and Stellite<sup>®</sup> 6B), a high chromium nickel alloy (Hastelloy<sup>®</sup> G30) and a copper-based alloy (ToughMet<sup>®</sup> 3) had been selected as candidate alloys to replace those currently being used at the Otjihase Mine (Chapter 4). These alloys were tested corrosion resistance in synthetic mine water, to ascertain whether they could cope with the corrosion in gold-copper-pyrite underground mines. Not all the tests were done on Hastelloy G30 and ToughMet 3, because of the limited available materials, and since they were not performing well and likely to be not considered for further evaluations, no more materials were obtained.

The microstructures of the samples were studied before and after corrosion and wear tests, using optical and scanning electron microscopy. Vickers hardness tests were performed to determine the hardnesses of the samples, and their grain sizes were calculated. Corrosion was studied by cyclic potentiodynamic polarisation in synthetic mine water at different pH values. The compositions of the synthetic mine water was analysed before and after the corrosion tests. Friction and sliding wear tests were also done using a tribometer. The results were used to choose the best alloys to resist corrosion and wear in the mine environment, and ULTIMET and Stellite 6B alloys were the best.

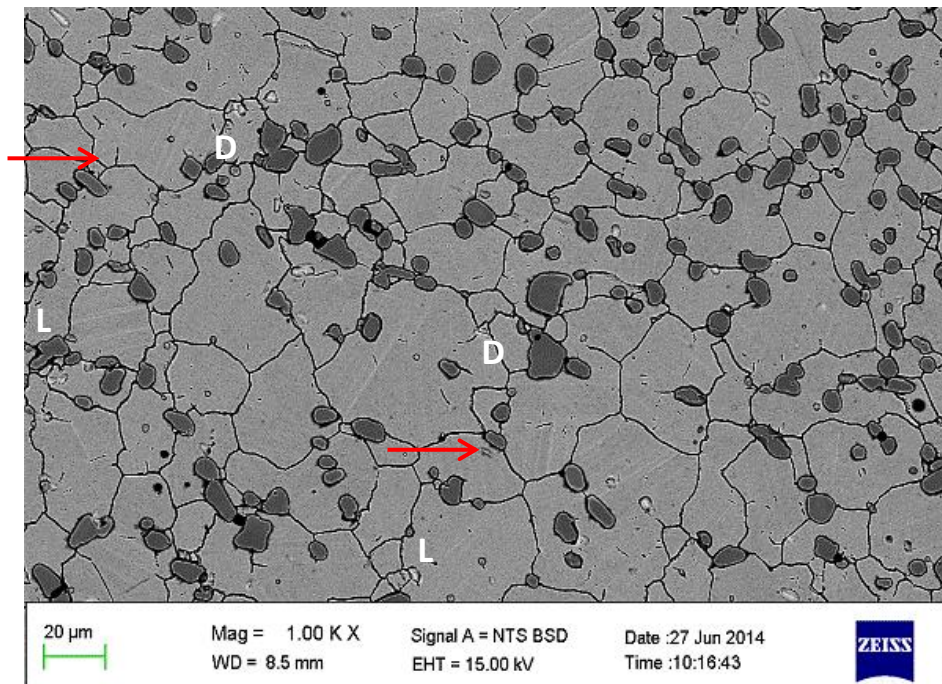
## 5.2 Microstructures

The SEM-BSE micrographs of the ULTIMET, Stellite 6B, ToughMet 3 and Hastelloy G30 before corrosion tests are shown in Figures 5.1-5.3. The microstructures of ULTIMET (Figure 5.1) and Stellite 6B (Figure 5.2) consisted of well defined equiaxed  $\gamma$  (the cobalt-rich solid solution with Cr) grains with twinning, but there was less clear twinning in the Stellite 6B, which also had large  $\text{Cr}_7\text{C}_3$  at the grain boundaries, confirmed by XRD. The twins were much clearer in the optical micrograph (Appendix A) than SEM (Figure 5.2). ToughMet 3 (Figure 5.3) had larger irregular grains, which were easier to see at low magnification. Hastelloy G30 showed very similar grain structures to ULTIMET (Figure 5.4) (the optical image was much clearer than the SEM image, which is shown in Appendix A).



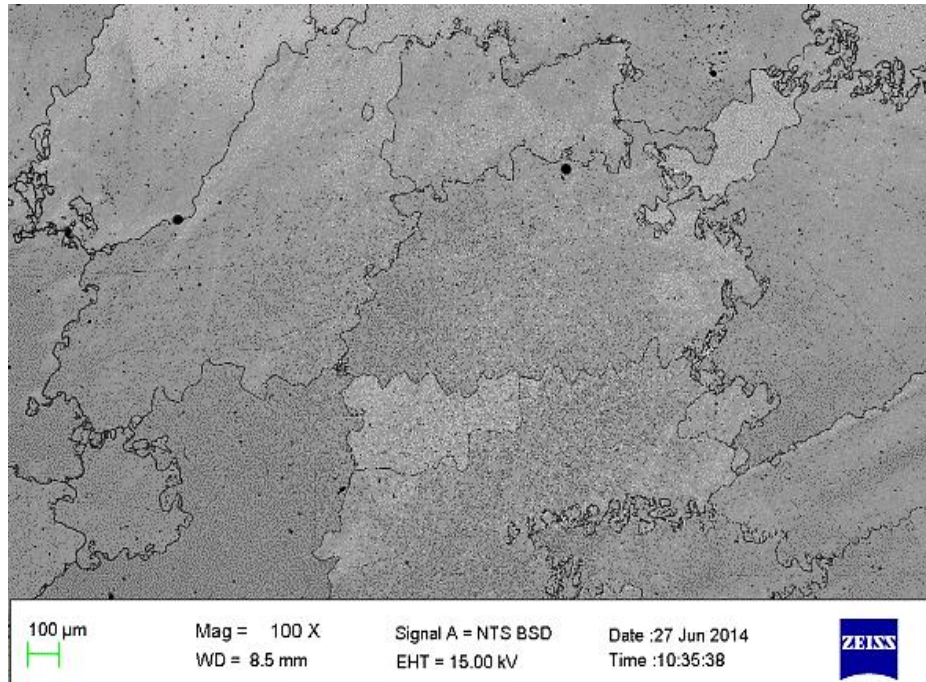


**Figure 5.1.** SEM-BSE micrograph of as-received ULTIMET, showing equiaxed (dark, D and light, L) and twins in the  $\gamma$  grains (T), and a thin grain boundary layer.

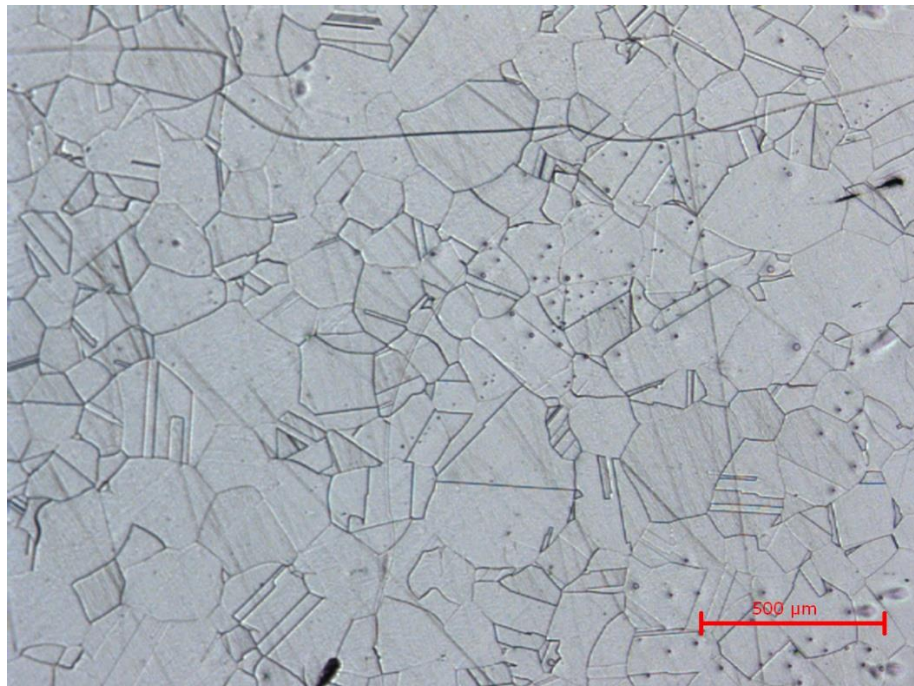


**Figure 5.2.** SEM-BSE micrograph of as-received Stellite 6B, showing equiaxed (light, L) grains and twins in the  $\gamma$  grains (arrows) in the matrix, with  $\text{Cr}_7\text{C}_3$  (dark, D) at the grain boundaries.





**Figure 5.3.** SEM-BSE micrograph of as-received ToughMet 3, showing large and irregular single-phase grains.



**Figure 5.4.** Optical micrographs of as-received Hastelloy G30, showing equiaxed grains.

EDX analysis of the ULTIMET (Table 5.1) showed similar compositions for all the light, dark and twinned grains of Figure 5.1, with Co and Cr as the major components. The different contrasts arose from the different orientations of the grains, and this has been reported

before, even in the BSE mode.<sup>147</sup> There were fine grain boundary precipitates, which may be  $\gamma$  (cobalt-rich solid solution) or  $\text{Cr}_7\text{C}_3$ ,<sup>148</sup> although the carbide is more likely.

Table 5.2 shows EDX analysis of the Stellite 6B alloy. The light major phase had Co and Cr as major elements, while the dark grain boundary phase had Cr and C as the major components, identified as  $\text{Cr}_7\text{C}_3$  by XRD. However, there was an over-reporting in EDX results for C and O (Tables 5.1 and 5.2), which was due to contamination despite repeated sample preparation. SEM-EDX for ToughMet 3 (Table 5.3) showed single-phase grains, with Cu, Ni and Sn. Hastelloy G30 had Ni, Cr and Fe as major elements, with Mo, W, Co, Cu, Mn, Si and Al as minor elements (Table 5.4).

**Table 5.1.** EDX analysis (wt%) of ULTIMET (Figure 5.1) before cyclic potentiodynamic polarisation measurements.

Element	Overall	Grains	Grain boundary
C	3.5 ± 1.0	2.8 ± 1.0	6.8 ± 2.0
Si	0.3 ± 0.0	0.3 ± 0.1	-
Cr	24.4 ± 0.2	24.7 ± 1.0	23.6 ± 0.4
Mn	0.8 ± 0.1	0.9 ± 0.01	1.0 ± 0.0
Fe	2.8 ± 0.0	2.8 ± 0.1	2.8 ± 0.1
Co	51.9 ± 1.0	52.3 ± 1.0	50 ± 0.3
Ni	8.7 ± 0.1	8.8 ± 0.2	8.4 ± 0.2
Mo	5.4 ± 0.0	5.1 ± 2.0	5.1 ± 0.3
W	2.1 ± 0.0	2.1 ± 0.1	2.2 ± 0.3
Identity	-	$\gamma$	$\text{Cr}_7\text{C}_3$

**Table 5.2.** EDX analysis (wt%) of Stellite 6B (Figure 5.2) before cyclic potentiodynamic polarisation measurements.

Element	Stellite 6B		
	Overall	Light phase	Dark phase
C	7.6 ± 0.0	3.9 ± 1.0	10.6 ± 0.2
O	7.4 ± 1.0	6.5 ± 0.3	-
Si	0.4 ± 0.0	0.5 ± 0.1	-
Cr	29.5 ± 1.0	24.0 ± 0.1	75.3 ± 0.3
Mn	1.5 ± 0.1	1.6 ± 0.1	1.3 ± 0.1
Fe	1.7 ± 0.1	1.9 ± 0.1	0.6 ± 0.0
Co	46.2 ± 0.1	53.7 ± 0.1	9.3 ± 0.1
Ni	1.7 ± 0.1	2.1 ± 0.1	-
Mo	-	0.7 ± 0.4	-
W	4.8 ± 0.1	5.2 ± 0.2	3.1 ± 0.4
Identity	-	$\gamma$	$\text{Cr}_7\text{C}_3$

**Table 5.3.** EDX analysis (wt%) of ToughMet 3 (Figure 5.3) before cyclic potentiodynamic polarisation measurements.

Element	ToughMet 3	
	Overall	Grains
Ni	13.9 ± 0.1	14.9 ± 1.0
Cu	78.3 ± 0.2	76.7 ± 1.0
Sn	7.8 ± 0.1	8.4 ± 0.4
Identity	-	Cu, Ni, Sn

**Table 5.4.** EDX analysis (wt%) of Hastelloy G30 (Figure A<sub>2</sub>) before cyclic potentiodynamic polarisation measurements.

Element	Hastelloy G30		
	Overall	Light phase	Dark phase
Cu	1.7 ± 0.3	2.3 ± 0.2	2.4 ± 0.2
Al	0.2 ± 0.0	0.3 ± 0.1	-
Si	0.6 ± 0.3	0.1 ± 0.0	0.2 ± 0.0
Cr	29.75 ± 0.2	28.8 ± 0.2	28.9 ± 0.1
Mn	1.3 ± 0.0	1.1 ± 0.1	1.0 ± 0.1
Fe	15.34 ± 0.4	12.8 ± 0.0	12.9 ± 0.1
Co	2.68 ± 0.1	2.3 ± 0.1	2.4 ± 0.3
Ni	41.83 ± 0.5	44.8 ± 0.1	44.8 ± 0.3
Mo	3.47 ± 0.3	5.4 ± 0.1	5.3 ± 0.3
W	3.33 ± 0.1	2.1 ± 0.1	2.3 ± 0.1
Identity	-	Ni, Cr, Fe	Ni, Cr, Fe

### 5.3 Hardness and grain size values

The microhardness values (Table 5.5) of Stellite 6B and ToughMet 3 were the highest, followed by ULTIMET, while Hastelloy G30 had the lowest. The grain sizes of ULTIMET and Stellite 6B were both finer than ToughMet 3 and Hastelloy G30, Table 5.5. The high hardness of Stellite 6B, was probably the combined effect of the finer grains as well as the carbides, could be beneficial for improved wear properties. The carbide proportions of Stellite 6B were very variable, as shown by the high error.

**Table 5.5.** Microhardness and grain sizes of ULTIMET, Stellite 6B, ToughMet 3 and Hastelloy G30.

Sample	Hardness (HV <sub>3</sub> )	Grain size (μm)	Carbide proportion (%)
ULTIMET	304 ± 22	18.7 ± 6.0	<2
Stellite 6B	368 ± 13	20.5 ± 2.0	16 ± 15
ToughMet 3	368 ± 14	445.4 ± 78.0	-
Hastelloy G30	180 ± 10	139.0 ± 12.0	<1

#### 5.4 Chemical compositions of synthetic and acidified mine water before and after corrosion testing

Table 5.6 shows the properties of synthetic and acidified synthetic mine water before corrosion testing. When the pH of the solution was decreased, the values of conductivity, total dissolved solids (TDS) and salinity increased, with a decrease in resistivity, making the acidified synthetic mine water more corrosive than synthetic mine water. The change in TDS with pH was probably due to salt particles which might have precipitated during the acidification of synthetic mine water.

**Table 5.6.** Properties of synthetic and acidified synthetic mine water for corrosion testing.

Component	Synthetic mine water	Acidified synthetic mine water	
pH	6	3	1
Conductivity (mS.cm <sup>-1</sup> )	5.2	6.3	13.0
TDS (ppt)	2.5	3.1	6.4
Salinity (PSU)	2.8	3.4	7.5
Resistivity (Ohm.cm)	193.7	160	77.0

Tables 5.7 and 5.8 show the analyses of synthetic and acidified synthetic mine water after corrosion testing for ULTIMET, Stellite 6B and ToughMet 3. The Hastelloy G30 solution was not analysed then, because the equipment broke down. Very high concentrations of Cu, Mo, W, Ca and Na ions were recorded in all the solutions tested (synthetic and acidified synthetic mine water), as well as Co and Mg ions at higher concentrations. Lower concentrations were recorded for Cr, Fe, Ni, Si and Nb ions. For Cu and Mo in ULTIMET and ToughMet 3 solutions, ICP-OES was used instead of ICP-MS due to their high concentrations, while for Co and Cr (ULTIMET and Stellite 6B), ICP-MS was used instead of

ICP-OES due to their low concentrations. The analysis of anions by ion chromatography showed higher concentrations of chlorides and sulphates in the solution of ToughMet 3, than those for ULTIMET and Stellite 6B (Table 5.9). Nitrates and phosphates were not detected.

**Table 5.7.** Inductively coupled plasma mass spectrometry (ICP-MS) results of the test solutions after cyclic potentiodynamic polarisation in synthetic mine water at pH 1.

Sample test at pH 1	Concentration (ppb)			
	Cu	Mo	Sn	W
ULTIMET	339 ± 2	1149 ± 3	5 ± 2	392 ± 1
Stellite 6B	24 ± 3	184 ± 6	4 ± 2	872 ± 3
ToughMet 3	1311 ± 6	6 ± 2	0.6 ± 0	20 ± 9

**Table 5.8.** Inductively coupled plasma optical emission spectrometry (ICP-OES) results of the test solutions after cyclic potentiodynamic polarisation in synthetic mine water at pH 1.

pH 1	Concentration (ppm)							
	Ca	Co	Cr	Fe	Mg	Na	Ni	Si
ULTIMET	342 ± 1	54 ± 1	26 ± 1	15 ± 1	49 ± 2	441 ± 5	8 ± 2	0.6 ± 0.1
Stellite 6B	357 ± 5	71 ± 5	27 ± 5	3 ± 1	49 ± 5	370 ± 6	3 ± 1	0.5 ± 0.1
ToughMet 3	284 ± 9	-	-	0.2 ± 0	38 ± 3	271 ± 4	49 ± 1	0.3 ± 0.1

**Table 5.9.** Ion chromatography results of the test solutions after cyclic potentiodynamic polarisation in synthetic mine water at pH 1.

pH 1	Concentration (mg.L <sup>-1</sup> )			
	Chloride	Nitrate	Phosphate	Sulphate
ULTIMET	1330	Not detected	Not detected	1060
Stellite 6B	1290	Not detected	Not detected	1040
ToughMet 3	1560	Not detected	Not detected	1090

## 5.5 Cyclic potentiodynamic polarisation measurements

### 5.5.1 Cyclic potentiodynamic polarisation curves

Figure 5.5 shows the cyclic polarisation curves for hardfacing alloys in synthetic mine water at different acidic values. The corrosion potential ( $E_{corr}$ ) and corrosion current

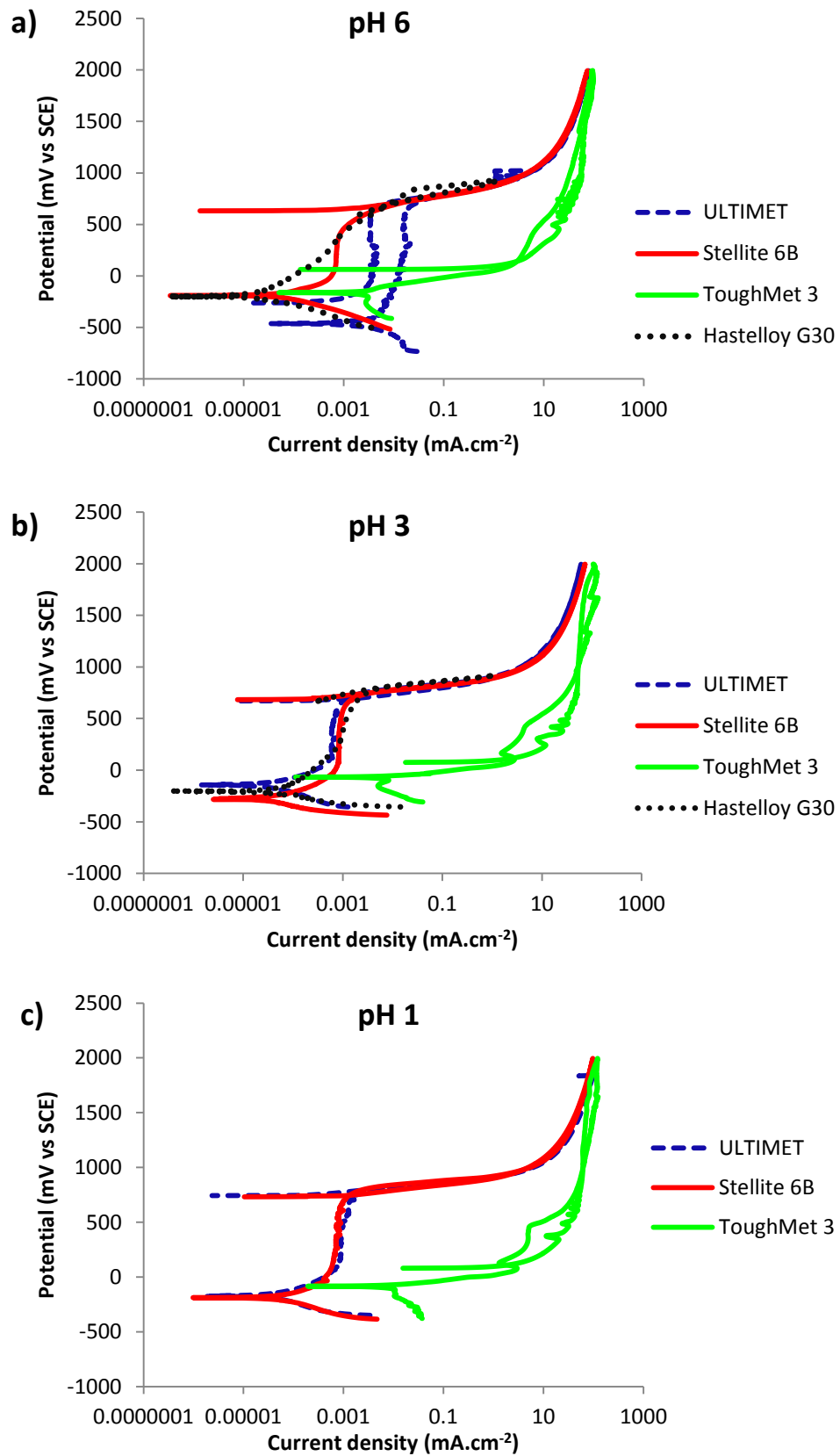
density ( $i_{corr}$ ) of ULTIMET Stellite 6B and Hastelloy G30 alloys were lower than those of ToughMet 3, which ultimately resulted in a higher corrosion rate for ToughMet 3. The summary of cyclic potentiodynamic polarisation measurements is given in Table 5.10. At pH 6, ULTIMET had an extended and stable passivation region. Spontaneous and extended passivation behaviour of Stellite 6B was observed at all pH tested. Hastelloy G30 showed no passivation at pH 6, while at pH 3, it almost passivated, similar to ULTIMET and Stellite 6B. ToughMet 3 had a pseudo-passivation region and a higher  $i_{corr}$  in the tested conditions. The curves for ULTIMET, Stellite 6B and Hastelloy G30 overlapped each other from the passive to the transpassive regions at all pH values. This indicates that the corrosion resistance of the two alloys were nearly equal, and the corrosion rates were nearly the same. The forward and reverse scans overlapped, therefore no hysteresis loops were observed in the ULTIMET, Stellite 6B or Hastelloy G30 polarisation scans. However, there were small hysteresis loops for ToughMet 3 in all solutions tested. The reverse scan for ULTIMET did not show a significant hysteresis curve at all. This indicated that ULTIMET had a high resistance to the growth of the existing pits that formed in the transpassive state.

There was no trend in  $E_{corr}$ ,  $i_{corr}$  and corrosion rates when the pH was lowered or increased for all alloys (Table 5.10). At all values, ToughMet 3 had the highest  $E_{corr}$ ,  $i_{corr}$  and corrosion rates. At pH 6, ToughMet 3 had the highest  $E_{corr}$  and corrosion rate, and ULTIMET had the lowest  $E_{corr}$ , while Hastelloy G30 had the lowest corrosion rate. At pH 3, ToughMet 3 had the highest  $E_{corr}$  while Hastelloy G30 had the lowest  $E_{corr}$  and corrosion rate. At pH 1, ToughMet 3 had highest  $E_{corr}$  and corrosion rate, and Stellite 6B had the lowest  $E_{corr}$ , while ULTIMET had the lowest corrosion rate. Hastelloy G30 was not tested at pH 1, because there was insufficient material, and since it was not performing well, there was little point in obtaining more materials. Thus, Hastelloy G30 is better than Stellite 6B and ULTIMET for applications at high pH, while at low pH either ULTIMET or Stellite 6B alloy may be used.

Polarisation behaviour of ToughMet 3 in synthetic mine water solutions was dominated by the dissolution of copper to a soluble cuprous chloride ion complex ( $CuCl_2^-$ ), and the solutions turned blue. In acidic solutions, the potentiodynamic behaviour showed two anodic peaks associated with the formation of  $Cu_2O$  (~55 mV) and  $CuO$  (~220 mV), accompanied by visible formation of a thick layer on the surface of the working electrode. The EDX results (Table 5.11) showed that the layer was mainly composed of Cu, Cl and O, thus, a cuprous chloride ( $CuCl$ )-cuprous oxide ( $Cu_2O$ ).

**Table 5.10.** Cyclic potentiodynamic polarisation test results of ULTIMET, Stellite 6B, ToughMet 3 and Hastelloy G30 alloys in synthetic and acidified synthetic mine water.

Sample	pH	$E_{\text{corr}}$ (mV)	$i_{\text{corr}}$ ( $\mu\text{A}\cdot\text{cm}^{-2}$ )	Corrosion rate ( $\text{mm}\cdot\text{y}^{-1}$ )
ULTIMET	6	-463	0.499	0.00483
Stellite 6B		-190	0.011	0.00011
ToughMet 3		-163	1.161	0.01410
Hastelloy G30		-195	0.005	0.00005
ULTIMET	3	-176	0.007	0.00007
Stellite 6B		-188	0.007	0.00007
ToughMet 3		-84	4.274	0.05180
Hastelloy G30		-206	0.022	0.00020
ULTIMET	1	-173	0.011	0.00011
Stellite 6B		-277	0.022	0.00019
ToughMet 3		-67	3.904	0.04730

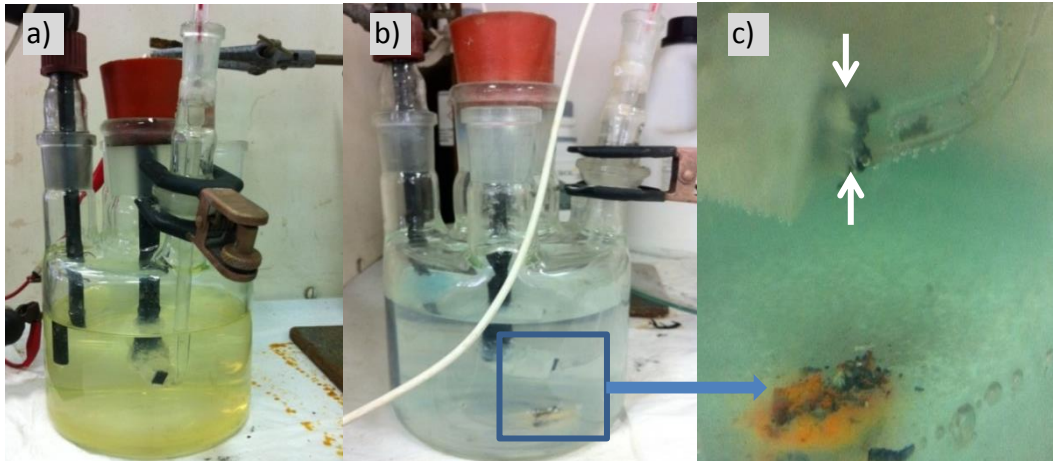


**Figure 5.5.** Cyclic potentiodynamic polarisation curves of ULTIMET, Stellite 6B, ToughMet 3 and Hastelloy G30 samples at ambient temperature in synthetic mine water at pH: a) 6, b) 3, and c) 1 (no Hastelloy G30).



### 5.5.2 Morphologies and compositions of the samples after corrosion tests

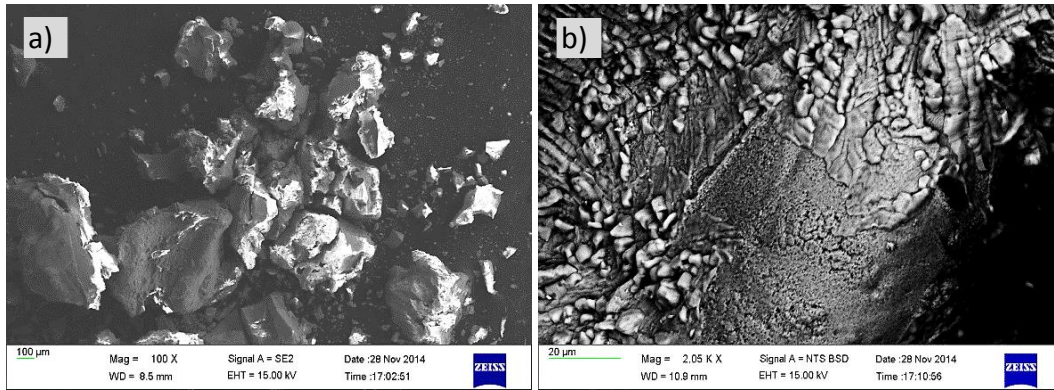
Both the as-prepared and acidified synthetic mine water test solutions for ULTIMET and Stellite 6B hardfacing alloys turned yellow after the polarisation tests (Figure 5.6 a)). For ToughMet 3, the solutions turned light blue (Figure 5.6 b), and a thick and silvery film was observed on the exposed area of ToughMet 3 in all solutions (Figure 5.6 c)). It turned into a combination of red rust, which for one test fell off to the bottom of the corrosion cell, and green after removal from the solution.



**Figure 5.6.** Cyclic potentiodynamic polarisation. Photographs of: a) ULTIMET and Stellite 6B (solution turned yellow), b) ToughMet 3 (solution turned blue), and c) ToughMet 3 sample: thick surface layer (arrows) and rust in the corrosion test cell.

Figure 5.7 shows SEM-SE micrographs of the thick layer on ToughMet 3 at low and high magnifications. EDX analysis taken from the areas in Figure 5.7 (a) showed fairly high concentrations of Cu, Cl and O, with Sn and S at lower levels (Table 5.11). Copper and Sn were selectively removed from the sample, leaving behind Ni and they would probably combine with Cl and O from the solution.

The optical micrographs of the surface morphologies of the samples after corrosion tests are given in Figure 5.8. ULTIMET showed general and intergranular corrosion. Stellite 6B showed intergranular corrosion, oxides on the surface and carbides, and ToughMet 3 had pitting, general and selective corrosion, with a thick layer on the surface. This is a two-fold reaction layer formed when copper is in a chloride containing electrolyte. It consists of copper (I) chloride (CuCl) and copper (I) oxide (Cu<sub>2</sub>O) underneath.



**Figure 5.7.** SEM-SE micrographs of the CuCl-Cu<sub>2</sub>O thick layer on the surface of the ToughMet 3 sample at: a) low, and b) high magnifications.

**Table 5.11.** EDX analysis of the CuCl-Cu<sub>2</sub>O thick layer on the surface of the ToughMet 3 sample after cyclic potentiodynamic polarisation in synthetic mine water.

Element	Composition (wt%)
O	20.2 ± 9.0
S	0.2 ± 0.1
Cl	27.1 ± 1.0
Cu	47.3 ± 2.3
Sn	5.0 ± 2.4

Figures 5.9–5.11 show SEM-SE micrographs of the hardfacing alloys after cyclic potentiodynamic polarisation in synthetic (pH 6) and acidified synthetic mine water (pH 3 and 1). The ULTIMET (Figures 5.9, 5.12 and 5.15) alloy had general corrosion with shallow pits and some intergranular corrosion in all solutions. At pH values of 6 and 3 (Figures 5.10 and 5.13), Stellite 6B showed intergranular corrosion, with carbides left inside pits and with some oxides as corrosion products on the surface. At pH 1 (Figure 5.16), Stellite 6B experienced predominantly uniform corrosion, with some intergranular corrosion and small pits around the carbides, with oxides on the surface. ToughMet 3 (Figures 5.11, 5.14 and 5.17) showed a severe general and selective corrosion attack in all solutions tested, with more attack at pH 1 (Figure 5.17). Tables 5.12 – 5.20 show EDX analysis of the surfaces of the samples after the corrosion tests.

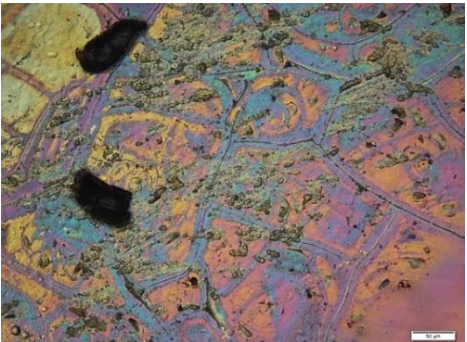


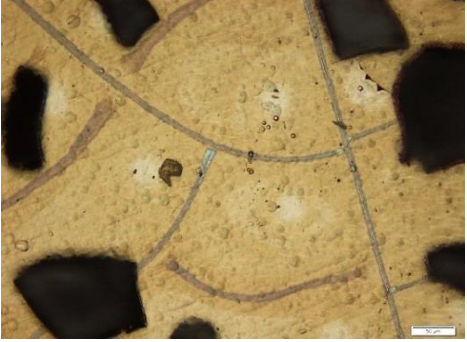
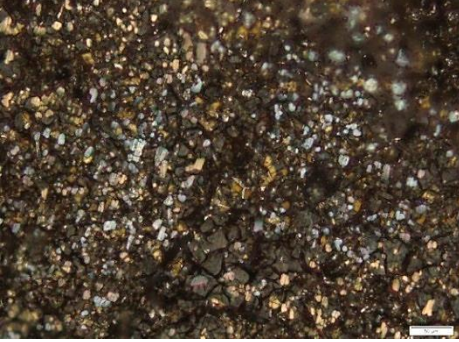
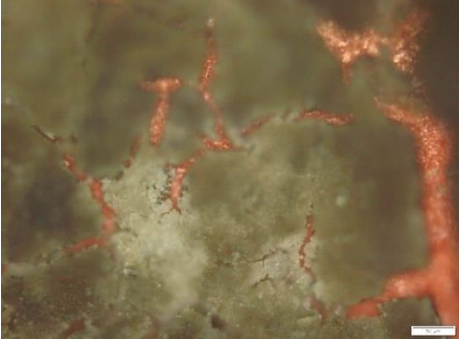

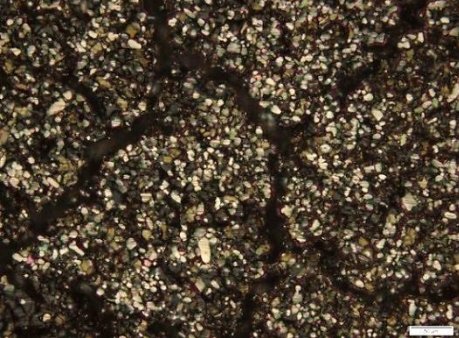
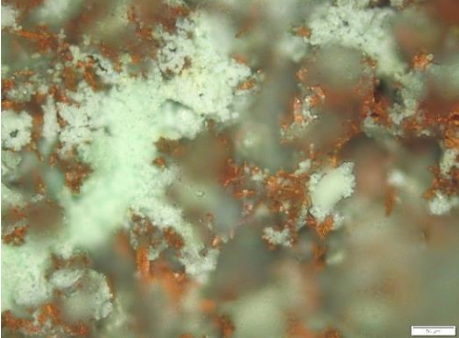
For the ULTIMET alloy, the overall analysis on the surface after corrosion tests showed low concentrations of Co, Cr, Mn, Fe and Ni in the test solutions, with more O, C, Mo and W left on the surface. This change had also been observed at grain boundaries on the surface, with high concentrations of Mo left on the surface. At pH 6 (Table 5.12), there

were high concentrations of C, O and Mo in the pits, and low concentrations at pH 3 (Table 5.15) and 1 (Table 5.18). However, the analysis of the pits could be inaccurate as the samples were no longer flat.

For the Stellite 6B alloy, the overall analysis on the surface after corrosion tests showed low concentrations of Co, Cr and Ni in the test solutions, with more C, O, Fe and W left on the surface. There was a higher concentration of O than C at the carbides at pH 3 (Table 5.16) and 1 (Table 5.19). This shows that an oxide film formed on top of the carbides, likely to be chromium oxide. In the pits, only Cr, Co, Mn, Fe, Mo and W were detected at pH 6 (Table 5.13). In addition to these, C and O were detected at pH 3 and 1.

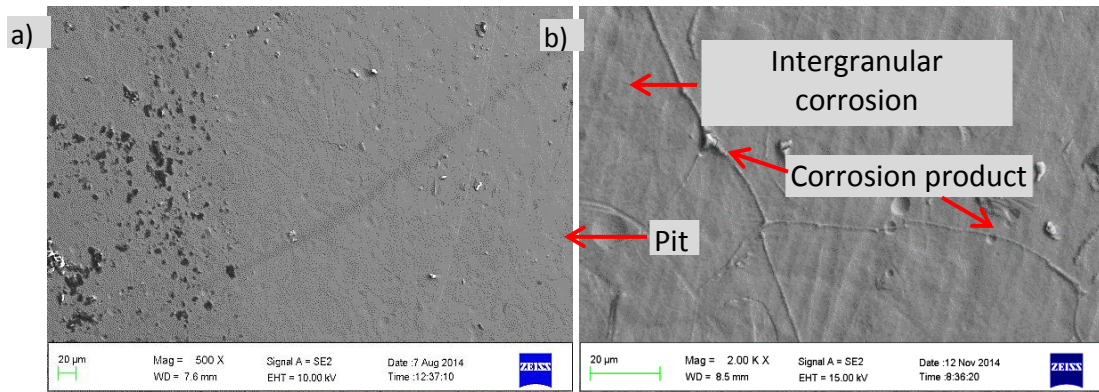
For the ToughMet 3 alloy, the overall analysis on the surface after corrosion tests showed low concentrations of Na, S, Ca and Ni in the test solutions, with more O, Cl and Cu left on the surface. Apart from Cu, these elements were from the test solutions. Tin was not detected at pH 6 (Table 5.14) and 1 (Table 5.20) for overall surface analysis, although it was found in pits at pH 1 only. High concentrations of Cu and Cl were in the pits at pH 6 and 3 (Tables 5.14 and 5.17), while at pH 1, high concentrations of O, Cl, Ni and Cu were detected (Table 5.20).



pH	ULTIMET	Stellite 6B	ToughMet 3	Description
6				<p>ULTIMET: general and intergranular corrosion.</p> <p>Stellite 6B: intergranular corrosion, surface oxides and carbides in pits.</p> <p>ToughMet 3: pitting, general and selective corrosion, with a partial layer on the surface.</p>
3				<p>ULTIMET: general and intergranular corrosion.</p> <p>Stellite 6B: attack similar to that at pH 6.</p> <p>ToughMet 3: attack similar to that at pH 6.</p>
1				<p>ULTIMET: more general + intergranular corrosion.</p> <p>Stellite 6B: attacked much more than at pH 6 and 3.</p> <p>ToughMet 3: attacked similar to that at pH 6.</p>

**Figure 5.8.** Optical micrographs of ULTIMET, Stellite 6B and ToughMet 3 samples after cyclic potentiodynamic polarisation in synthetic mine water at pH 6, 3 and 1.

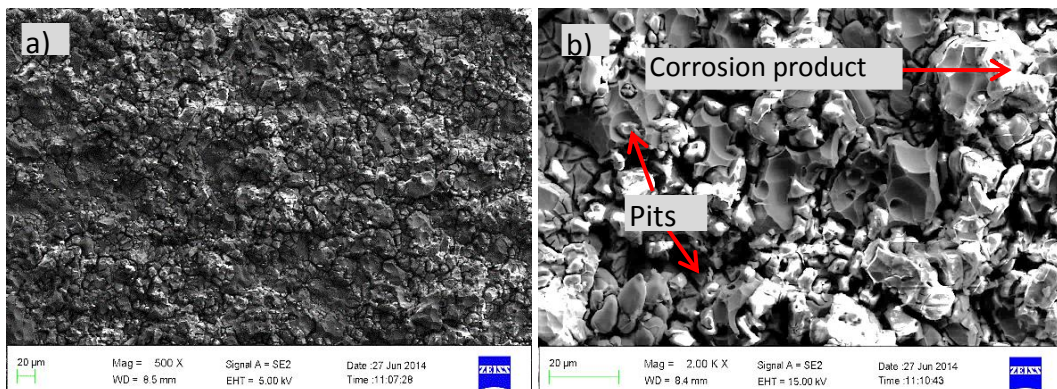




**Figure 5.9.** SEM-SE micrographs of the ULTIMET sample surface after cyclic potentiodynamic polarisation in synthetic mine water at pH 6, at: a) low, and b) high magnification, showing slight pitting and intergranular corrosion, and corrosion products.

**Table 5.12.** EDX analysis of the ULTIMET sample surface of Figure 5.9 after cyclic potentiodynamic polarisation in synthetic mine water at pH 6.

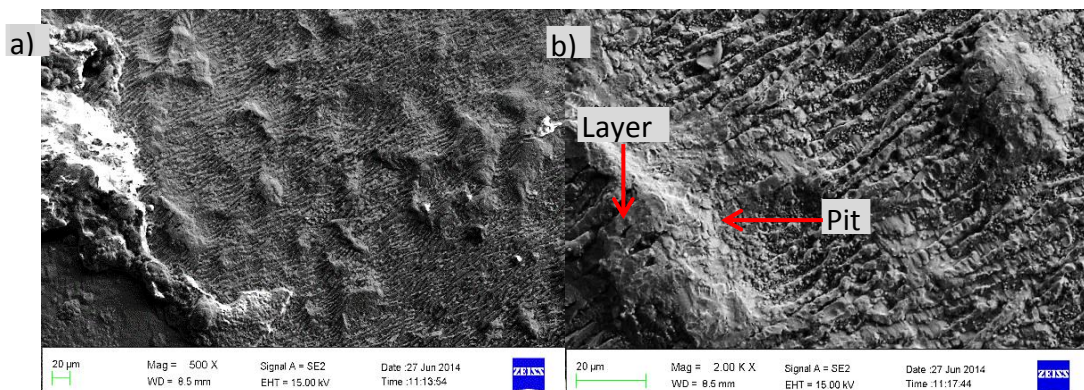
Element	Composition (wt%)			
	Overall before	Overall after	Grain boundaries	Pits
C	3.5 ± 1.0	5.6 ± 0.2	6.3 ± 2.0	7.2 ± 4.0
O	-	12.3 ± 0.4	13.6 ± 2.0	15.4 ± 4.0
Na	-	0.3 ± 0.0	0.3 ± 0.1	0.4 ± 0.1
Si	0.3 ± 0.0	0.3 ± 0.1	0.3 ± 0.0	0.2 ± 0.1
S	-	0.4 ± 0.1	0.3 ± 0.2	0.4 ± 0.1
Cr	24.4 ± 0.2	21.4 ± 0.1	21.2 ± 1.0	20.7 ± 1.3
Mn	0.8 ± 0.1	0.7 ± 0.0	0.7 ± 0.1	-
Fe	2.8 ± 0.0	2.3 ± 0.1	2.1 ± 0.0	2.0 ± 0.2
Co	51.9 ± 1.0	38.3 ± 0.1	36.1 ± 2.2	33.9 ± 7.0
Ni	8.7 ± 0.1	6.6 ± 0.4	6.1 ± 0.4	5.6 ± 1.0
Mo	5.4 ± 0.2	9.5 ± 0.1	10.4 ± 0.4	10.9 ± 0.4
W	2.1 ± 0.0	2.5 ± 0.1	2.7 ± 0.3	2.7 ± 1.0



**Figure 5.10.** SEM-SE micrographs of Stellite 6B sample surface after cyclic potentiodynamic polarisation in synthetic mine water at pH 6, showing intergranular corrosion, oxides on the surface and carbides in pits. a) low, and b) high magnification.

**Table 5.13.** EDX analysis of the Stellite 6B sample surface of Figure 5.10 after cyclic potentiodynamic polarisation in synthetic mine water at pH 6.

Element	Composition (wt%)			
	Overall before	Overall after	Corrosion products	Pits
C	7.6 ± 0.0	14.6 ± 1.0	11.5 ± 8.0	-
Ca	-	0.3 ± 0.0	-	-
O	7.4 ± 1.0	8.4 ± 0.3	8.4 ± 7.0	-
Na	-	0.3 ± 0.0	-	-
Si	0.4 ± 0.0	-	-	-
S	-	0.2 ± 0.1	-	-
Cr	29.5 ± 1.0	26.6 ± 0.1	38.0 ± 23.0	39.9 ± 22.0
Mn	1.5 ± 0.1	1.5 ± 0.0	2.4 ± 1.0	4.6 ± 4.0
Fe	1.7 ± 0.1	1.9 ± 0.0	1.1 ± 1.0	1.1 ± 1.0
Co	46.2 ± 0.1	38.8 ± 0.0	32.3 ± 17.0	39.0 ± 21.0
Ni	1.7 ± 0.1	-	-	-
Mo	-	-	0.8 ± 1.0	0.4 ± 0.4
W	4.8 ± 0.1	6.1 ± 1.0	5.2 ± 3.0	1.3 ± 2.0

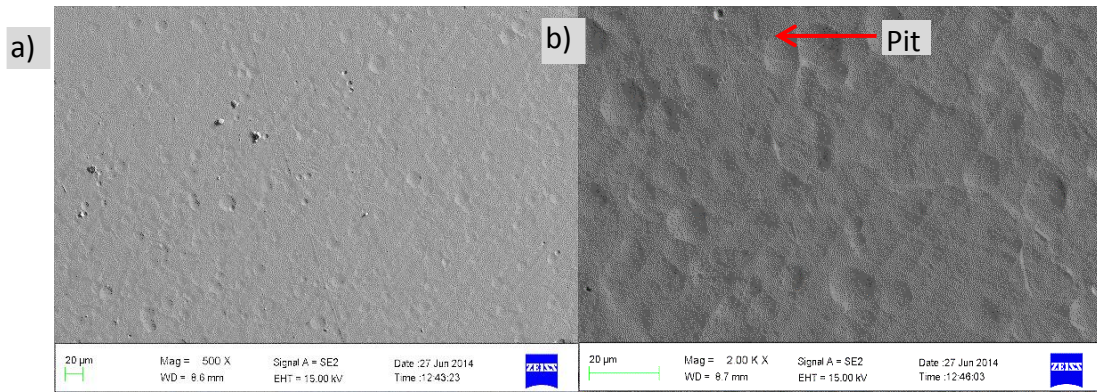


**Figure 5.11.** SEM-SE micrographs of the ToughMet 3 sample surface after cyclic potentiodynamic polarisation in synthetic mine water at pH 6, showing pitting, general and selective corrosion with a thick CuCl-Cu<sub>2</sub>O layer on the surface. a) low, and b) high magnification.

**Table 5.14.** EDX analysis of the ToughMet 3 sample surface of Figure 5.11 after cyclic potentiodynamic polarisation in synthetic mine water at pH 6.

Element	Composition (wt%)		
	Overall before	Overall after	Pits
O	-	11.3 ± 2.0	3.2 ± 1.0
Na	-	0.1 ± 0.0	0.2 ± 0.0
S	-	0.4 ± 0.0	0.1 ± 0.0
Cl	-	10.0 ± 3.0	3.4 ± 3.0
Ca	-	0.4 ± 0.0	-
Cu	78.3 ± 0.2	50.4 ± 7.0	86.8 ± 12.0
Ni	13.9 ± 0.1	0.6 ± 0.0	-
Sn	7.8 ± 0.1	-	-

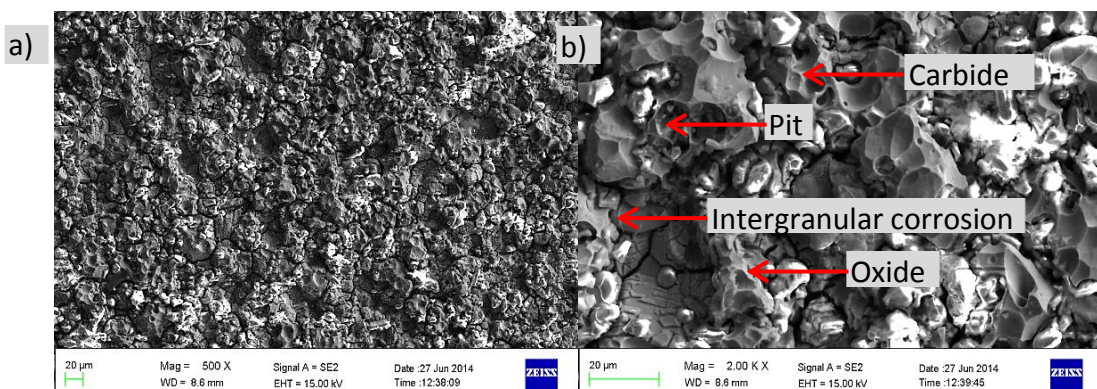




**Figure 5.12.** SEM-SE micrographs of the ULTIMET sample surface after corrosion in acidified synthetic mine water at pH 3, at: a) low, and b) high magnification, showing shallow pits.

**Table 5.15.** EDX analysis of the ULTIMET sample surfaces of Figure 5.12 after cyclic potentiodynamic polarisation in acidified synthetic mine water at pH 3.

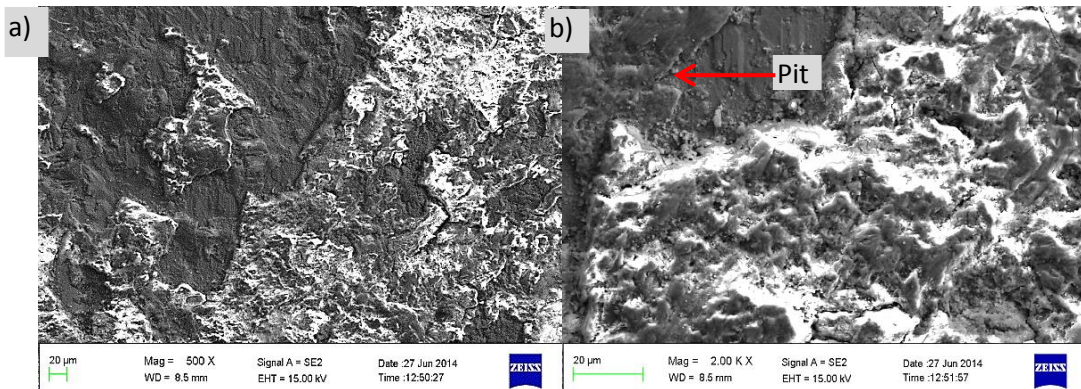
Element	Composition (wt%)		
	Overall before	Overall after	Pits
C	3.5 ± 1.0	4.7 ± 0.0	3.1 ± 2.0
O	-	3.4 ± 0.0	2.5 ± 0.1
Si	0.3 ± 0.0	-	-
Cr	24.4 ± 0.2	23.8 ± 1.0	24.4 ± 1.0
Mn	0.8 ± 0.1	0.8 ± 0.0	0.9 ± 0.1
Fe	2.8 ± 0.0	2.7 ± 0.0	2.7 ± 0.1
Co	51.9 ± 1.0	48.7 ± 0.0	50.0 ± 1.0
Ni	8.7 ± 0.1	8.0 ± 0.0	8.5 ± 0.2
Mo	5.4 ± 0.2	5.3 ± 1.0	5.3 ± 0.3
W	2.1 ± 0.0	2.5 ± 0.0	2.4 ± 0.3



**Figure 5.13.** SEM-SE micrographs of Stellite 6B surface after cyclic potentiodynamic polarisation (acidified synthetic mine water, pH 3). a) low, and b) high magnification, showing intergranular corrosion, oxides on the surface and carbides in pits.

**Table 5.16.** EDX analysis of the Stellite 6B sample surfaces of Figure 5.13 after cyclic potentiodynamic polarisation in acidified synthetic mine water at pH 3.

Element	Composition (wt%)		
	Overall before	Overall after	Carbides
C	7.6 ± 0.0	11.3 ± 1.0	5.2 ± 2.0
O	7.4 ± 1.0	7.0 ± 0.1	10.4 ± 7.0
Na	-	0.2 ± 0.1	-
Si	0.4 ± 0.0	0.4 ± 0.1	-
S	-	0.3 ± 0.0	-
Ca	-	0.2 ± 0.0	-
Cr	29.5 ± 1.0	27.5 ± 0.0	41.0 ± 20.0
Mn	1.5 ± 0.1	1.7 ± 0.2	2.6 ± 2.0
Fe	1.7 ± 0.1	2.0 ± 0.0	1.8 ± 0.6
Co	46.2 ± 0.1	42.8 ± 1.0	30.1 ± 15.0
Ni	1.7 ± 0.1	1.0 ± 0.1	-
Mo	-	5.5 ± 0.1	1.3 ± 0.5
W	4.8 ± 0.1	5.5 ± 0.1	7.2 ± 5.0

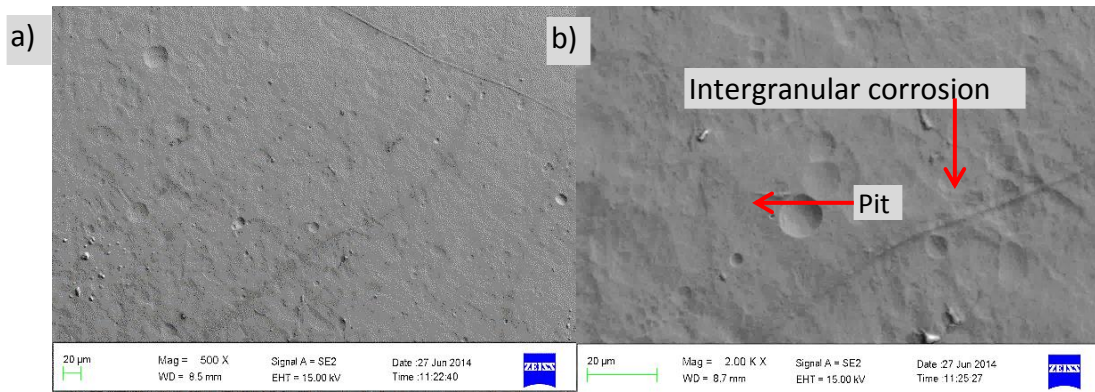


**Figure 5.14.** SEM-SE micrographs of ToughMet 3 after cyclic potentiodynamic polarisation (acidified synthetic mine water, pH 3). a) low, and b) high magnification, showing pitting, general and selective corrosion.

**Table 5.17.** EDX analysis (wt%) of the ToughMet 3 sample surfaces of Figure 5.14 after cyclic potentiodynamic polarisation in acidified synthetic mine water at pH 3.

Element	Composition (wt%)			
	Overall before	Overall after	Pits	Corrosion products
C	-	-	3.9 ± 2.0	3.6 ± 2.0
O	-	12.9 ± 2.0	1.71 ± 1.0	1.3 ± 1.0
Cl	-	20.3 ± 5.0	42.3 ± 20.0	23.6 ± 17.0
Ca	-	0.2 ± 0.1	-	-
Ni	13.9 ± 0.1	0.2 ± 0.0	-	0.4 ± 0.2
Cu	78.3 ± 0.2	61.4 ± 2.0	51.4 ± 20.0	36.2 ± 28.0
Sn	7.8 ± 0.1	5.0 ± 1.0	-	-

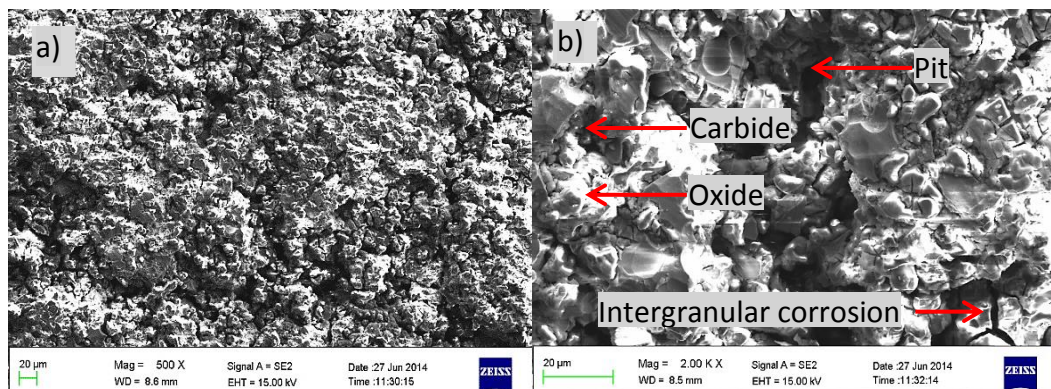




**Figure 5.15.** SEM-SE micrographs of the ULTIMET sample surface after cyclic potentiodynamic polarisation in acidified synthetic mine water at pH 1, at: a) low, and b) high magnification showing pitting, and slight intergranular corrosion.

**Table 5.18.** EDX analysis of the ULTIMET sample surfaces of Figure 5.15 after cyclic potentiodynamic polarisation in acidified synthetic mine water at pH 1.

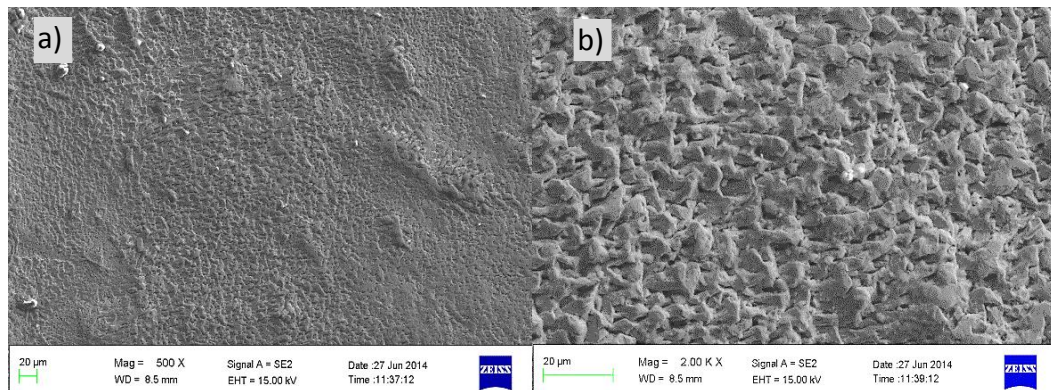
Element	Composition (wt%)		
	Overall before	Overall after	Pits
C	3.5 ± 1.0	3.9 ± 1.0	3.6 ± 1.0
O	-	3.3 ± 0.2	2.9 ± 1.0
Si	0.3 ± 0.0	-	-
Cr	24.4 ± 0.2	23.8 ± 0.1	24.4 ± 0.2
Mn	0.8 ± 0.1	0.9 ± 0.1	0.8 ± 0.1
Fe	2.8 ± 0.0	2.7 ± 0.0	2.8 ± 0.1
Co	51.9 ± 1.0	49.2 ± 1.0	49.8 ± 0.4
Ni	8.7 ± 0.1	8.3 ± 0.0	8.4 ± 0.2
Mo	5.4 ± 0.2	5.2 ± 0.1	4.1 ± 2.0
W	2.1 ± 0.0	2.5 ± 0.1	2.5 ± 0.3



**Figure 5.16.** SEM-SE micrographs of the Stellite 6B sample surface after cyclic potentiodynamic polarisation in acidified synthetic mine water at pH 1, at: a) low, and b) high magnification, showing general and intergranular corrosion, oxides on the surface and carbides in pits.

**Table 5.19.** EDX analysis of the Stellite 6B sample surfaces of Figure 5.16 after cyclic potentiodynamic polarisation in acidified synthetic mine water at pH 1.

Element	Composition (wt%)			
	Overall before	Overall after	Carbides	Pits
C	7.6 ± 0.0	6.6 ± 1.0	4.8 ± 3.0	4.2 ± 1.0
O	7.4 ± 1.0	12.6 ± 0.2	-	16.4 ± 8.0
Na	-	0.2 ± 0.0	-	-
S	-	0.8 ± 0.1	-	-
Si	0.4 ± 0.0	-	-	-
Cr	29.5 ± 1.0	29.8 ± 0.2	75.3 ± 6.0	28.5 ± 4.0
Mn	1.5 ± 0.1	1.4 ± 0.1	1.9 ± 1.0	1.7 ± 1.0
Fe	1.7 ± 0.1	1.5 ± 0.0	0.8 ± 0.1	2.0 ± 0.2
Co	46.2 ± 0.1	35.8 ± 0.2	11.3 ± 2.0	33.4 ± 14.0
Ni	1.7 ± 0.1	1.4 ± 0.0	-	-
Mo	-	0.9 ± 0.4	-	1.3 ± 0.7
W	4.8 ± 0.1	8.7 ± 0.4	11.4 ± 6.0	-



**Figure 5.17.** SEM-SE micrographs of the ToughMet 3 sample surface after cyclic potentiodynamic polarisation in acidified synthetic mine water at pH 1, at: a) low, and b) high magnification, showing severe general and selective corrosion on the grains.

**Table 5.20.** EDX analysis of the ToughMet 3 sample surfaces of Figure 5.17 after cyclic potentiodynamic polarisation in acidified synthetic mine water at pH 1.

Element	Composition (wt%)		
	Overall before	Overall after	Pits
C	-	27.1 ± 1.0	12.4 ± 5.0
O	-	7.8 ± 0.2	10.0 ± 5.0
S	-	0.3 ± 0.1	-
Cl	-	2.0 ± 0.2	1.5 ± 1.0
Ca	-	0.8 ± 0.0	-
Ni	13.9 ± 0.1	0.4 ± 0.0	0.9 ± 0.3
Cu	78.3 ± 0.2	61.5 ± 1.0	69.0 ± 21.0
Sn	7.8 ± 0.1	-	0.5 ± 0.2

## 5.6 Friction and sliding wear results

Figure 5.18 shows the friction behaviour of ULTIMET and Stellite 6B alloys sliding against 100Cr steel balls as a function of sliding distance. ToughMet 3 and Hastelloy G30 samples were not tested for friction and wear, because of the limited materials, and since they were not performing well and likely to be not considered for further evaluations. At 5N (Figure 5.18 a), the coefficient of friction ( $\mu$ ) for ULTIMET alloy increased from 0.15 to 0.40 then decreased to 0.30, and reached steady state between 0.35 to 0.37 after 5m. For Stellite 6B,  $\mu$  increased from 0.17 to 0.88 in 20 m, then attained steady state between 0.81 and 0.89 for 180 m. Stellite 6B had a higher  $\mu$  of  $0.89 \pm 0.0$  (maximum) compared to  $0.4 \pm 0.0$  (maximum) for ULTIMET. The wear rate  $k$  for ULTIMET was  $1.6 \times 10^{-4} \text{ mm}^3 (\text{N.m})^{-1}$  and  $7.8 \times 10^{-5} \text{ mm}^3 (\text{N.m})^{-1}$  for Stellite 6B.

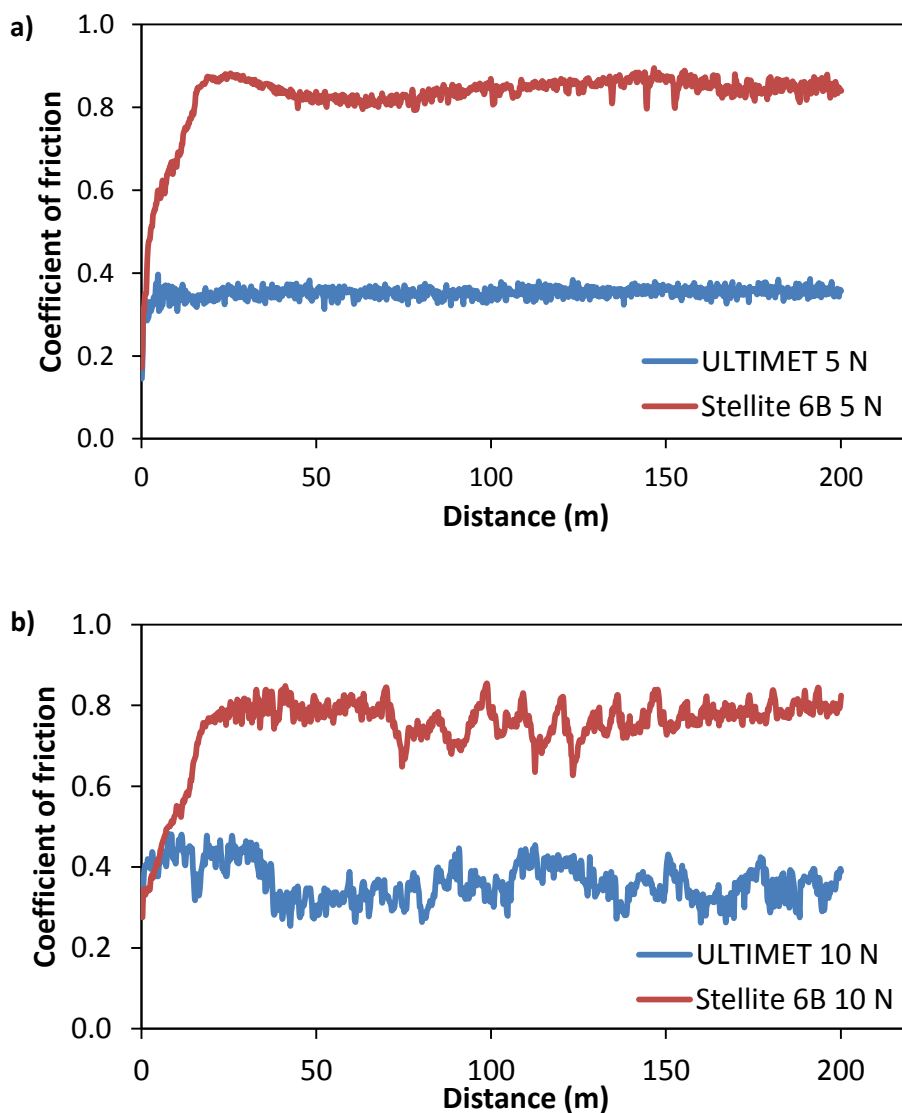
At 10 N, as shown in Figure 5.18 b), the coefficient of friction  $\mu$  for ULTIMET alloy increased from 0.13 to 0.48 then decreased to 0.31, and reached steady state after 40 m between 0.25 to 0.44. For Stellite 6B,  $\mu$  increased from 0.27 to 0.84 in 20 m, and attained steady state between 0.62 and 0.84 after 110 m. Stellite 6B had a higher  $\mu$  of 0.70 compared to 0.40 for ULTIMET. The wear rate  $k$  for ULTIMET was  $7.7 \times 10^{-5} \text{ mm}^3 (\text{N.m})^{-1}$  and Stellite 6B was  $5.6 \times 10^{-5} \text{ mm}^3 (\text{N.m})^{-1}$ .

As sliding occurs, the ball will plough (cut) the surface, producing grooves. It was observed that the abrasive wear mechanisms for ULTIMET sample against the ball were by irregular cutting (causing a wavy appearance), grooves, cracks, and severe spalling at both loads, while for Stellite 6B wear occurred by grooving. The widest wear tracks with coarser grooves and intermittent contact (Figure 5.19 a)), and thus the highest volume loss, occurred on the ULTIMET compared to Stellite 6B sample (Figure 5.19 b)), and Stellite 6B alloy was the most resistant to sliding wear at both loads.

SEM-SE micrographs of the worn surfaces of the ULTIMET and Stellite 6B samples showed furrow marks, which are typical evidence of sliding wear where material was removed from the surfaces. There was wavy and fairly long continuous furrows in ULTIMET (Figure 5.20 a) and c)), which were fewer in the Stellite 6B sample (Figure 5.20 b) and d)). The waviness in ULTIMET samples may have been caused by low friction between the 100Cr steel balls and the samples, resulting in intermittent contact. Figure 5.21 a) and b) are the parts of the wear tracks of ULTIMET and Stellite 6B. SEM micrographs showed ULTIMET experienced delamination, slip bands and slip steps on the surface near the wear track (Figure 5.22 a) and c)). Stellite 6B had debris collected in the grooves (Figure 5.22 b) and

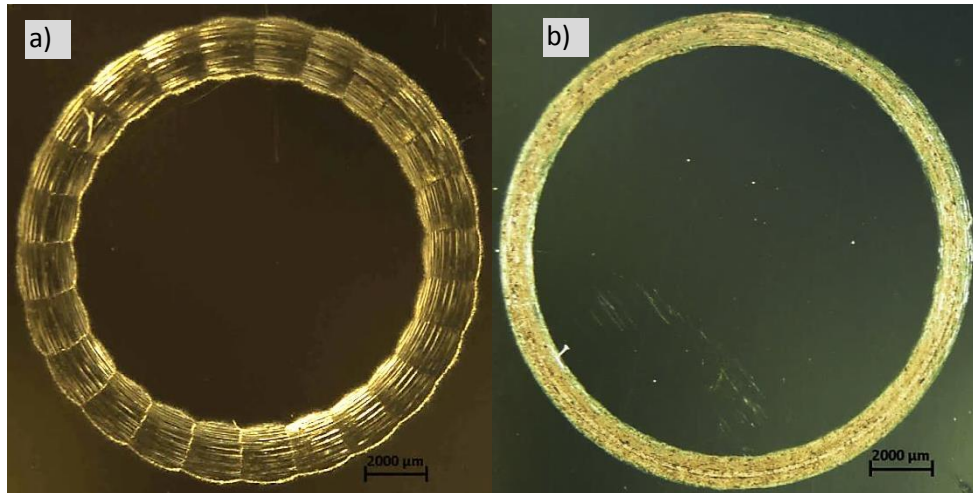
d)). The matrix phase was ploughed out, leaving carbides on the surface which were clearly seen under SEM-BSE mode.

Table 5.21 shows the EDX analysis of ULTIMET and Stellite 6B wear tracks from Figures 5.20 a) and b), 5.21 a), and 5.22 a) and b) after ball-on-disc sliding wear at 5 N and 10 N. EDX analysis of the ULTIMET sample showed Co, Cr, Ni and Mo as major constituents on the wear tracks, with Mn, W, O, C and Si as minor components. For Stellite 6B, the overall EDX showed Co, Cr, O and Mn as major constituents on the wear tracks, with Ni, W, O, Si and Mo as minor components.



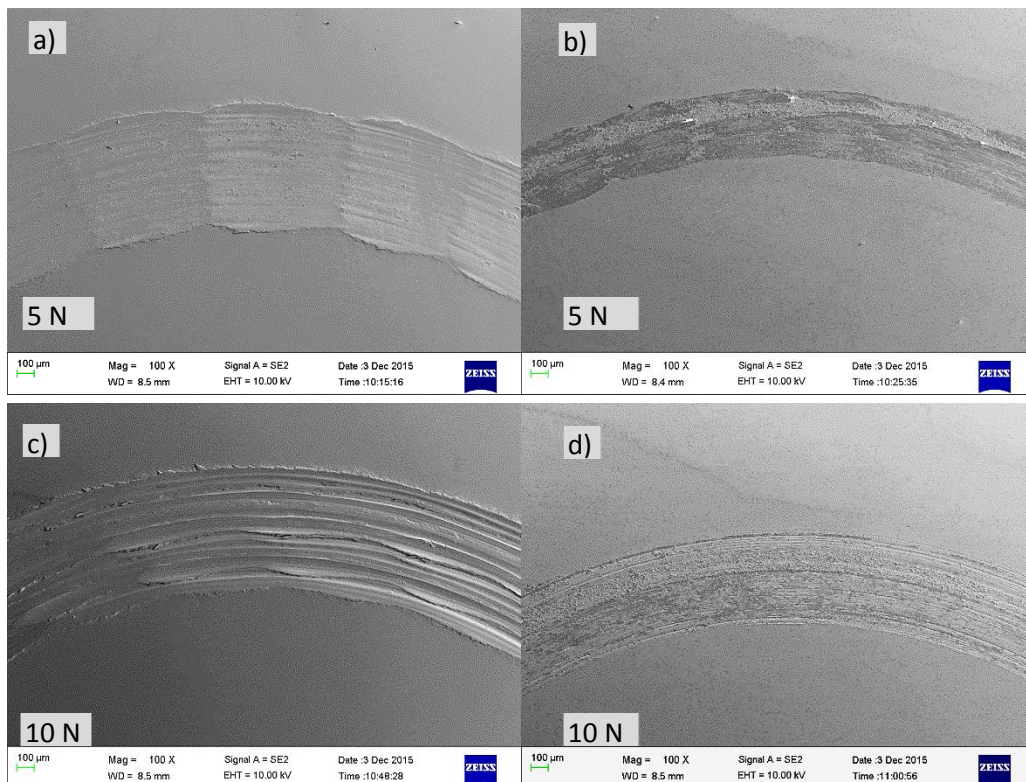
**Figure 5.18.** Friction behaviour of ULTIMET and Stellite 6B alloys against 100Cr steel balls at: a) 5 N, and b) 10 N.



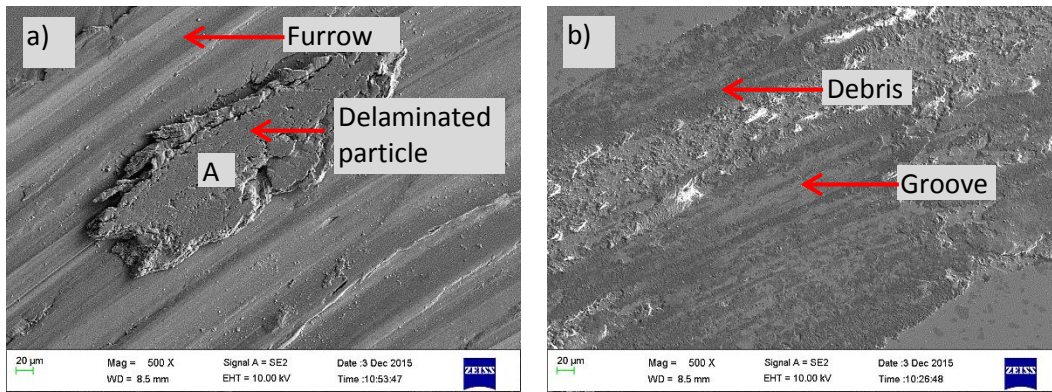


**Figure 5.19.** Stereo microscope macrographs of: a) ULTIMET, and b) Stellite 6B after ball-on-disc sliding wear at room temperature.

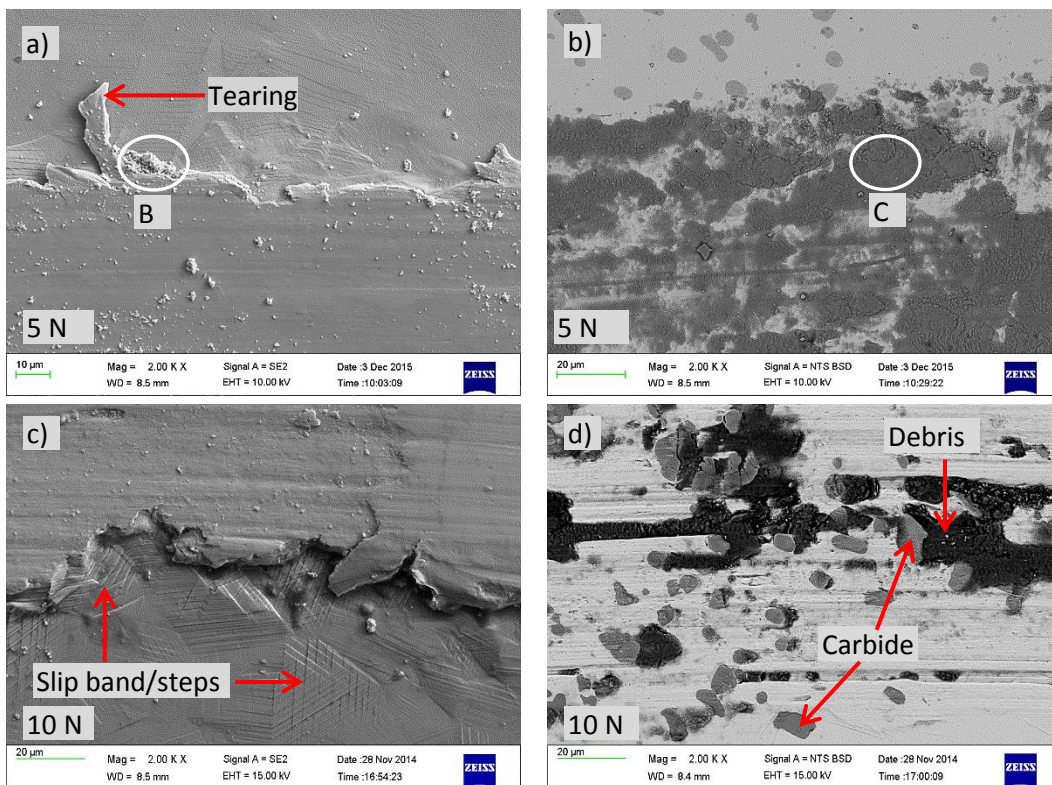
EDX analysis (Table 5.21) of delaminated particles of the ULTIMET samples (position A of Figure 5. 21 a)) showed Co, Cr, Ni and O as major elements, and Mo, Fe, W, Mn, C and Si as minor constituent on the wear track. For position B (Figure 5. 22 a)), the difference was only on O content which was lower than position A. EDX analysis of the Stellite 6B (position C of Figure 5. 22 b)) sample showed high contents of Co, Cr, O and Fe, with low content of Ni, W, C, Mo and Si on the wear track.



**Figure 5.20.** SEM-SE micrographs of: a) and c) ULTIMET, and b) and d) Stellite 6B after ball-on-disc sliding wear at 5 N and 10 N, showing wider wear tracks of ULTIMET than Stellite 6B at both loads.



**Figure 5.21.** SEM-SE micrographs after ball-on-disc sliding wear of: (a) ULTIMET, showing fairly long continuous furrows, and flattered and delaminated particles on the furrows, and (b) Stellite 6B, showing much debris collected in the grooves.



**Figure 5.22.** SEM-SE micrographs of: a) and c) ULTIMET, showing tearing, slip bands and slip steps on the surface near the wear track, and b) and d) SEM-BSE image: Stellite 6B, showing debris in the grooves, and the matrix phase ploughed out, leaving carbides on the surface.



**Table 5.21.** EDX analysis of the ULTIMET and Stellite 6B sample surfaces of Figures 5.20 a) and b), 5.21 a), and 5.22 a) and b) after ball-on-disc sliding wear at 5N.

Element	Composition (wt%)				
	Overall on wear track		ULTIMET		Stellite 6B
	ULTIMET	Stellite 6B	Position A	Position B	Position C
C	0.7 ± 0.0	2.2 ± 0.0	0.8 ± 0.5	0.9 ± 0.0	1.7 ± 1.0
O	1.0 ± 0.1	19.0 ± 1.0	9.6 ± 1.0	3.3 ± 2.0	25.5 ± 2.0
Si	0.2 ± 0.0	0.2 ± 0.0	0.2 ± 0.0	0.2 ± 0.0	0.2 ± 0.0
Cr	24.8 ± 0.3	27.1 ± 1.0	22.8 ± 1.0	24.3 ± 0.0	25.0 ± 2.0
Mn	3.0 ± 0.5	8.0 ± 1.0	1.6 ± 0.0	3.3 ± 0.0	-
Fe	-	-	2.2 ± 0.0	-	12.7 ± 2.0
Co	52.3 ± 0.1	37.0 ± 1.0	46.0 ± 0.0	50.0 ± 3.0	29.6 ± 4.0
Ni	12.6 ± 0.4	3.3 ± 0.0	11.2 ± 1.0	12.6 ± 1.0	2.9 ± 0.0
Mo	3.6 ± 0.2	0.5 ± 0.0	3.6 ± 0.0	3.7 ± 0.0	0.4 ± 0.0
W	1.6 ± 0.2	2.5 ± 0.0	1.7 ± 0.0	1.6 ± 0.0	2.0 ± 0.0

## 5.7 Summary

ULTIMET, Stellite 6B, and Hastelloy G30 consisted of equiaxed  $\gamma$  grains with twinning. Stellite 6B also had large  $\text{Cr}_7\text{C}_3$  at the grain boundaries. ToughMet 3 contained larger irregular grains.

The hardness ranking of the bulk alloys was: ToughMet 3 ( $368 \pm 14 \text{ HV}_3$ ) = Stellite 6B ( $368 \pm 13 \text{ HV}_3$ ) > ULTIMET ( $304 \pm 22 \text{ HV}_3$ ) > and Hastelloy G30 ( $180 \pm 10 \text{ HV}_3$ ).

At high pH, Hastelloy G30 had a high  $E_{\text{corr}}$  and a lower corrosion rate than ULTIMET and Stellite 6B, while at lower pH, ULTIMET showed slightly high  $E_{\text{corr}}$  and lower, but very similar corrosion rates to Stellite 6B. ToughMet 3 had higher  $E_{\text{corr}}$  and a high corrosion rate at all pH levels.

After corrosion tests, ULTIMET showed general and intergranular corrosion. Stellite 6B also experienced an intergranular corrosion, oxides on the surface and carbides in pits. ToughMet 3 showed pitting, general and selective corrosion.

From the results, Hastelloy G30 had low corrosion rates in synthetic mine water, but it had a lowest hardness, which could mean low wear resistance. ToughMet 3 had high corrosion rates in synthetic mine water, which was not acceptable for the application, even though it had a high hardness, which could have given good wear resistance. Thus, Hastelloy G30 and ToughMet 3 were not considered for further experiments.

ULTIMET experienced delamination, slip bands and slip steps on the surface near the wear track while Stellite 6B had debris collected in the grooves, with the matrix phase was ploughed out, leaving carbides on the surface after a ball-on-disc sliding wear test.

# CHAPTER 6: RESULTS FROM THE SPRAY-COATED MATERIALS

---

## 6.1 Introduction

This chapter presents the results from the characterisation of powders and the HVOF thermally sprayed coatings of candidate alloys which are being considered as potential coatings on the mild steel substrates currently used for the pump components at Otjihase Underground Mine. The powders studied were nominal 0.3 wt% Ru and nominal 0.6 wt% Ru ULTIMET and Stellite 6, which were the best candidates from the bulk alloys study (Chapter 5), with  $\text{Cr}_2\text{O}_3$  used as a benchmark. Small quantities of Ru were added to some of the powders in an attempt to improve the properties. The particle sizes and morphology of the powders were studied. XRD of the powders and the coated samples were done, with Rietveld refinement. The coated samples and the mild steel substrate were also subjected to corrosion, friction and sliding wear and tribocorrosion measurements.

## 6.2. Powder characterisation

### 6.2.1 Particle sizes of the powders

The particle size distributions of the powders (Table 6.1) were given by  $D_{10}$ ,  $D_{50}$ ,  $D_{90}$  and average values, as obtained from the Malvern laser diffraction technique, where  $D_{10}$ ,  $D_{50}$  and  $D_{90}$  are the equivalent volume mean diameters of the particles at 1<sup>st</sup>, 5<sup>th</sup> and 9<sup>th</sup> percentiles. Ruthenium had highest mean particle size, followed by Stellite 6, ULTIMET, NiCrAlY (the bond coat) and chromium oxide. The size distributions of the powders are given in Figures 6.1-6.5. Stellite 6 (Figure 6.2) had the highest particle size ( $D_{50}$ ), then NiCrAlY (Figure 6.4) and ULTIMET (Figure 6.1), and both had narrow particle distributions.  $\text{Cr}_2\text{O}_3$  (Figure 6.3) and Ru (Figure 6.5) had the highest particle size and a wider distribution, which were bi-modal because the particles were agglomerated, and there was even a small peak for very fine particles. This means that unlike for the other particles which had narrow distributions, the Malvern analyses for the Ru powders are not likely to be accurate. The peaks for the ruthenium powders were: finest and least ~15  $\mu\text{m}$ ; middle ~18  $\mu\text{m}$ ; largest and most ~700  $\mu\text{m}$ .

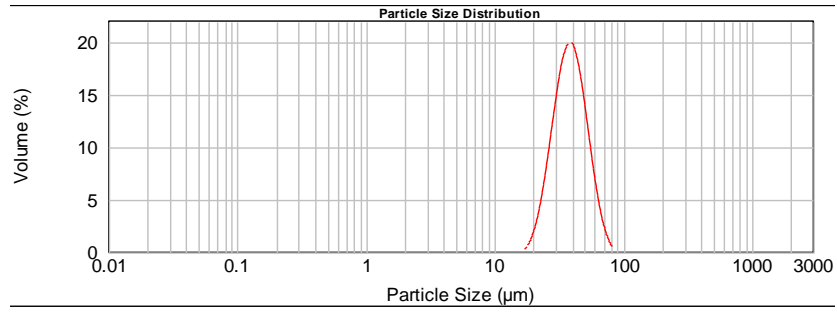


### 6.2.2 Surface morphology of the powders

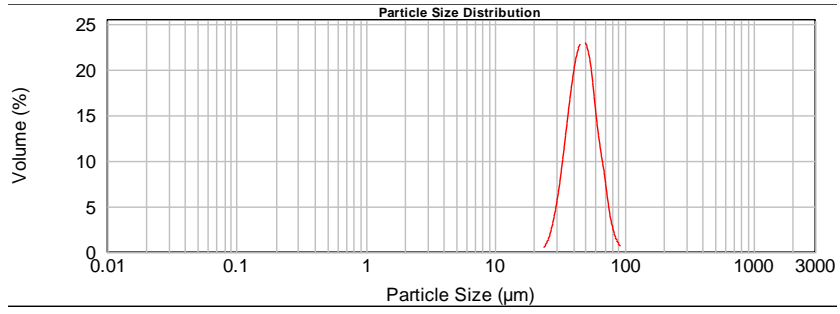
The surface morphologies of the powders taken by SEM in backscattered electron (BSE) mode are given in Figures 6.6-6.8, and the sizes from these small samples in the micrographs appeared smaller than the Malvern particle size analysis. ULTIMET (Figure 6.6), Stellite 6 (Figure 6.7), NiCrAlY (Figures 6.8 c) and d)) powders were spherical particles, sometimes with 'buds', with dendrites being visible, while the Cr<sub>2</sub>O<sub>3</sub> powder (Figure 6.8 a) and b)) had angular particles with smooth facets. The ruthenium powder was angular, sometimes in plates, with different sizes (Figures 6.6 e) and 6.7 e) and agglomerated. ULTIMET and Stellite 6 powders with ruthenium had their smallest particles enclosed in the ruthenium powder after mixing.

**Table 6.1.** Particle sizes and distributions of the powders (by Malvern particle size analysis) in Figures 6.1-6.5.

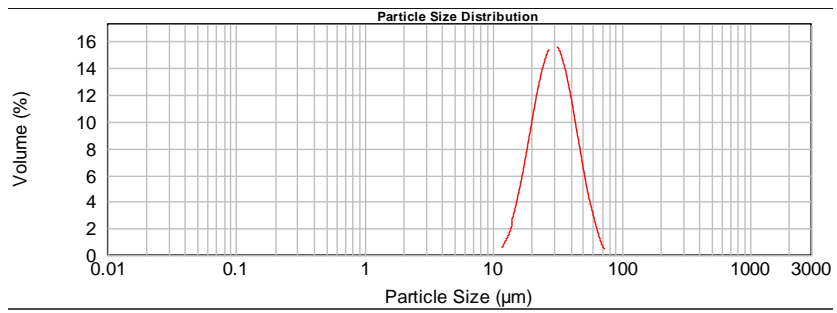
Powder	Particle size distribution (µm)			
	D <sub>10</sub>	D <sub>50</sub>	D <sub>90</sub>	Average
ULTIMET	26.3	38.4	55.8	40.1
Stellite 6	34.1	47.4	65.9	49.1
Cr <sub>2</sub> O <sub>3</sub>	18.2	29.6	47.5	31.8
NiCrAlY	26.3	36.8	51.4	38.2
Ru	47.6	555.8	1116.8	573.4



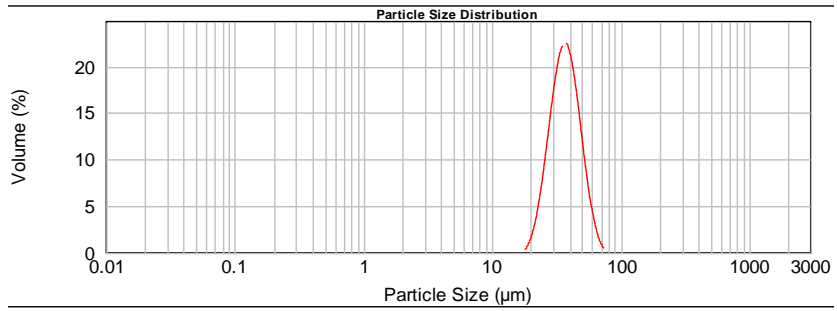
**Figure 6.1.** Particle size analysis of ULTIMET powders.



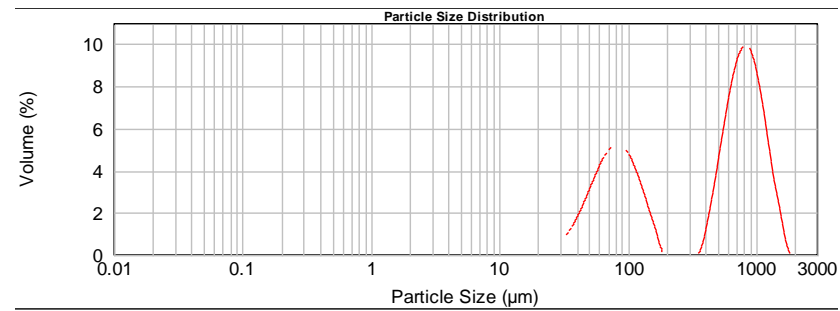
**Figure 6.2.** Particle size analysis of Stellite 6 powders.



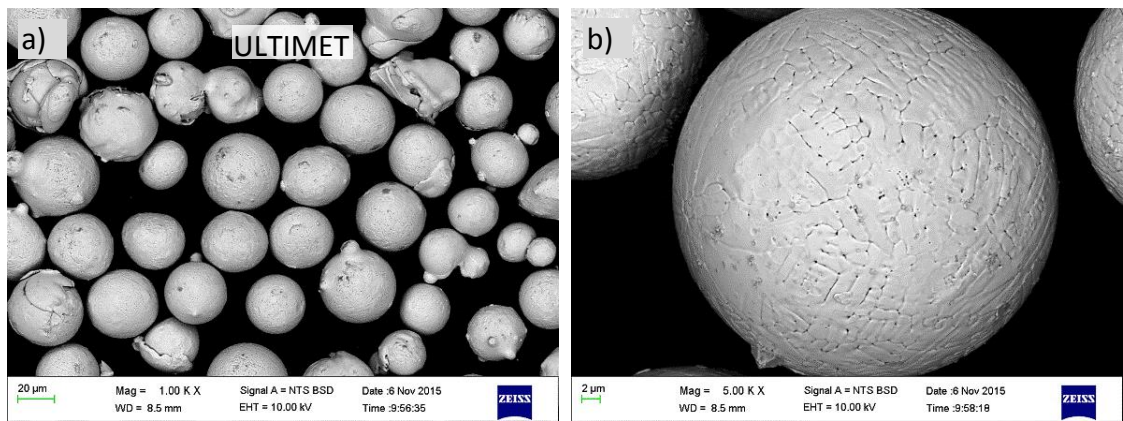
**Figure 6.3.** Particle size analysis of Cr<sub>2</sub>O<sub>3</sub> powders.



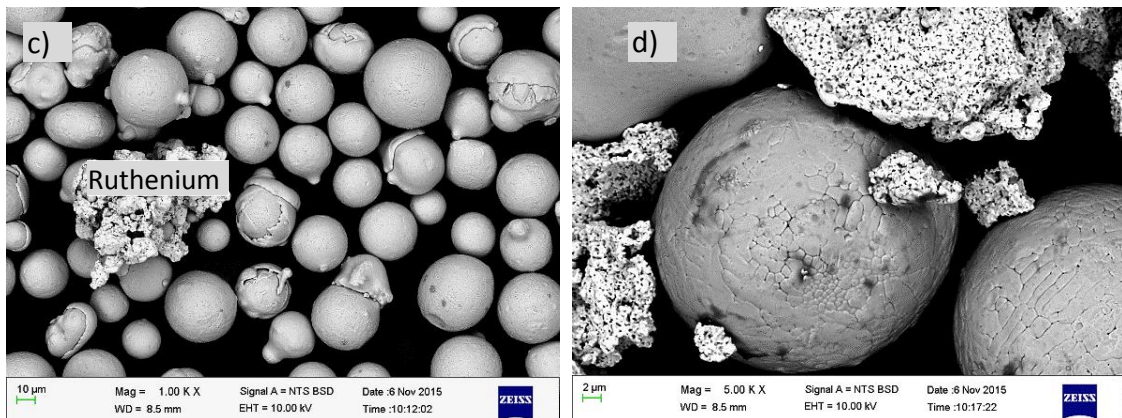
**Figure 6.4.** Particle size analysis of NiCrAlY powders.



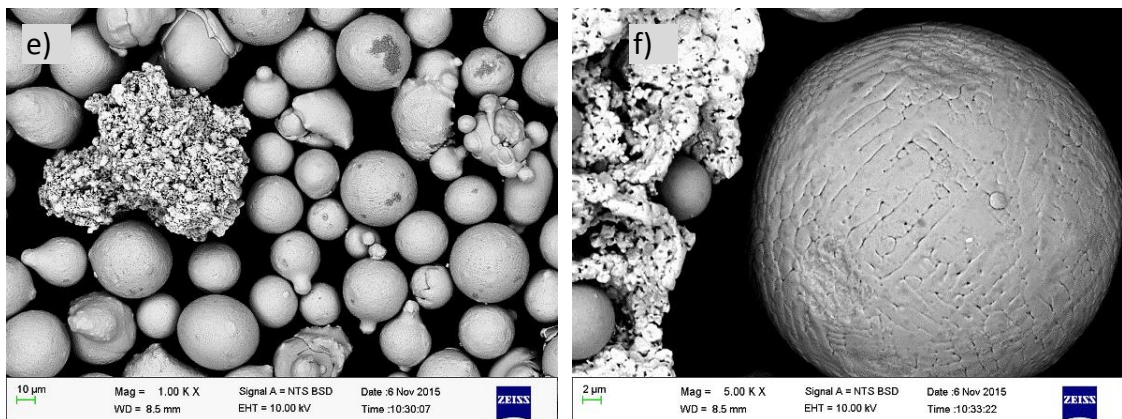
**Figure 6.5.** Particle size analysis of ruthenium powders.



0 wt% Ru



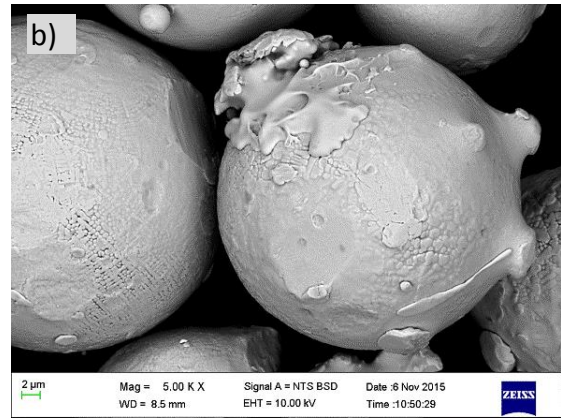
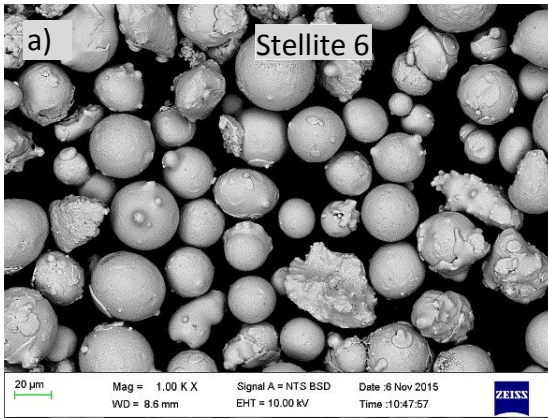
Nominal 0.3 wt% Ru



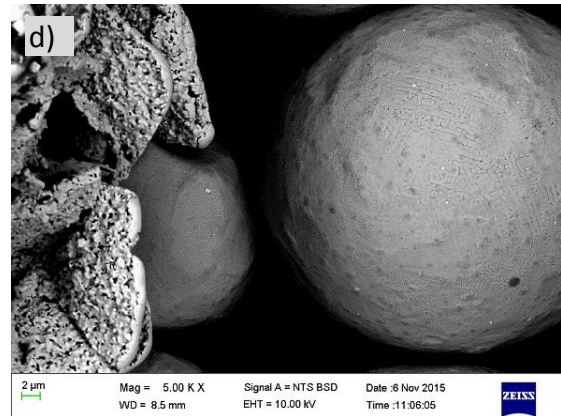
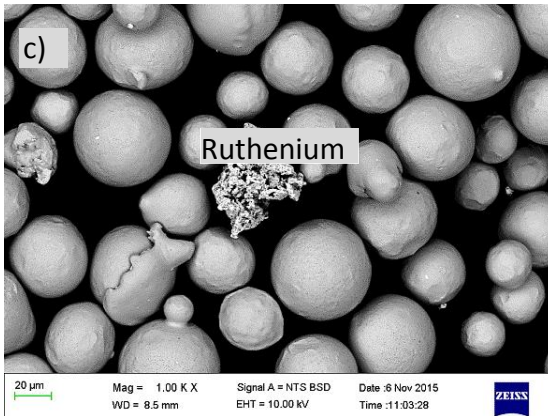
Nominal 0.6 wt% Ru

**Figure 6.6.** SEM-BSE micrographs showing the morphologies of ULTIMET powders, with a) and b) no Ru, c) and d) nominal 0.3 wt% Ru, and e) and f) nominal 0.6 wt% Ru, showing spherical particles with surface dendrites, and their smallest particles enclosed in ruthenium powder after mixing.

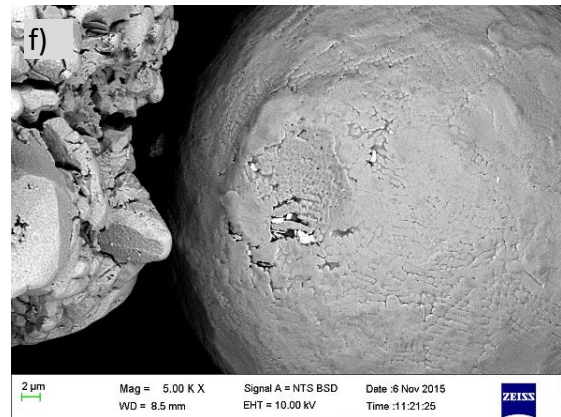
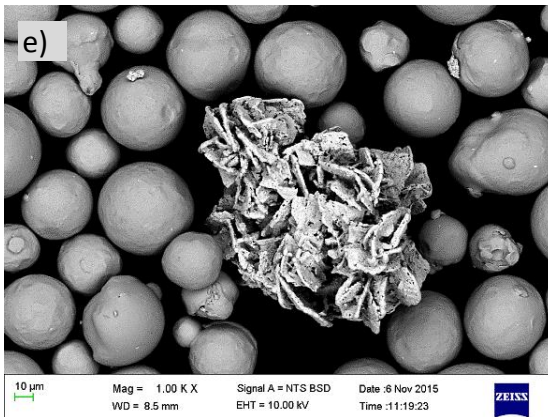




0 wt% Ru



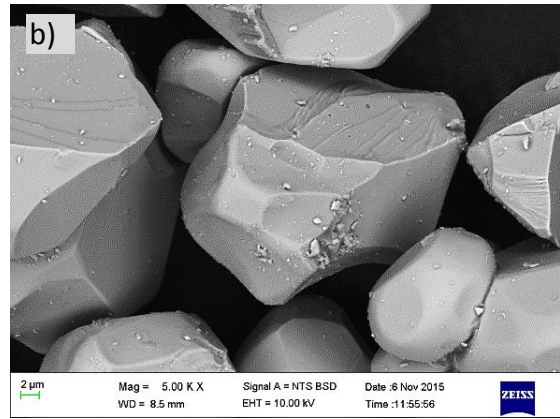
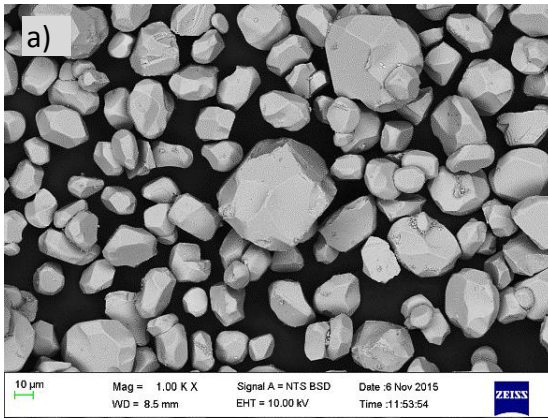
Nominal 0.3 wt% Ru



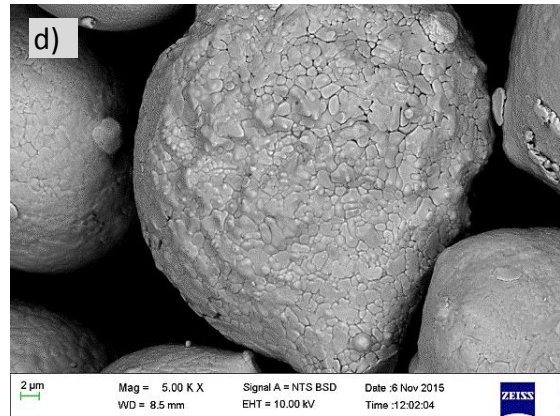
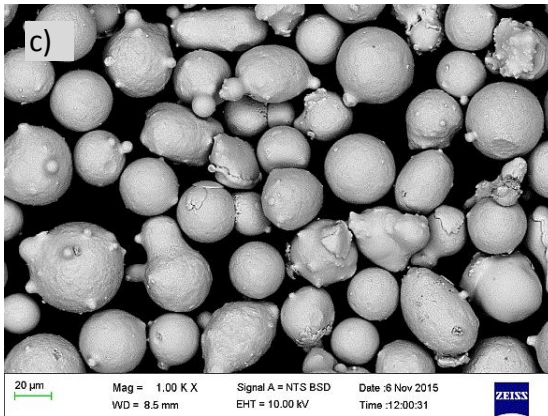
Nominal 0.6 wt% Ru

**Figure 6.7.** SEM-BSE micrographs showing the morphologies of Stellite 6 powders: a) and b) with 0 wt% Ru, c) and d) with nominal 0.3 wt% Ru, and e) and f) with nominal 0.6 wt% Ru, showing spherical particles with dendrites.

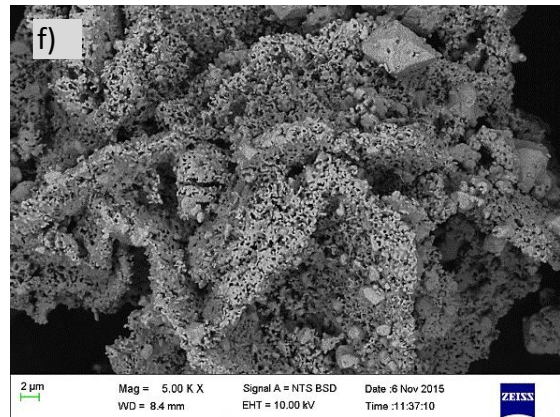
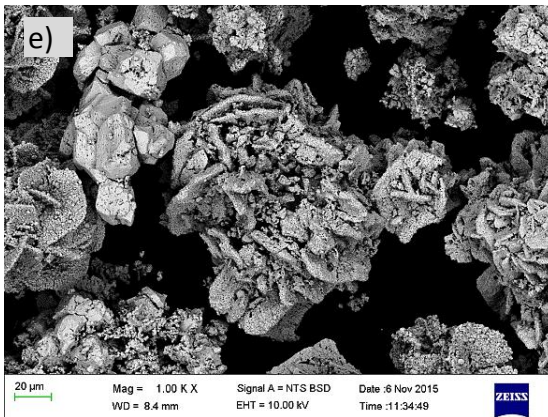




Cr<sub>2</sub>O<sub>3</sub> powder



NiCrAlY bond coating powder



Ruthenium powder

**Figure 6.8.** SEM micrographs showing the morphologies of: a) and b) Cr<sub>2</sub>O<sub>3</sub>, c) and d) NiCrAlY, and e) and f) ruthenium powders.

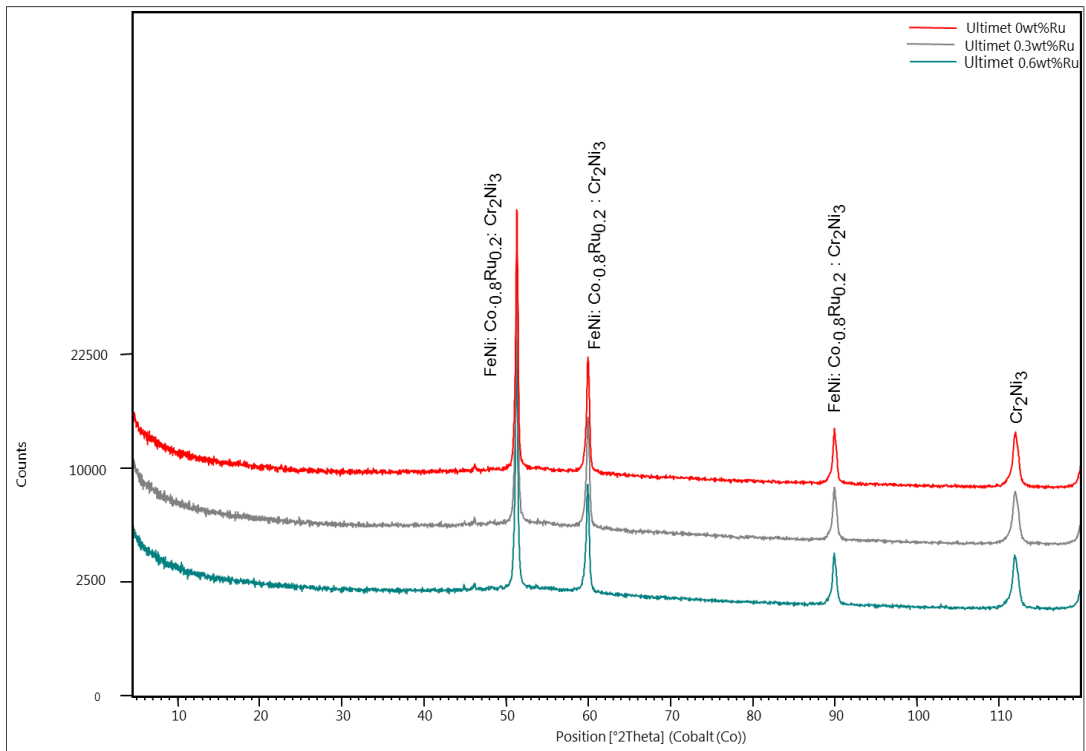
### 6.2.3 Energy dispersive X-ray and X-ray diffraction analysis of the powders

Table 6.2 shows the compositions of the powders. ULTIMET had Co, Cr, Ni as major constituents, with minor amounts of Mn, Mo, W and Si. Stellite 6 had similar compositions, but with little Ni and slightly more W than ULTIMET. Ruthenium content was only recorded for the nominal 0.6 wt% compositions of ULTIMET and Stellite 6. This could be due to loss of ruthenium particles during spray coating or inhomogeneous distribution of powders during mixing and spray coating. Only chromium (70.0 ± 1.0 wt%) and oxygen (31.0 ± 1.0 wt%) were detected in the chromium oxide powders, as expected.

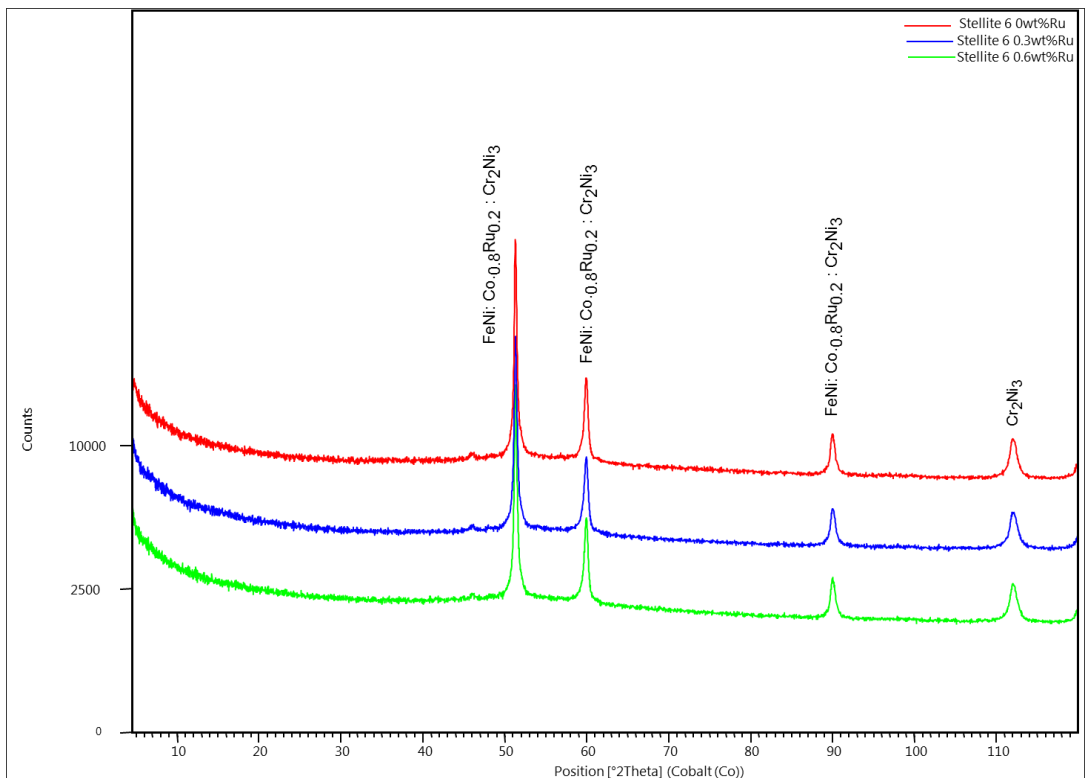
The XRD patterns of coating powders are shown in Figures 6.9-6.12. ULTIMET (Figure 6.9) and Stellite 6 (Figure 6.10) coating compositions without Ru had similar phases of FeNi and Cr<sub>2</sub>Ni<sub>3</sub>. In addition to these phases, ULTIMET and Stellite 6 coatings with nominal 0.3 wt% Ru and nominal 0.6 wt% Ru additions had Co<sub>0.8</sub>Ru<sub>0.2</sub>. No M<sub>7</sub>C<sub>3</sub> or M<sub>23</sub>C<sub>6</sub> (where M is a metal) were detected, which are typical cobalt-based carbides. The chromium oxide powders (Figure 6.11 from Figure 6.8 a)) consistently had single phase Cr<sub>2</sub>O<sub>3</sub>, as expected, while NiCrAlY bond coating powders (Figure 6.12 from Figure 6.8 c)) contained Ni, FeNi, NiAl and AlCr phases.

**Table 6.2.** EDX analysis of the powders for coating.

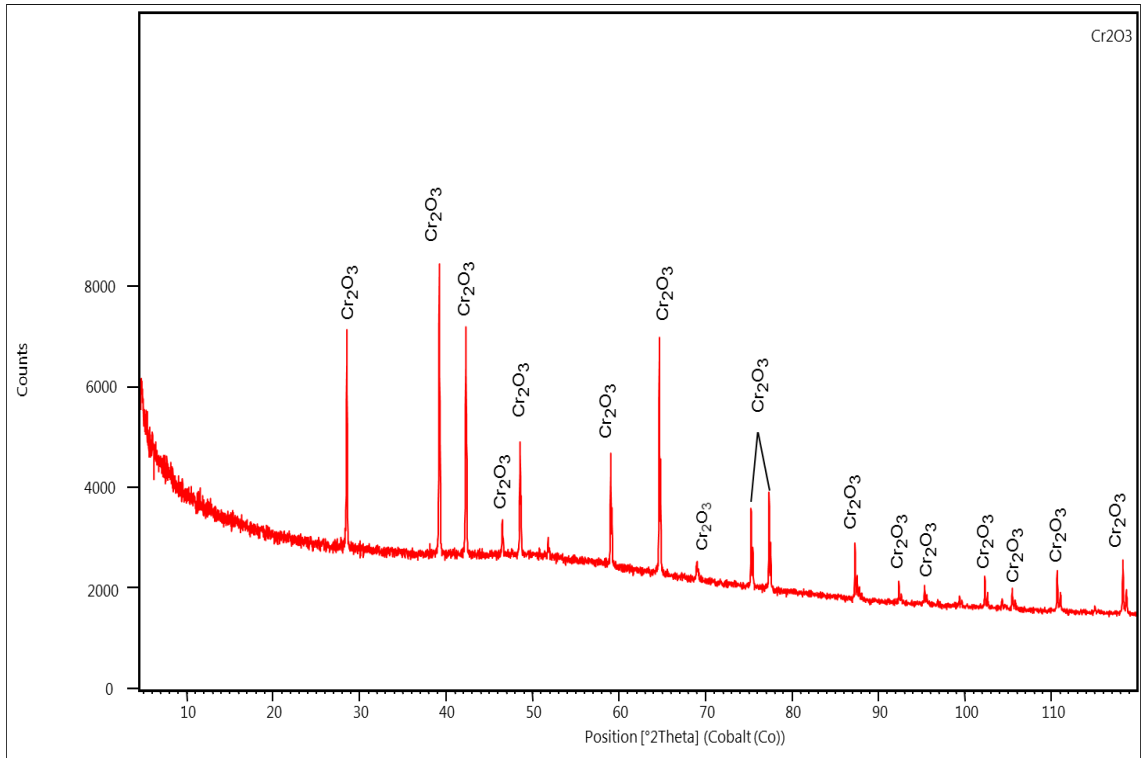
Element (wt%)	ULTIMET	Stellite 6	ULTIMET	Stellite 6	ULTIMET	Stellite 6	Cr <sub>2</sub> O <sub>3</sub>	NiCrAlY
	0 wt% Ru		Nominal 0.3 wt% Ru		Nominal 0.6 wt% Ru			
Si	0.4 ± 0.0	0.9 ± 0.0	0.4 ± 0.0	0.7 ± 0.0	0.4 ± 0.1	0.7 ± 0.1	-	-
Cr	31.0 ± 0.4	35.0 ± 1.0	32.0 ± 1.0	31.0 ± 2.0	31.0 ± 1.0	31.0 ± 1.0	70.0 ± 1.0	23.4 ± 0.0
Mn	4.5 ± 1.0	2.7 ± 2.0	4.0 ± 1.0	6.0 ± 1.0	3.4 ± 1.0	5.6 ± 1.0	-	-
Co	46.7 ± 1.0	55.0 ± 2.0	47.0 ± 1.0	55.0 ± 2.0	47.0 ± 1.0	55.0 ± 2.0	-	-
Ni	12.0 ± 1.0	4.4 ± 0.0	11.7 ± 1.0	3.8 ± 0.0	12.0 ± 1.0	3.6 ± 0.0	-	66.3 ± 0.0
Mo	3.6 ± 0.2	0.2 ± 0.0	3.0 ± 1.0	0.3 ± 0.2	3.2 ± 1.0	0.2 ± 0.0	-	-
Ru	-	-	-	-	1.0 ± 0.0	1.5 ± 0.0	-	-
W	1.6 ± 0.2	4.0 ± 0.0	1.7 ± 0.0	2.6 ± 0.1	1.7 ± 0.2	2.6 ± 0.0	-	-
Al	-	-	-	-	-	-	-	8.9 ± 0.0
O	-	-	-	-	-	-	31.0 ± 1.0	-
Y	-	-	-	-	-	-	-	1.4 ± 0.0



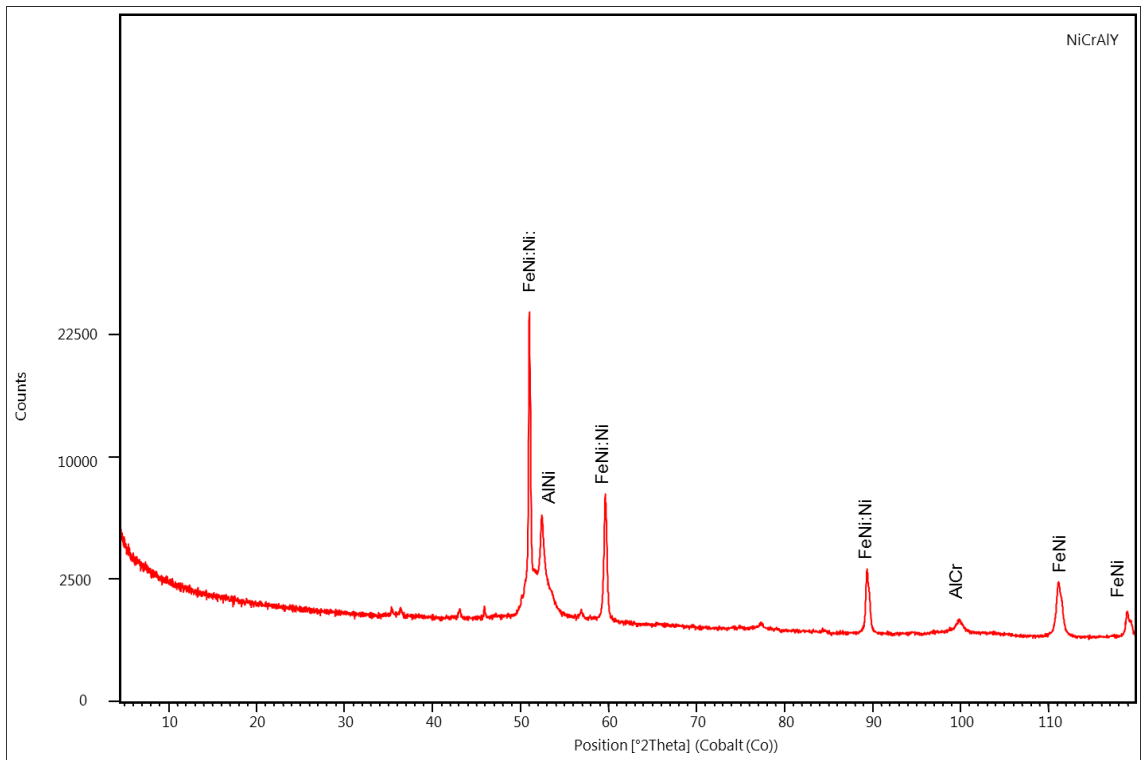
**Figure 6.9.** XRD patterns of the ULTIMET powders with no Ru, 0.3 and 0.6 wt% Ru.



**Figure 6.10.** XRD patterns of the Stellite 6 powders with no Ru, 0.3 and 0.6 wt% Ru.



**Figure 6.11.** XRD pattern of the  $\text{Cr}_2\text{O}_3$  powder.



**Figure 6.12.** XRD pattern of NiCrAlY bond coating powder.



## 6.3 Characterisation of the coatings

### 6.3.1 Surface morphology of the coatings

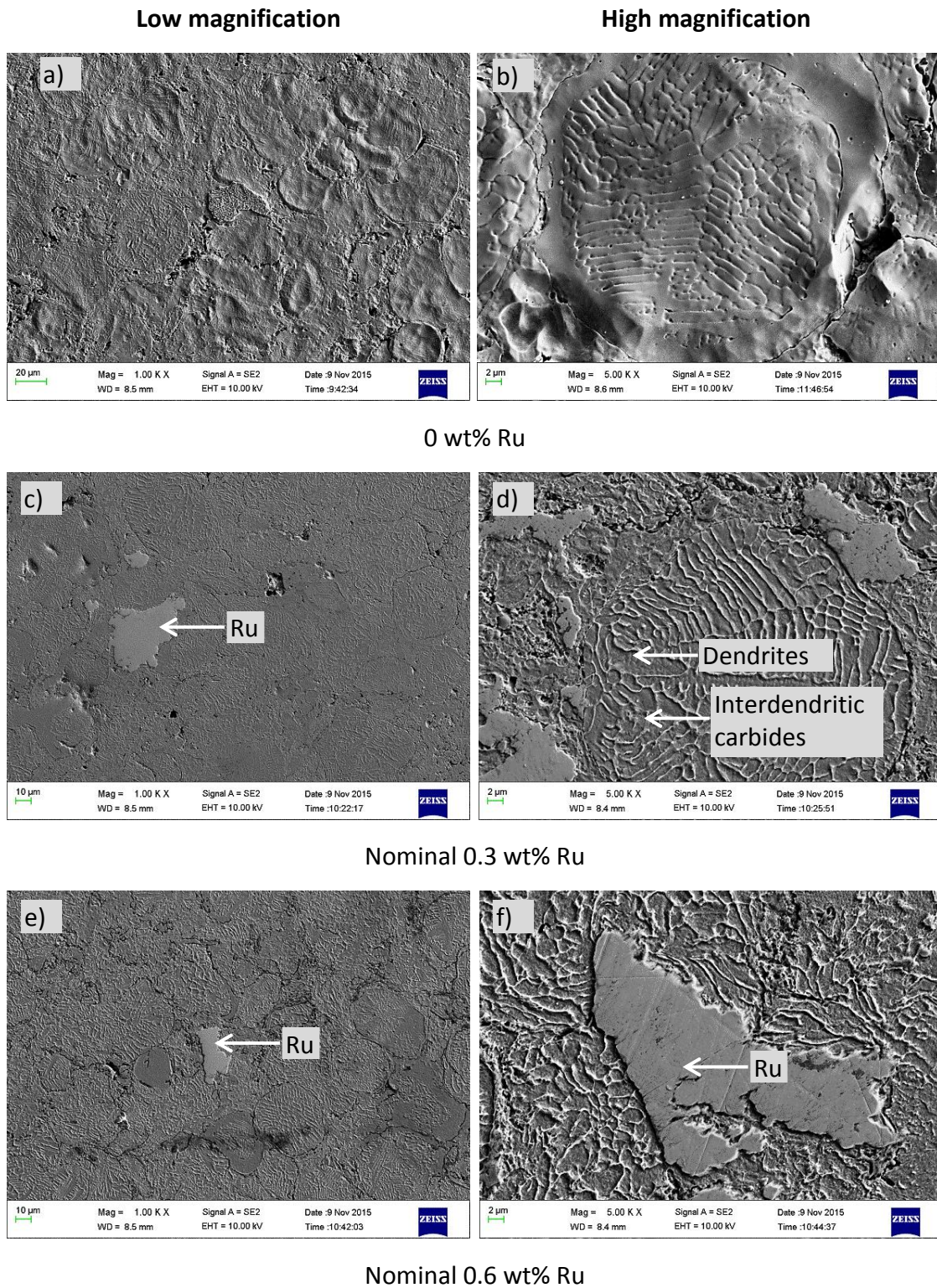
The surface morphologies of the coatings recorded by SEM in secondary electron (SE) mode are given in Figures 6.13-6.15. Nominal 0.3 wt% Ru and 0.6 wt% Ru ULTIMET (Figure 6.13) and Stellite 6 (Figure 6.14) had dendrites surrounded by a network of interdendritic carbides, although there were regions where the dendrites could not be discerned. Round particles in the ULTIMET coating were discernible in Figure 6.13 f), while in the Stellite 6 coating, they were more clearly visible (Figure 6.14), and two have been outlined in Figure 6.14 a). These were assumed to be the original spherical particles from thermal spraying of the source powders. The ruthenium was not well distributed, and the Ru particles were assumed to have not fully melted during thermal deposition. No cracks were observed by SEM on the surfaces of the ULTIMET and Stellite 6 coatings. The Cr<sub>2</sub>O<sub>3</sub> coating (Figure 6.15) showed dendrites on the top surface, cracking parallel to the mild steel substrate and delamination, with some gaps between the Cr<sub>2</sub>O<sub>3</sub> and bond coating. The individual 'splats' from thermal spraying could be seen.

### 6.3.2 Energy dispersive X-ray and X-ray diffraction results of the coatings

Table 6.3 shows the EDX results of the coatings, and where the errors are shown as zero, they were actually less than 0.1%. Like the powder samples, ULTIMET had Co, Cr, Ni as the major constituents, with minor amounts of Mn, Mo, W and Si. Stellite 6 had similar compositions, but with less Ni and a little more W than ULTIMET. The Ru contents might not be accurate, because EDX is only accurate to within ~1 wt%. Although there was a good agreement with nominal 0.3 wt% Ru coatings, the value for the nominal 0.6 wt% Ru was approximately half of what it should have been (~0.2 wt% Ru) for ULTIMET, but 1.5 wt% Ru for Stellite 6. This could be due to Ru being lost during spray coating of ULTIMET (although it was not lost for Stellite 6), but is more likely to be due to the inhomogeneous distribution of the powders during mixing and spray coating, especially since Ru is heavier than the other elements. Only Cr (69.5 ± 1.0 wt%) and O (30.5 ± 1.0 wt%) were detected in the Cr<sub>2</sub>O<sub>3</sub> coating, as expected. The nominal compositions of the coatings are not representative of the actual compositions.

Figures 6.16-6.19 show the XRD patterns of the coatings. ULTIMET coatings with no Ru, nominal 0.3 wt% Ru and nominal 0.6 wt% (Figure 6.16) consisted of fcc austenite ( $\gamma$ ) and FeNiCrMoCo phases. Carbide and oxide phases were not detected. For the Stellite 6 coatings with no Ru, nominal 0.3 wt% Ru and nominal 0.6 wt% Ru (Figures 6.17) patterns, FeNiCrMoCo, CrC and MoC phases were detected. The carbides may be M<sub>7</sub>C<sub>3</sub> or M<sub>23</sub>C<sub>6</sub>,

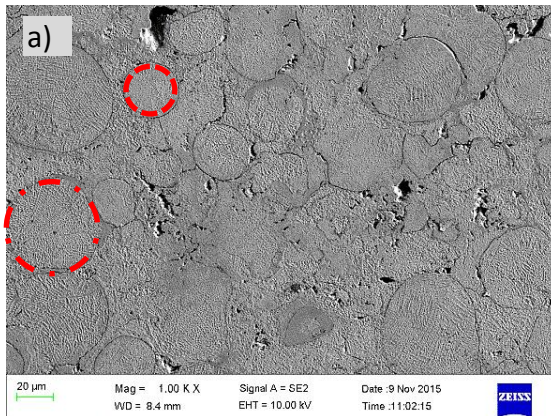
where M = Cr or Mo. XRD patterns of  $\text{Cr}_2\text{O}_3$  showed the eskolaite ( $\text{Cr}_2\text{O}_3$ ) phase, as expected. For mild steel substrate, only Fe ferrite ( $\alpha$ ) phase was detected.



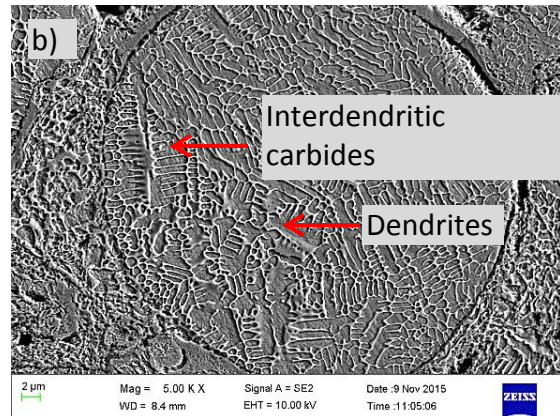
**Figure 6.13.** SEM-SE micrographs showing the morphologies of ULTIMET coatings, with: a) and b) no Ru, c) and d) nominal 0.3 wt% Ru, and e) and f) nominal 0.6 wt% Ru, showing equiaxed dendrites surrounded by a network of interdendritic carbides.



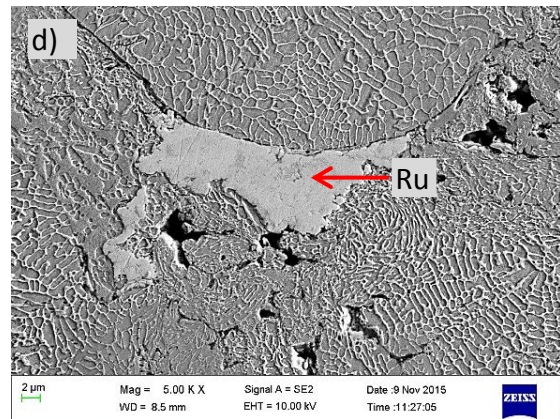
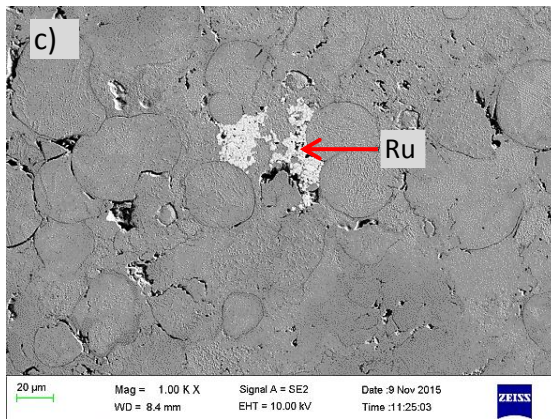
### Low magnification



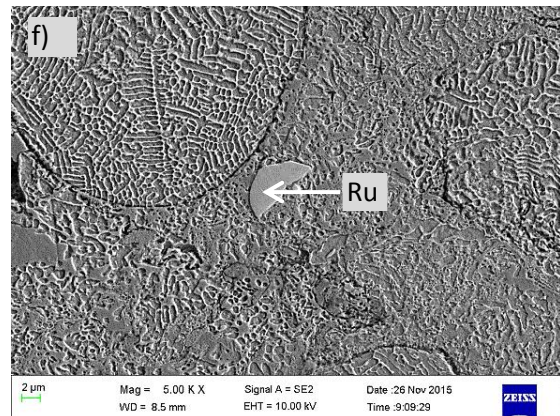
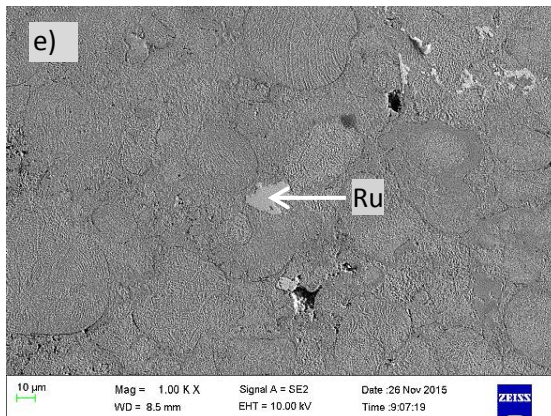
### High magnification



### 0 wt% Ru

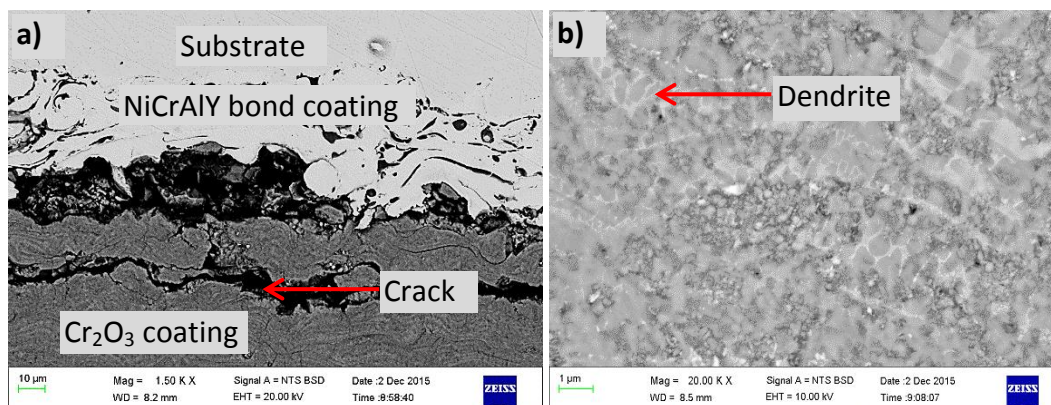


### Nominal 0.3 wt% Ru



### Nominal 0.6 wt% Ru

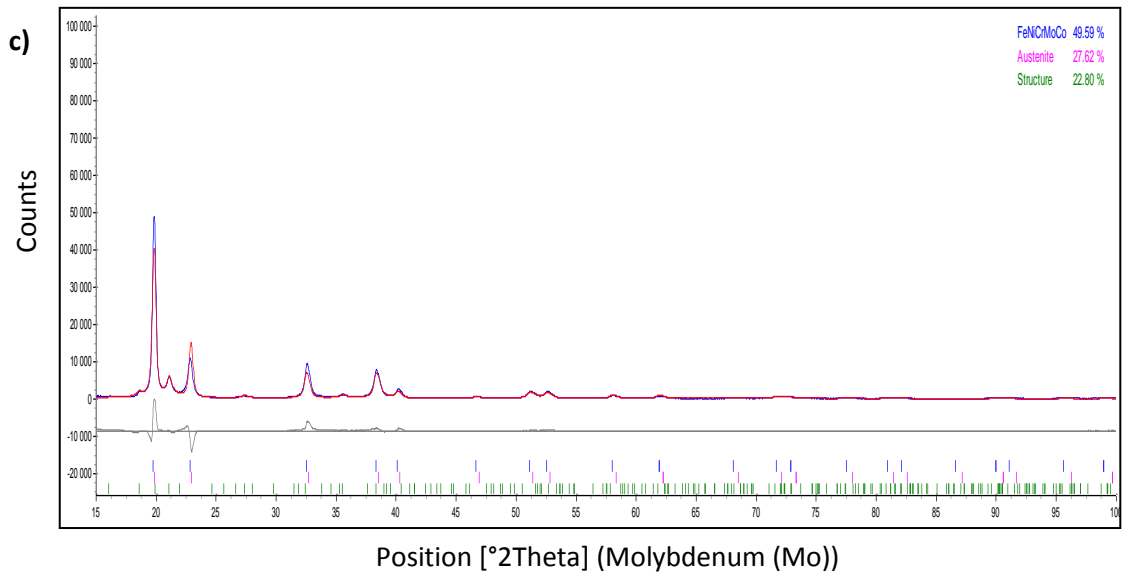
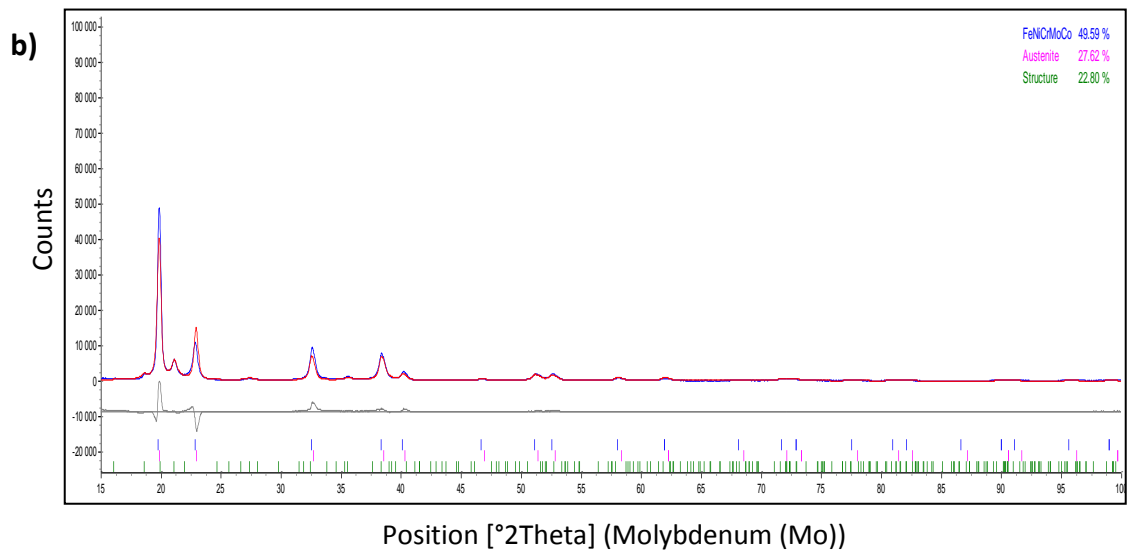
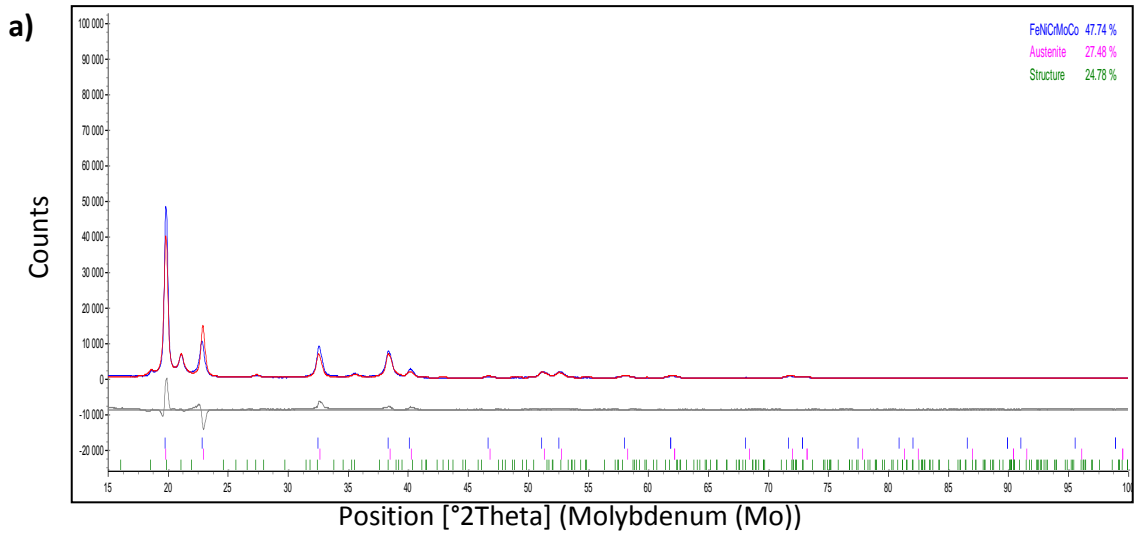
**Figure 6.14.** SEM-SE micrographs showing morphologies of Stellite 6 coatings, with: a) showing the sprayed particles outlined, b) no Ru, c) and d) nominal 0.3 wt% Ru, and e) and f) nominal 0.6 wt% Ru, showing circular particles with equiaxed dendrites surrounded by a network of interdendritic carbides.



**Figure 6.15.** SEM-BSE micrographs showing the morphologies of: a) Cr<sub>2</sub>O<sub>3</sub> top coating and NiCrAlY bond coating, showing cracking parallel to the substrate, and b) Cr<sub>2</sub>O<sub>3</sub> top coating at higher magnifications, showing dendrites.

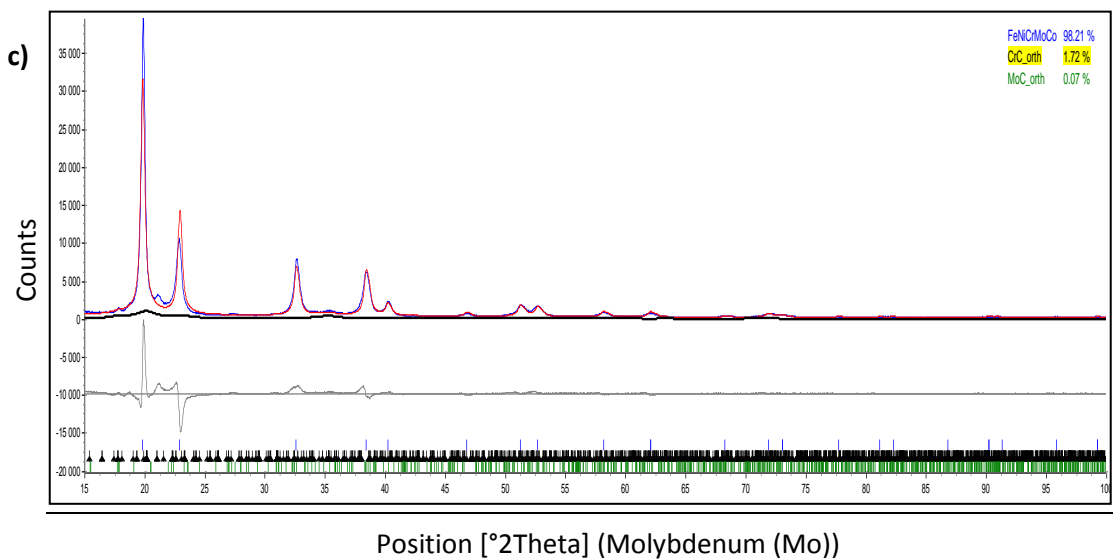
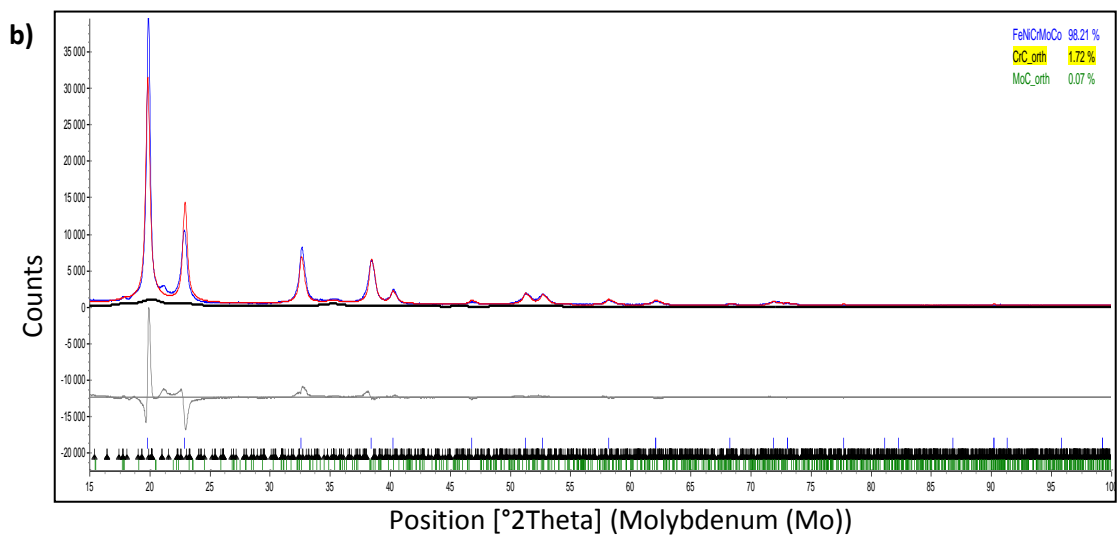
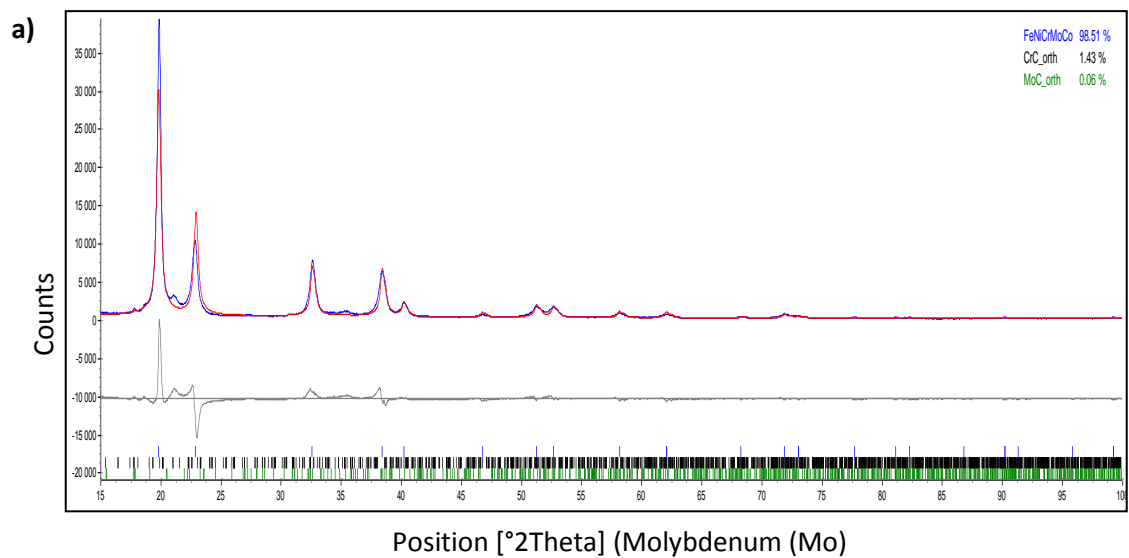
**Table 6.3.** EDX analysis of the coatings before tests.

Element (wt%)	ULTIMET	Stellite 6	ULTIMET	Stellite 6	ULTIMET	Stellite 6	Cr <sub>2</sub> O <sub>3</sub>	NiCrAlY
	0 wt% Ru		Nominal 0.3 wt% Ru		Nominal 0.6 wt% Ru			
C	1.7 ± 0.0	2.7 ± 1.0	1.3 ± 0.0	2.7 ± 0.0	1.7 ± 0.0	-	-	-
Si	0.3 ± 0.0	0.7 ± 0.0	0.2 ± 0.0	0.7 ± 0.0	0.3 ± 0.0	0.7 ± 0.0	-	-
Cr	28.0 ± 1.0	33.1 ± 1.0	29.0 ± 1.0	30.0 ± 1.0	29.5 ± 0.0	30.5 ± 1.0	69.5 ± 1.0	3.4 ± 0.0
Mn	1.0 ± 0.0	2.3 ± 1.0	0.8 ± 0.0	3.8 ± 1.0	0.8 ± 0.0	5.6 ± 1.0	-	-
Fe	0.2 ± 0.2	-	0.6 ± 0.2	0.1 ± 0.2	-	-	-	-
Co	50.0 ± 0.0	53.0 ± 1.0	52.0 ± 1.0	55.0 ± 1.0	48.8 ± 0.0	55.2 ± 2.0	-	-
Ni	13.0 ± 1.0	3.4 ± 1.0	12.0 ± 0.0	3.4 ± 0.0	12.3 ± 0.0	3.6 ± 0.0	-	6.3 ± 0.0
Mo	4.5 ± 0.0	0.4 ± 0.0	4.0 ± 1.0	0.3 ± 0.0	4.5 ± 0.0	0.2 ± 0.0	-	-
Ru	-	-	0.3 ± 0.0	0.2 ± 0.0	0.2 ± 0.0	1.5 ± 0.0	-	-
W	2.0 ± 0.0	4.2 ± 0.0	2.0 ± 0.0	3.8 ± 0.0	2.0 ± 0.0	2.6 ± 0.0	-	-
Al	-	-	-	-	-	-	-	8.9 ± 0.0
O	-	-	-	-	-	-	30.5 ± 1.0	-
Y	-	-	-	-	-	-	-	1.4 ± 0.0

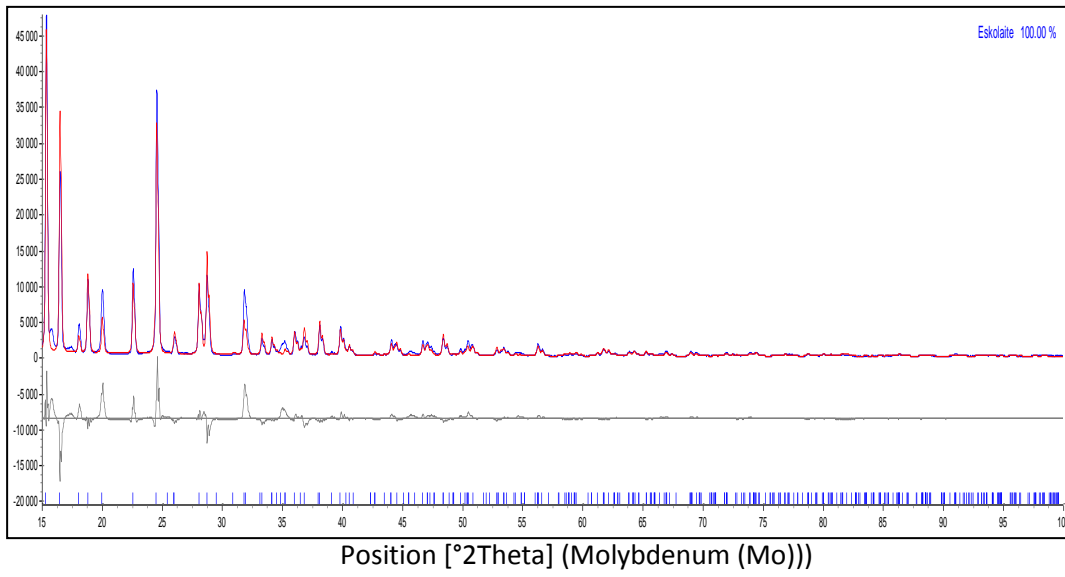


**Figure 6.16.** XRD pattern of the ULTIMET coatings with: a) no, b) nominal 0.3 wt% Ru and c) nominal 0.6 wt% Ru.

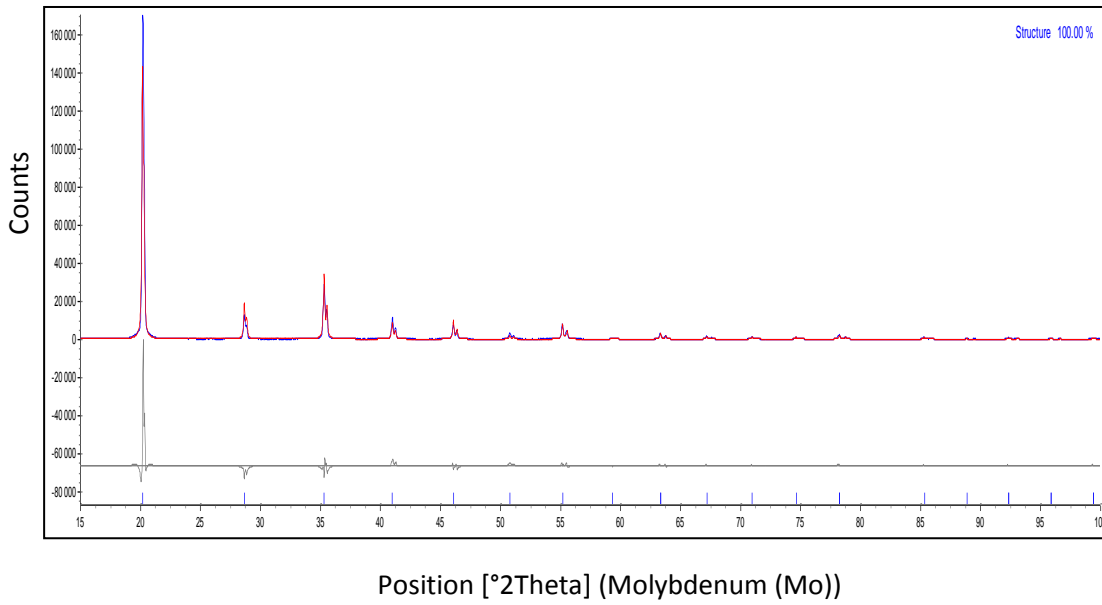




**Figure 6.17.** XRD pattern of Stellite 6 coatings with: a) no, b) nominal 0.3 wt% Ru and c) nominal 0.6 wt% Ru.



**Figure 6.18.** XRD pattern of  $\text{Cr}_2\text{O}_3$  coating.



**Figure 6.19.** XRD pattern of mild steel substrate.

### 6.3.3 Hardness

Microhardness measurements were done to determine the effect of Ru additions to ULTIMET and Stellite 6 coatings, and also to determine the hardness of the Cr<sub>2</sub>O<sub>3</sub> coating and the mild steel substrate. The results are presented in Table 6.4, showing high errors (up to  $\pm 77$  HV<sub>2</sub>), apart from the mild steel substrate which had an error of only of  $\pm 5$  HV<sub>2</sub>.

Ruthenium increased the hardness of ULTIMET coatings by 36-80 HV<sub>2</sub>, although the errors were large, as well as for Stellite 6 coatings, although the effect was variable with larger errors than for the coatings without Ru. The highest hardnesses were for Stellite 6 with nominal 0.3 wt% Ru and nominal 0.6 wt% Ru, which were harder than ULTIMET. The Cr<sub>2</sub>O<sub>3</sub> coating had the highest hardness, while mild steel substrate had the lowest.

**Table 6.4.** Hardnesses (HV<sub>2</sub>) of ULTIMET, Stellite 6, Cr<sub>2</sub>O<sub>3</sub> coatings and mild steel substrate.

Sample		Hardness (HV <sub>2</sub> )
ULTIMET	No Ru	386 ± 21
	Nominal 0.3 wt% Ru	466 ± 31
	Nominal 0.6 wt% Ru	422 ± 32
Stellite 6	No Ru	440 ± 25
	Nominal 0.3 wt% Ru	543 ± 21
	Nominal 0.6 wt% Ru	547 ± 49
Cr <sub>2</sub> O <sub>3</sub>		1260 ± 77
Mild steel		160 ± 50

## 6.4 Corrosion results

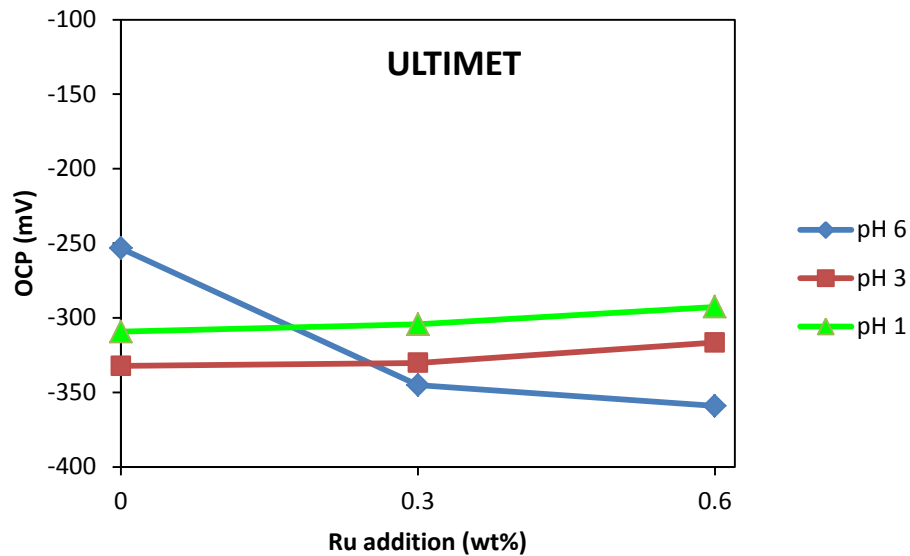
### 6.4.1 Open circuit corrosion potential results

Open circuit potentials of all the samples stabilised over time, and did not correspond to those obtained during the potentiodynamic measurements. However, all the alloys demonstrated stable behaviour at the end of the scans, indicating that thin passive films formed on their surfaces. The open circuit corrosion potential (OCP) variations of the ULTIMET, Stellite 6 coatings with no Ru, nominal 0.3 and nominal 0.6 wt% Ru, Cr<sub>2</sub>O<sub>3</sub> coatings and mild steel substrates after exposure to synthetic mine water (pH 6, 3 and 1) for the period of one hour, at ambient temperature ( $22.0 \pm 0.2^\circ\text{C}$ ), are shown in Appendix B.

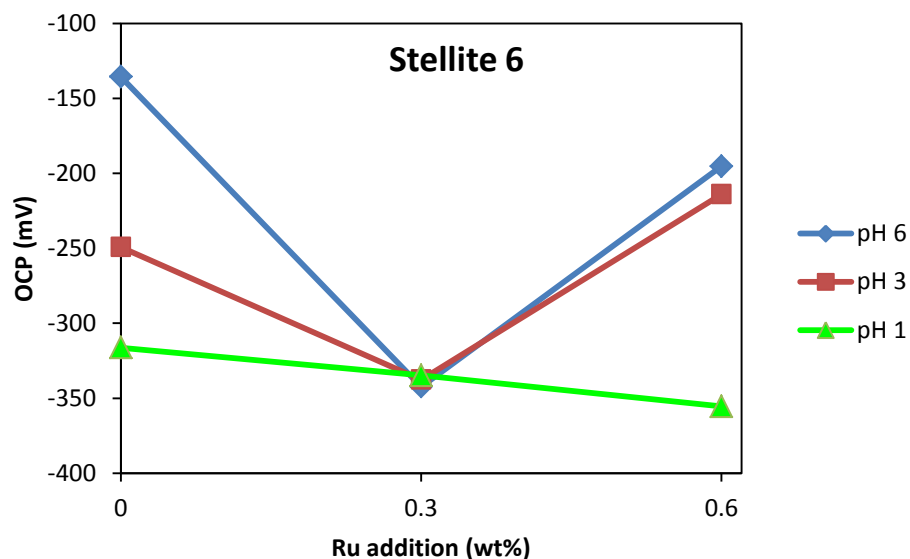
The effect of Ru addition on OCP on ULTIMET, Stellite 6 and Cr<sub>2</sub>O<sub>3</sub> coatings and mild steel substrate at various pH is given in Figures 6.20-6.24. With increased Ru, OCP decreased for ULTIMET coating at lower pH (Figures 6.20, 6.22-6.24). At higher pH values, OCP



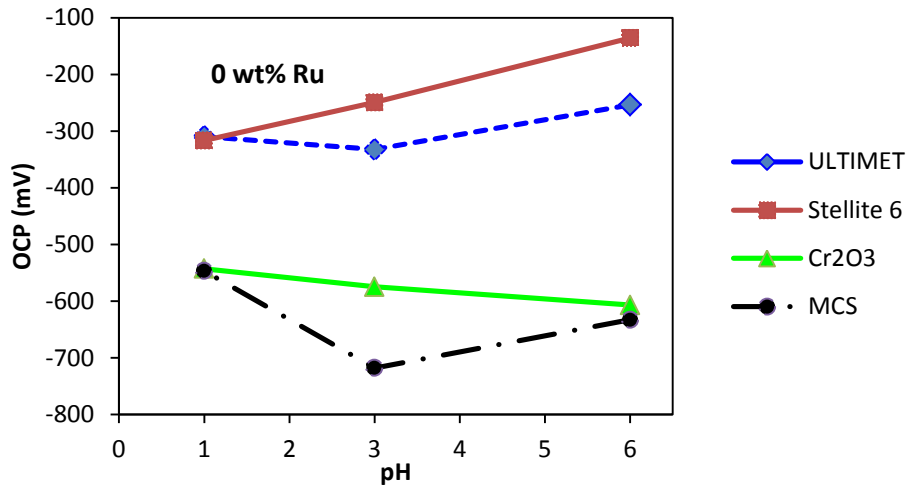
increased with increased Ru content with the highest OCP recorded at pH 6. For Stellite 6 (Figures 6.21-6.24), OCP changed with no trend with increased Ru. At pH values of 6 and 3, OCP dropped from high values, and then increased as Ru content was increased. For pH 1, OCP decreased with increased Ru content. The nominal 0.3 wt% Ru Stellite 6 coating had same OCP values at all pH values. For Cr<sub>2</sub>O<sub>3</sub> coatings, OCP increased with decreasing pH (Figures 6.22-6.24). The mild steel had lower OCP at pH 3, and higher OCP at pH 1 (Figures 6.22-6.24).



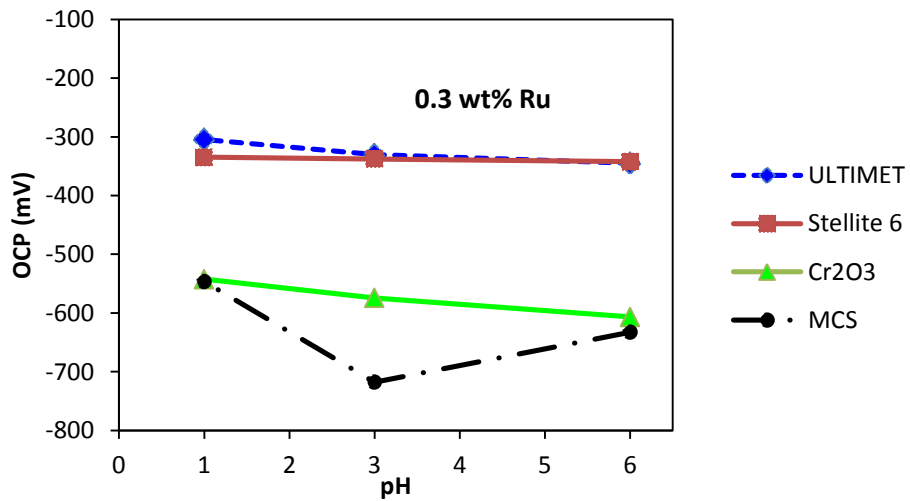
**Figure 6.20.** Effect of Ru addition on OCP of ULTIMET coatings at various pH.



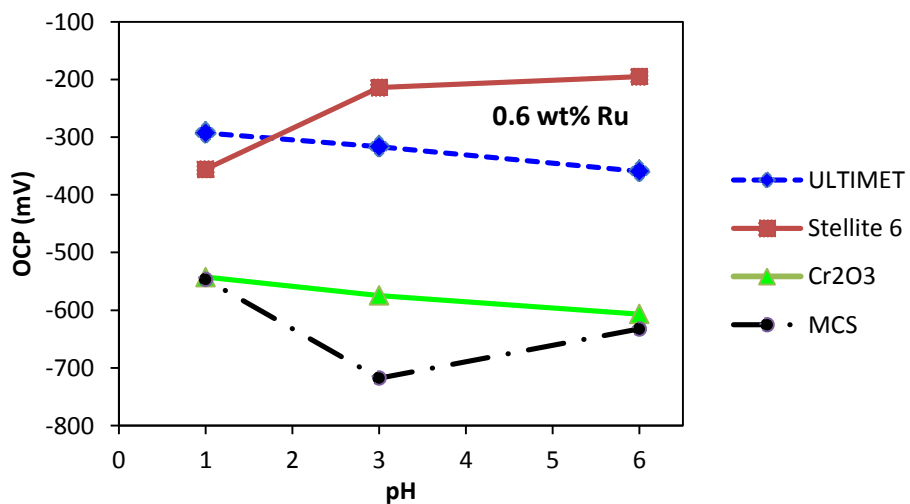
**Figure 6.21.** Effect of Ru addition on OCP of Stellite 6 coatings at various pH.



**Figure 6.22.** Effect of pH on OCP of ULTIMET and Stellite 6 coatings with no Ru, and Cr<sub>2</sub>O<sub>3</sub> coatings and mild steel substrate.



**Figure 6.23.** Effect of pH on OCP of ULTIMET and Stellite 6 coatings with nominal 0.3 wt% Ru, and Cr<sub>2</sub>O<sub>3</sub> coatings and mild steel substrate.



**Figure 6.24.** Effect of pH on OCP of ULTIMET and Stellite 6 coatings with nominal 0.6 wt% Ru, and Cr<sub>2</sub>O<sub>3</sub> coatings and mild steel substrate.

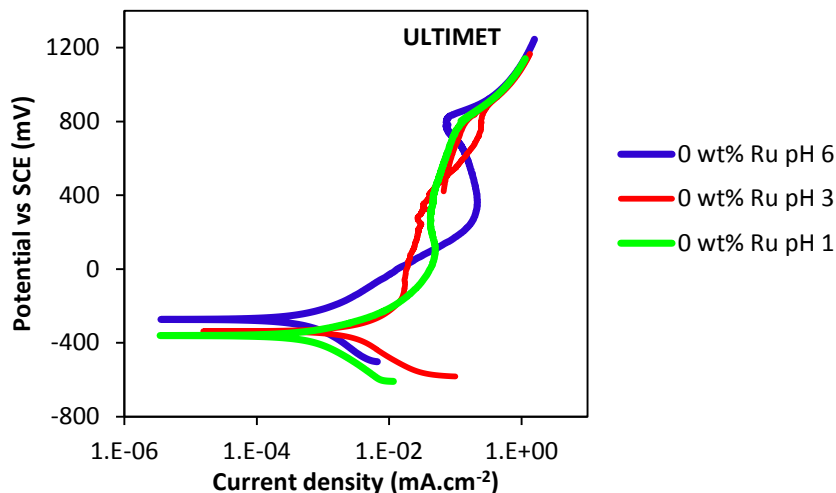
## 6.4.2 Cyclic potentiodynamic polarisation curves

### *ULTIMET coatings*

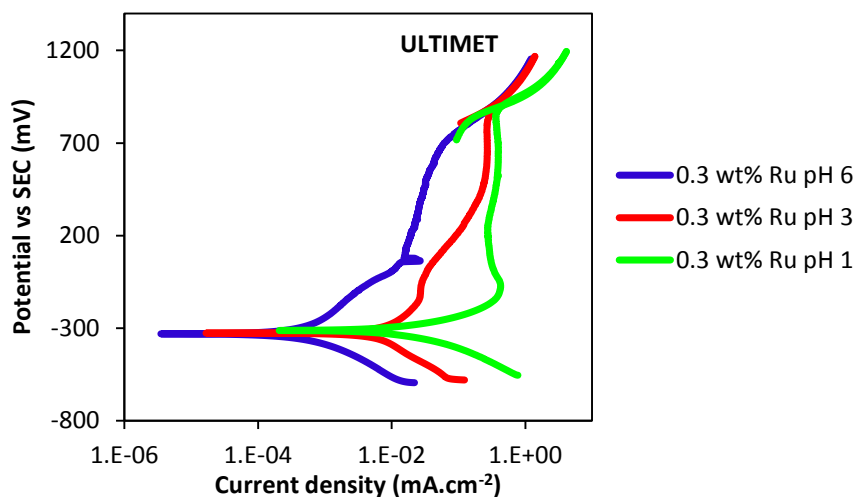
Figures 6.25-6.27 present potentiodynamic polarisation curves of the ULTIMET with various amount of Ru coatings in synthetic mine water (pH 6, 3 and 1). All the coatings displayed active-passive transition behaviour. The coating without Ru (Figure 6.25) showed pseudo-passivation behaviour at pH 6 from 200 to 800 mV, followed by pitting. This was due to the formation of an unprotective thin film of  $\text{Cr}_2\text{O}_3$  at high pH. At pH 3, non-spontaneous passivation behaviour was observed, and at pH 1, the coating demonstrated spontaneous passivation with a stable and wide passivation range associated with the formation of protective thin film of  $\text{Cr}_2\text{O}_3$  at low pH. There were no hysteresis loops observed before the pitting potential ( $\sim 800$  mV).

Figure 6.26 shows the potentiodynamic polarisation behaviour of ULTIMET coatings with nominal 0.3 wt% Ru, showing active-passive transitions at all pH values. There was no hysteresis loops on the reverse scan before the pitting potentials ( $\sim 800$  mV). Table 6.5 shows corrosion potentials, current densities and corrosion rates of ULTIMET coatings with nominal 0.3 wt% Ru in synthetic mine water (pH 6, 3 and 1). At pH 6,  $E_{\text{corr}}$ ,  $i_{\text{corr}}$  and corrosion rates were lower than for pH 3 and 1.

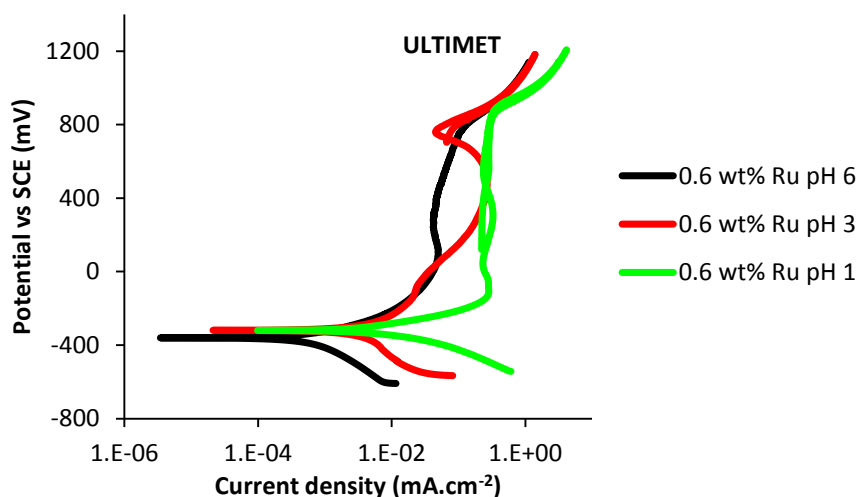
The potentiodynamic polarisation behaviour of ULTIMET coatings with nominal 0.6 wt% Ru at all pH values is shown in Figure 6.27. No hysteresis loops were observed on all the reverse scans before the pitting potential ( $\sim 800$  mV). The lowest  $E_{\text{corr}}$  was recorded at pH 6. The coatings with nominal 0.6 wt% Ru also had similar pitting ( $E_{\text{pit}}$ ) and repassivation ( $E_{\text{rp}}$ ) potentials between 800 and 850 mV.



**Figure 6.25.** Cyclic potentiodynamic polarisation curves at ambient temperature of ULTIMET coatings with no Ru in synthetic mine water at pH 6, 3 and 1.

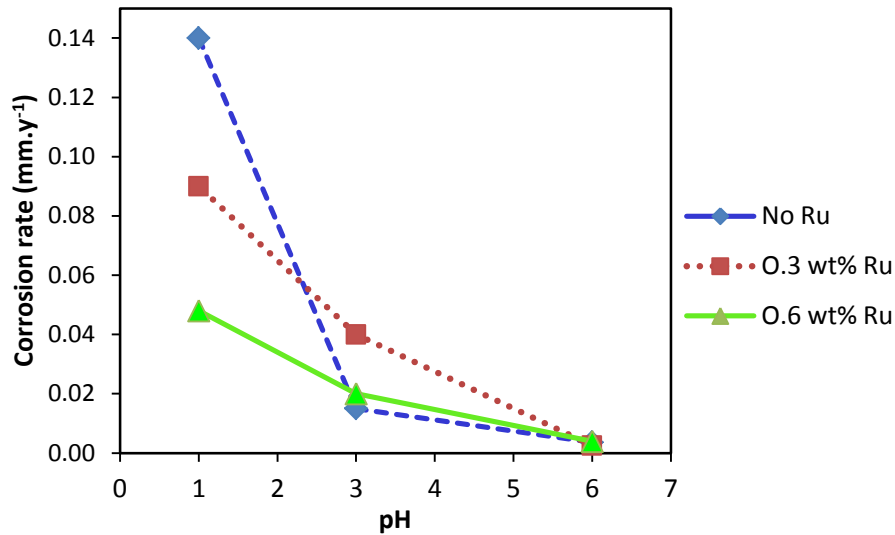


**Figure 6.26.** Cyclic potentiodynamic polarisation curves at ambient temperature of ULTIMET coatings with nominal 0.3 wt% Ru in synthetic mine water at pH 6, 3 and 1.

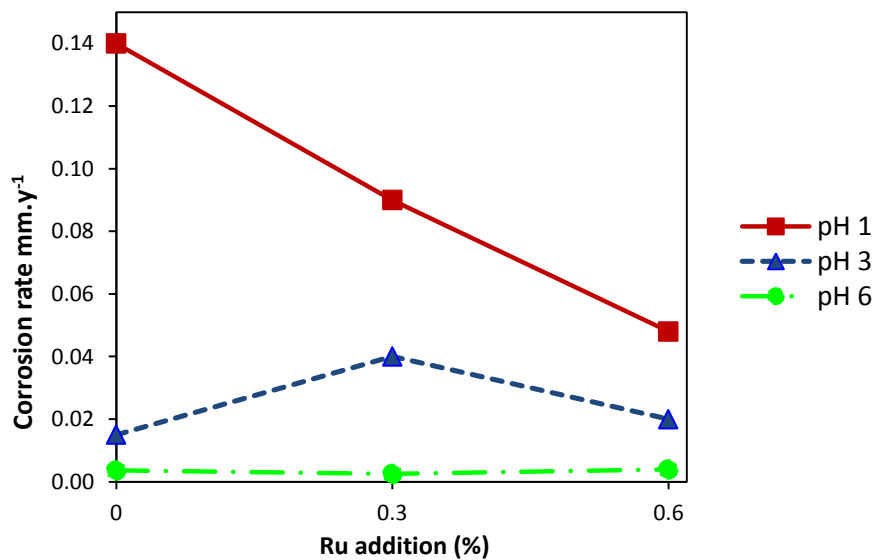


**Figure 6.27.** Cyclic potentiodynamic polarisation curves at ambient temperature of ULTIMET coatings with nominal 0.6 wt% Ru in synthetic mine water at pH 6, 3 and 1.

The effect of Ru addition and pH (6, 3 and 1) on corrosion rate is shown on Figures 6.28-6.29. The corrosion rate decreased as the Ru content increased at pH 6. Corrosion rates changed with no trend when both pH and ruthenium addition were increased or decreased at pH 3 and 1. Corrosion rate also increased when the pH was decreased. From these results, ULTIMET with nominal 0.3 wt% Ru at pH 6 had better corrosion resistance than the rest of ULTIMET coatings at all pH values. However, low corrosion rates were observed in the ULTIMET coating without ruthenium at all pH values.



**Figure 6.28.** Corrosion rate at ambient temperature of ULTIMET coatings with no Ru, nominal 0.3 wt% Ru and nominal 0.6 wt% Ru in synthetic mine water at pH 6, 3 and 1.



**Figure 6.29.** Effect of ruthenium addition on corrosion rate of ULTIMET coatings with no Ru, nominal 0.3 wt% Ru and nominal 0.6 wt% Ru in synthetic mine water at ambient temperature and pH 6, 3 and 1.

The corrosion potentials, current densities and corrosion rates of ULTIMET coatings with no Ru, nominal 0.3 wt% Ru and nominal 0.6 wt% Ru in synthetic mine water (pH 6, 3 and 1) are shown in Table 6.5. With decreased pH,  $E_{\text{corr}}$  decreased with increased corrosion rate and  $i_{\text{corr}}$  for ULTIMET coatings with no Ru, nominal 0.3 wt% Ru and nominal 0.6 wt% Ru. However, corrosion current density for ULTIMET coatings with nominal 0.3 wt% Ru showed no trend with decreased pH, and increased with decreased pH for ULTIMET coatings with nominal 0.6 wt% Ru.

**Table 6.5.** Cyclic potentiodynamic polarisation results at ambient temperature of ULTIMET coatings with no Ru, nominal 0.3 wt% Ru and nominal 0.6 wt% Ru in synthetic mine water (pH 6, 3 and 1).

ULTIMET	pH	$E_{corr}$ (mV)	$i_{corr}$ ( $\mu\text{A}\cdot\text{cm}^{-2}$ )	Corrosion rate ( $\text{mm}\cdot\text{y}^{-1}$ )
No Ru	6	-273	0.34	0.0036
	3	-337	1.50	0.0150
	1	-339	13.20	0.1400
Nominal 0.3 wt% Ru	6	-331	0.24	0.0025
	3	-327	3.90	0.0400
	1	-313	0.88	0.0900
Nominal 0.6 wt% Ru	6	-361	0.38	0.0039
	3	-320	1.90	0.0200
	1	-319	4.60	0.0480

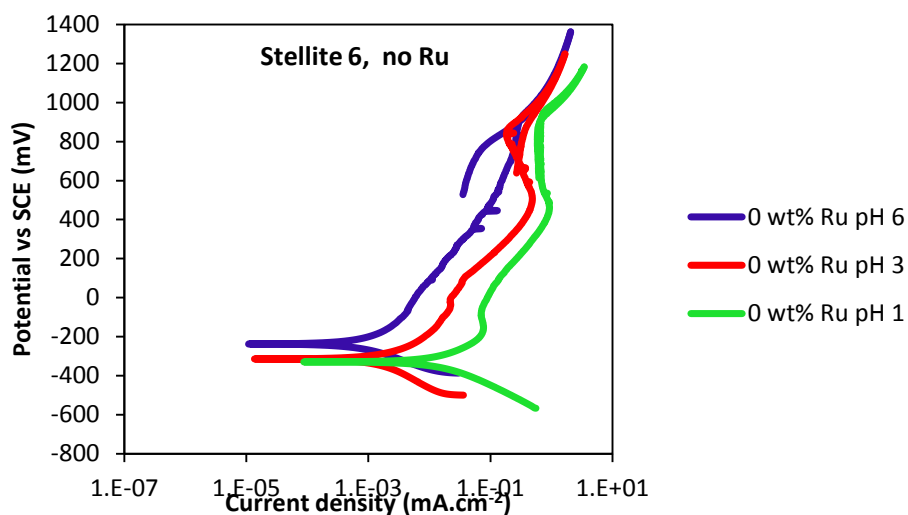
### Summary

From these results, at pH 6 all ULTIMET coatings, regardless of Ru content, had better corrosion resistance than at the higher acidities of pH 3 and 1. The nominal 0.3 wt% Ru ULTIMET coating at pH 6 showed the lowest corrosion rate, making it the best corrosion resistant ULTIMET coating in synthetic mine water.

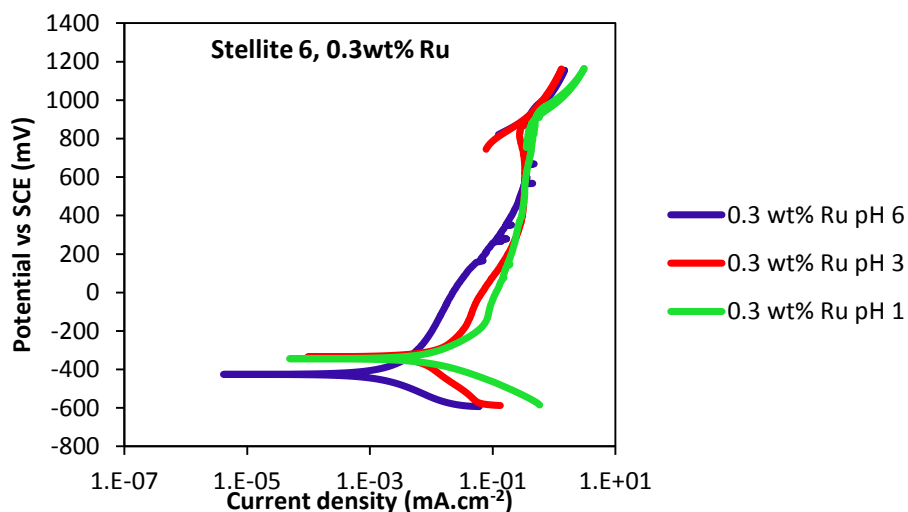
### Stellite 6 coatings

Potentiodynamic polarisation curves of the Stellite 6 coatings with different Ru contents in synthetic mine water at pH 6, 3 and 1 are shown in Figures 6.30-6.32. All the coatings displayed non-distinct active-passive transition behaviour. The coatings without Ru (Figure 6.30) showed poor passivation behaviour at pH 6 and 3, although at pH 1, there was pseudo-spontaneous passivation between -152 and -75 mV, and then transpassive behaviour. The reverse scan did not show a hysteresis loop ( $\sim 800$  mV).

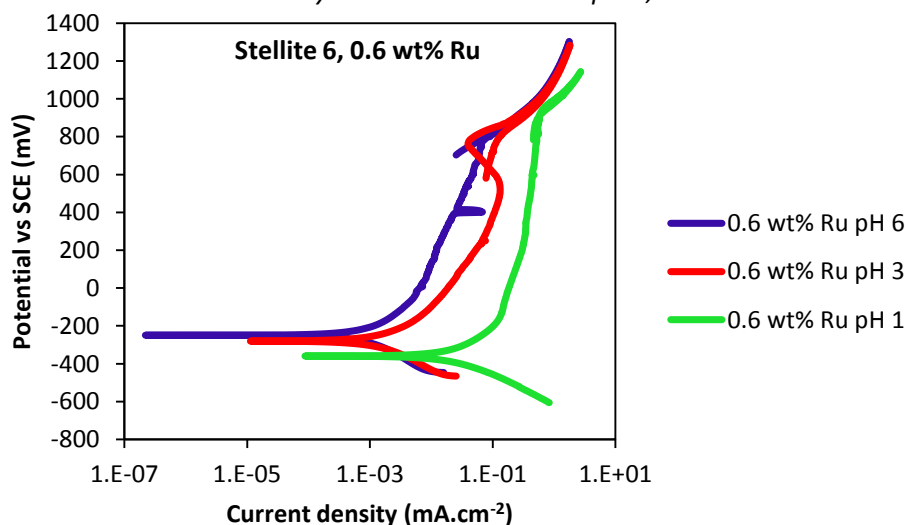
Figure 6.31 shows the potentiodynamic polarisation behaviour of Stellite 6 coatings with nominal 0.3 wt% Ru, with active-passive transitions at all pH values. No hysteresis loops were observed on the reverse scans. Stellite 6 coatings with nominal 0.6 wt% Ru (Figure 6.32) at pH 6, 3 and 1 had similar potentiodynamic polarisation behaviour to those with no Ru and nominal 0.3 wt% Ru. No hysteresis loops were observed on the reverse scans before the pitting potential ( $\sim 800$  mV).



**Figure 6.30.** Cyclic potentiodynamic polarisation curves at ambient temperature of Stellite 6 coatings with no Ru in synthetic mine water at pH 6, 3 and 1.



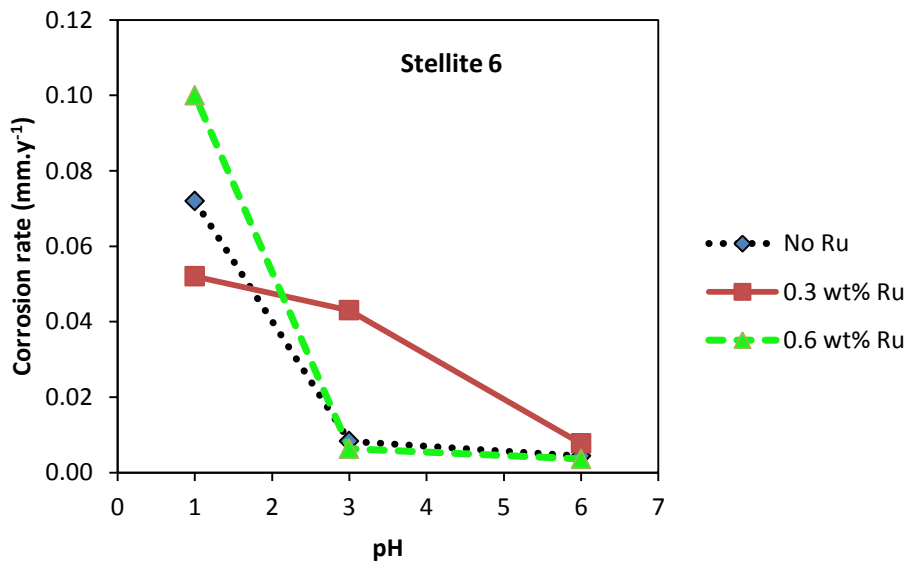
**Figure 6.31.** Cyclic potentiodynamic polarisation curves, at ambient temperature of Stellite 6 coatings with nominal 0.3 wt% Ru in synthetic mine water at pH 6, 3 and 1.



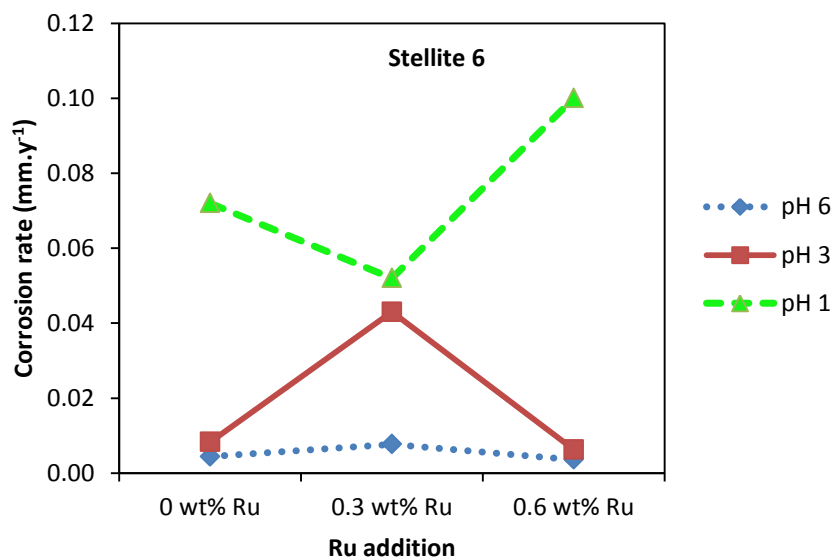
**Figure 6.32.** Cyclic potentiodynamic polarisation curves at ambient temperature of Stellite 6 coatings with nominal 0.6 wt% Ru in synthetic mine water at pH 6, 3 and 1.



The effect of Ru addition and pH (6, 3 and 1) on corrosion rate of Stellite 6 coatings is shown on Figures 6.33 and 6.34. With decreased pH,  $E_{corr}$  decreased with increased corrosion rate and  $i_{corr}$  for Stellite 6 coatings with no Ru. For Stellite 6 coatings with nominal 0.3 wt% Ru and 0.6 wt% Ru,  $i_{corr}$  and corrosion rate increased with decreased pH. Corrosion potential for Stellite 6 coatings with nominal 0.3 wt% Ru changed with no trend with decreased pH, and it decreased with decreased pH for Stellite 6 coatings with nominal 0.6 wt% Ru. Corrosion rate increased as pH was lowered for all the Stellite 6 coatings.



**Figure 6.33.** Corrosion rate at ambient temperature of Stellite 6 coatings with no Ru, nominal 0.3 wt% Ru and nominal 0.6 wt% Ru in synthetic mine water at pH 6, 3 and 1.



**Figure 6.34.** Effect of ruthenium additions on corrosion rate at ambient temperature of Stellite 6 coatings with no Ru, nominal 0.3 wt% Ru and nominal 0.6 wt% Ru in synthetic mine water at pH 6, 3 and 1.

The corrosion potentials, current densities and corrosion rates of Stellite 6 coatings without Ru in synthetic mine water (pH 6, 3 and 1) are shown in Table 6.6. The coating without Ru had a higher corrosion potential ( $E_{corr}$ ) than the other coatings at all pH values. It also had a lower corrosion current density ( $i_{corr}$ ) at pH 6 and a lower corrosion rate at pH 3. The corrosion rate changed without any trend as the pH decreased.

Table 6.6 shows corrosion potentials, current densities and corrosion rates of Stellite 6 coatings with nominal 0.3 wt% Ru in synthetic mine water (pH 6, 3 and 1). The corrosion potential for Stellite 6 coating with nominal 0.3 wt% Ru changed with no trend with decreased pH. Stellite 6 coating with nominal 0.6 wt% Ru at pH 6 had the lowest corrosion rate, making it the best corrosion resistant coating at this pH.

The coatings with nominal 0.6 wt% Ru also had similar  $E_{pit}$  and  $E_{rp}$  potentials between 800 and 850 mV. The lowest  $E_{corr}$  was recorded at pH 6 (Figure 6.32 and Table 6.6). Stellite 6 with nominal 0.6 wt% Ru at pH 6 had the lowest corrosion rate, making it the best corrosion resistant coating in synthetic mine water at this pH.

**Table 6.6.** Cyclic potentiodynamic polarisation results of Stellite 6 coatings with no Ru, nominal 0.3 wt% Ru and nominal 0.6 wt% Ru in synthetic mine water at pH 6, 3 and 1, at ambient temperature.

Stellite 6	pH	$E_{corr}$ (mV)	$i_{corr}$ ( $\mu\text{A}\cdot\text{cm}^{-2}$ )	Corrosion rate ( $\text{mm}\cdot\text{y}^{-1}$ )
No Ru	6	-237	0.50	0.0044
	3	-315	0.95	0.0083
	1	-329	8.30	0.0720
Nominal 0.3 wt% Ru	6	-425	0.88	0.0077
	3	-337	4.90	0.0430
	1	-344	5.90	0.0520
Nominal 0.6 wt% Ru	6	-250	0.40	0.0036
	3	-280	0.72	0.0063
	1	-360	11.10	0.1000

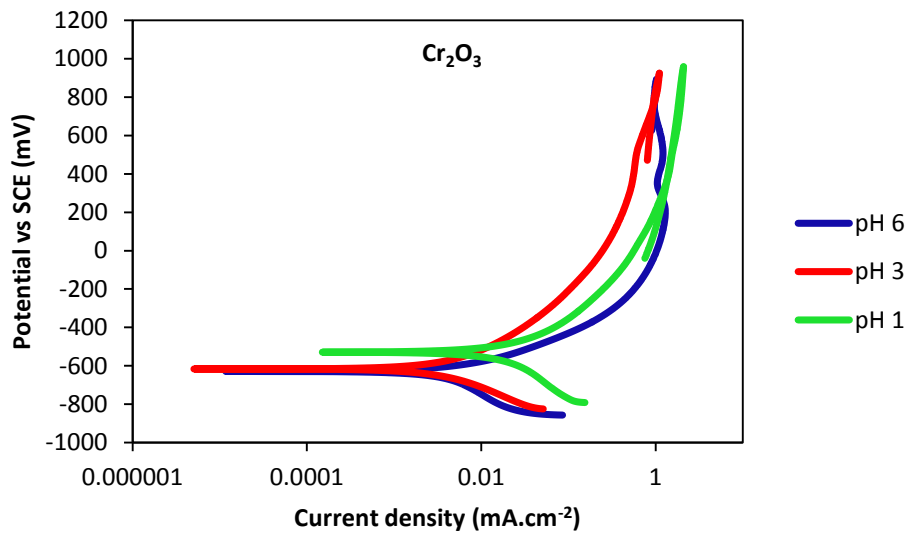
### Summary

All the Stellite 6 coatings showed the best corrosion resistance at pH 6, and the highest corrosion rates at pH 1. The best Stellite 6 coating contained nominal 0.6 wt% Ru, with the lowest corrosion rate at pH 6 and 3.

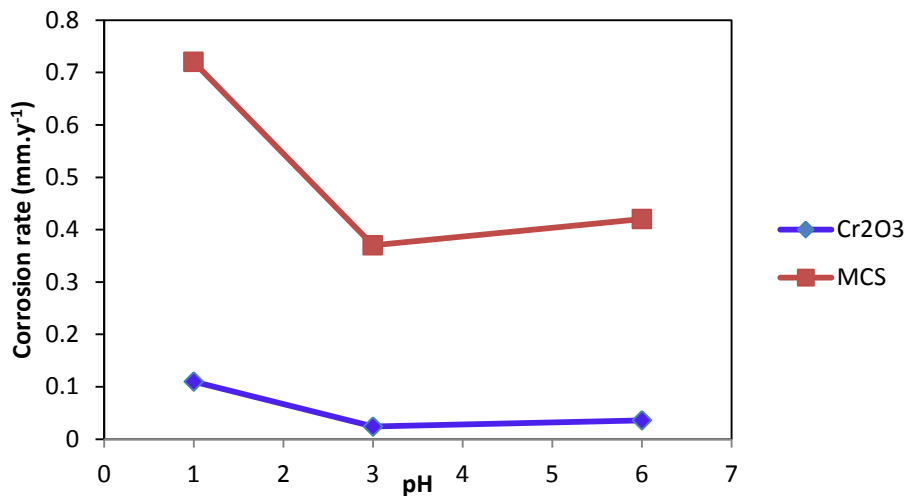
### Cr<sub>2</sub>O<sub>3</sub> coating

Figure 6.35 shows the potentiodynamic polarisation behaviour of Cr<sub>2</sub>O<sub>3</sub> coatings in synthetic mine water at different pH values. The coatings demonstrated active behaviour at all pH values. High corrosion rate was recorded at pH 1, followed by pH 6 and pH 3 with the lowest (Figure 6.36).

Table 6.7 show the corrosion parameters recorded. When the pH was decreased, E<sub>corr</sub> increased. Corrosion current density changed with no trend with decreased pH. At pH 1, the Cr<sub>2</sub>O<sub>3</sub> coating had the highest E<sub>corr</sub>, i<sub>corr</sub> and corrosion rate, whereas its lowest corrosion rate was at pH 3. The corrosion resistance of Cr<sub>2</sub>O<sub>3</sub> coatings were not better than ULTIMET and Stellite 6 coatings. Hence, Cr<sub>2</sub>O<sub>3</sub> is not better than ULTIMET and Stellite 6 coatings in synthetic mine water, and would not solve the corrosion problem at Otjihase Mine.



**Figure 6.35.** Cyclic potentiodynamic polarisation curves at ambient temperature of Cr<sub>2</sub>O<sub>3</sub> coatings in synthetic mine water at pH 6, 3 and 1.



**Figure 6.36.** Corrosion rate at ambient temperature of Cr<sub>2</sub>O<sub>3</sub> and mild steel in synthetic mine water at pH 6, 3 and 1.

**Table 6.7.** Cyclic potentiodynamic polarisation results at ambient temperature of Cr<sub>2</sub>O<sub>3</sub> coatings in synthetic mine water at pH 6, 3 and 1.

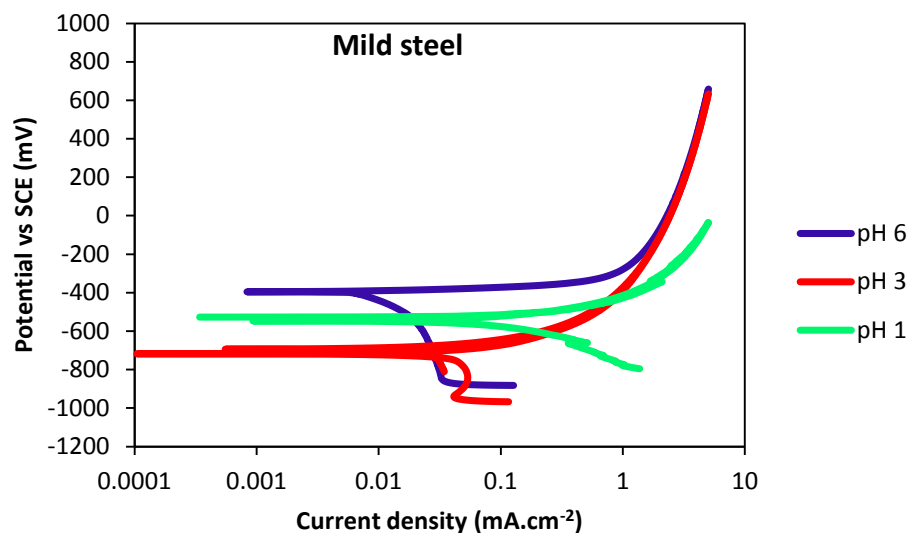
pH	E <sub>corr</sub> (mV)	i <sub>corr</sub> (μA.cm <sup>-2</sup> )	Corrosion rate (mm.y <sup>-1</sup> )
6	-630	2.30	0.036
3	-616	1.60	0.024
1	-529	7.20	0.110

### Summary

Corrosion resistance for Cr<sub>2</sub>O<sub>3</sub> is not better than ULTIMET and Stellite 6 coatings in synthetic mine water, and would not solve the corrosion problem at Otjihase Mine.

### Mild steel substrate

Figure 6.37 shows the potentiodynamic polarisation behaviour of the mild steel substrate. The substrate showed no passivation behaviour and no hysteresis at all pH values. It has the highest corrosion rates than the other samples (ULTIMET, Stellite 6 and Cr<sub>2</sub>O<sub>3</sub>). The highest corrosion rate was recorded at pH 1, followed by pH 6 and pH 3 with the lowest (Figure 6.36). Table 6.8 shows the corrosion recorded, indicating that the mild steel substrate at pH 3 had the lowest corrosion rate. With decreased pH, E<sub>corr</sub>, i<sub>corr</sub> and corrosion rate for mild steel changed with no trend.



**Figure 6.37.** Cyclic potentiodynamic polarisation curves at ambient temperature of the mild steel substrates in synthetic mine water at pH 6, 3 and 1.

**Table 6.8.** Cyclic potentiodynamic polarisation results at ambient temperature of the mild steel substrates in synthetic mine water at pH 6, 3 and 1.

pH	$E_{\text{corr}}$ (mV)	$i_{\text{corr}}$ ( $\mu\text{A}\cdot\text{cm}^{-2}$ )	Corrosion rate ( $\text{mm}\cdot\text{y}^{-1}$ )
6	-400	36.30	0.42
3	-719	31.80	0.37
1	-547	62.30	0.72

### Summary

Mild steel had highest corrosion rates than the other samples (ULTIMET, Stellite 6 and  $\text{Cr}_2\text{O}_3$ ) at all pH values.

### 6.4.3 SEM-EDX results after cyclic potentiodynamic polarisation

Figures 6.38-6.45 show SEM-SE micrographs of the surfaces of ULTIMET and Stellite 6 coatings with no Ru, 0.3 and 0.6 wt% Ru,  $\text{Cr}_2\text{O}_3$  coatings and mild steel substrates after cyclic potentiodynamic polarisation in synthetic (pH 6) and acidified synthetic mine water (pH 3 and 1). ULTIMET (Figures 6.38-6.40) and Stellite 6 (Figures 6.41-6.43) coatings experienced similar corrosion responses at all pH values. The surfaces were more corroded when the pH decreased. They showed general corrosion with corrosion products on the surfaces which increased at pH 3 and 1. There was intergranular corrosion between the main particles. The dendrites and interdendritic carbides were less degraded compared to the uncorroded samples. Ruthenium additions reduced the attack of the particle boundaries, with less attack on Stellite 6 surfaces with nominal 0.3 wt% Ru than that of nominal 0.6 wt% Ru. With decreased pH, there was more attack on sample surfaces (especially between the particles), with seemingly more attack on the coating with nominal 0.6 wt% Ru than nominal 0.3 wt% Ru. No trend between the microstructures and ruthenium additions could be deduced for the different pH investigated. However, ruthenium in the samples appeared unattacked at all pH values.

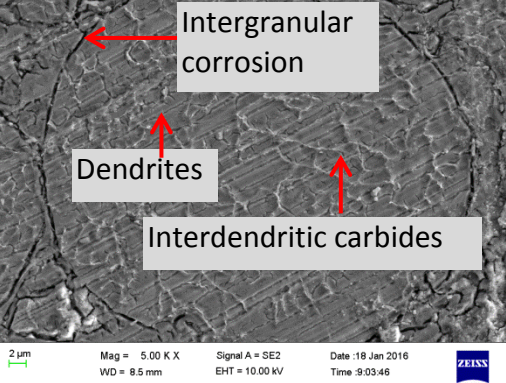
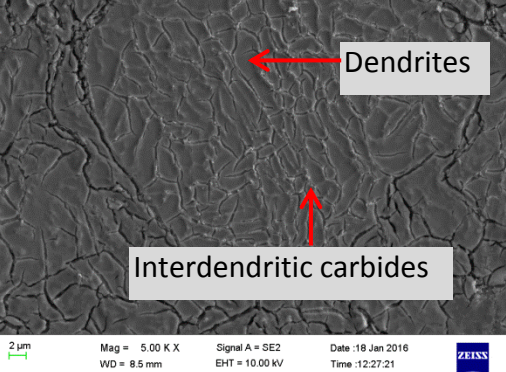
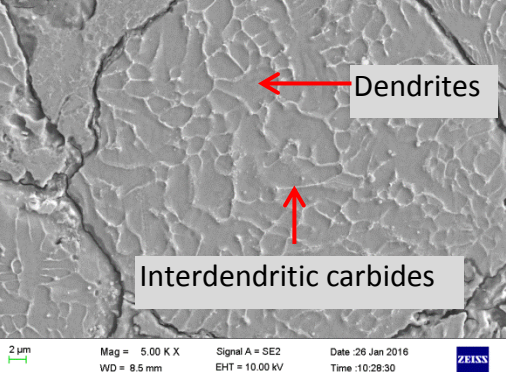
Chromium oxide coatings (Figure 6.44) showed general corrosion with corrosion products in pits, while the mild steel substrates (Figure 6.45) showed severe general corrosion with corrosion products covering the whole surface.

Tables 6.9-6.12 show EDX analysis of the surfaces of the samples after the corrosion. For the ULTIMET (Table 6.9) coatings with no Ru, nominal 0.3 wt% Ru and nominal 0.6 wt% Ru, the overall EDX analysis on the surfaces after corrosion showed high concentrations of Cr, Co, O and W at all pH values and compositions. The high presence of Cr and O

indicated a chromium oxide film formed on the surfaces. Other detected elements were Ni, Mo, W, with minor constituents of S, Si, Na and Cl, with Fe detected at all pH values for samples with Ru, and nominal 0.6 wt% Ru at pH 1. The S, Na and Cl were exogenous products. No trends were observed in material loss on the surfaces with increased pH or Ru. Ruthenium was not detected due to the volume detection limit.

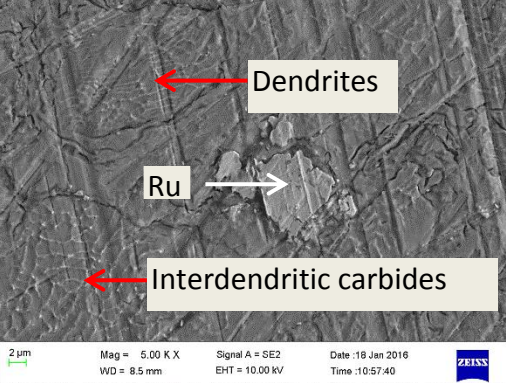
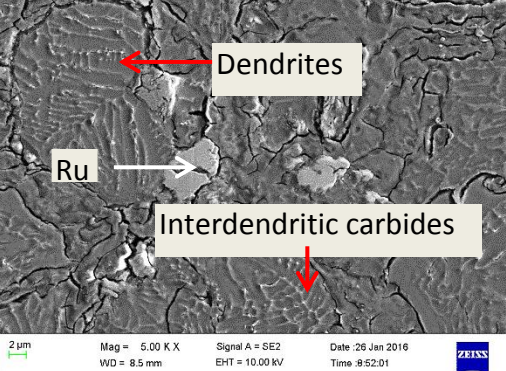
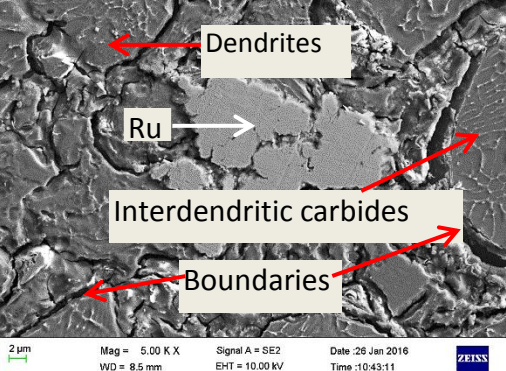
For the Stellite 6 coatings (Table 6.10) with no Ru, nominal 0.3 wt% Ru and nominal 0.6 wt% Ru, the overall analysis on the surface after corrosion showed high concentrations of Cr, Co, O and W at all pH values and compositions. Like the ULTIMET coatings after corrosion, Cr and O on the surfaces of the Stellite 6 coatings could form a chromium oxide as a protective film against corrosion. Other elements as minor constituents were Fe, S, Si, Cl and Mo, where S and Cl were exogenous products. No trend was observed for material loss on the surfaces with increased pH or Ru. Ruthenium was only detected in the Stellite 6 coatings with nominal 0.6 wt% Ru sample at all pH values.

The overall EDX analysis for  $\text{Cr}_2\text{O}_3$  coatings (Table 6.11) after corrosion showed little change when the pH was decreased. High concentrations of Cr and O were recorded at all pH values, as expected. Exogenous products detected at pH 3 and 1 were the Cl ions in small concentrations. For mild substrates, Fe and O were the major elements detected at all pH. Other ions were S, Si and Mg. S and Mg were exogenous products from the synthetic mine water.

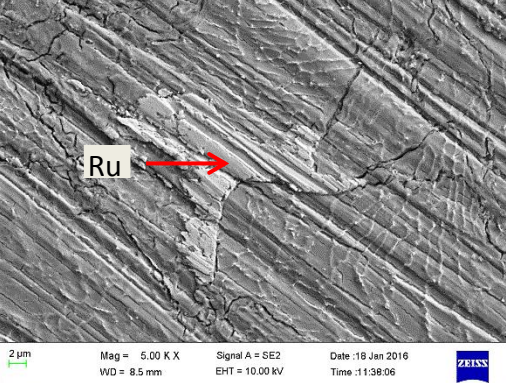
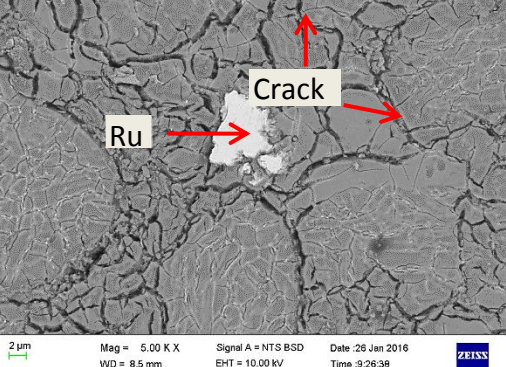
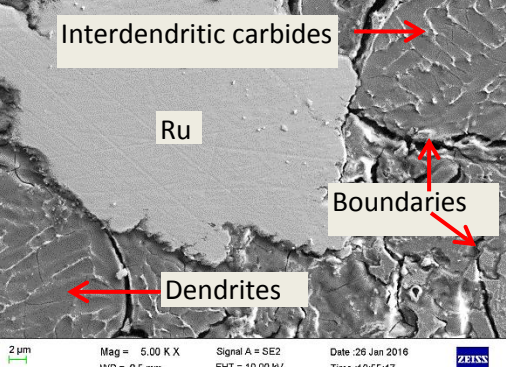
<p><b>pH 6</b></p>		<p>General corrosion with corrosion products on the surface, and corrosion at the boundary between main particles (Intergranular corrosion). Degradation on dendrites and interdendritic carbides.</p>
<p><b>pH 3</b></p>		<p>General corrosion with corrosion products on the surface, and corrosion at the boundary between main particles. More degradation on dendrites and interdendritic carbides.</p>
<p><b>pH 1</b></p>		<p>General corrosion with corrosion products on the surface. Degradation on dendrites and interdendritic carbides and more attack on the particle boundaries.</p>

**Figure 6.38.** SEM-SE surface micrographs of the ULTIMET coating without Ru after cyclic potentiodynamic polarisation in synthetic mine water at ambient temperature and pH 6, 3 and 1, showing general corrosion, corrosion products on the surfaces and degradation at particle boundaries.

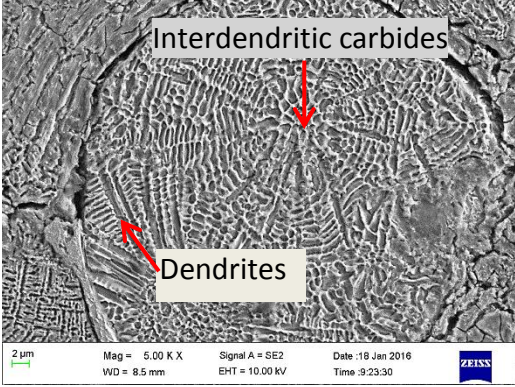
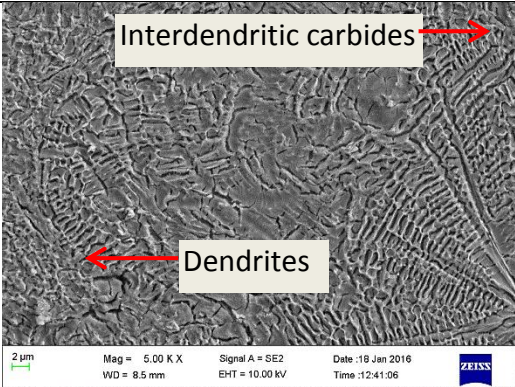
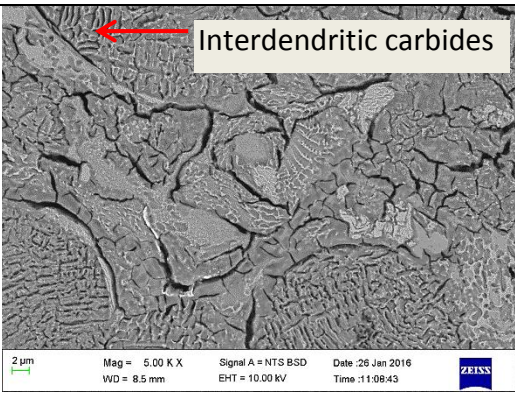


<p><b>pH 6</b></p>		<p>General corrosion with corrosion products on the surface. Degradation on dendrites and interdendritic carbides.</p>
<p><b>pH 3</b></p>		<p>General corrosion with corrosion products on the surface, and corrosion at the boundary between main particles. Degradation on dendrites and interdendritic carbides.</p>
<p><b>pH 1</b></p>		<p>General corrosion with corrosion products on the surface. Severe degradation on dendrites and interdendritic carbides and more attack on the particle boundaries.</p>

**Figure 6.39.** SEM-SE surface micrographs of the ULTIMET coatings with nominal 0.3 wt% Ru after cyclic potentiodynamic polarisation in synthetic mine water at pH 6, 3 and 1, at ambient temperature, showing general corrosion, corrosion products on the surfaces and degradation at particle boundaries, with undissolved Ru particles (light) at all pH.

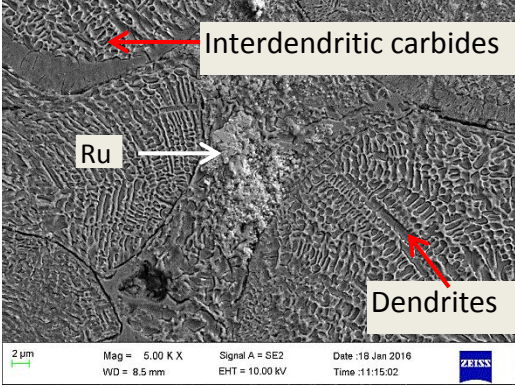
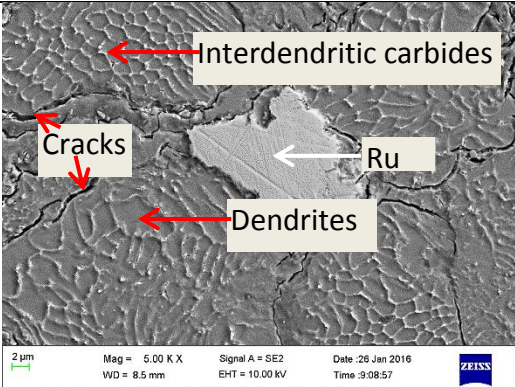
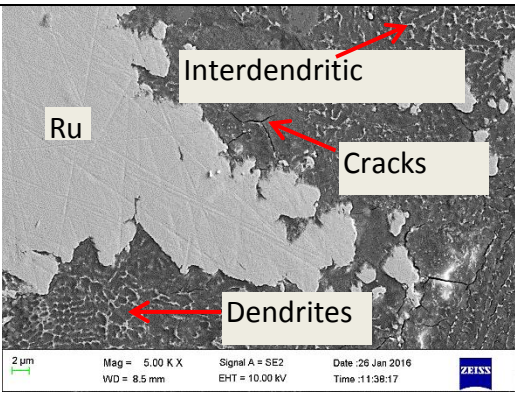
<p><b>pH 6</b></p>		<p>Corrosion mechanisms as for nominal 0.3 wt% Ru ULTIMET coating at pH 6. The light particle is Ru which did not dissolve.</p>
<p><b>pH 3</b></p>		<p>Corrosion mechanisms as for nominal 0.3 wt% Ru ULTIMET coating at pH 3, with more cracks on the corrosion products. The light particle is Ru which did not dissolve.</p>
<p><b>pH 1</b></p>		<p>General corrosion with corrosion products on the surface. Severe degradation on dendrites and interdendritic carbides and more attack on the particle boundaries (intergranular corrosion).</p>

**Figure 6.40.** SEM-SE surface micrographs of the ULTIMET coatings with nominal 0.6 wt% Ru after cyclic potentiodynamic polarisation in synthetic mine water at pH 6, 3 and 1, at ambient temperature, showing general corrosion, corrosion products on the surfaces and degradation at particle boundaries, with undissolved Ru particles (light) at all pH.

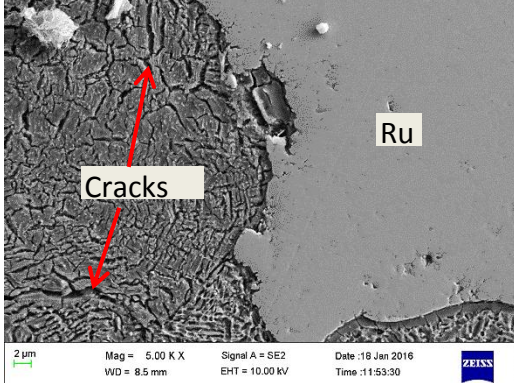
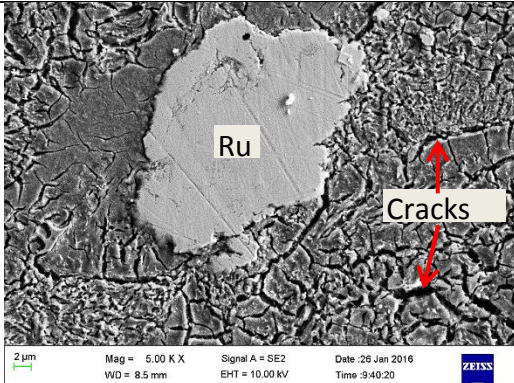
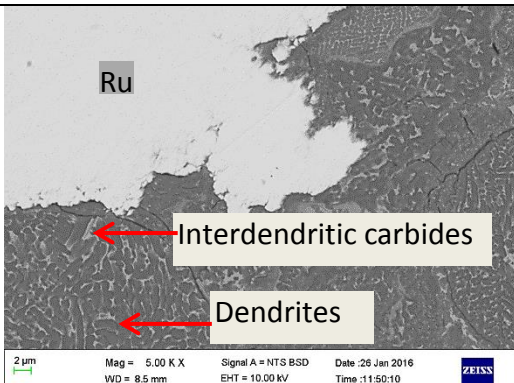
pH 6		<p>General corrosion with corrosion products on the surface, and corrosion at the boundaries between main particles (intergranular corrosion). Little degradation on dendrites and interdendritic carbides.</p>
pH 3		<p>General corrosion with corrosion products on the surface. Degradation on dendrites and interdendritic carbides.</p>
pH 1		<p>General corrosion with corrosion products on the surface. Severe degradation on dendrites and interdendritic carbides and corroded particle boundaries, with more cracks on the corrosion products.</p>

**Figure 6.41.** SEM-SE surface micrographs of the Stellite 6 coatings without Ru after cyclic potentiodynamic polarisation in synthetic mine water at pH 6, 3 and 1, at ambient temperature, showing general corrosion, corrosion products and degradation at particle boundaries, and boundary corrosion between main particles.

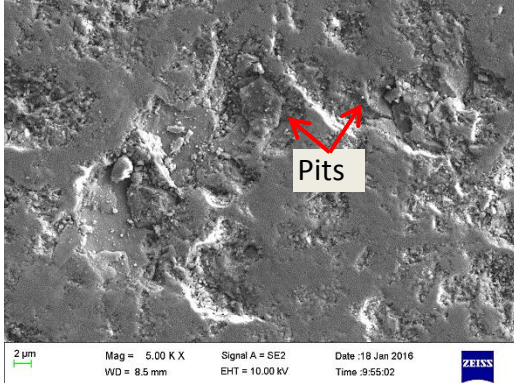
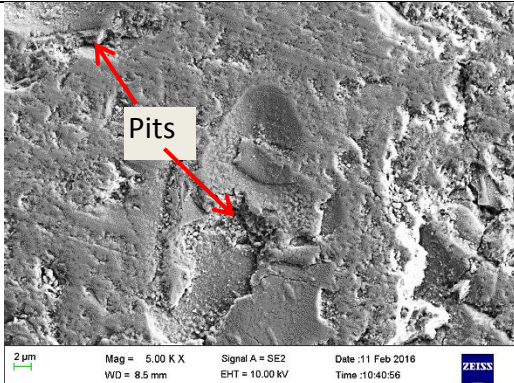
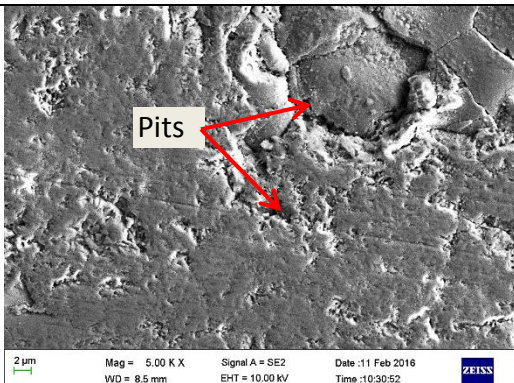


<p><b>pH 6</b></p>		<p>General corrosion with corrosion products on the surface. Little degradation on dendrites and interdendritic carbides.</p>
<p><b>pH 3</b></p>		<p>General corrosion with corrosion products on the surface. Degradation on dendrites, interdendritic carbides and particle boundaries, with cracks.</p>
<p><b>pH 1</b></p>		<p>General corrosion with corrosion products on the surface. Severe degradation on dendrites and interdendritic carbides.</p>

**Figure 6.42.** SEM-SE surface micrographs of the Stellite 6 coatings with nominal 0.3 wt% Ru after cyclic potentiodynamic polarisation in synthetic mine water at pH 6, 3 and 1, at ambient temperature, showing general corrosion, corrosion products and degradation at particle boundaries, with undissolved Ru particles (light) at all pH.

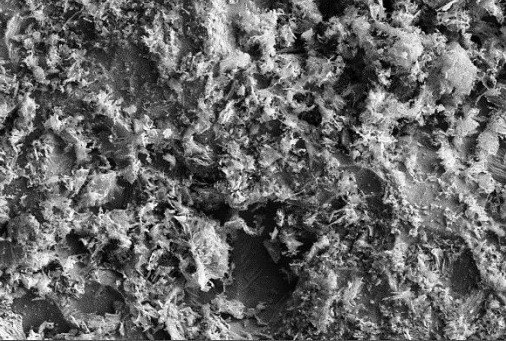
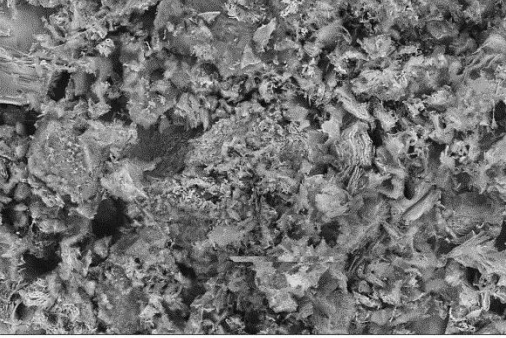
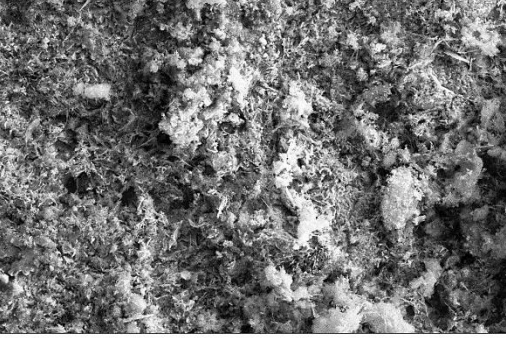
<p><b>pH 6</b></p>		<p>General corrosion with corrosion products on the surface. Severe degradation on dendrites and interdendritic carbides, with cracks on the corrosion products.</p>
<p><b>pH 3</b></p>		<p>General corrosion with corrosion products on the surface. Severe degradation on dendrites and interdendritic carbides, with cracks in the corrosion products.</p>
<p><b>pH 1</b></p>		<p>General corrosion with corrosion products on the surface. Severe degradation on dendrites and attack on the particle boundaries.</p>

**Figure 6.43.** SEM-SE surface micrographs of the Stellite 6 coatings with nominal 0.6 wt% Ru after cyclic potentiodynamic polarisation in synthetic mine water at pH 6, 3 and 1, at ambient temperature, showing general corrosion, corrosion products and degradation at particle boundaries, with undissolved Ru particles (light) at all pH.

<p><b>pH 6</b></p>		<p>General corrosion and corrosion products in pits</p>
<p><b>pH 3</b></p>		<p>General corrosion and corrosion products in pits</p>
<p><b>pH 1</b></p>		<p>General corrosion and corrosion products in pits</p>

**Figure 6.44.** SEM-SE surface micrographs of  $\text{Cr}_2\text{O}_3$  coatings after cyclic potentiodynamic polarisation in synthetic mine water at pH 6, 3 and 1, at ambient temperature showing general corrosion and corrosion products in pits.



<p><b>pH 6</b></p>	 <p>2 μm    Mag = 5.00 K X    Signal A = SE2    Date :18 Jan 2016  WD = 8.5 mm    EHT = 10.00 kV    Time :10:17:51    ZEISS</p>	<p>General corrosion with corrosion products covered the whole surface.</p>
<p><b>pH 3</b></p>	 <p>2 μm    Mag = 5.00 K X    Signal A = NTS BSD    Date :26 Jan 2016  WD = 8.5 mm    EHT = 10.00 kV    Time :11:55:17    ZEISS</p>	<p>General corrosion with corrosion products covered the whole surface.</p>
<p><b>pH 1</b></p>	 <p>2 μm    Mag = 5.00 K X    Signal A = SE2    Date :26 Jan 2016  WD = 8.5 mm    EHT = 10.00 kV    Time :12:07:42    ZEISS</p>	<p>Severe general corrosion with corrosion products covered the whole surface.</p>

**Figure 6.45.** SEM-SE surface micrographs of mild steel substrate after cyclic potentiodynamic polarisation in synthetic mine water at pH 6, 3 and 1, at ambient temperature showing general corrosion and corrosion products on entire surface.

**Table 6.9.** EDX analysis (wt%) of the ULTIMET sample surface of Figures 6.38-6.40 after cyclic potentiodynamic polarisation in synthetic mine water at pH 6, 3 and 1, at ambient temperature.

Element (wt%)	No Ru			Nominal 0.3 wt% Ru			Nominal 0.6 wt% Ru		
	pH 6	pH 3	pH 1	pH 6	pH 3	pH 1	pH 6	pH 3	pH 1
O	17.6 ± 2.0	17.4 ± 1.0	13.7 ± 0.4	13.5 ± 0.4	16.2 ± 1.0	17.1 ± 1.0	13.9 ± 0.4	19.6 ± 1.0	17.9 ± 1.0
Na	0.2 ± 0.0	0.2 ± 0.1	-	0.5 ± 0.1	-	-	0.3 ± 0.1	-	-
Si	0.2 ± 0.1	0.2 ± 0.1	0.3 ± 0.0	-	0.3 ± 0.1	0.3 ± 0.1	0.3 ± 0.0	0.3 ± 0.0	0.3 ± 0.1
S	0.6 ± 0.3	0.7 ± 0.2	1.2 ± 0.2	1.0 ± 0.1	0.9 ± 0.2	1.5 ± 0.2	0.6 ± 0.2	0.8 ± 0.2	1.5 ± 0.3
Cl	-	-	0.2 ± 0.1	0.2 ± 0.1	-	-	0.1 ± 0.0	-	-
Cr	34.4 ± 2.0	34.8 ± 1.0	31.1 ± 1.0	33.0 ± 1.0	33.4 ± 2.0	35.1 ± 1.0	33.3 ± 1.0	37.6 ± 1.2	35.2 ± 1.3
Fe	3.5 ± 1.0	4.4 ± 1.0	5.4 ± 2.0	-	-	-	-	-	4.3 ± 2.3
Co	25.6 ± 2.0	24.7 ± 1.0	33.6 ± 1.0	33.3 ± 1.0	30.4 ± 1.0	29.0 ± 1.0	32.3 ± 1.0	23.1 ± 0.3	26.2 ± 1.0
Ni	7.6 ± 0.3	6.0 ± 0.2	8.2 ± 0.2	8.7 ± 0.2	8.1 ± 0.3	7.6 ± 0.2	8.3 ± 0.2	5.8 ± 0.3	6.4 ± 1.0
Mo	4.8 ± 0.4	6.4 ± 1.0	3.8 ± 0.4	5.2 ± 0.4	5.9 ± 0.2	4.4 ± 0.4	6.1 ± 0.4	6.7 ± 0.4	3.8 ± 1.0
W	5.5 ± 0.3	5.2 ± 0.1	2.6 ± 0.2	4.5 ± 0.2	4.7 ± 0.4	4.9 ± 0.3	4.5 ± 0.4	6.1 ± 0.3	4.2 ± 0.4



**Table 6.10.** EDX analysis (wt%) of the Stellite 6 coating surfaces of Figures 6.41-6.43 after cyclic potentiodynamic polarisation in synthetic mine water at pH 6, 3 and 1, at ambient temperature.

Element (wt%)	No Ru			Nominal 0.3 wt% Ru			Nominal 0.6 wt% Ru		
	pH 6	pH 3	pH 1	pH 6	pH 3	pH 1	pH 6	pH 3	pH 1
O	17.5 ± 0.2	17.3 ± 1.0	18.4 ± 1.0	11.0 ± 1.0	15.0 ± 1.0	16.9 ± 1.0	20.8 ± 0.2	19.6 ± 0.4	11.5 ± 8.0
Si	0.5 ± 0.3	0.8 ± 0.1	0.6 ± 0.0	0.7 ± 0.1	0.3 ± 0.1	0.5 ± 0.1	0.9 ± 0.1	0.6 ± 0.0	0.5 ± 0.1
S	0.5 ± 0.1	0.8 ± 0.3	1.6 ± 0.1	0.2 ± 0.0	0.9 ± 0.2	0.8 ± 0.1	0.8 ± 0.1	1.1 ± 0.2	0.7 ± 0.0
Cl	-	0.2 ± 0.0	1.8 ± 0.2	-	-	0.8 ± 0.2	-	-	0.5 ± 0.1
Cr	44.0 ± 1.0	40.5 ± 1.0	36.7 ± 1.3	40.0 ± 2.0	33.7 ± 0.4	33.8 ± 2.0	42.0 ± 0.4	40.7 ± 0.4	32.8 ± 3.0
Fe	-	3.7 ± 1.4	-	-	-	22.0 ± 2.0	-	4.5 ± 0.3	18.0 ± 3.3
Co	21.3 ± 0.2	22.4 ± 1.0	18.2 ± 1.2	33.1 ± 1.0	31.8 ± 1.0	17.6 ± 1.0	18.6 ± 1.0	17.3 ± 1.0	24.5 ± 1.3
Ni	1.6 ± 0.1	1.4 ± 0.3	14.0 ± 0.4	4.7 ± 2.0	8.3 ± 0.2	2.0 ± 0.3	0.8 ± 0.0	1.4 ± 0.2	2.3 ± 0.3
Mo	0.5 ± 0.3	0.8 ± 0.4	-	0.6 ± 0.4	5.5 ± 0.4	-	0.4 ± 0.2	0.6 ± 0.1	-
Ru	-	-	-	-	-	-	0.3 ± 0.0	0.5 ± 0.2	0.3 ± 0.2
W	14.1 ± 1.0	12.0 ± 0.4	8.7 ± 0.3	9.6 ± 1.0	4.6 ± 0.3	5.7 ± 0.3	15.2 ± 0.4	13.8 ± 0.4	5.3 ± 1.0

**Table 6.11.** EDX analysis (wt%) of Cr<sub>2</sub>O<sub>3</sub> coating surfaces of Figure 6.44 after cyclic potentiodynamic polarisation in synthetic mine water at pH 6, 3 and 1, at ambient temperature.

Element (wt%)	pH 6	pH 3	pH 1
O	32.7 ± 0.3	31.5 ± 0.3	31.9 ± 1.2
Cl	-	0.1 ± 0.0	0.2 ± 0.0
Cr	67.3 ± 0.3	68.3 ± 0.3	68.0 ± 1.1

**Table 6.12.** EDX analysis (wt%) of mild steel substrate surfaces of Figure 6.45 after cyclic potentiodynamic polarisation in synthetic mine water at pH 6, 3 and 1, at ambient temperature.

Element (wt%)	pH 6	pH 3	pH 1
C	6.6 ± 0.1	-	-
O	6.2 ± 0.2	11.0 ± 3.6	14.8 ± 1.0
Si	0.4 ± 0.0	-	0.2 ± 0.0
S	0.2 ± 0.0	-	-
Mg	-	0.2 ± 0.1	-
Cl	-	0.4 ± 0.2	-
Fe	86.6 ± 0.4	88.4 ± 3.6	85.0 ± 1.0

## 6.5 Friction and sliding wear characteristics

### 6.5.1 Coefficients of friction, penetration depths and wear rates

#### **5N force**

The friction behaviour of ULTIMET and Stellite 6 coatings with no Ru, nominal 0.3 wt% Ru and nominal 0.6 wt% Ru, Cr<sub>2</sub>O<sub>3</sub> coatings and mild steel substrates sliding against 100Cr steel balls at 5N as a function of sliding distance is given in Figures 6.46, 6.48 and 6.50.

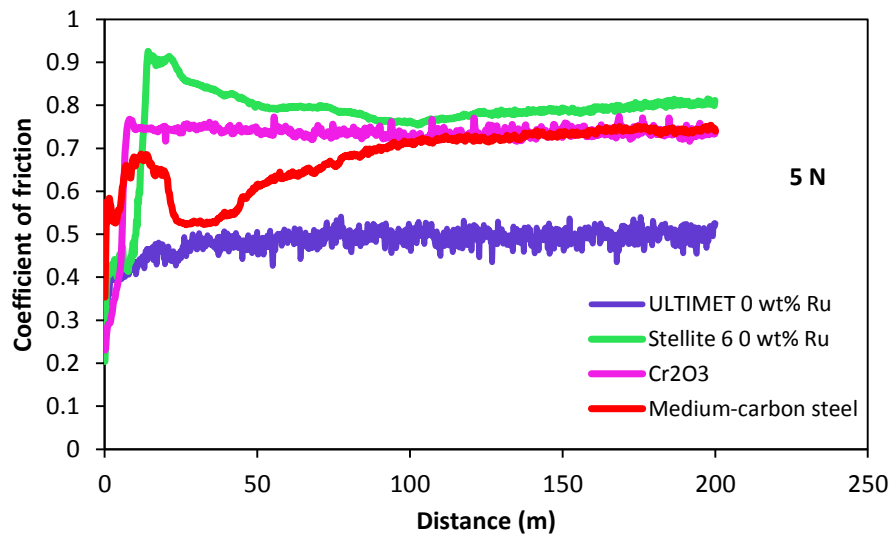
ULTIMET (Figure 6.46): the coefficient of friction ( $\mu$ ) increased from 0.30 to 0.40, decreased slightly to 0.38, then increased to 0.50 and gained steady state conditions between 0.48 and 0.50 after 25m. For Stellite 6 (Figure 6.46),  $\mu$  increased from 0.20 to 0.40 in 2.50m, and then increased to 0.89, decreased to 0.77 and attained steady state at 0.80 for 164.30m. For Cr<sub>2</sub>O<sub>3</sub> (Figure 6.46),  $\mu$  increased from 0.23 to 0.77 in 6.30m, and decreased to 0.74 then attained steady state for 192.50m, while for mild steel (Figure 6.46),  $\mu$  increased from 0.35 to 0.70 in 0.50m, and decreased to 0.50. It then increased to 0.68 at 8.40m, and reached steady state of 0.72 in 162.20m.

#### **10N force**

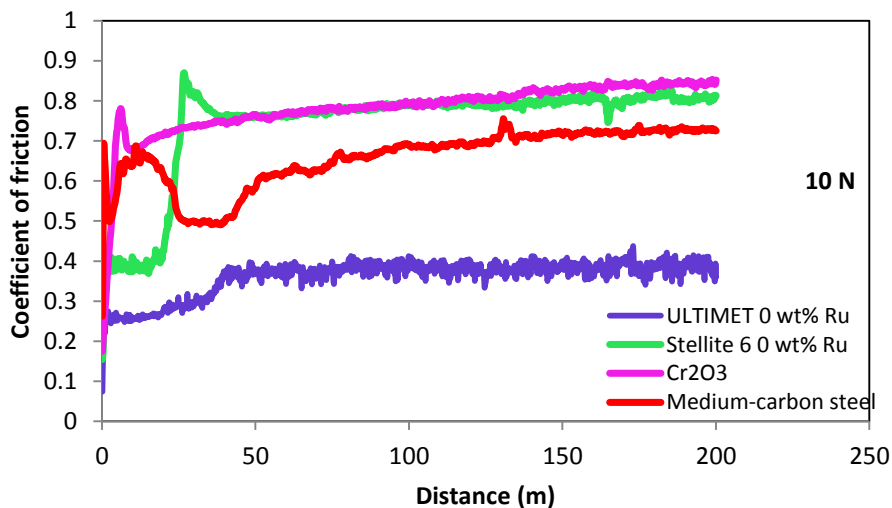
The friction behaviour of ULTIMET and Stellite 6 coatings with no Ru, nominal 0.3 wt% Ru and nominal 0.6 wt% Ru, Cr<sub>2</sub>O<sub>3</sub> coating and mild steel substrates sliding against 100Cr steel balls as a function of sliding distance at 10N is given in Figures 6.47, 6.49 and 6.51. At the 10N load, the sliding behaviours were similar to those at 5N. Stellite 6 had the lowest wear rate,  $k$  (Table 6.4). At 5N, the lowest  $k$  was recorded for Stellite 6 with nominal 0.3 wt% Ru, while at 10N, the lowest  $k$  was recorded for Stellite 6 with 0.6 wt%

Ru. This identified Stellite 6 to be the best material tested for applications where wear may be a problem.

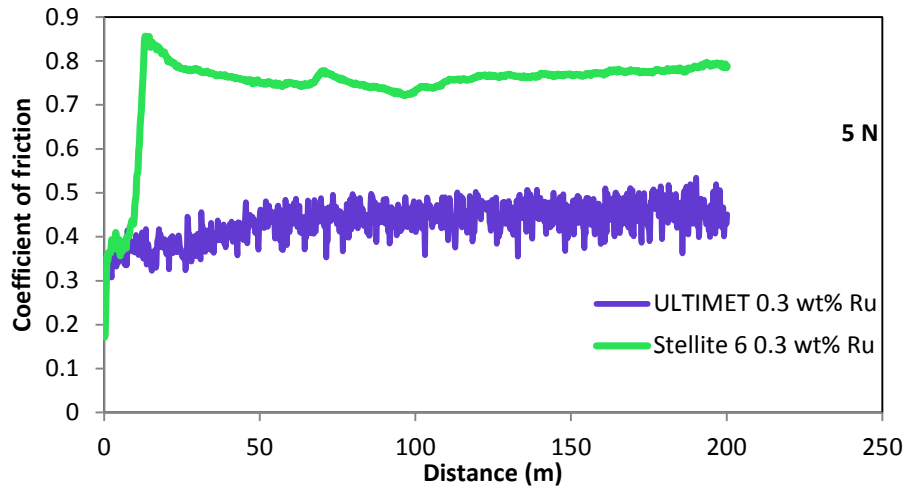
The coefficients of friction, forces of friction, maximum penetration depths ( $Pd_{max}$ ) and wear rates of ULTIMET and Stellite 6 coatings with no Ru, nominal 0.3 wt% Ru and nominal 0.6 wt% Ru,  $Cr_2O_3$  coatings and mild steel substrates at 5N and 10N against 100Cr steel balls are given in Tables 6.9-6.10. At 5N, the samples had low forces of friction, which increased as the load was increased. The wear rates were low at 5N, and high at 10N.



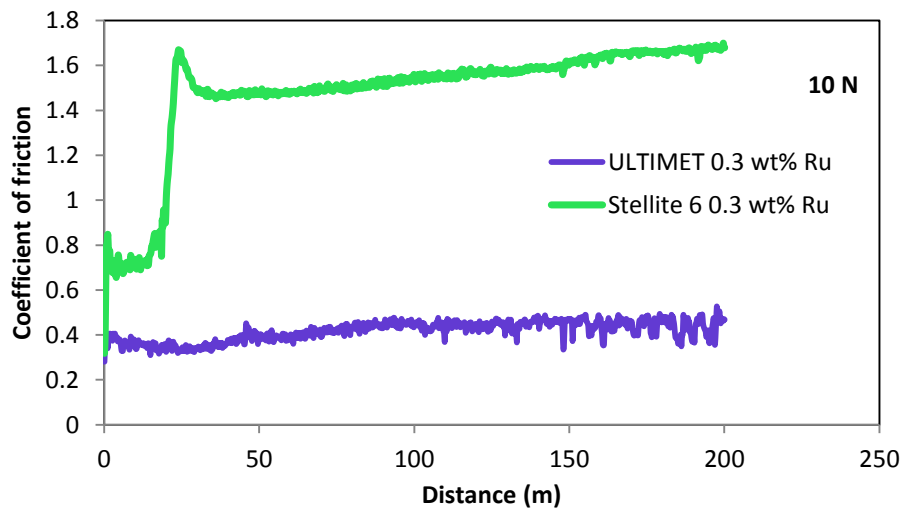
**Figure 6.46.** Friction behaviour of ULTIMET and Stellite 6 coatings without Ru,  $Cr_2O_3$  coating, and mild steel against 100Cr steel balls at 5N, showing Stellite 6 had the highest coefficient of friction at 200 m.



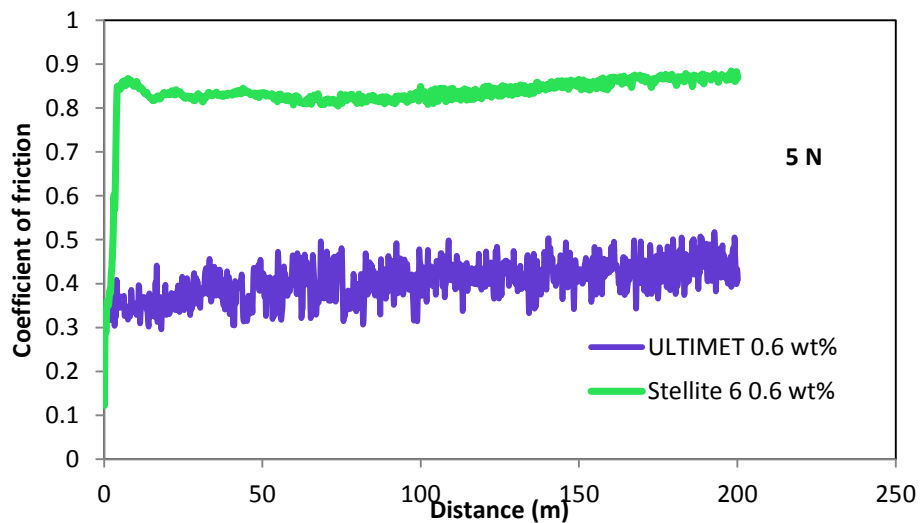
**Figure 6.47.** Friction behaviour of ULTIMET and Stellite 6 coatings without Ru,  $Cr_2O_3$  coating and mild steel substrate against 100Cr steel balls at 10N, showing  $Cr_2O_3$  had the highest coefficient of friction at steady state, at 200 m.



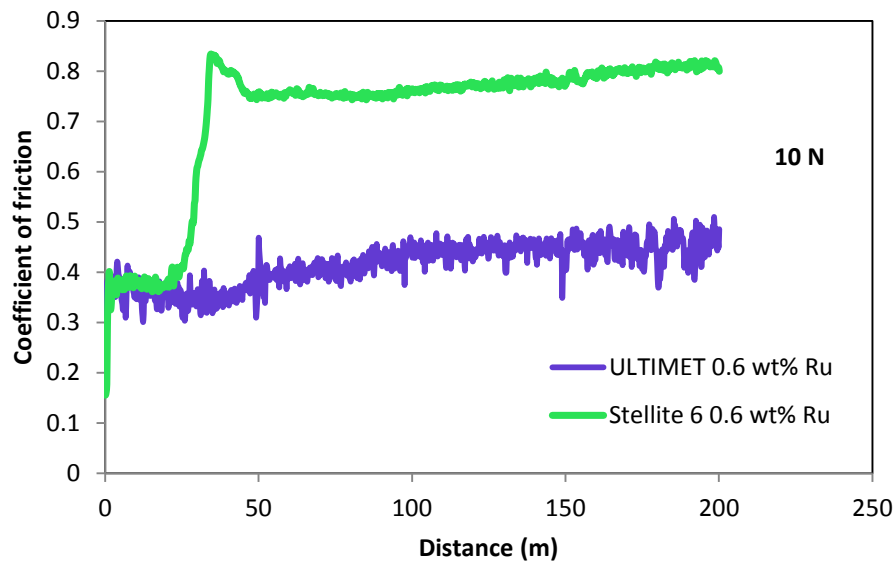
**Figure 6.48.** Friction behaviour of ULTIMET and Stellite 6 coatings with nominal 0.3 wt% Ru against 100Cr steel balls at 5N, showing Stellite 6 had a higher coefficient of friction at 200 m.



**Figure 6.49.** Friction behaviour of ULTIMET and Stellite 6 coatings with nominal 0.3 wt% Ru against 100Cr steel balls at 10N, showing Stellite 6 had a higher coefficient of friction at 200 m.



**Figure 6.50.** Friction behaviour of ULTIMET and Stellite 6 coatings with nominal 0.6 wt% Ru against 100Cr steel balls at 5N, showing Stellite 6 had a higher coefficient of friction at 200 m.



**Figure 6.51.** Friction behaviour of ULTIMET and Stellite 6 coatings with nominal 0.6 wt% Ru against 100Cr steel balls at 10N, showing Stellite 6 had a higher coefficient of friction at 200 m.

**Table 6.13.** Coefficients of friction, forces of friction, maximum penetration depths ( $Pd_{max}$ ) and wear rates of ULTIMET and Stellite 6 coatings with no Ru, nominal 0.3 and nominal 0.6 wt% Ru,  $Cr_2O_3$  coatings and mild steel substrates at 5N.

Sample		Coefficient of friction, $\mu$	Force of friction (N)	Penetration depth, $Pd_{max}$ ( $\mu\text{m}$ )	Wear rate, $k$ , $\text{mm}^3 \cdot (\text{N} \cdot \text{m})^{-1} \times 10^{-5}$
ULTIMET	No Ru	$0.5 \pm 0.0$	$2.4 \pm 0.1$	8.2	1.4
	0.3 wt% Ru	$0.4 \pm 0.0$	$2.2 \pm 0.2$	8.3	1.2
	0.6 wt% Ru	$0.4 \pm 0.0$	$2.8 \pm 0.2$	8.1	1.3
Stellite 6	No Ru	$0.8 \pm 0.1$	$3.9 \pm 0.5$	8.4	1.3
	0.3 wt% Ru	$0.7 \pm 0.1$	$3.7 \pm 0.5$	8.4	0.7
	0.6 wt% Ru	$0.8 \pm 0.0$	$4.2 \pm 0.3$	8.4	1.1
$Cr_2O_3$		$0.7 \pm 0.1$	$3.6 \pm 0.3$	8.2	1.3
Mild steel		$0.7 \pm 0.1$	$3.4 \pm 0.4$	7.9	1.4

It was evident that the wear rate was generally a function of the hardness of the surfaces. The harder surfaces had lower wear rates than the softer surfaces. All coatings, apart from  $Cr_2O_3$ , demonstrated this characteristic.

### 6.5.2 Wear mechanisms in sliding wear

Figures 6.52-6.57 show morphologies of ULTIMET and Stellite 6 coatings with no Ru and nominal 0.6 wt% Ru,  $Cr_2O_3$  coatings and mild steel substrates sliding against 100Cr steel balls as a function of sliding distance at 5N and 10N. All samples showed predominantly abrasive wear, characterised by grooves, cracks, and severe spalling at both loads. The spalled particles became debris and third bodies. ULTIMET coatings (Figures 6.52 and

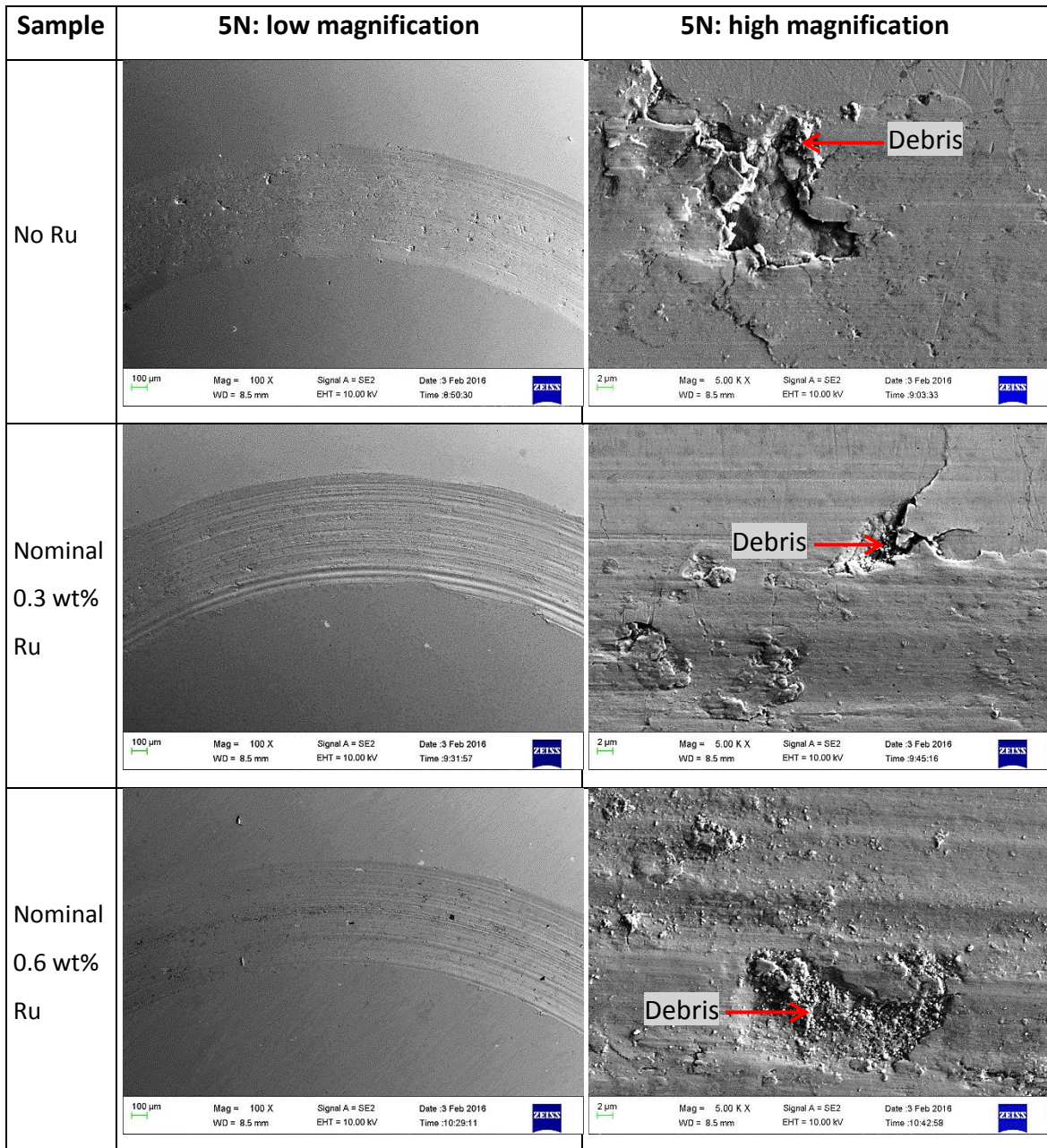
6.53) had the widest wear tracks, shallow grooves, some large pits, delaminated particles and debris, which were more at 10N. ULTIMET coatings with nominal 0.3 wt% Ru experienced smearing at 10N. Stellite 6 coatings (Figures 6.54 and 6.55) had the narrowest wear tracks, and had similar wear mechanisms to ULTIMET coatings at both loads. In addition, Stellite 6 had more debris than ULTIMET coatings. ULTIMET coatings with nominal 0.3 wt% Ru exhibited grooves with waviness for both loads. The Stellite 6 coatings with no Ru at 5N, and nominal 0.6 wt% Ru at 10N also exhibited grooves with waviness. The waviness in ULTIMET and Stellite 6 coatings may have been caused by loose clamping of the samples on the stage, resulting in an intermittent mechanism as the 100Cr steel balls sliding on them. Chromium oxide coatings (Figure 6.56) also had narrow wear tracks, especially at 10N, with pits filled with debris. The mild steel substrates (Figure 6.57) had furrows and shallow grooves, with debris collected in grooves.

**Table 6.14.** Coefficients of friction, forces of friction, maximum penetration depths ( $Pd_{max}$ ) and wear rates of ULTIMET and Stellite 6 coatings with no Ru, nominal 0.3 wt% Ru and nominal 0.6 wt% Ru,  $Cr_2O_3$  coatings and mild steel substrates at 10N.

Sample		Coefficient of friction, $\mu$	Force of friction (N)	Penetration depth, $Pd_{max}$ ( $\mu\text{m}$ )	Wear rate, $k \text{ mm}^3 \cdot (\text{N}\cdot\text{m})^{-1} \times 10^{-5}$
ULTIMET	No Ru	$0.4 \pm 0.0$	$3.6 \pm 0.5$	8.0	8.6
	0.3 wt% Ru	$0.4 \pm 0.0$	$4.2 \pm 0.4$	8.3	7.8
	0.6 wt% Ru	$0.4 \pm 0.0$	$4.2 \pm 0.4$	7.3	5.1
Stellite 6	No Ru	$0.7 \pm 0.0$	$7.4 \pm 1.3$	8.1	4.6
	0.3 wt% Ru	$1.5 \pm 0.3$	$7.4 \pm 1.3$	7.8	4.9
	0.6 wt% Ru	$0.7 \pm 0.1$	$7.2 \pm 1.4$	7.9	3.2
$Cr_2O_3$		$0.8 \pm 0.1$	$7.8 \pm 0.7$	7.8	6.0
Mild steel		$0.7 \pm 0.1$	$6.6 \pm 0.7$	7.3	7.2

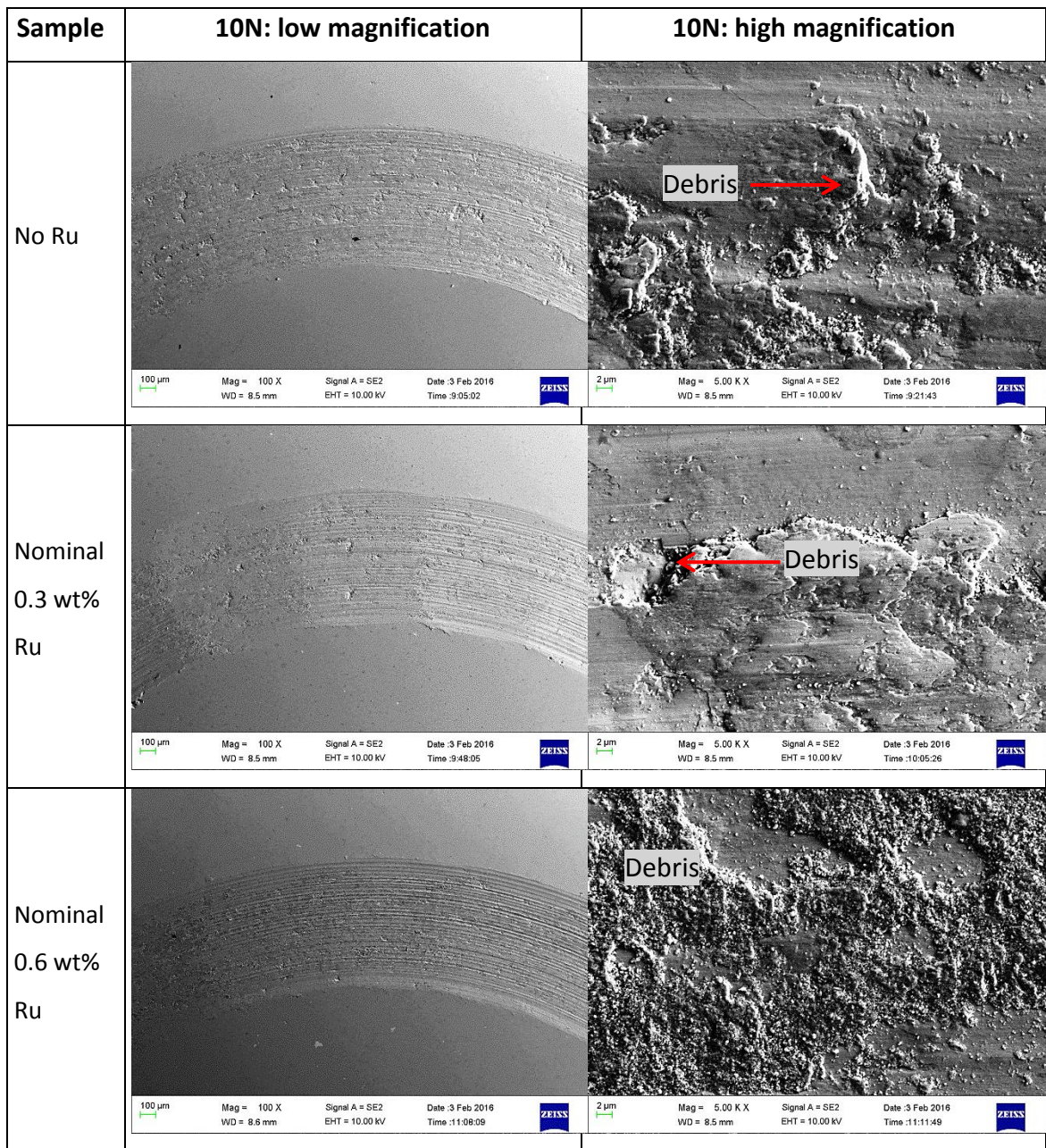
Tables 6.15-6.22 show EDX analysis of wear tracks of ULTIMET and Stellite 6 coatings with no Ru, nominal 0.3 wt% Ru and nominal 0.6 wt% Ru,  $Cr_2O_3$  coatings and mild steel substrates from Figures 6.52-6.57 after ball-on-disc sliding wear at 5N and 10N. EDX analysis of the ULTIMET coatings without Ru (Table 6.13) showed Co, Cr, Ni and Mo as major constituents on the wear tracks, with Mn, W, O, C and Si as minor components at both loads. The analysis of the debris at 10N revealed these constituents, with high O content, and so it was assumed to be an oxide, especially as no sulphur or chlorine were detected. In addition, Fe was detected in the debris. With increased load, all contents

decreased, apart from O. There were little changes in the compositions for the ULTIMET coatings with nominal 0.3 wt% Ru (Table 6.14) from the coatings without Ru at both loads. Ruthenium was detected at both loads. Table 6.15 shows wear track compositions of ULTIMET coatings with nominal 0.6 wt% Ru, showing almost similar compositions as ULTIMET with no Ru and nominal 0.3 wt% Ru at both loads, with Ru detected at 5N only. With increased load, all compositions decreased apart from O, and since no sulphur or chlorine was found, the debris was assumed to be oxides.



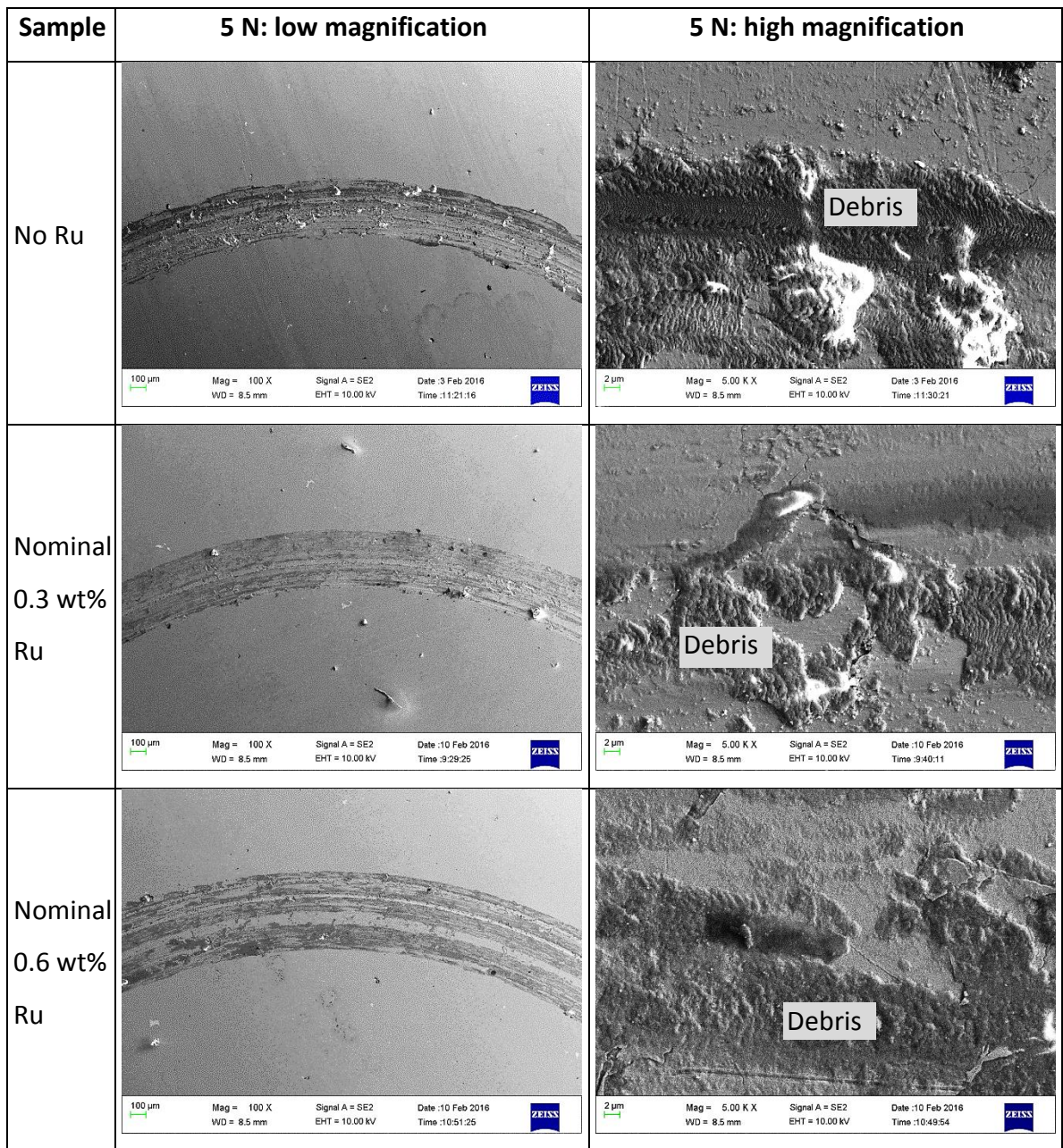
**Figure 6.52.** SEM-SE micrographs of ULTIMET coatings with no Ru, nominal 0.3 wt% Ru and nominal 0.6 wt% Ru after ball-on-disc sliding wear at 5N, showing wide wear tracks and damage with debris in pits.





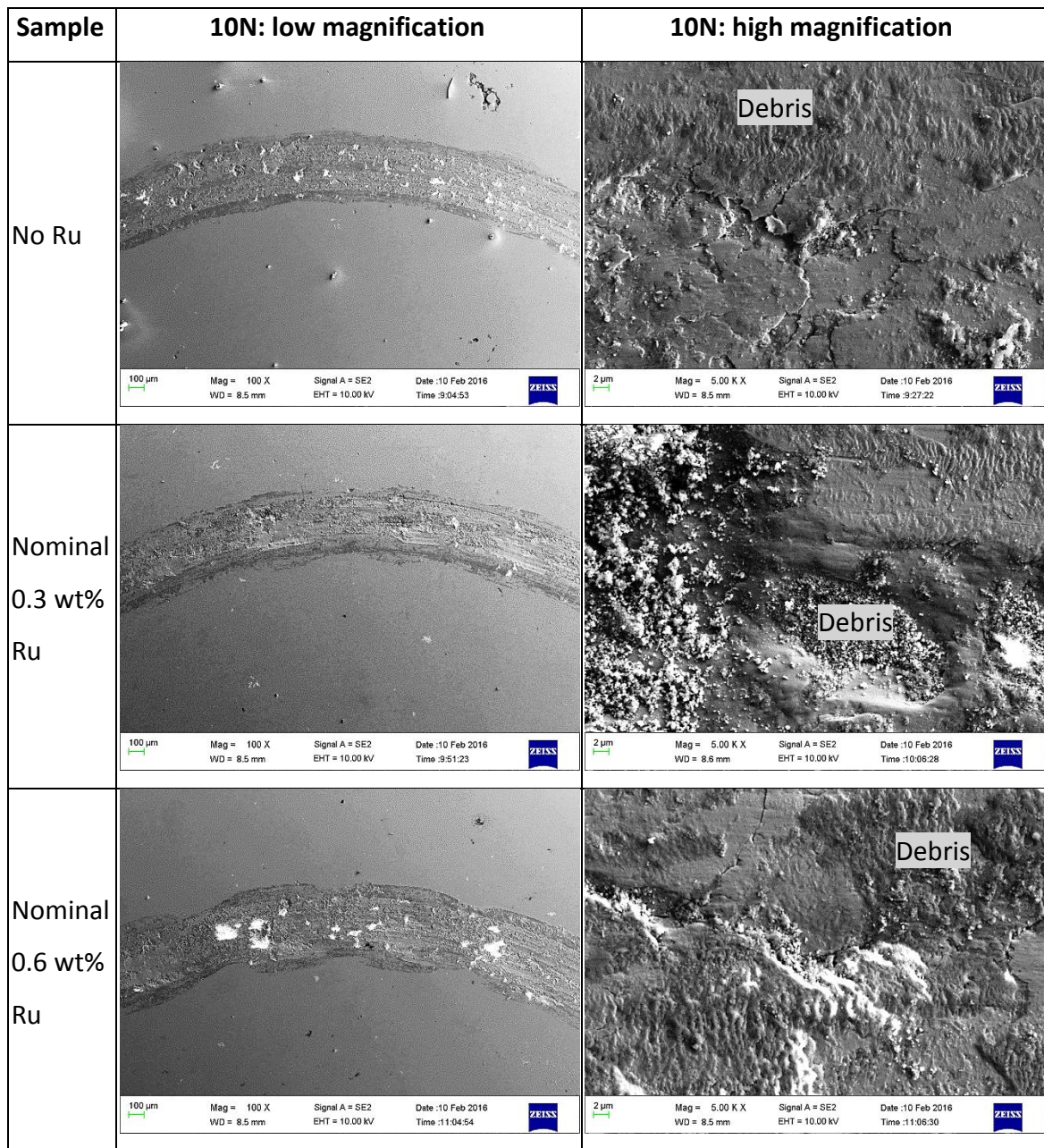
**Figure 6.53.** SEM-SE micrographs of ULTIMET coatings with no Ru, nominal 0.3 wt% Ru and nominal 0.6 wt% Ru after ball-on-disc sliding wear at 10N, showing wide wear tracks and damage with debris in pits.





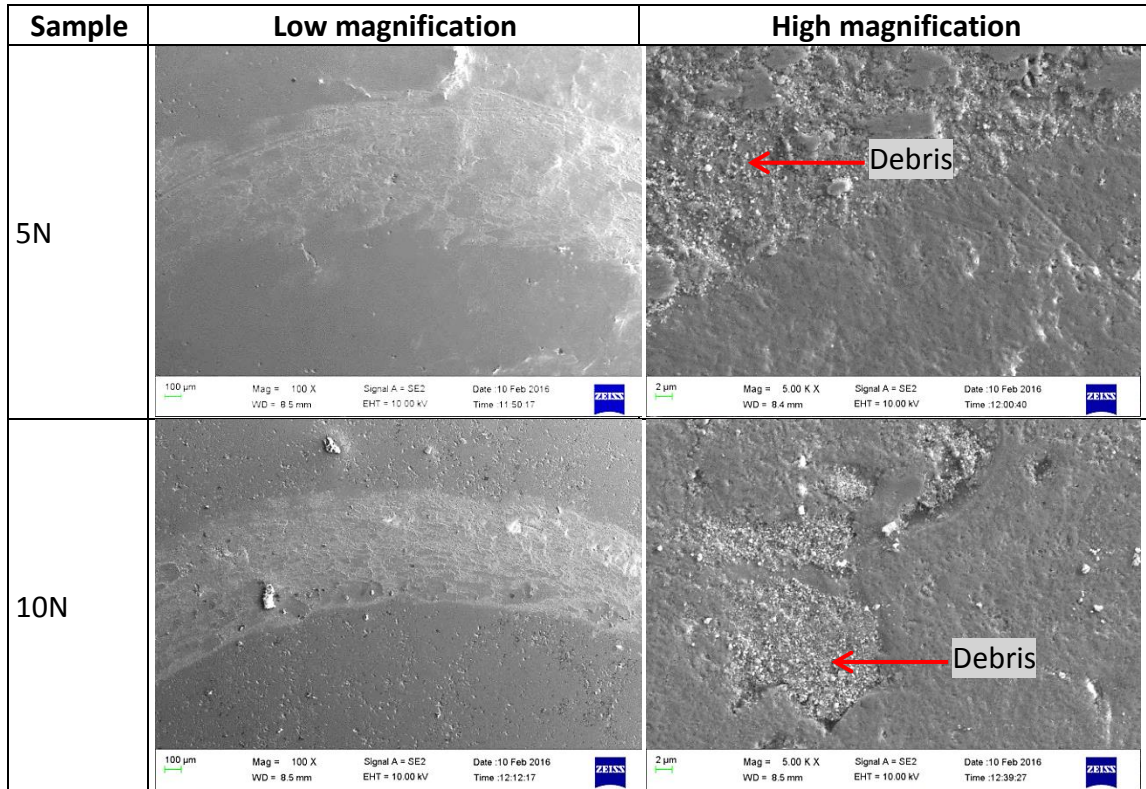
**Figure 6.54.** SEM-SE micrographs of Stellite 6 coatings with no Ru, nominal 0.3 wt% Ru and nominal 0.6 wt% Ru after ball-on-disc sliding wear at 5N, showing wide wear tracks and damage with debris on the surface.



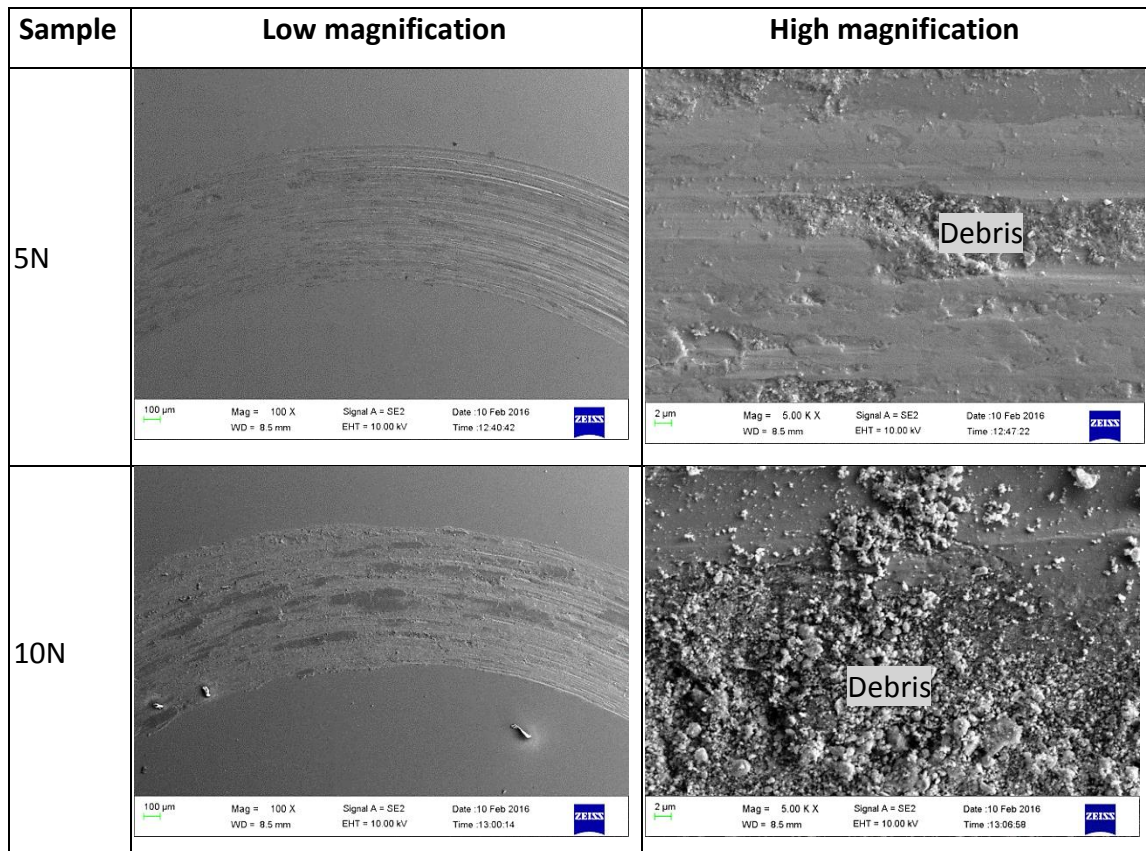


**Figure 6.55.** SEM-SE micrographs of Stellite 6 coatings with no Ru, nominal 0.3 wt% Ru and nominal 0.6 wt% Ru after ball-on-disc sliding wear at 10N, showing wide wear tracks and damage with debris on the surface.





**Figure 6.56.** SEM-SE micrographs of  $\text{Cr}_2\text{O}_3$  coatings after ball-on-disc sliding wear at 5N and 10N, showing wide wear tracks and damage with debris in pits.



**Figure 6.57.** SEM-SE micrographs of mild steel substrates after ball-on-disc sliding wear at 5N and 10N, showing wide wear tracks and damage with debris in pits.

**Table 6.15.** EDX analysis of the ULTIMET coatings without Ru of Figures 6.52 and 6.53 after ball-on-disc sliding wear at 5N and 10N.

Element (wt%)	Wear track		Oxide
	5N	10N	10N
C	0.7 ± 0.4	1.1 ± 0.2	1.7 ± 0.3
O	1.6 ± 1.2	5.5 ± 0.1	13.9 ± 1.0
Si	0.2 ± 0.1	0.2 ± 0.0	0.2 ± 0.0
Fe	-	-	0.5 ± 0.2
Cr	25.2 ± 1.4	26.4 ± 1.0	25.0 ± 0.3
Mn	2.3 ± 1.0	-	-
Co	50.4 ± 1.0	47.9 ± 1.0	41.3 ± 1.0
Ni	13.4 ± 0.3	12.7 ± 0.1	11.1 ± 0.3
Mo	4.1 ± 0.2	4.3 ± 0.2	3.8 ± 0.1
W	2.0 ± 0.1	1.9 ± 0.1	1.7 ± 0.2

**Table 6.16.** EDX analysis of the ULTIMET coatings with nominal 0.3 wt% Ru of Figures 6.52 and 6.53 after ball-on-disc sliding wear at 5N and 10N.

Element (wt%)	Wear track	
	5N	10N
C	0.6 ± 0.1	0.5 ± 0.2
O	1.4 ± 1.0	3.8 ± 0.3
Si	0.2 ± 0.0	0.2 ± 0.1
Cr	24.7 ± 1.0	26.5 ± 1.0
Mn	3.1 ± 1.0	2.2 ± 1.0
Co	50.7 ± 1.0	49.5 ± 1.4
Ni	13.1 ± 1.0	12.8 ± 1.0
Mo	4.1 ± 1.0	3.7 ± 1.0
Ru	0.3 ± 0.1	0.2 ± 0.1
W	1.8 ± 0.1	1.8 ± 0.2

**Table 6.17.** EDX analysis of the ULTIMET coatings with nominal 0.6 wt% Ru of Figures 6.52 and 6.53 after ball-on-disc sliding wear at 5N and 10N.

Element (wt%)	Wear track		Oxide	
	5N	10N	5N	10N
C	2.2 ± 1.0	1.6 ± 0.4	6.8 ± 2.4	4.3 ± 0.3
O	1.5 ± 1.0	3.9 ± 2.2	9.2 ± 2.2	15.3 ± 1.0
Si	0.2 ± 0.0	0.2 ± 0.1	0.3 ± 0.0	0.3 ± 0.0
Cr	25.8 ± 1.0	26.0 ± 1.0	24.6 ± 0.2	26.7 ± 0.2
Mn	1.2 ± 0.1	1.0 ± 0.4	1.3 ± 1.2	-
Co	49.2 ± 1.0	48.4 ± 2.0	41.3 ± 3.0	38.2 ± 1.0
Ni	13.1 ± 1.0	12.9 ± 0.3	11.0 ± 1.0	10.3 ± 0.3
Mo	4.3 ± 0.2	4.1 ± 0.2	3.8 ± 0.2	3.4 ± 0.2
Ru	0.4 ± 0.1	-	-	-
W	1.9 ± 0.1	1.8 ± 0.3	1.5 ± 0.2	1.5 ± 0.2

**Table 6.18.** EDX analysis of the Stellite 6 coatings with no Ru (Figures 6.54 and 6.55) after ball-on-disc sliding wear at 5N and 10N.

Element (wt%)	Wear track		Oxide	
	5N	10N	5N	10N
C	3.4 ± 0.3	3.7 ± 1.0	3.0 ± 1.0	4.1 ± 1.0
O	11.3 ± 2.0	13.6 ± 1.3	23.3 ± 2.0	21.7 ± 6.0
Si	0.7 ± 0.0	0.6 ± 0.0	0.5 ± 0.0	0.6 ± 0.2
Cr	29.1 ± 1.0	27.8 ± 1.0	27.0 ± 1.0	26.0 ± 2.0
Fe	3.0 ± 2.0	3.4 ± 0.3	7.4 ± 1.0	9.7 ± 4.0
Co	46.5 ± 2.3	44.3 ± 1.0	32.8 ± 2.0	32.9 ± 8.0
Ni	3.3 ± 1.0	3.3 ± 0.4	3.2 ± 0.0	2.8 ± 1.0
Mo	0.2 ± 0.0	-	0.4 ± 0.0	-
W	3.3 ± 0.1	3.1 ± 0.2	2.5 ± 0.0	2.3 ± 1.0

**Table 6.19.** EDX analysis of the Stellite 6 coatings with nominal 0.3 wt% Ru (Figures 6.54 and 6.55) after ball-on-disc sliding wear at 5N and 10N.

Element (wt%)	Wear track		Oxide	
	5N	10N	5N	10N
C	3.8 ± 1.0	2.1 ± 0.0	2.0 ± 1.0	2.4 ± 0.0
O	11.9 ± 2.0	13.5 ± 1.0	22.0 ± 2.0	20.5 ± 6.0
Si	0.7 ± 0.0	0.7 ± 0.0	0.5 ± 0.0	0.6 ± 0.0
Cr	28.0 ± 1.0	28.2 ± 1.0	26.8 ± 2.0	25.9 ± 2.0
Fe	3.5 ± 2.0	2.4 ± 1.0	12.1 ± 2.0	8.6 ± 5.0
Co	45.9 ± 3.0	46.4 ± 1.0	31.9 ± 4.0	36.4 ± 9.0
Ni	3.1 ± 0.0	3.2 ± 0.0	2.6 ± 0.0	2.9 ± 0.0
Mo	-	0.4 ± 0.0	-	-
W	3.1 ± 0.0	3.2 ± 0.0	2.1 ± 0.0	2.8 ± 1.0

**Table 6.20.** EDX analysis of the Stellite 6 coatings with nominal 0.6 wt% Ru (Figures 6.54 and 6.55) after ball-on-disc sliding wear at 5N and 10N.

Element (wt%)	Wear track		Oxide	
	5N	10N	5N	10N
C	5.7 ± 1.0	3.1 ± 0.0	8.1 ± 4.0	2.7 ± 1.0
O	13.5 ± 1.0	15.2 ± 2.0	16.6 ± 2.0	18.4 ± 4.0
Si	0.6 ± 0.0	0.6 ± 0.0	0.5 ± 0.0	0.5 ± 0.0
Cr	26.2 ± 1.0	26.3 ± 0.0	25.1 ± 2.0	24.7 ± 1.0
Fe	4.6 ± 1.0	3.7 ± 2.0	8.1 ± 1.0	12.6 ± 5.0
Co	43.4 ± 1.0	45.1 ± 2.0	35.6 ± 3.0	35.8 ± 8.0
Ni	3.0 ± 0.0	3.0 ± 0.0	3.1 ± 0.0	3.0 ± 1.0
W	3.0 ± 0.0	3.0 ± 0.0	2.8 ± 0.0	2.4 ± 1.0

**Table 6.21.** EDX analysis of the Cr<sub>2</sub>O<sub>3</sub> coatings (Figure 6.56) after ball-on-disc sliding wear at 5N and 10N.

Element (wt%)	Wear track		Oxide	
	5N	10N	5N	10N
C	2.4 ± 0.0	2.8 ± 1.0	2.3 ± 0.0	2.6 ± 1.0
O	25.0 ± 2.0	23.5 ± 1.0	23.4 ± 1.0	26.4 ± 4.0
Cr	33.9 ± 3.0	22.9 ± 3.0	26.1 ± 3.0	39.9 ± 17.0
Fe	38.8 ± 5.0	50.8 ± 1.0	48.2 ± 3.0	31.0 ± 2.0

**Table 6.22.** EDX analysis of mild steel substrates (Figure 6.57) after ball-on-disc sliding wear at 5N and 10N.

Element (wt%)	Wear track		Oxide	
	5N	10N	5N	10N
C	3.3 ± 0.0	2.7 ± 0.0	3.5 ± 2.0	2.5 ± 1.0
O	11.9 ± 1.0	18.1 ± 2.0	16.8 ± 9.0	15.8 ± 13.0
Si	0.3 ± 0.0	0.2 ± 0.0	0.3 ± 0.0	0.3 ± 0.0
Fe	84.5 ± 1.0	79.0 ± 2.0	79.4 ± 10.0	81.4 ± 14.0

## 6.6 Tribocorrosion results in synthetic mine water

### 6.6.1 Tribocorrosion open circuit potential results

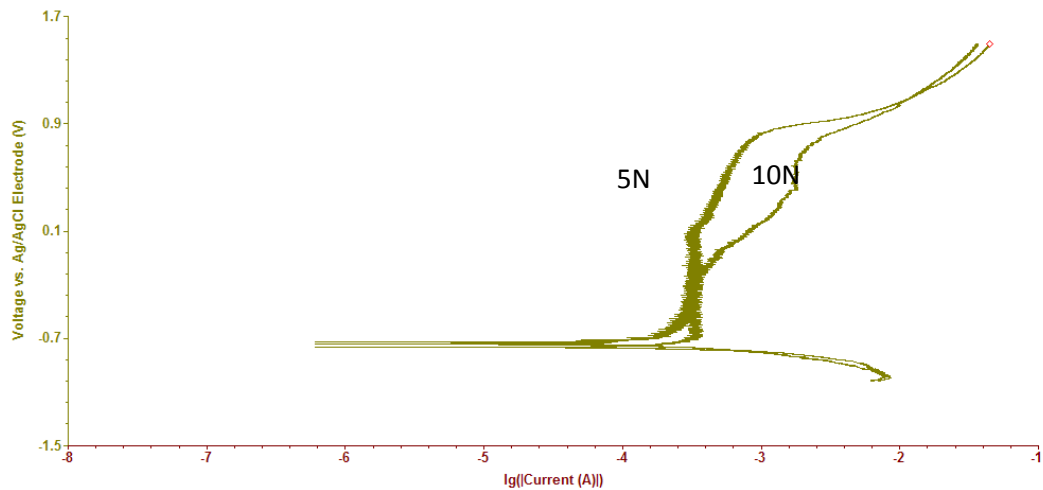
The open circuit potential measurements were not obtained due to malfunctioning of the tribometer. However, the absence of these measurements did not affect the overall results and conclusions.

### 6.6.2 Tribocorrosion potentiodynamic polarisation curves

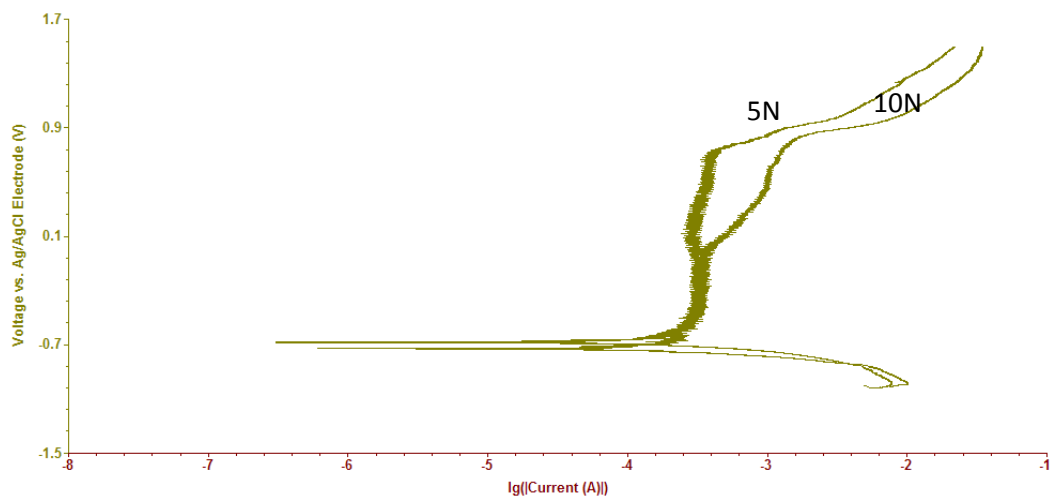
Figures 6.58 and 6.59 show the tribocorrosion potentiodynamic polarisation curves obtained for ULTIMET coatings with no Ru (Figure 6.58) and nominal 0.6 wt% Ru (Figure 6.59) in synthetic mine water under tribocorrosion conditions, and the results are summarised in Table 6.23. The samples demonstrated almost similar tribocorrosion polarisation behaviours at both loads. Both samples experienced a spontaneous and extended passivation from -700 to 100 mV, and then pitting.

With increased load, tribocorrosion rates increased for all the samples. Tribocorrosion rates decreased with increased ruthenium content. The nominal 0.6 wt% Ru ULTIMET coating at 5N exhibited better tribocorrosion resistance than at 10N.





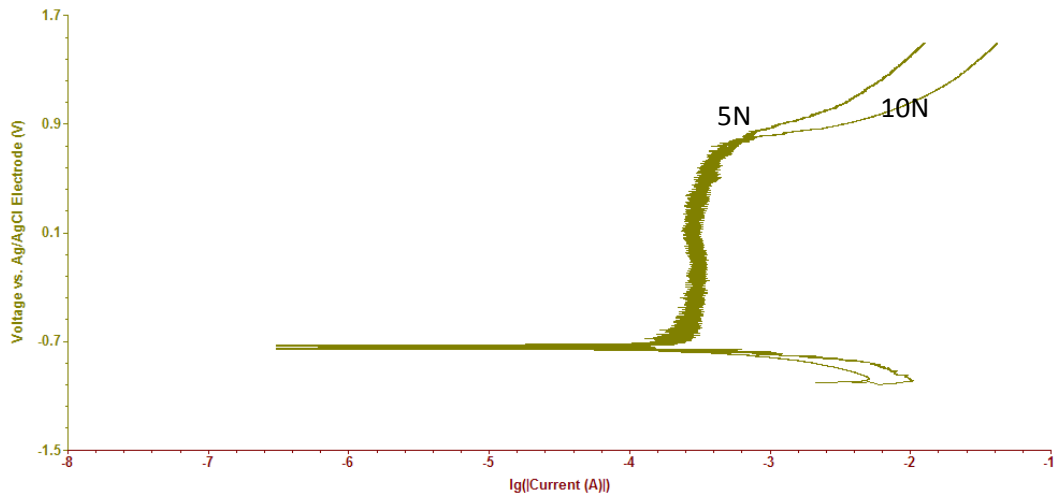
**Figure 6.58.** Tribocorrosion potentiodynamic polarisation curves of ULTIMET coatings without Ru in synthetic mine water under loads of 5N and 10N.



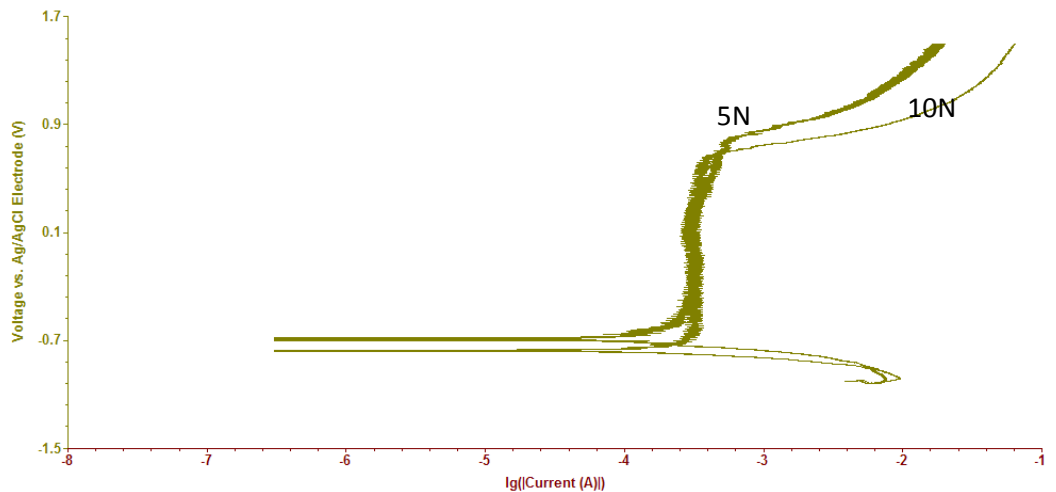
**Figure 6.59.** Tribocorrosion potentiodynamic polarisation curves of ULTIMET coatings with nominal 0.6 wt% Ru in synthetic mine water under loads of 5N and 10N at ambient temperature.

Figures 6.60 and 6.61 show the tribocorrosion potentiodynamic polarisation curves obtained for Stellite 6 coatings with no Ru (Figure 6.60) and nominal 0.6 wt% Ru (Figure 6.61) in synthetic mine water under tribocorrosion conditions. The samples demonstrated similar polarisation behaviour at both loads. Both samples experienced a spontaneous and extended passivation from -700 to 740 mV, and had similar pitting potentials and currents.

Similar to ULTIMET samples, the nominal 0.6 wt% Ru Stellite 6 exhibited better tribocorrosion resistance at 5N than at 10N. However, their corrosion rates were slightly different (Table 6.23). With Ru additions, the tribocorrosion rates decreased at all loads, and increased when the load was increased.



**Figure 6.60.** Tribocorrosion potentiodynamic polarisation curves of Stellite 6 coatings without Ru in synthetic mine water under loads of 5N and 10N at ambient temperature.

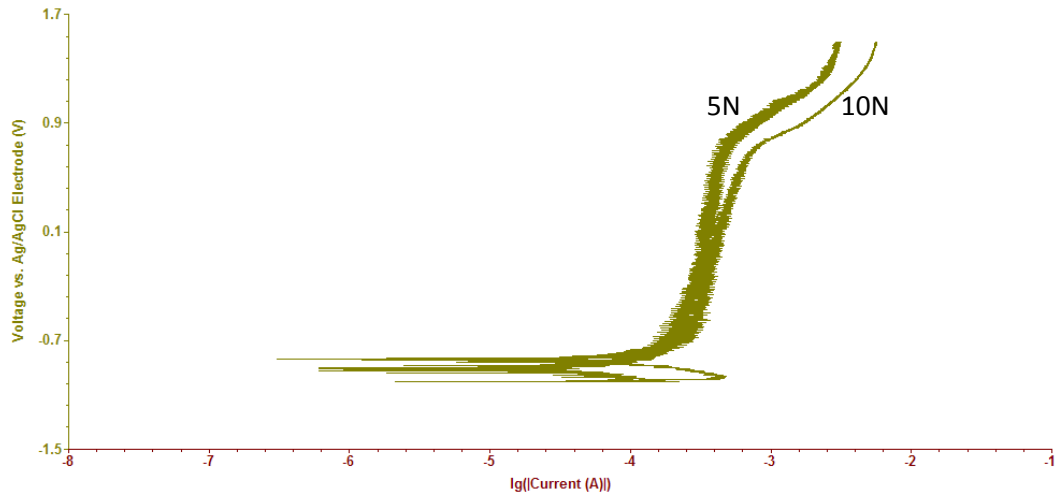


**Figure 6.61.** Tribocorrosion potentiodynamic polarisation curves of Stellite 6 coatings with nominal 0.6 wt% Ru in synthetic mine water under loads of 5N and 10N at ambient temperature.

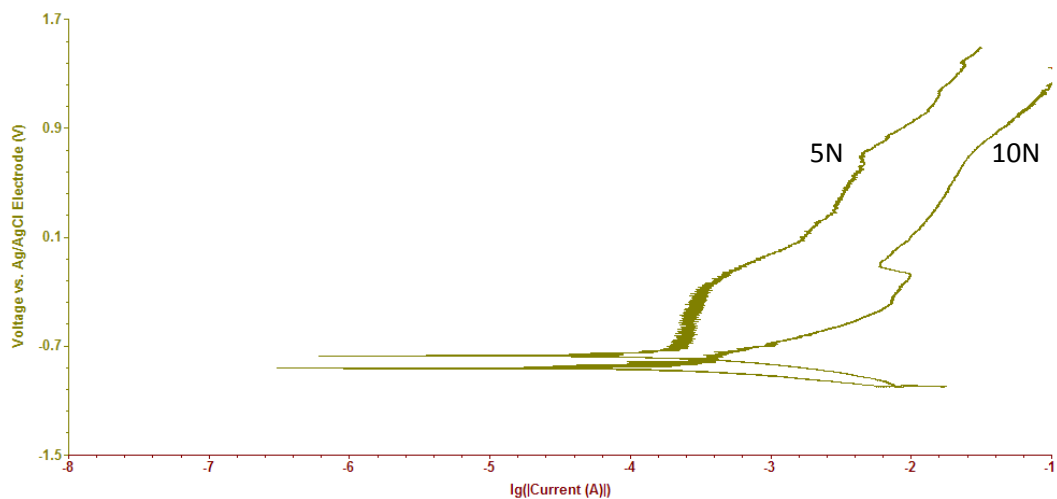
Figure 6.62 shows the tribocorrosion potentiodynamic polarisation curves obtained for  $\text{Cr}_2\text{O}_3$  coatings on mild steel in synthetic mine water under tribocorrosion conditions, and Table 6.23 summarises the results. The samples had similar polarisation behaviour at both loads. Both samples experienced non-spontaneous and extended passivation from -700 to 100 mV, and had similar transpassive potentials and different passive current densities.  $\text{Cr}_2\text{O}_3$  exhibited better tribocorrosion resistance at 5N. With increased load, the tribocorrosion rate increased.

Figure 6.63 shows the tribocorrosion potentiodynamic polarisation curves obtained for mild steel substrates in synthetic mine water under tribocorrosion conditions and the

results are summarised in Table 6.23. The samples had dissimilar polarisation behaviour at both loads. There was spontaneous and extended passivation from -700 to -220 mV, and then pitting potential at 5N, while at 10N, the sample had a slight pseudo-passivation behaviour between -380 and -220 mV, and then pitting. The mild steel substrate showed a better tribocorrosion resistance at 5N. With increased load, the wear rate increased.



**Figure 6.62.** Tribocorrosion potentiodynamic polarisation curves of  $\text{Cr}_2\text{O}_3$  coatings on mild steel in synthetic mine water under loads of 5N and 10N at ambient temperature.



**Figure 6.63.** Tribocorrosion potentiodynamic polarisation curves of mild steel substrates in synthetic mine water under loads of 5N and 10N at ambient temperature.

**Table 6.23.** Tribocorrosion potentiodynamic polarisation results of ULTIMET and Stellite 6 coatings with no Ru and nominal 0.6 wt% Ru, Cr<sub>2</sub>O<sub>3</sub> coatings and steel substrates under loads of 5N and 10N in synthetic mine water.

Sample		Load (N)	E <sub>corr</sub> (mV)	i <sub>corr</sub> (μA. cm <sup>-2</sup> )	CR (mm.y <sup>-1</sup> )
ULTIMET	No Ru	5	-700	56.60	0.60
Stellite 6			-750	52.00	0.50
Cr <sub>2</sub> O <sub>3</sub>			-900	26.90	0.40
Mild steel			-800	63.70	0.70
ULTIMET	No Ru	10	-800	77.50	0.80
Stellite 6			-700	68.40	0.60
Cr <sub>2</sub> O <sub>3</sub>			-900	59.10	0.90
Mild steel			-700	86.10	1.00
ULTIMET	Nominal 0.6 wt% Ru	5	-700	46.70	0.50
Stellite 6			-700	43.10	0.40
ULTIMET		10	-700	67.90	0.70
Stellite 6			-770	55.10	0.50

From the tribocorrosion results (Table 6.23), Cr<sub>2</sub>O<sub>3</sub> coatings had the lowest tribocorrosion rate at 5N compared to ULTIMET and Stellite 6 coatings and mild steel substrates. At 10 N, Stellite 6 had the lowest tribocorrosion rate. For coatings with nominal 0.6 wt% Ru, Stellite 6 coatings had the lowest tribocorrosion rates than ULTIMET coatings at both 5N and 10N loads, making Stellite 6 with nominal 0.6 wt% Ru the best coating for tribocorrosion resistance.

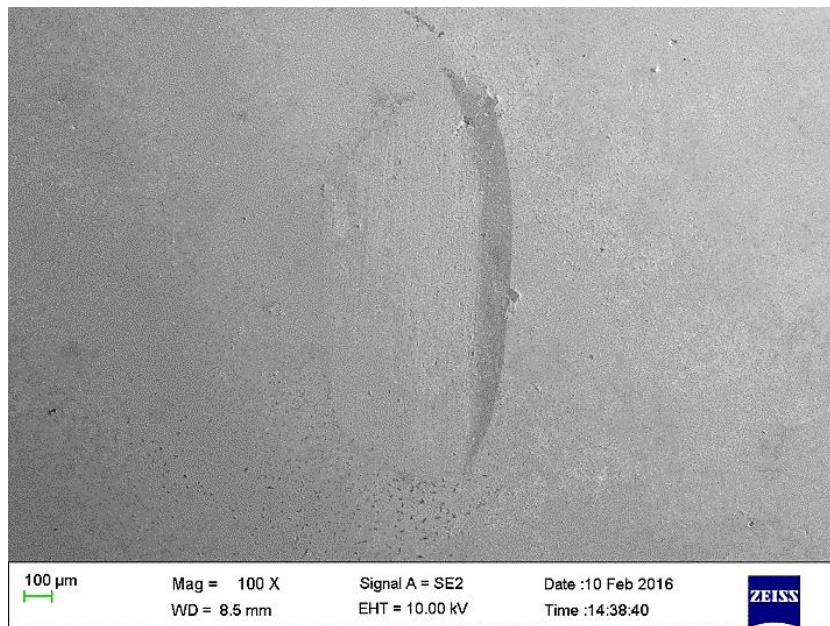
### 6.6.3 SEM-EDX results after tribocorrosion potentiodynamic polarisation

Figure 6.64 shows an example of a scar after reciprocating ball-on-disc tribocorrosion on a sample after at 5N and 10N. Figures 6.65-67 show morphologies of ULTIMET and Stellite 6 coatings with no Ru and nominal 0.6 wt% Ru, Cr<sub>2</sub>O<sub>3</sub> coatings and mild steel substrates after reciprocating zirconia oxide (ZrO<sub>2</sub>) balls sliding against these samples, as a function of sliding distance at 5N and 10N. The wear in all samples was predominantly abrasive wear, characterised by grooves, cracks, and severe spalling at both loads.

The micrographs of the ULTIMET (Figure 6.65) coatings showed fairly rough wear scars, smooth grooves, cracks and spalling at both loads, which was also experienced in Stellite 6 coatings (Figure 6.66). Debris was observed in the wear scars, and was more for Stellite 6 coatings. The wear tracks for the Cr<sub>2</sub>O<sub>3</sub> coatings (Figure 6.67) showed pits and with debris, and the mild steel substrates (Figure 6.67) showed severe damage, covered in debris all over the wear tracks.

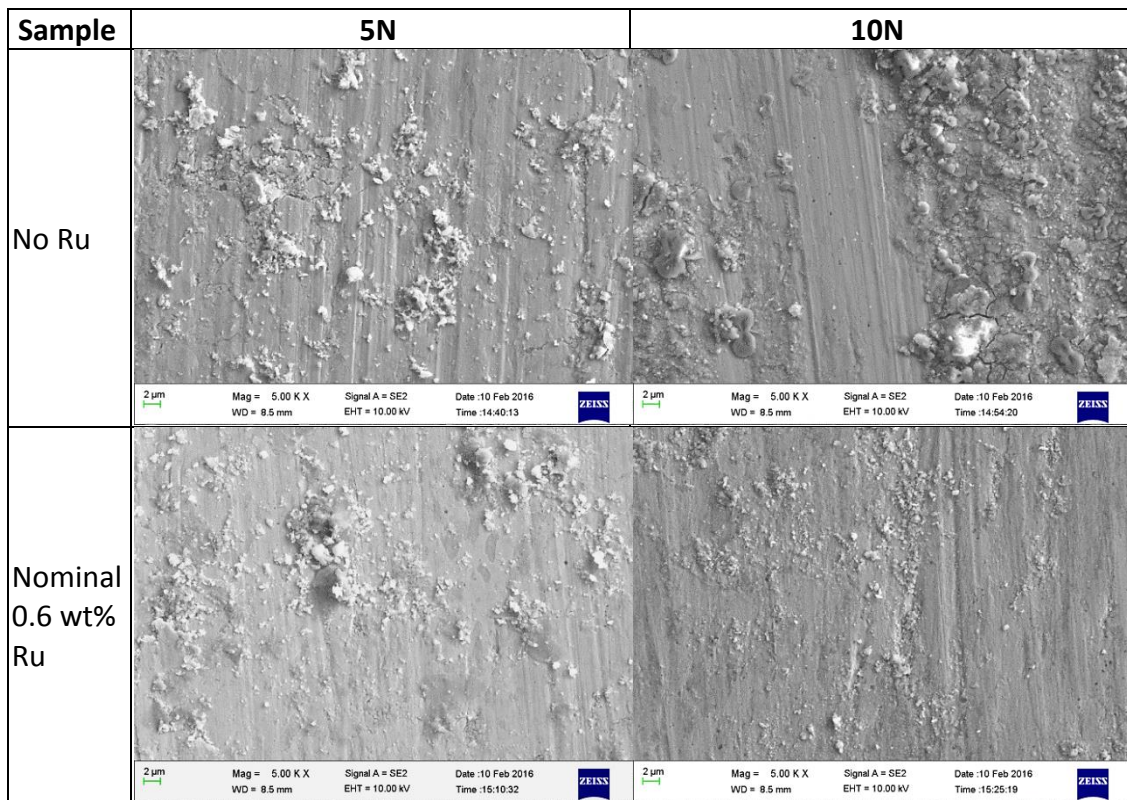
Tables 6.24-6.27 show the EDX results of the wear scar of the ULTIMET and Stellite 6 coatings with no Ru and nominal 0.6 wt% Ru, Cr<sub>2</sub>O<sub>3</sub> coatings and mild steel substrates after reciprocating ball-on-disc at 5N and 10N in synthetic mine water at room temperature.

ULTIMET coatings (Table 6.24) had Co, Cr, Ni as the major constituents, with minor amounts of Mn, Mo, W, O, C, Si, Cl and Ca, and Na and Fe were only detected at 10N. Stellite 6 (Table 6.25) had Co and Cr as major elements, with minor amounts of Ni, W, Mn, O, Cl, Si and C, and Mo detected at 10N only. The amounts decreased with increased loads, apart from C, O and Cl which increased with increased load. Major elements detected in the Cr<sub>2</sub>O<sub>3</sub> coatings (Table 6.26) were Cr and O (as expected), and Mg, S, and Cl were detected in minor amounts, and Ca was only detected at 5N. For the mild steel substrates (Table 6.27), Fe, O and C were the major elements on the wear scar, with Si and S in minor amounts, and Cl detected at 10N only. Elements such as Na, Ca, Mg, S and Cl were exogenous tribocorrosion products from the solution.

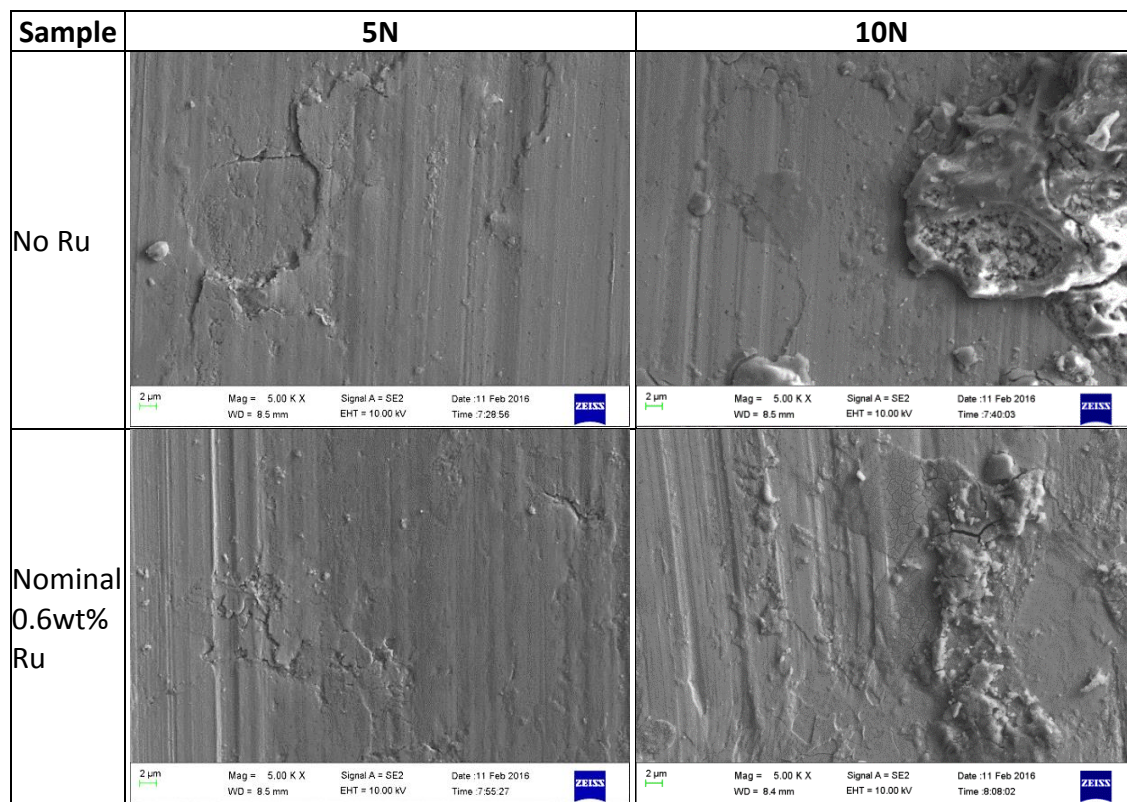


**Figure 6.64.** Example of tribocorrosion scar on a sample after reciprocating ball-on-disc at 5N or 10N.

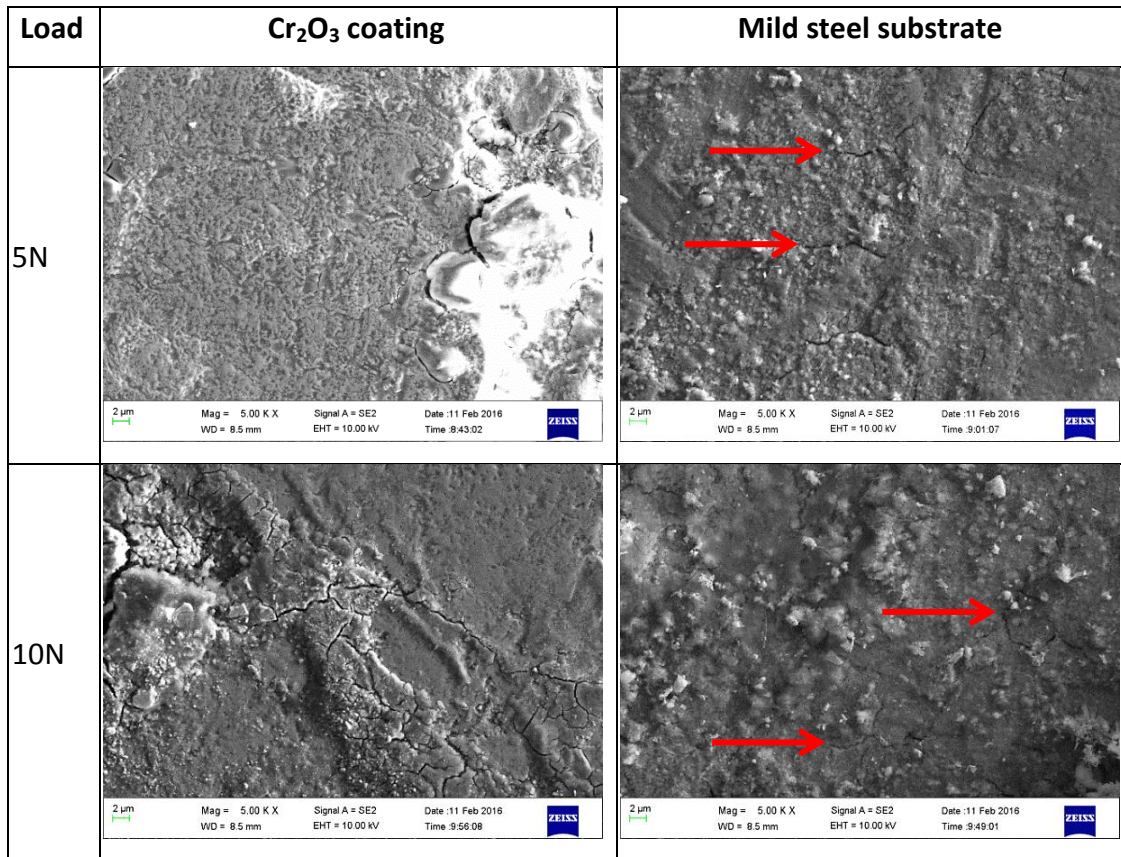




**Figure 6.65.** SEM-SE micrographs of ULTIMET coatings with no Ru and nominal 0.6 wt% Ru after reciprocating ball-on-disc at 5N and 10N, showing damage on wear tracks and debris in furrows.



**Figure 6.66.** SEM-SE micrographs of Stellite 6 coatings (no Ru and nominal 0.6 wt% Ru) after reciprocating ball-on-disc at 5N and 10N:-wear track damage and debris in furrows.



**Figure 6.67.** SEM-SE micrographs of Cr<sub>2</sub>O<sub>3</sub> coatings and mild steel substrate after reciprocating ball-on-disc at 5N and 10N, showing wear track damage, debris and cracks (arrows).

**Table 6.24.** EDX analysis of ULTIMET coatings with no Ru and nominal 0.6 wt% Ru of Figure 6.65 after reciprocating ball-on-disc at 5N and 10N in synthetic mine water at room temperature.

Element (wt%)	No Ru		Nominal 0.6 wt% Ru	
	5N	10N	5N	10N
C	1.7 ± 0.3	5.1 ± 3.9	3.1 ± 1.0	3.2 ± 0.4
O	6.5 ± 1.0	12.1 ± 4.2	5.4 ± 2.0	9.1 ± 2.0
Na	-	0.3 ± 0.1	0.3 ± 0.1	-
Si	0.2 ± 0.0	0.2 ± 0.1	0.3 ± 0.1	0.2 ± 0.0
S	1.2 ± 0.4	1.1 ± 0.1	0.9 ± 0.4	0.5 ± 0.1
Cl	0.4 ± 0.0	0.6 ± 0.4	0.4 ± 0.1	1.0 ± 0.3
Ca	-	0.7 ± 0.4	0.4 ± 0.2	0.4 ± 0.2
Cr	27.5 ± 0.2	26.4 ± 1.4	25.9 ± 1.1	24.8 ± 1.0
Fe	-	9.4 ± 3.1	0.7 ± 0.0	-
Co	45.0 ± 1.0	31.9 ± 14.2	45.4 ± 2.1	42.4 ± 1.4
Ni	12.3 ± 1.0	6.6 ± 2.0	11.8 ± 1.0	12.0 ± 0.3
Mo	3.3 ± 1.3	3.9 ± 0.4	3.5 ± 0.4	4.8 ± 1.0
W	2.1 ± 0.2	1.8 ± 0.3	1.8 ± 0.1	1.8 ± 0.2



**Table 6.25.** EDX analysis of Stellite 6 coatings with no Ru and nominal 0.6 wt% Ru of Figure 6.66 after reciprocating ball-on-disc at 5N and 10N in synthetic mine water at room temperature.

Element (wt%)	No Ru		Nominal 0.6 wt% Ru	
	5N	10N	5N	10N
C	2.0 ± 0.3	2.8 ± 1.0	1.7 ± 0.5	2.8 ± 1.0
O	3.2 ± 1.3	8.3 ± 4.2	4.2 ± 1.2	10.1 ± 5.9
Si	0.6 ± 0.1	0.6 ± 0.2	0.7 ± 0.1	0.6 ± 0.1
Cl	0.3 ± 0.0	3.7 ± 1.0	0.2 ± 0.0	2.3 ± 0.4
Cr	28.4 ± 1.1	25.1 ± 6.0	28.6 ± 1.0	26.6 ± 2.0
Mn	4.6 ± 0.4	3.8 ± 0.8	3.9 ± 1.0	2.7 ± 0.3
Co	53.5 ± 2.0	49.2 ± 6.4	52.8 ± 1.2	47.9 ± 10.0
Ni	4.0 ± 1.0	3.8 ± 0.4	3.3 ± 0.3	3.6 ± 1.0
Mo	-	-	0.8 ± 0.2	0.6 ± 0.2
W	3.5 ± 0.4	2.8 ± 1.0	4.0 ± 0.4	3.0 ± 1.0

**Table 6.26.** EDX analysis of Cr<sub>2</sub>O<sub>3</sub> coatings of Figure 6.67 after reciprocating ball-on-disc at 5N and 10N in synthetic mine water at room temperature.

Element (wt%)	5N	10N
O	35.6 ± 2.2	37.8 ± 1.4
Mg	1.1 ± 0.5	0.2 ± 0.1
S	1.1 ± 0.6	2.7 ± 1.1
Cl	0.3 ± 0.1	0.3 ± 0.1
Ca	-	0.3 ± 0.1
Cr	63.0 ± 3.0	58.6 ± 3.0

**Table 6.27.** EDX analysis of mild steel substrates of Figure 6.67 after reciprocating ball-on-disc at 5N and 10N in synthetic mine water at room temperature.

Element (wt%)	5N	10N
C	11.3 ± 2.2	4.7 ± 3.0
O	27.9 ± 3.0	30.9 ± 3.0
Si	0.4 ± 0.1	1.8 ± 1.0
S	0.8 ± 0.2	1.3 ± 0.4
Cl	-	0.7 ± 0.3
Fe	59.6 ± 2.0	60.7 ± 3.0

## **6.7 Tribocorrosion potentiodynamic polarisation curves in acid mine water from Otjihase Mine**

The tribocorrosion potentiodynamic polarisation curves were not obtained due to malfunctioning of the tribometer. However, the absence of these measurements did not affect the overall results and conclusions.

## **6.8 Summary**

Stellite 6 had the highest particle size ( $D_{50}$ ), then NiCrAlY and ULTIMET.  $Cr_2O_3$  and Ru had the highest particle size than Stellite 6, and wider size distributions.

ULTIMET, Stellite 6 and NiCrAlY powders were spherical particles, with dendrites being visible, while the  $Cr_2O_3$  powder had angular particles with smooth facets. Ruthenium powder had agglomerated particles, sometimes in plate form.

The highest hardness was for Stellite 6 with nominal 0.6 wt% Ru. The  $Cr_2O_3$  coating had the highest hardness, while mild steel substrate had the lowest.

The best Stellite 6 coating had nominal 0.6 wt% Ru, and exhibited lower corrosion rates at pH 6 and 3 than the ULTIMET coating.

For coatings with nominal 0.6 wt% Ru, Stellite 6 coatings had the lowest tribocorrosion rates than ULTIMET coatings at both 5N and 10N loads, making nominal 0.6 wt% Ru Stellite 6 the best coating for tribocorrosion resistance.

# CHAPTER 7: DISCUSSION: COMPARISON OF THE PROPERTIES OF THE SUBSTITUTE ALLOYS AND THE CURRENT MATERIALS

---

## 7.1 Introduction

This chapter discusses the results obtained from the experiments used to evaluate the corrosion, wear and tribocorrosion behaviour of the materials currently used, the selected substitute alloys, as bulk or as coatings and the chromium oxide bench mark coating in the synthetic mine water. The mine environment needs good corrosion resistance and good wear resistance, thus corrosion and wear had been studied, together with hardness and microstructure. These properties were used to explain the performance of all of the materials studied.

## 7.2 Corrosion at the Otjihase Underground Mine

The most affected pump component at Otjihase Mine was a shaft sleeve, a rotating part of the pump stuffing box, which transfers energy from an electric motor to the pump's impeller. When the pump operates, the shaft sleeve often experiences corrosion from slurry and wear from debris trapped in the packing gland, which further accelerates corrosion.<sup>146</sup> The sleeve fits into the stuffing box with packing glands, where the latter provides a seal against leakage where the shaft passes through the casing. There is friction between the shaft sleeve and the packing glands, causing the former to heat up and the debris in packing gland to scratch the shaft sleeves, resulting in cutting grooves on the shaft sleeves, and leakage from the pump.<sup>149, 150</sup>

The pumps also operate in a chloride- and sulphate-containing mine water. The presence of the chlorine and sulphate ions in the mine water were suspected to be mainly responsible for a low pH as these would likely to form hydrochloric and sulphuric acid, making the mine water to be acidic with high conductivity and salinity.<sup>69</sup> The high content of TDS could also make the mine water more aggressive. As a result, the pump components from the Otjihase Underground Mine could not cope with the synergetic action during operation, especially at the Conveyor 6 pump, which showed high corrosion rates.

The corrosion characteristics of the Otjihase Mine pump components were evaluated in synthetic mine water, and experienced general corrosion, with fine pits as seen using the

SEM (Figures 4.17-4.19). The pump components in the actual Otjihase Mine water (Figures 4.4 b), 4.7 and 4.8) also experienced general and pitting corrosion, and wear, agreeing with the study done by Ash *et al.*<sup>73</sup> The pits and abrasive attack on the pump components would later cause failure of shaft, and result in leakages, flooding on the mine and unacceptably frequent maintenance down-time and replacement of parts.

### 7.3 Approaches for reducing corrosion and wear in mines

Lalvani<sup>69</sup> described four approaches to mitigate the problems of corrosion and wear in mines:

- Changing the construction materials
- Cathodic protection
- Redesign of processes and equipment and
- Dechlorination of coal (not relevant for the Otjihase Mine, which is a copper mine, so this is not discussed further).

Changing the construction materials approach involves materials selection to improve corrosion and wear in the mine. This was the approach that was selected as the method to solve corrosion and wear problems at the Otjihase Underground Mine. Since the current materials: Ni-Cr-Fe coatings on mild steel substrates, and cast iron were obviously not lasting long enough (in some cases, the pumps lasted less than six weeks),<sup>151</sup> better materials have to be found. This led to the identification of: ULTIMET, Stellite 6B, ToughMet 3 and Hastelloy G30 alloys as possible candidates to substitute for the current materials corrosion and wear testing, as well characterisation of their microstructures. Since coatings are also used in the mine, the best potential substitute materials were tested as coatings as well. Some of the potential substitute materials did not perform as well as the others, so these were not tested further. In addition, Cr<sub>2</sub>O<sub>3</sub> was used as a bench mark in the evaluation of the coatings, since it is used as a coating in industry.<sup>62, 64, 65, 67</sup> This is discussed later, and was the major part of the thesis.

Other methods for protection of the pump components against corrosion and wear at the mine could include laser cladding.<sup>68</sup> The hot dip galvanising method used at Phalaborwa Copper mine<sup>80</sup> in South Africa, as well as chemical and physical vapour deposition (CVP/PVD) on steels as studied by Díaz *et al.*<sup>81</sup> is unlikely to be suitable for protection pump components at the Otjihase Underground Mine, because these coatings are usually thin and with low hardness (apart from PVD) compared to other coating methods, *e.g.* thermal spray.

Cathodic protection is unlikely to be a solution to the corrosion in the pumps, because the anodes used could cause obstruction in the pump cavities, and decrease the efficiency of the pumps. Anode materials are usually softer, and so these would be vulnerable to wear in the mine, and will not last long. Considering Lalvani's<sup>69</sup> approach, two of the four options were not suitable, and one did not apply. It is against this background to select materials that can effectively work in the Otjihase Mine.

Redesigning of the processes and equipment could solve corrosion and wear problems at the mine, but need major inputs from the mine, and is beyond the scope of this work. Any new design would probably need to be done with the help of the Otjihase Mine personnel. Any redesign would have to take into account the fact that the pumps run continuously (at least until they break down), as well as the synergistic effect of the corrosive mine water and the friction between particles and the shaft and the sleeve of the pumps.

#### **7.4 Mine environment**

Mine water containing  $\text{SO}_4^-$ ,  $\text{Na}^+$ ,  $\text{Ca}^+$ ,  $\text{Mg}^{2+}$  and  $\text{Cl}^-$  ions with different pH values is often corrosive.<sup>70</sup> The Otjihase Underground Mine water contains these species, and  $\text{Cu}^{2+}$ ,  $\text{NO}_3^-$  and pH values varying from acidic (mainly) to mildly alkaline (only occasionally) (Figures 4.13-4.15), which varies seasonally, as well as a low resistivity and high total dissolved solids (TDS). The atmosphere contains nitrogen, oxygen, water vapour, chlorine, and other gases, but these were not measured due to lack of equipment at the mine. The presence of these components, as well as chloride and sulphate concentrations could lower the pH of the mine water, making it more aggressive to the pump components in the Otjihase Underground Mine.

The effect of water compositions on pump components from nine sumps of four anthracite mines water sumps in Pennsylvania, USA, was studied by Ash *et al.*<sup>73</sup>. The mine water from the sumps was almost similar (Table 2.2) to the water from the Otjihase Underground Mine water sumps (Table 4.6), but with much lower sulphate, higher total dissolved solids, and the chlorides were almost half that at the Otjihase Underground Mine. Ash *et al.*<sup>73</sup> reported that stainless steel bowls and impellers, pump shaft and sleeves, wearing rings and some pipes were corroded in water sumps with pH ranges from 2.7 to 7.7, while pump components corroded in the mine water with the pH values of 3.8 to 7.8, which could change seasonally.

The 1020 steel and 304 stainless steel consisted of 5 wt% Cr specimens tested for 19 days in the anthracite mine water sumps dissolved completely (Table 2.4), indicating that 11 to

12 % Cr was necessary to provide adequate resistance to corrosion.<sup>73</sup> The corrosion rate of the 1020 steel was  $4.47 \text{ mm.y}^{-1}$  and for the 304 stainless steel specimens was  $2.06 \text{ mm.y}^{-1}$ , determined using immersion method. These rates were higher than the rates of the materials used in the Otjihase Mine (Table 4.6), except for cast iron at low pH, which was  $2.8 \text{ mm.y}^{-1}$ . The higher concentrations of chlorides and sulphates would cause the water sumps at the Otjihase Underground Mine to be more aggressive than the anthracite mines water sumps in Pennsylvania, so the 1020 steel and 304 stainless steel would not be suitable for the environment.

## **7.5. Microstructures**

### **7.5.1 Analytical techniques**

One of the problems with this work was that accurate measurements for the compositions of the alloys and coatings were needed to derive the effect of various elements on the corrosion resistance. However, the accurate measurements for Ru, C and O could not be obtained by EDX analysis although this was the technique used to provide an appropriate value. The Ru content was not accurately measured, because the additions were below the accurate detection limit of the EDX, and C was always difficult because it is a light element, and the samples are always susceptible to carbon contamination. Oxygen contamination is also a problem. Thus, analyses should preferably be done with other techniques than SEM-EDX, using techniques like inductively plasma optical emission spectrometry (ICP-OES) or electron probe micro-analyser (EPMA) with wavelength-dispersive spectrometry (WDS), to accurately measure C, Ru and O contents.

### **7.5.2 Bulk samples**

All the bulk samples were polycrystalline, with two of them having carbides, and two were single phase. These alloys would have their own inherent properties, which are also affected by the grain sizes and the distribution of any carbides (Tables 5.5 and 7.1). The samples were not heat treated to optimise the microstructures, and some heat treatment could have been done, which could have improved the properties. Heat treatments were not done, because the aim was to identify the best materials, and any optimisation would be for subsequent study.

Decreasing the grain sizes would increase the hardness, but there is always the concern that the increased grain boundary area would decrease the corrosion resistance, since grain boundaries are usually corroded first. A better distribution of the carbides might also have been beneficial, especially for Stellite 6B, which had fairly large carbides on the

grain boundaries and within the grains, and ULTIMET, which had few carbides exclusively on the grains. These microstructures could have been changed by heat treatment, but as selecting of materials was the focus of the study, heat treatment were not done.

### **7.5.3 Coatings**

While it is realised that thermal spraying might not have given an optimum surface and hence not the best results, the technique was used, because it was easily available. Thus, the coatings could be made and compared. For the final coatings and application in mines, a different technique could be used, such as laser cladding.

The dendritic microstructures for both ULTIMET and Stellite 6 powders occurred because the cobalt solid solution solidified first, with the carbides solidifying interdendritically afterwards. The dendritic microstructures were retained in the coating, and also there were individual globular-like regions were in the coating (Figure 6.14 a), which were assumed to be the individual particles which arrived at the substrate surface from thermal spraying. The harder carbide particles improved the hardness. Stellite 6 had more interdendritic carbides than ULTIMET, thus a high hardness.  $\text{Cr}_2\text{O}_3$  had also dendritic structure, and was single phase, with an inherently high hardness.<sup>152</sup>

The Ru did not dissolve fully, since it was frequently observed as discrete particles, rather than being dissolved in the matrix. This has been attributed to the high melting point of Ru ( $\sim 2334^\circ\text{C}$ ),<sup>93</sup> and could also have been due to separation during powder feeding, because ruthenium has a high density. However, the ruthenium did not go into solid solution as well as would have been expected from the Co-Ru phase diagram,<sup>153</sup> and so the bad distribution of Ru is probably mainly due to its high melting point, and possibly its higher density.

### **7.5.4 Comparison of the bulk samples and the coatings**

The microstructures of the ULTIMET and Stellite 6 coatings were much finer than the bulk alloys, as well as being much uniform in distribution. Additionally, the carbides in ULTIMET appeared to have higher proportions than in the bulk alloy. This could have meant the measurements of carbides were problematic since they were on the grain boundaries, and sometimes difficult to discern. The fine structures should have meant that the properties were much better than for the bulk alloys, providing that the coating were thick enough and of sufficient quality. The sizes of the globular particles of the coatings (Table 7.1) were at least twice that of the grains of the bulk alloys, which could have had detrimental properties, even though the microstructures within the globules



were finer. However, the ruthenium distribution was very poor, and probably related to the agglomeration of the ruthenium powders, and would not have been beneficial (Figures 6.5, 6.6 e) and 6.7 e)).

The powder sizes of the ULTIMET and Stellite 6 were larger than the bulk grain sizes. In the coatings, the globule sizes ranged between twice and half the size of the average powder sizes, suggesting that each powder particles might have been melted and transported individually during thermal spraying. This could suggest that the powder should be milled before thermal spraying for more homogeneity. Although ruthenium was not well distributed within the coatings, the size of the ruthenium particles was similar to the middle peak of the powder distribution (Figure 6.5). Thus, it appears that the agglomerations of the ruthenium powders were broken up prior to the actual thermal spraying, or were not fed into the equipment, and the finest particles were possibly lost and were not thermally sprayed. These findings also show that the ruthenium powder should be milled prior to thermal spraying.

**Table 7.1.** Grain sizes and carbide fraction of the bulk alloys, average powder sizes, and globular and ruthenium particle sizes of the coatings.

Sample	Bulk grain size ( $\mu\text{m}$ )	Bulk carbide fraction (%)	Av. powder size – coatings ( $\mu\text{m}$ )	Globular size in coatings ( $\mu\text{m}$ )	Ru particle size in coatings ( $\mu\text{m}$ )
ULTIMET	18.7 $\pm$ 6.0	<2	40.1	0 Ru: 98.7 $\pm$ 24.4	-
				0.3 Ru: 79.9 $\pm$ 14.8	71.1 $\pm$ 19.3
				0.6 Ru: 56.5 $\pm$ 8.0	37.8 $\pm$ 5.5
Stellite 6B	20.5 $\pm$ 2.0	16 $\pm$ 15	49.1	0 Ru: 48.1 $\pm$ 9.8	-
				0.3 Ru: 50.8 $\pm$ 10.4	53.0 $\pm$ 13.0
				0.6 Ru: 22.3 $\pm$ 6.0	48.1 $\pm$ 13.0
ToughMet 3	445.4 $\pm$ 78.0	-	-	-	-
Hastelloy G30	139.0 $\pm$ 12.0	<1	-	-	-
Cr <sub>2</sub> O <sub>3</sub>	-	-	31.8	-	-
NiCrALY	-	-	38.2	-	-
Ru	-	-	573.4	-	-

Both ULTIMET and Stellite 6 lost carbon, iron and gained chromium (proportionately), nickel after thermal spraying, with silicon, manganese, molybdenum and tungsten remaining about the same, whereas cobalt varied. This showed that the compositions changed after thermal spraying.

For ULTIMET coatings, the EDX analyses for ruthenium were low and probably inaccurate due to the limitations of the EDX measurements less than 1 wt%, whereas for nominal 0.6 wt% Ru Stellite 6 coatings, the EDX analyses did show an increase of ruthenium to 1.5 wt% Ru. This probably means that the Ru distribution was inhomogeneous within the samples, might also have been affected by the spraying.

## 7.6 Hardness of the bulk samples and the coatings

The alloys tested would have their own inherent hardnesses (Table 5.2), which would also have been affected by the grain sizes and the distribution of any carbides. Any carbides would improve wear resistance, *e.g.* Stellite 6B.

The effect of Ru additions on the hardness of ULTIMET and Stellite 6 coatings was large, and with high scatter (Tables 5.4 and 7.2). This was caused by the poor ruthenium distribution (Figures 6.13 c-f) and 6.14 c-f)), and attributed to inhomogeneous distribution of large Ru particles (corresponding to the powder particle size) during mixing and thermal spraying, leading to the microstructures with unequal distributions of Ru. The ULTIMET coating with nominal 0.3 wt% Ru had the highest hardness compared to nominal 0.6 wt% Ru or the coating without Ru, but was within the error margin of the nominal 0.6 wt% Ru coating. For Stellite 6 coatings, when the Ru content was increased, the hardness also increased, but negligibly.

The hardness of the Stellite 6 coatings was higher than the ULTIMET coating. This was due to the harder chromium-rich interdendritic carbides.<sup>139, 154</sup> The higher W content of Stellite 6 than ULTIMET also contributed to the formation of additional carbides and thus a higher overall hardness.

From the XRD results (Figures 6.16 and 6.17) and micrographs (Figures 5.1 and 5.2), it was evident that Stellite 6 contained CrC and MoC which would have contributed to its higher hardness.<sup>146</sup>

The hardness values of the coatings were similar to those of Haynes 6B and 25 alloys reported by Levy and Crook<sup>115</sup>, in the range of 24–38 Rockwell C (~250–370 HV). Other authors measured much higher hardness values on different cobalt-based alloys; Yu *et al.*<sup>114</sup> quoted hardness values of 450–540 HV. Antony<sup>113</sup> found Co-Cr-W-C alloys to have hardness values in the range of 37–55 Rockwell C (~360–620 HV), and lower hardness values of 19–40 Rockwell C (~230–390 HV) in Co-Cr-W/Mo-Ni/Fe-C alloys. For Cr<sub>2</sub>O<sub>3</sub>, the results were also within the range reported by Ahn and Kwon<sup>122</sup> and Cetinel *et al.*<sup>64</sup> with hardness values of 1000–1300 HV.

**Table 7.2.** Hardness measurements of the coatings and the bulk samples.

Material	Coating	Coating hardness (HV <sub>2</sub> )	Bulk hardness (HV <sub>3</sub> )
ULTIMET	No Ru	386 ± 21	304 ± 22
	Nominal 0.3 wt% Ru	466 ± 31	-
	Nominal 0.6 wt% Ru	422 ± 32	-
Stellite 6	No Ru	440 ± 25	368 ± 13
	Nominal 0.3 wt% Ru	543 ± 21	-
	Nominal 0.6 wt% Ru	547 ± 49	-
Cr <sub>2</sub> O <sub>3</sub>		1260 ± 77	-
Mild steel		160 ± 5	

## 7.7 Corrosion results

### 7.7.1 Bulk alloys

Since the Otjihase Mine has varying pH values, any replacement materials must be able to cope with these. There was obviously a problem with the current alloys, which corroded very quickly, from one to around six weeks.<sup>151</sup>

At pH 6, the ranking of the corrosion rates (mm.y<sup>-1</sup>) of the samples from the Otjihase Mine and bulk alloys was: mild steel (0.2200) > cast iron (0.0470) > ToughMet 3 (0.0140) > ULTIMET (0.0048) > Ni-Cr-Fe (0.0010) > Stellite 6B (0.0001) > Hastelloy G30 (0.00005).

At pH 3, the ranking of the corrosion rates (mm.y<sup>-1</sup>) of the samples from the Otjihase Mine and bulk alloys was: cast iron (0.350) > Ni-Cr-Fe (0.120) > ToughMet 3 (0.0518) > mild steel (0.025) > Hastelloy G30 (0.0002) > ULTIMET = Stellite 6 B (0.00007).

At pH 1, the ranking of the corrosion rates (mm.y<sup>-1</sup>) of the samples from the Otjihase Mine and bulk alloys was: Cast iron (2.860) > mild steel (0.480) > Ni-Cr-Fe (0.150) > ToughMet 3 (0.0470) > Stellite 6B (0.00019) > ULTIMET (0.00011).

From the ranking of the corrosion rates, at high pH level (6), the Ni-Cr-Fe coating had a lower corrosion rate than ULTIMET and ToughMet 3 for the bulk alloys, and a higher rate than Stellite 6B. As the pH was lowered (3 and 1), Ni-Cr-Fe had much higher corrosion rates than the bulk alloys. This meant that Ni-Cr-Fe corroded too much in an acidic environment. Although Hastelloy G30 had good corrosion resistance (the lowest corrosion rate) at pH 6, it had higher corrosion rates than Stellite 6B and ULTIMET in acidic environments (pH 3 and 1). ULTIMET had good properties in acidic conditions, but

it was worse than the Ni-Cr-Fe coating in the neutral environment. Mild steel had a higher corrosion rate than cast iron at pH 6, and a lower corrosion rate than cast iron and the Ni-Cr-Fe coating at pH 3. At pH1, it was high although lower than cast iron. The mild steel was worse than the bulk alloys at all pH values, except for being better than ToughMet 3 at pH 3.

Thus ULTIMET and Stellite 6B were better than all the existing materials used in the mine overall, and could be good substitutes against corrosion. However, ULTIMET showed a very low corrosion rate in the acidic environment. This increased slightly in the neutral environment, but this corrosion rate was still very low.

All the test solutions for ULTIMET and Stellite 6B hardfacing alloys had turned yellow during the polarisation tests, which was probably due to dissolved  $\text{CrO}_4^{2-}$  ions.<sup>155</sup> The potentiodynamic polarisation curves for all samples (Figure 5.5) showed pitting, which was confirmed by the SEM (Figures 5.9-5.11). With decreased pH, Ni-Cr-Fe suffered more crevice and pitting corrosion, as shown by the potentiodynamic polarisation curves and the SEM images, thus its overall corrosion rate increased (Table 4.1). The presence of chlorine ions in the solution was the major cause of the pits.<sup>50, 51, 84</sup> It was very surprising that Ni-Cr-Fe did not demonstrate passivation behaviour with such a high amount of chromium (Table 4.3). At all pH values, cast iron had more negative corrosion potentials than the bulk alloys. Its corrosion current densities were lower than the bulk alloys, because of the pseudo-passivation effect of cast iron due to the pseudo-protective film formation.

The high chromium content in Hastelloy G30, Stellite 6B and ULTIMET alloys (Table 3.1) caused an extended and stable passivation region (Figure 5.5). In addition, tungsten and molybdenum content could control the resistance to oxidation, by forming thin passive films when the alloys were in corrosive environments. This film lowered the corrosion rates with noticeable increased potentials.<sup>12, 59, 138, 156, 157</sup> ToughMet 3 had a pseudo-passivation region due to thick and silvery growth on the surface as copper dissolved at all pH values (Figure 5.6 c)). The absence of hysteresis loops indicated high resistance to localised corrosion<sup>36</sup>, while a small hysteresis loops for ToughMet 3 indicated a slight susceptibility to localised corrosion.<sup>36</sup>

The ULTIMET and Stellite 6B bulk alloys would be better options during material selections, and replace coating Ni-Cr-Fe coating. The substrate had also shown high corrosion rates at high pH, and its corrosion rate at pH 3 was much better than that of the Ni-Cr-Fe coating, but much worse than the bulk alloys, which demonstrated lower

corrosion rates. It should be noted that, at all pH values, the ULTIMET and Stellite 6B alloys may be used as a replacement for cast iron valves at the Otjihase Underground Mine.

The overall EDX analysis of the samples after cyclic potentiodynamic polarisation measurements showed almost similar results in all solutions tested, with Co, Cr, Mn, Mo, Fe and W for ULTIMET and Stellite 6B, and Cu and Ni for ToughMet 3. ICP-MS/OES results on the solutions showed much higher concentrations of these elements in solutions after the tests, demonstrating that the elements were released into the test solutions. The dissolution may have been caused by the low pH of the solution (due to the sulphur-containing ore) and aggressive chlorides.<sup>50, 51</sup>

### 7.7.2 Coatings

For both ULTIMET and Stellite 6, the corrosion rates of the coating were higher than their bulk alloys, which suggest problems with the coating procedures or the coating was not thick enough or it did not adhere well or the inherent energy of the coatings was higher than that of the bulk, thus it became more prone to corrosion. However, the coating was not noticed to peel off, showing that adherence probably was not a problem. For all coatings, with and without ruthenium, as the acidity increased, the corrosion rate increased. The high corrosion rates of Cr<sub>2</sub>O<sub>3</sub> coating was surprising, and did not agree with Liu *et al.*<sup>75</sup>, Dong *et al.*<sup>67</sup> and Li *et al.*<sup>66</sup> This was probably due to the poor adherence of Cr<sub>2</sub>O<sub>3</sub> to the bonding coat (Figure 6.15), and the cracks which would allow oxygen penetration.<sup>66, 138</sup> However, the bonding coat did not appear to be deposited well, which could have been the source of this problem, and a better deposition method is needed.

Open circuit potentials (OCPs) of the ULTIMET, Stellite 6 coatings with no Ru, nominal 0.3 wt% Ru and nominal 0.6 wt% Ru, Cr<sub>2</sub>O<sub>3</sub> coatings and mild steel substrates stabilised over time (Appendix B). This showed that stable passive films formed on their surfaces or possibly the saturation of ions in the electrolyte could have stabilised the OCP. OCP changed with no recognised trends for the ULTIMET and Stellite 6 coatings without Ru, as well as for the mild steel substrates. When Ru was added, OCP increased with decreased pH for the ULTIMET coatings, while for Stellite 6 coatings, OCP decreased with decreased pH. For Cr<sub>2</sub>O<sub>3</sub> coatings, OCP increased with decreased pH. Mild steel substrates had the lowest OCP at pH 3, and the highest at pH 1.

The corrosion rates of all the samples at pH 1 were higher than at pH 3 and 6, which was due to the presence of more chlorides in the solution and this is expected, and was also found by Olaseinde<sup>93</sup> and Sherif *et al.*<sup>89</sup>.

At pH 6, the ranking of the corrosion rates ( $\text{mm.y}^{-1}$ ) of the coatings, substrate and valve samples was: mild steel (0.220) > Cast iron (0.047) >  $\text{Cr}_2\text{O}_3$  (0.036) > nominal 0.3 wt% Ru-Stellite 6 (0.0077) > 0 wt% Ru-Stellite 6 (0.0044) > nominal 0.6 wt% Ru-ULTIMET (0.0039) > nominal 0.6 wt% Ru-Stellite 6 = 0 wt% Ru-ULTIMET (0.0036) > nominal 0.3 wt% Ru-ULTIMET (0.0025) > Ni-Cr-Fe (0.001).

At pH 3, the ranking of the corrosion rates ( $\text{mm.y}^{-1}$ ) of the coatings, substrate and valve samples was: cast iron (0.350) > Ni-Cr-Fe (0.120) > nominal 0.3 wt% Ru-Stellite 6 (0.043) > nominal 0.3 wt% Ru-ULTIMET (0.04) > mild steel (0.025) >  $\text{Cr}_2\text{O}_3$  (0.024) > nominal 0.6 wt% Ru-ULTIMET (0.02) > 0 wt% Ru-ULTIMET (0.015) > 0 wt% Ru-Stellite 6 (0.0083) > nominal 0.6 wt% Ru-Stellite 6 (0.0063).

At pH 1, the ranking of the corrosion rates ( $\text{mm.y}^{-1}$ ) of the coatings, substrate and valve samples was: cast iron (2.860) > mild steel (0.480) > Ni-Cr-Fe (0.150) > 0 wt% Ru-ULTIMET (0.140) >  $\text{Cr}_2\text{O}_3$  (0.110) > nominal 0.6 wt% Ru-Stellite 6 (0.100) > nominal 0.3 wt% Ru-ULTIMET (0.090) > 0 wt% Ru-Stellite 6 (0.072) > nominal 0.3 wt% Ru-Stellite 6 (0.052) > nominal 0.6 wt% Ru-ULTIMET (0.048).

For pH 6, Ni-Cr-Fe had the lowest corrosion rate, whereas at pH 3 and 1, it had one of the highest corrosion rates, as seen in the bulk alloys. For pH 6, Ni-Cr-Fe had the lowest corrosion rate, whereas at pH 3 and 1, it had one of the highest corrosion rates, as seen in the bulk alloys. This was because, at high pH, a protective film was formed, which inhibited diffusion of hydrogen ions, while at low pH, this film was disrupted by the evolution of hydrogen, which then exposed the metal to the solution, resulting in an increase in oxygen depolarisation and hydrogen evolution, which increased the corrosion rate.<sup>158</sup> Also, increasing the chloride ion content in the solution increased the corrosion rate, as these ions break down the passivity of the material, and so accelerate corrosion.<sup>159</sup> There was little difference between the corrosion rates of: nominal 0.3 wt% Ru-Stellite 6 (0.0077), 0 wt% Ru-Stellite 6 (0.0044), nominal 0.6 wt% Ru-ULTIMET (0.0039), nominal 0.6 wt% Ru-Stellite 6 = 0 wt% Ru-ULTIMET (0.0036) and nominal 0.3 wt% Ru-ULTIMET (0.0025), although these were used to rank the coatings above, perhaps they should be ranked together.

For pH 3, 0 wt% Ru-Stellite 6 (0.0083) and nominal 0.6 wt% Ru-Stellite 6 (0.0063) coatings were by far the best, whereas 0 wt% Ru-Stellite 6 (0.072) > nominal 0.3 wt% Ru-Stellite 6 (0.052) > nominal 0.6 wt% Ru-ULTIMET (0.048) were the best for pH 1.

The corrosion on the bulk alloys was mainly general with slight pitting, whereas the thermal spray coatings showed that corrosion had taken place around the edges of the globular particles, with little corrosion on the carbides and no degradation of the ruthenium particles. If the globular particles were smaller, then the attack might be less effective, since it would be spread over more boundaries. This could be done by reducing the powder sizes by milling without compromising the flow properties of the powders. A better ruthenium distribution would probably reduce corrosion resistance.

For the ULTIMET and Stellite 6 coatings at pH 6, thin protective pseudo-passive films of  $\text{Cr}_2\text{O}_3$  (shown by EDX) would form on the surface, and lower corrosion rates by stopping the anodic dissolution reaction at high pH,<sup>156, 157</sup> as well as reducing the diffusion of corrosive ions from the solution into the coatings.<sup>156, 157</sup> Conversely, at pH 3, non-spontaneous passivation occurred, and at pH 1 (Figure 6.23), the coating was stable, with a wide range of spontaneous passivation, due to protective chromium oxide thin films on the surfaces.<sup>59, 89, 91</sup>

Adding ruthenium to ULTIMET gave varying results with no trend. There was little difference in corrosion rates for pH 6. For pH 3, the worse corrosion rates were for nominal 0.3 wt% Ru, whereas for pH 1, 0.6 wt% Ru had the lowest corrosion rates. The corrosion rates of the coated samples were generally higher than the bulk samples. This was probably because of the corrosion occurring at the edges of the globular particles, which overruled the beneficial effect of adding ruthenium.

Adding ruthenium to Stellite 6 only decreased the corrosion rate for nominal 0.6wt% Ru in pH 6 and 3, and for pH 1, the addition of nominal 0.3wt% Ru had the lowest corrosion rates. Stellite 6 coatings with increased Ru content had increased passivity, agreeing with additions of Ru improving passivity.<sup>89, 93</sup> The lack of hysteresis loops before the pitting potential at all pH values, indicated high resistance to localised corrosion,<sup>36</sup> although it was recognised that the corrosion rates of the coated samples were generally higher than the bulk samples. Again, this was probably due to corrosion at the edges of the globular particles, which was greater than effect of adding ruthenium.

Both ULTIMET and Stellite 6 coatings showed general corrosion mechanisms, with corrosion products on the surfaces and attack of the dendrites, with the interdendritic carbides standing proud. Under sulphidation conditions, Smolenska<sup>160</sup> found the carbides decomposed, and there was severe corrosion along the dendrite boundaries. The carbides acted as anodes to the rest of the matrix, and therefore they were attacked preferentially.<sup>161, 162</sup> Both ULTIMET and Stellite 6 have carbon, with 0.1 wt% C in ULTIMET



against 1.1 wt% C in Stellite 6 (Table 3.2), which was responsible for the different proportions of carbides. Thus, Stellite 6 had more carbides than ULTIMET (Figures 6.41-43, Table 7.1), and the carbides were well distributed in both.

Regarding the ASTM A516 Grade 70 mild steel substrate (and the mild steel from the mine), the corrosion mechanisms in synthetic mine water were similar, and agreed with Mohebbi and Li<sup>50</sup>, Sherif *et al.*<sup>41</sup> and Makar *et al.*<sup>47</sup>.

The corrosion potentials of the ASTM A516 Grade 70 steel (Table 6.8) and the mild steel from the mine (Table 4.6) were almost similar. The corrosion current densities of the ASTM A516 Grade 70 steel were much higher than the mild steel from the mine, showing that the mild steel from the mine had the lower corrosion rate. However, the study by Mobin *et al.*<sup>46</sup> on the effect of heavy metal ions on the corrosion behaviour of carbon steel showed that the presence of heavy metals in solutions accelerated the corrosion rates of steels. Therefore, it would be expected that the mine water having heavy metals would be much more aggressive than the synthetic mine water, which did not have added heavy metals.

### **7.7.3 Comparison of the bulk samples and the coatings**

The potentiodynamic polarisation behaviour showed that the bulk samples (Figure 5.5) had similar passive regions to the coatings (Figures 6.25-6.27 and 6.30-6.32) (around -200 to 800 mV) at all pH levels. The bulk alloys had lower protection potentials (~600 mV) than the coatings (~800 mV), which did not change with decreased pH. This means that if the potential would be kept below the protection potential, these materials would not experience corrosion, *e.g.* pitting corrosion, since a protective film or oxide would still be intact with the material in the mine water.<sup>22, 36</sup>

Comparing the bulk and the coatings, the corrosion rates of the ULTIMET coatings were worse, especially at high acidities, whereas the Stellite 6 were worse at all conditions. The corrosion on the bulk alloys was mainly general corrosion with some pitting, whereas the thermal spray coatings experienced corrosion at the edges of the globular particles.

## **7.8 Abrasive wear results**

### **7.8.1 Bulk alloys**

In order to solve problems with abrasive wear, hardness of the materials should be considered. From Table 7.2, the higher hardness of Stellite 6B than ULTIMET was partly

due to the carbides in the matrix and at grain boundaries (Figures 5.1 and 5.2). These carbides could not be prone to ploughing during sliding.

At 5 N, the ranking of the coefficients of friction of the bulk samples was: Stellite 6B (0.89) > ULTIMET (0.40). Similarly, the ranking of the wear rates ( $\text{mm}^3 \cdot (\text{N} \cdot \text{m})^{-1}$ ) was: ULTIMET ( $1.6 \times 10^{-4}$ ) > Stellite 6B ( $7.8 \times 10^{-5}$ ). In both cases, there was a reasonable difference between them, although there were  $\pm 0.2 \text{ mm}^3 \cdot (\text{N} \cdot \text{m})^{-1}$  errors.

At 10 N, the ranking of the coefficients of friction of the bulk samples was: Stellite 6B (0.70) > ULTIMET (0.40), and for the wear rates ( $\text{mm}^3 \cdot (\text{N} \cdot \text{m})^{-1}$ ) was: ULTIMET ( $7.7 \times 10^{-5}$ ) > Stellite 6B ( $5.6 \times 10^{-5}$ ). The ranking was the same for both 5 N and 10 N, although the difference between the wear rates was less.

From the ranking of the coefficients of friction of the bulk samples, ULTIMET had a lower coefficient of friction than Stellite 6B at both loads. The coefficient of friction for ULTIMET did not change when the load was increased, whereas for Stellite 6B, the coefficient of friction decreased when the load was increased. Thus, Stellite B had a higher coefficient of friction and lower wear rate than ULTIMET (Figure 5.18), due to the chromium-rich carbides which resist abrasion<sup>139, 154</sup>, which also made Stellite 6B harder than ULTIMET. The higher W content contributed to the formation of additional carbides. This meant that ULTIMET lost more material, giving higher wear rates and lower coefficients of friction than Stellite 6B at all loads. However, there was no significant relationship between coefficients of friction and wear rates, but rather between hardness and wear rates.

The abrasive wear results of ULTIMET and Stellite 6B contradicted the results of by Liu *et al.*<sup>62</sup>, Gohar and Rahnejat<sup>96</sup> and Ahn and Kwon<sup>122</sup> that materials with low coefficient of frictions should have low wear rates. However, Moore<sup>120</sup> found that the coefficients of friction of materials vary, which was also supported by Zang and Battiston<sup>116</sup> in their friction and wear study of cobalt- and iron-based superalloys and ceramics where some alloys with low coefficients of friction experienced heavy wear loss (*i.e.* high wear rates). This could be associated with other factors, such as interface temperature or surface waviness during the tests.<sup>98</sup> Also, it should be noted that, two materials with the same coefficient of friction may exhibit different wear rates.

Comparing the worn surfaces under the SEM, ULTIMET experienced more mechanical damage than Stellite 6B (Figures 5.18 and 5.19) due to its lower hardness. Despite the high hardness of Stellite 6B, the matrix phase was ploughed out, leaving carbides on the

surface, because carbides are difficult to deform<sup>126</sup>. Thus, Stellite 6B had lower wear rates and higher coefficient of friction than ULTIMET. Therefore, Stellite 6B was the best alloy to resist abrasion at these loads.

The decrease in contents of Si, W and Mo, and the increase in C, and the gaining of O on the wear track of ULTIMET and Stellite 6B was a further indication that wear had taken place. Oxygen gained on the wear track was due to oxide film formed, which was facilitated by the high surface temperatures during sliding, and it was also broken down.<sup>163, 164</sup> At this stage, the samples could no longer withstand the pressure due to sliding. As a result, ULTIMET experienced tearing, slip bands and slip steps, grooves and spalling with less debris (Figure 5.22 c)), while Stellite 6B experienced fewer grooves, more debris, and more carbides left on the surface (Figure 5.22 e)).

The wear rates of the bulk alloys were similar to the wear rate of Stellite 6B, %: 56.8Co-30Cr-4W-1Mo-1.1C-2.4Fe-2.5Ni-0.7Si-1.5Mn, ( $3.13 \times 10^{-6} \text{ mm}^3 \cdot (\text{N} \cdot \text{m})^{-1}$ ) by Sebastiani *et al.*<sup>146</sup> However, the abrasive wear test was done under a lubricated environment. The wear mechanisms consisted of a mixture of two-body grooving, which occurred when the steel ball (harder body) slides over the test sample (softer surface) and three-body abrasive wear of the cobalt-rich matrix, where abrasive delaminated particles (third bodies) became trapped between steel ball and the sample, acting as abrasive media.

### 7.8.2 Coatings

Both ULTIMET and Stellite 6 coatings had dendritic microstructures with interdendritic carbides and the globular particles which were the “splats” from the coating process. The interdendritic carbides were mostly CrC. When hard carbides of Stellite 6 coatings contacted with the steel ball during the sliding wear tests, the carbides resisted sliding wear, leading to lower wear rates than for the ULTIMET coatings, which had fewer interdendritic carbides. This effect of carbides on wear of materials was reported by Antony<sup>113</sup>, Yu *et al.*<sup>114</sup>, Chen and Dong<sup>126</sup> and Sebastiani *et al.*<sup>146</sup> This also agreed with Zhang *et al.*<sup>12</sup>, Yangtao *et al.*<sup>54</sup> and Klarstrom *et al.*<sup>148</sup>.

It was expected that the high coefficient of friction would yield a higher wear rate as reported by Liu *et al.*<sup>62</sup>, Gohar and Rahnejat<sup>96</sup> and Ahn and Kwon<sup>122</sup>. Contradicting this, the ULTIMET coatings had lower coefficients of friction, and higher wear rates than Stellite 6 coatings. However, Zang and Battiston<sup>116</sup> studied the friction and wear of cobalt- and iron-based superalloys and ceramics, and found that ceramics with carbon had lower friction coefficient and wear rates, whereas ceramics without carbon had higher friction coefficients and higher wear rates. The iron and steels had lower friction coefficients and

higher wear rates than the ceramics with carbon. Cermets showed more scatter: WC-Co had a similar friction coefficient, but less wear loss than to steel. Thus, Zang and Battiston<sup>116</sup> deduced that the relationship between coefficients of friction and wear is not a simple one. The relationship between the coefficient of friction and wear rate is also probably affected by the particular wear mechanisms, and could also be due to interface temperature or surface waviness during the tests.<sup>98</sup>

At 5 N, the ranking of the coefficients of friction of the coated samples was: 0 wt% Ru-Stellite 6 = nominal 0.6 wt% Ru-Stellite 6 (0.8) > nominal 0.3 wt% Ru-Stellite 6 = Cr<sub>2</sub>O<sub>3</sub> = mild steel (0.7) > 0 wt% Ru-ULTIMET (0.5) > nominal 0.3 wt% Ru-ULTIMET = nominal 0.6 wt% Ru-ULTIMET (0.4), and the wear rate ((mm<sup>3</sup>.(N.m)<sup>-1</sup>) x 10<sup>-5</sup>) ranking was: 0 wt% Ru-ULTIMET = mild steel (1.4) > nominal 0.6 wt% Ru-ULTIMET = 0 wt% Ru-Stellite 6 = Cr<sub>2</sub>O<sub>3</sub> (1.3) > nominal 0.3 wt% Ru-ULTIMET (1.2) > nominal 0.6 wt% Ru-Stellite 6 (1.1) > nominal 0.3 wt% Ru-Stellite 6 (0.7). These values were very similar, and so it is difficult to discern a trend (Figure 7.1).

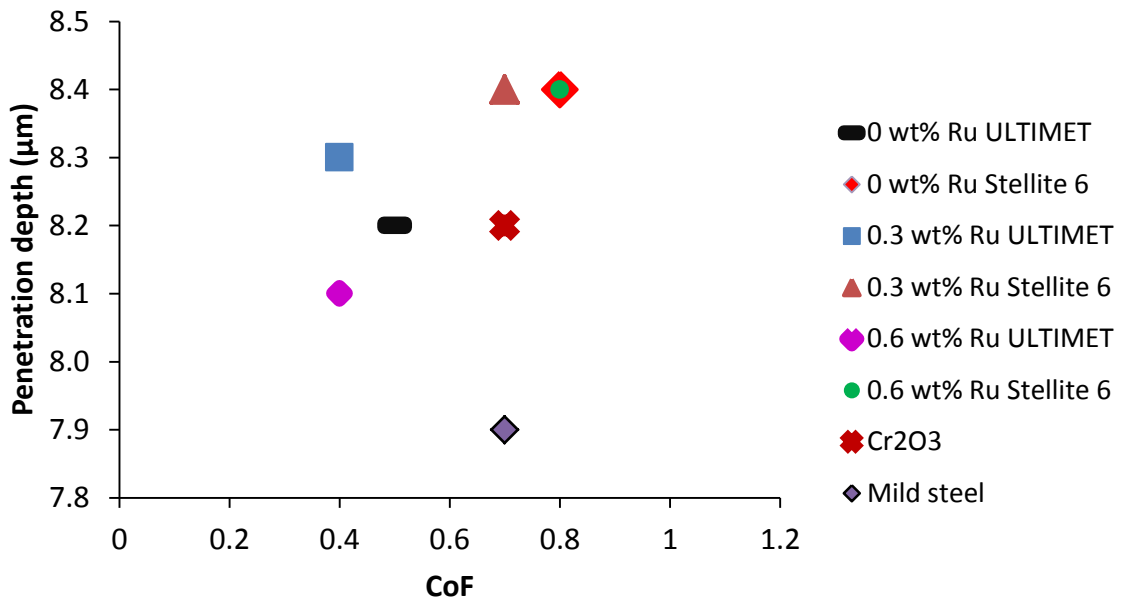
At 10 N, the ranking of the coefficients of friction of the coating samples was: nominal 0.3 wt% Ru-Stellite 6 (1.5) > Cr<sub>2</sub>O<sub>3</sub> (0.8) > 0 wt% Ru-Stellite 6 = nominal 0.6 wt% Ru-Stellite 6 = mild steel (0.7) > 0 wt% Ru-ULTIMET = nominal 0.3 wt% Ru-ULTIMET = nominal 0.6 wt% Ru-ULTIMET, and the wear rate ((mm<sup>3</sup>.(N.m)<sup>-1</sup>) x 10<sup>-5</sup>) ranking was: 0 wt% Ru-ULTIMET (8.6) > nominal 0.3 wt% Ru-ULTIMET (7.8) > mild steel (7.2) > Cr<sub>2</sub>O<sub>3</sub> (6.0) > nominal 0.6 wt% Ru-ULTIMET (5.1) > nominal 0.3 wt% Ru-Stellite 6 (4.9) > 0 wt% Ru-Stellite 6 > nominal 0.6 wt% Ru-Stellite 6 (3.2). Again, this shows no discernible trend (Figure 7.2), although there was more difference in the values than for the lower force.

The effect of Ru additions on the wear resistance of ULTIMET and Stellite 6 coatings was difficult to discern because there was little difference between the results at the 5 N load. At 10 N, there was more difference between the results, but no discernible trend. However, it has already been realised that there were problems with both the ruthenium distribution, and the quality of the coatings, so it would have been surprising to find a relationship between the added ruthenium and the properties.

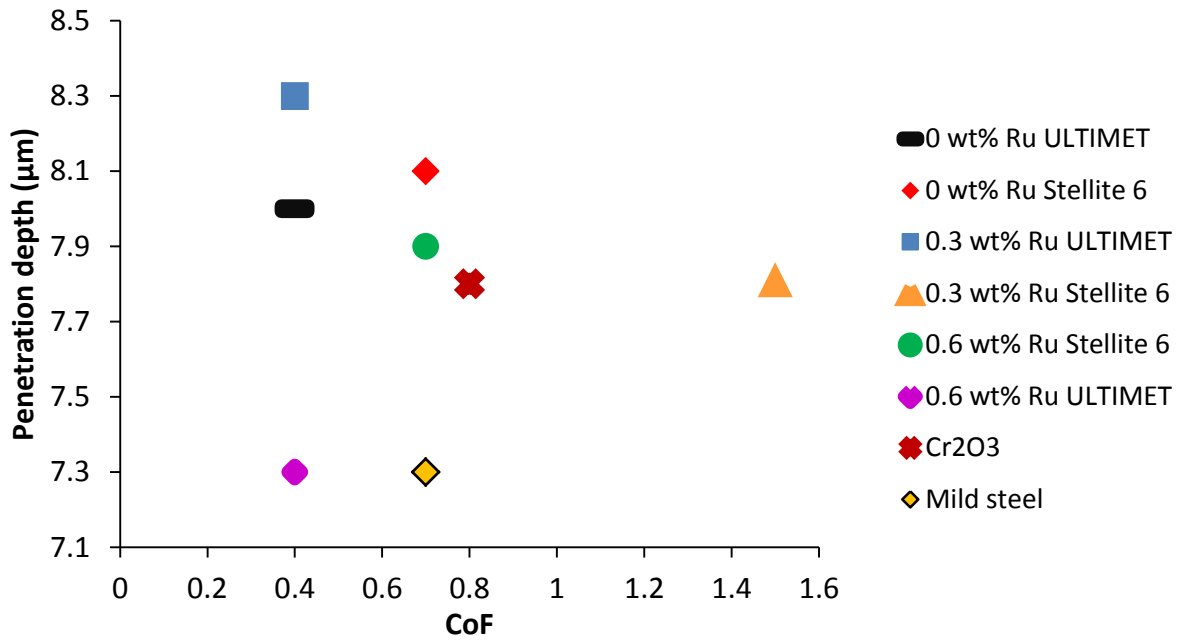
EDX analyses for all coatings showed oxygen on wear tracks. This meant an oxide film formed due to high surface temperature during sliding, and it was broken down,<sup>163, 164</sup> similar to the bulk materials. ULTIMET exhibited tearing, slip bands and slip steps, grooves cracks and spalling with less debris, while Stellite 6B had fewer grooves, more debris, and more of the carbides left of the surface (Figure 5.22 d)). These wear mechanisms were also found by other researchers in different environments.<sup>100-102, 105, 106, 108</sup>

There was not any trend between the penetration depth and wear rate (Figures 7.1 and 7.2), and the coatings acted differently with the different loads, suggesting that the scatter was high. The wear rates of the coatings (Figures 7.3 and 7.4) were much higher than for the 10 N load than for 5 N. Also the wear rates were much higher than for Stellite 6B, % (56.8Co-30Cr-4W-1Mo-1.1C-2.4Fe-2.5Ni-0.7Si-1.5Mn) ( $3.13 \times 10^{-6} \text{ mm}^3 \cdot (\text{N} \cdot \text{m})^{-1}$ ) tested by by Sebastiani *et al.*<sup>146</sup>, because that wear test was done under oil lubrication.

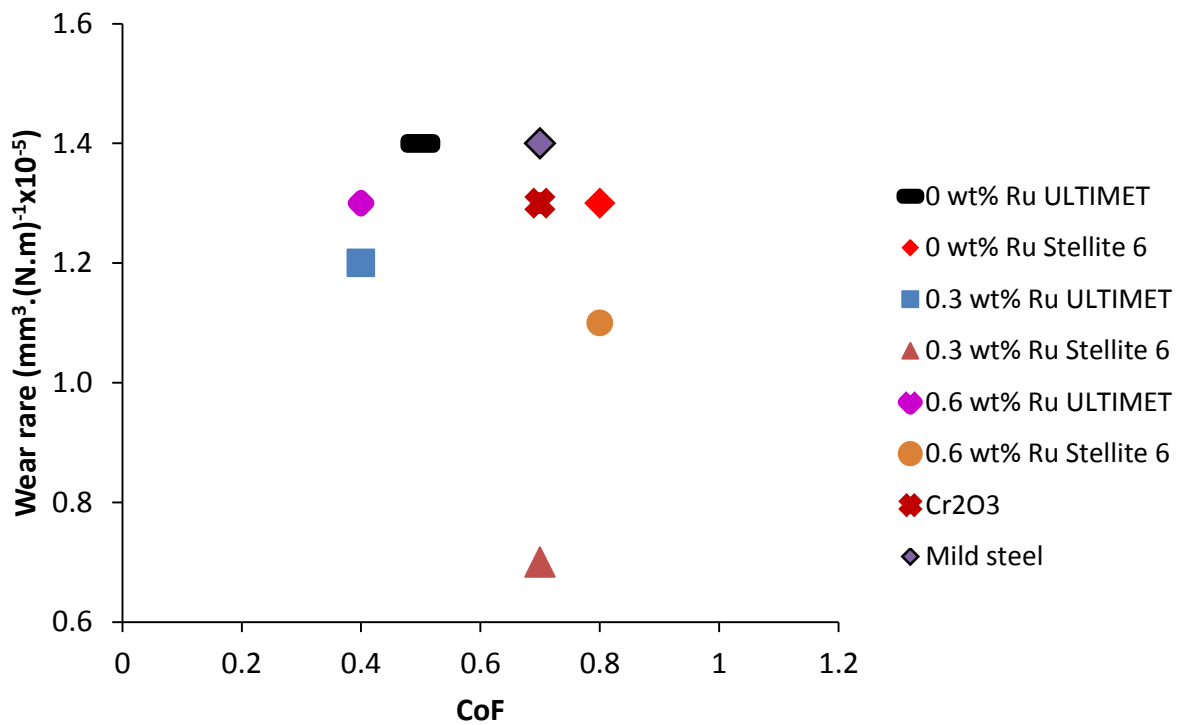
Stellite 6 coatings generally had smaller volumes of lost material than ULTIMET (although nominal 0.3 wt% Ru-Stellite 6 coating had a lower wear rate at the 5 N load). Therefore, taking the bad distribution of ruthenium and the poor coating quality into account, the Stellite 6 coating was the best coating to resist abrasion at these loads, especially nominal 0.6 wt% Ru Stellite 6 coating. It is recommended that this material be considered as a substitute coating for that currently being used at the Otjihase Underground Mine since it showed better abrasion and wear resistance results, even with poor Ru distribution.



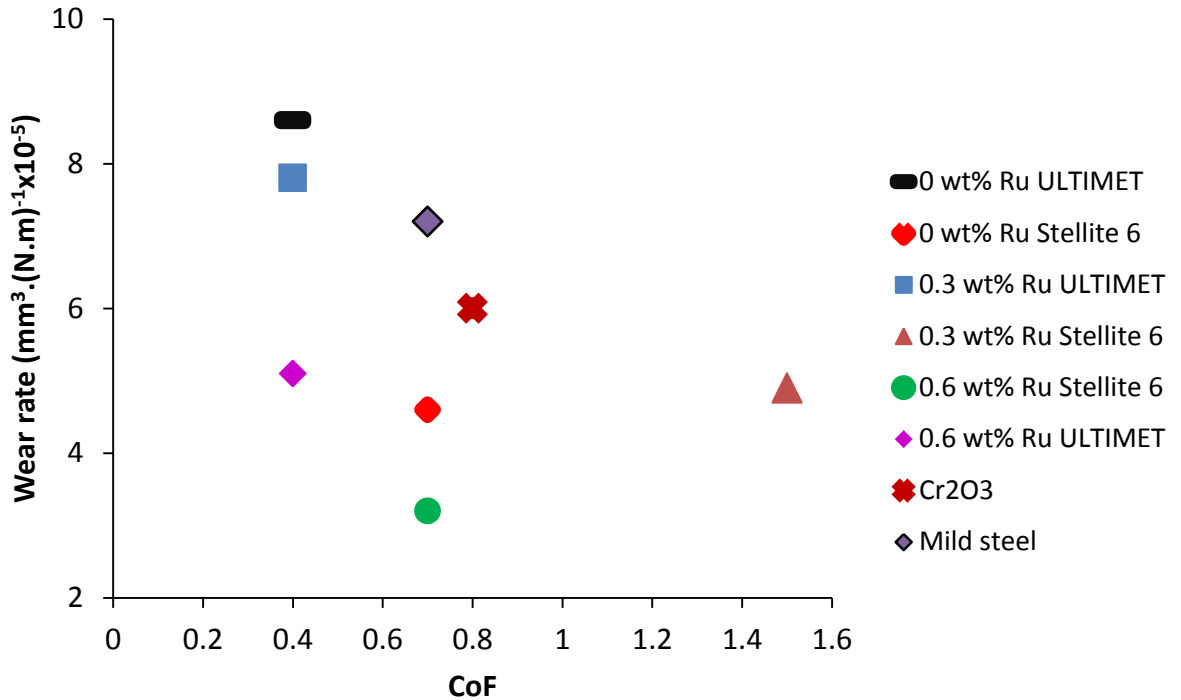
**Figure 7.1.** Relationship between coefficient of friction and penetration depth of 0, nominal 0.3 wt% Ru and nominal 0.6 wt% Ru ULTIMET and Stellite 6, Cr<sub>2</sub>O<sub>3</sub> coatings and mild steel at 5 N.



**Figure 7.2.** Relationship between coefficient of friction and penetration depth of 0, nominal 0.3 wt% Ru and nominal 0.6 wt% Ru ULTIMET and Stellite 6, Cr<sub>2</sub>O<sub>3</sub> coatings and mild steel at 10 N.



**Figure 7.3.** Relationship between coefficient of friction and wear rate of 0, nominal 0.3 wt% Ru and nominal 0.6 wt% Ru ULTIMET and Stellite 6, Cr<sub>2</sub>O<sub>3</sub> coatings and mild steel at 5 N.

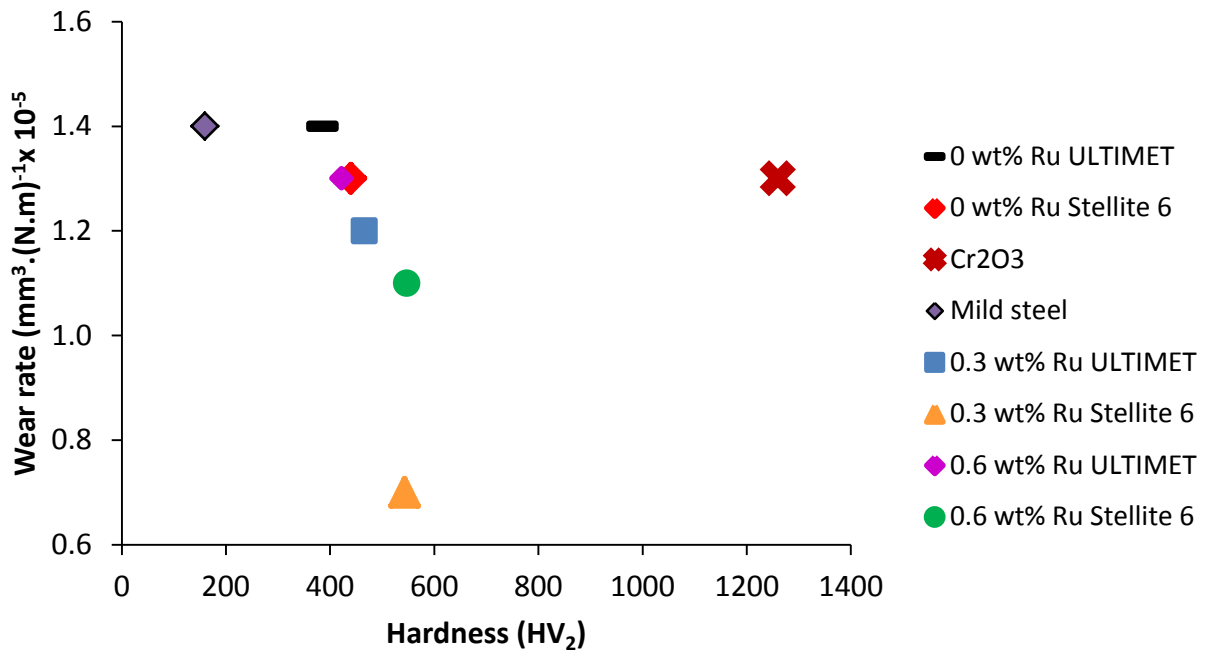


**Figure 7.4.** Relationship between coefficient of friction and wear rate of 0, nominal 0.3 wt% Ru and nominal 0.6 wt% Ru ULTIMET and Stellite 6, Cr<sub>2</sub>O<sub>3</sub> coatings and mild steel at 10 N.

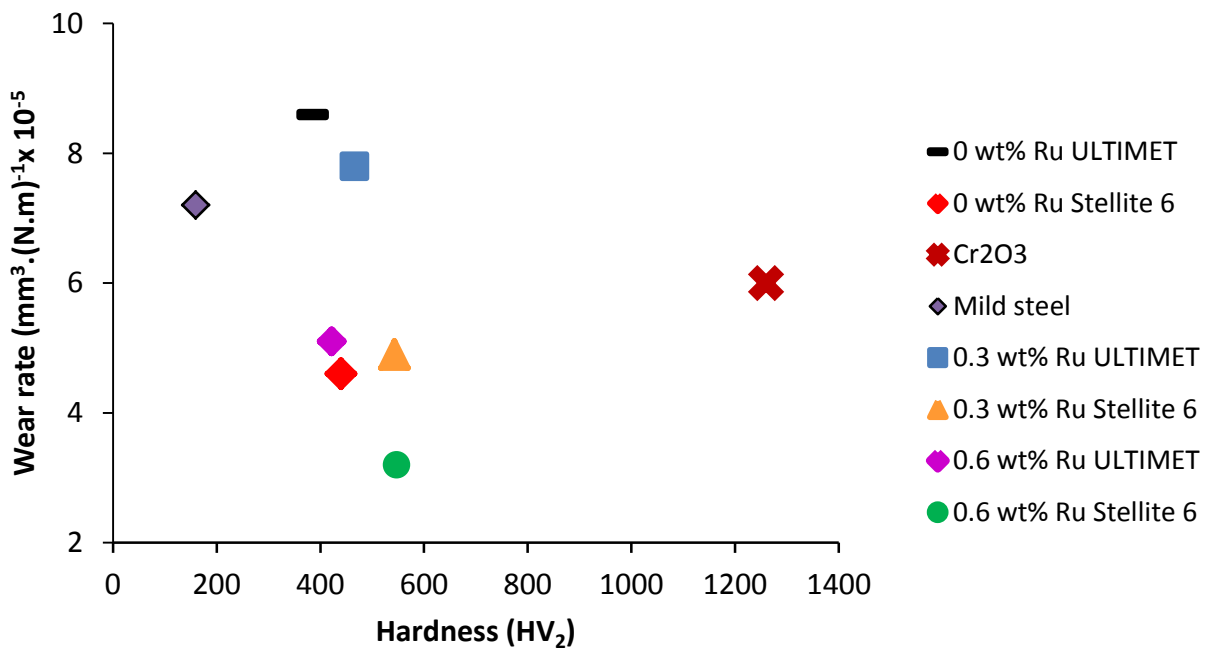
The hardness ranking of the coatings and mild steel was: mild steel ( $160 \pm 5$ ) < 0 wt% Ru ULTIMET ( $386 \pm 21$ ) < nominal 0.6 wt% Ru ULTIMET ( $422 \pm 32$ ) < 0 wt% Ru Stellite 6 ( $440 \pm 25$ ) < nominal 0.3 wt% Ru ULTIMET ( $466 \pm 31$ ) < nominal 0.3 wt% Ru Stellite 6 ( $543 \pm 21$ ) < nominal 0.6 wt% Ru Stellite 6 ( $547 \pm 49$ ) < Cr<sub>2</sub>O<sub>3</sub> ( $1260 \pm 77$ ), and the wear rate ((mm<sup>3</sup>.(N.m)<sup>-1</sup>) x 10<sup>-5</sup>) ranking at 5 N was: 0 wt% Ru-ULTIMET = mild steel (1.4) > nominal 0.6 wt% Ru-ULTIMET = 0 wt% Ru-Stellite 6 = Cr<sub>2</sub>O<sub>3</sub> (1.3) > nominal 0.3 wt% Ru-ULTIMET (1.2) > nominal 0.6 wt% Ru-Stellite 6 (1.1) > nominal 0.3 wt% Ru-Stellite 6 (0.7). At 10 N, and the wear rate ((mm<sup>3</sup>.(N.m)<sup>-1</sup>) x 10<sup>-5</sup>) ranking at 10 N was: 0 wt% Ru-ULTIMET (8.6) > nominal 0.3 wt% Ru-ULTIMET (7.8) > mild steel (7.2) > Cr<sub>2</sub>O<sub>3</sub> (6.0) > nominal 0.6 wt% Ru-ULTIMET (5.1) > nominal 0.3 wt% Ru-Stellite 6 (4.9) > 0 wt% Ru-Stellite 6 > nominal 0.6 wt% Ru-Stellite 6 (3.2).

From the hardness and wear rate rankings, no discernible trend was found in the coatings (apart from Cr<sub>2</sub>O<sub>3</sub>, which is quite a different type of coating) and mild steel (Figures 7.5 and 7.6), although there was more difference in the values than for the lower force.





**Figure 7.5.** Relationship between hardness and wear rate of 0, nominal 0.3 wt% Ru and nominal 0.6 wt% Ru ULTIMET and Stellite 6, Cr<sub>2</sub>O<sub>3</sub> coatings and mild steel at 5 N.



**Figure 7.6.** Relationship between hardness and wear rate of 0, nominal 0.3 wt% Ru and nominal 0.6 wt% Ru ULTIMET and Stellite 6, Cr<sub>2</sub>O<sub>3</sub> coatings and mild steel at 10 N.

### 7.8.3 Comparison of the bulk samples and the coatings

The friction and wear behaviour showed that the bulk samples (Figure 6.46-6.51.) had similar coefficients of friction to the coatings (0.40-0.89), ignoring the coefficient of friction of nominal 0.3 wt% Ru Stellite 6 coating at 10 N load, which did not fit the trend. This wear test result might have been over reported ( $\mu > 1$ ), because of the poor quality of the coating. The ball probably have broken the coating and reached onto the surface, hence over reporting of the value, although there was no evidence seen under SEM (Figure 6.55).

Comparing the bulk and the coatings, the wear rates of the coatings were low at low load with nominal 0.3 wt% Ru Stellite 6 had the lowest wear rates, and the wear rates of the coatings were almost similar to the bulk at high load with the nominal 0.6 wt% Ru Stellite 6 had the lowest wear rates. The wear mechanism the bulk alloys was two- and three-body, showing delamination and grooves in all samples (Figures 5.20-5.21), and for the coatings was mainly two-body, showing grooves, cracks and some pits in all samples (Figures 6.52-6.56).

### 7.9 Tribocorrosion results

Pumps at the Otjihase Underground Mine pump corrosive water and slurries from underground reservoirs to the surface to prevent flooding of the mine. When a pump operates, its shaft sleeve often experiences wear by debris trapped in the packing gland, and once the coating has been removed, corrosion from slurry further accelerates tribocorrosion. Once this has occurred, a need of replacing the corroded pump parts is obvious, which leads to a loss in production and takes much time and money. A nobler and yet hard enough material should be selected to overcome this corrosive wear problem at the Otjihase Underground Mine.

At pH 6 and 5 N, the ranking of the tribocorrosion rates ( $\text{mm.y}^{-1}$ ) of the coatings and mild steel samples was: mild steel (0.70) > 0 wt% Ru-ULTIMET (0.60) > 0 wt% Ru-Stellite 6 (0.50) >  $\text{Cr}_2\text{O}_3$  (0.40). The ranking of the tribocorrosion rates ( $\text{mm.y}^{-1}$ ) of the coatings with 0.6 wt% Ru and mild steel samples under 5 N was: mild steel (0.70) > nominal 0.6 wt% Ru-ULTIMET (0.50) > nominal 0.6 wt% Ru-Stellite 6 =  $\text{Cr}_2\text{O}_3$  (0.40)

At pH 6 and 10 N, their ranking of the tribocorrosion rates ( $\text{mm.y}^{-1}$ ) was: mild steel (1.00) >  $\text{Cr}_2\text{O}_3$  (0.90) > 0 wt% Ru-ULTIMET (0.80) > 0 wt% Ru-Stellite 6 (0.60), while the ranking of the tribocorrosion rates ( $\text{mm.y}^{-1}$ ) of the coatings with nominal 0.6 wt% Ru and mild steel samples under 5 N was: mild steel (1.00) >  $\text{Cr}_2\text{O}_3$  (0.90) > nominal 0.6 wt% Ru-ULTIMET

(0.70) > nominal 0.6 wt% Ru-Stellite 6 (0.50). The benefit of ruthenium addition would probably only be seen at low pH levels.

For all the coatings and mild steel substrate, the tribocorrosion rates at 5 N were generally lower than at 10 N, as expected. The higher wear rates at 10 N would be expected from the higher force, and possibly the coatings were not thick enough to withstand the load. For ULTIMET and Stellite 6 coatings, the tribocorrosion rates decreased with increased ruthenium addition. The potentiodynamic polarisation behaviour of ULTIMET and Stellite 6 coatings were comparable to plasma carburised Stellite 21 Co–Cr alloy (Co–27.0 Cr–0.3 C–2.5 Ni–5.5 Mo (wt%)) studied by Chen and Dong<sup>126</sup> in in 3.5% NaCl solution. The coatings had more negative tribocorrosion potentials (between 700 and 900 mV) and high tribocorrosion current densities (between 43.10 to 77.50  $\mu\text{A}\cdot\text{cm}^{-2}$ ). The passivity behaviour of the coatings was enhanced by the chromium content, which helped the formation of a thin passive layer or oxide film, which enhanced tribocorrosion resistance.<sup>12, 59, 139, 165</sup> Also, the tungsten and molybdenum contents would control the resistance to external surface degradation by abrasion and oxidation resistance, by forming carbides which resist abrasion.<sup>149, 159</sup>

The high tribocorrosion rates of the  $\text{Cr}_2\text{O}_3$  coating were surprising. This was probably due to the cracks, which would allow oxygen penetration.<sup>66, 138</sup> The cracks propagated due to bad adherence of  $\text{Cr}_2\text{O}_3$  to the bonding coat (Figure 6.15). The mild steel suffered tribocorrosion at all loads much more than the coatings, despite it experiencing pseudo-passivation.

EDX analyses (Tables 6.24-6.27 compared to Table 6.3) showed much O, indicating that an oxide was formed during the tests. This was a protective film or oxide that was formed during the test, and had been broken down during rubbing.<sup>161, 162</sup>

The wear mechanism of coatings and mild steel was predominantly abrasive wear, characterised by grooves, cracks, and severe spalling at both loads. These wear mechanisms were similar to those reported by Negroni<sup>123</sup>, Ponthiaux *et al.*<sup>124</sup> and Metikoš-Huković and Babić<sup>58</sup>, even though different test parameters and conditions were used.

Stellite 6 with nominal 0.6 wt% Ru was the best coating for tribocorrosion resistance, due to its resistance to abrasion oxidation. Thus, it is recommended for further consideration as a substitute coating for those currently being used coating at the Otjihase

Underground Mine, but with a better distribution of ruthenium and a better deposition method.

### 7.10 Proposed alloys for pump system at Otjihase Mine

Based on the results of this study, it is proposed to recommend the following alternative materials for consideration for the pump system at Otjihase Mine:

- a) Stellite 6 (with nominal 0.6 wt% Ru addition) coated steel – for pump shaft sleeves
- b) Stellite 6B alloy – for valves.

This is based on the fact that the stellite 6 coatings and stellite 6B alloy achieved the highest tribocorrosion resistance.

### 7.11 Cost comparison between current pump materials and the proposed alternative pump materials

The prices of these metal powders per kilogram were provided by WEARTECH Pty (Ltd) (Table 7.3). The prices of the cobalt-based powders were marginally higher than those of the nickel- and copper-based powders. INCONEL Alloy 600 (Ni-Cr-Fe), used as a coating on the mild steel sleeve, with a cast iron pump experienced severe erosion-corrosion at the Otjihase Underground Mine, and they had to be replaced after around six weeks at approximately US\$ 15 080 (~R 226 200) per annum for three pumps only. If a more resistant material could be used, *e.g.* Stellite 6B, then the annual maintenance cost will come down, since Stellite 6B is expected to last longer (Table 7.4), since it has a higher corrosion resistance than the Ni-Cr-Fe coating, and is only US\$5 per kg (6.25%) more expensive. The cost comparison was only done on the sleeve where most of the damage occurred.

**Table 7.3.** Cost of alloys as provided by WEARTECH Pty (Ltd), November 2014.

Alloy	Cost (US\$/kg)
ULTIMET (UNS R31233)	135 (~R 2 025)
Stellite 6B (UNS R30006)	85 (~R 1 275)
Ru (99.9%)	2 090 (~R 20 898)

The material costs of the coated shaft sleeves of the three pumps at the Otjihase Underground Mine was US\$ 870 (~R 13 050), *i.e.* ~US\$ 290 (~R4 350) each. According to the personnel at the Otjihase Underground Mine, the replacement of the shaft sleeves may occur every 6 weeks at the cost of US\$ 15 080 (~R 226 200) per annum, excluding

labour, maintenance, down-time, production losses, de-commissioning, machining and installation.<sup>151</sup>

The mass of the material needed for coating ( $m$ ) was determined by the product of the density of the material ( $\rho_m$ ) and the volume ( $V_m$ ) to be coated (Equation 7.1). This mass multiplied by the cost of the material per kilogram,  $\mu$  (dimension cost) gave the cost of the sleeve coating material (Equation 7.2). The relationship of the coating thickness ( $\delta_t = 0.5$  mm) to the corrosion rate ( $CR$ ) of a material gave the predicted life of a material (Equation 7.3), while the relationship of the cost of the sleeve coating material to the predicted life gave the cost of the material per year (Tables 7.4 and 7.5). By assumption, corrosion is allowed to continue for the whole coating thickness. In practice, it might be better to replace the material when the coating is 0.1 mm thick before it causes failure of the shaft, and results in leakages, flooding of the surroundings and unacceptably frequent maintenance, down-time and replacement of parts.

$$m = \rho_m \cdot V_m \quad \text{Equation 7.1}$$

$$\text{Cost of sleeve coating material} = m \cdot \mu \quad \text{Equation 7.2}$$

$$\text{Predicted life} = \frac{\delta_t}{CR} \quad \text{Equation 7.3}$$

$$\text{Annual cost of material} = \frac{\text{Cost}}{\text{Predicted life}} \quad \text{Equation 7.4}$$

**Table 7.4.** Cost and predicted life of materials due to corrosion in synthetic mine water at pH 6, 3 and 1.

Sample	pH	Corrosion rate	Predicted life	Cost
		(mm.y <sup>-1</sup> )	(years)	(US\$/y)
ULTIMET: bulk	6	0.0050	103.5	0.53
ULTIMET No Ru		0.0040	139.0	0.40
ULTIMET + 0.3 wt% Ru		0.0030	200.0	0.29
ULTIMET + 0.6 wt% Ru		0.0040	128.0	0.47
Stellite 6B		0.0001	4545.5	0.01
Stellite 6 No Ru		0.0040	113.6	0.29
Stellite 6 + 0.3 wt% Ru		0.0080	65.0	0.55
Stellite 6 + 0.6% Ru		0.0040	139.0	0.27
Ni-Cr-Fe		0.0100	50	0.60
ULTIMET: bulk	3	0.0001	7143.0	0.01
ULTIMET No Ru		0.0150	33.3	1.65
ULTIMET + 0.3 wt% Ru		0.0400	12.5	4.61
ULTIMET + 0.6 wt% Ru		0.0200	25.0	2.41

Stellite 6B	1	0.0001	7143.0	0.01
Stellite 6 No Ru		0.0080	60.2	0.55
Stellite 6 + 0.3 wt% Ru		0.0400	11.6	3.05
Stellite 6 + 0.6% Ru		0.0060	79.4	0.48
Ni-Cr-Fe		0.1200	4.0	7.25
ULTIMET: bulk		0.0001	4545.5	0.01
ULTIMET No Ru		0.1400	3.6	15.43
ULTIMET + 0.3 wt% Ru		0.0900	5.6	10.38
ULTIMET + 0.6 wt% Ru		0.0480	10.4	5.78
Stellite 6B		0.0002	2631.6	0.01
Stellite 6 No Ru		0.0700	7.0	4.75
Stellite 6 + 0.3 wt% Ru		0.0520	9.6	3.69
Stellite 6 + 0.6% Ru		0.1000	5.0	7.57
Ni-Cr-Fe		0.1500	3.0	9.06

The cost comparisons of the materials due to tribocorrosion (Table 7.5) were determined using the same equations as the costs due to corrosion (Equations 7.1-7.4). The actual Ni-Cr-Fe coating on the sleeve used in the pump on the Otjihase Underground Mine failed in 6 weeks, and was 0.5 mm thick, therefore the corrosion rate for Ni-Cr-Fe coating was 8.7 mm.y<sup>-1</sup>.

**Table 7.5.** Cost and predicted life of materials due to tribocorrosion in synthetic mine water at pH 6.

Sample	pH	Corrosion rate	Predicted life	Cost
		(mm.y <sup>-1</sup> )	(years)	(US\$/y)
ULTIMET No Ru	6	0.8	0.6	88.15
ULTIMET + 0.6 wt% Ru		0.7	0.7	84.29
Stellite 6 No Ru		0.6	0.8	39.61
Stellite 6 + 0.6 wt% Ru		0.5	1.0	37.87
Ni-Cr-Fe		8.7	0.1	523.41

It was assumed that the maximum corrosion limit on the bulk alloys is also 0.5 mm. Basically, a material with lower corrosion rates obviously had a longer predicted life (Figures 7.7, 7.9 and 7.11). The cost ranking (US\$/y) of the bulk materials due to corrosion at pH 6 was: Ni-Cr-Fe (0.60) > ULTIMET (0.53) > Stellite 6B (0.01), at pH 3 the ranking was: Ni-Cr-Fe (7.25) > ULTIMET (0.01) > Stellite 6B (0.005), and at pH 1, the ranking was: Ni-Cr-Fe (9.06) > ULTIMET = Stellite 6B (0.01). At all pH values, the cost for Ni-Cr-Fe coating was higher than for ULTIMET and Stellite 6B alloys (Figure 7.7). It also had a lower predicted life than Stellite 6B and ULTIMET alloys at all pH levels (Figure 7.8).

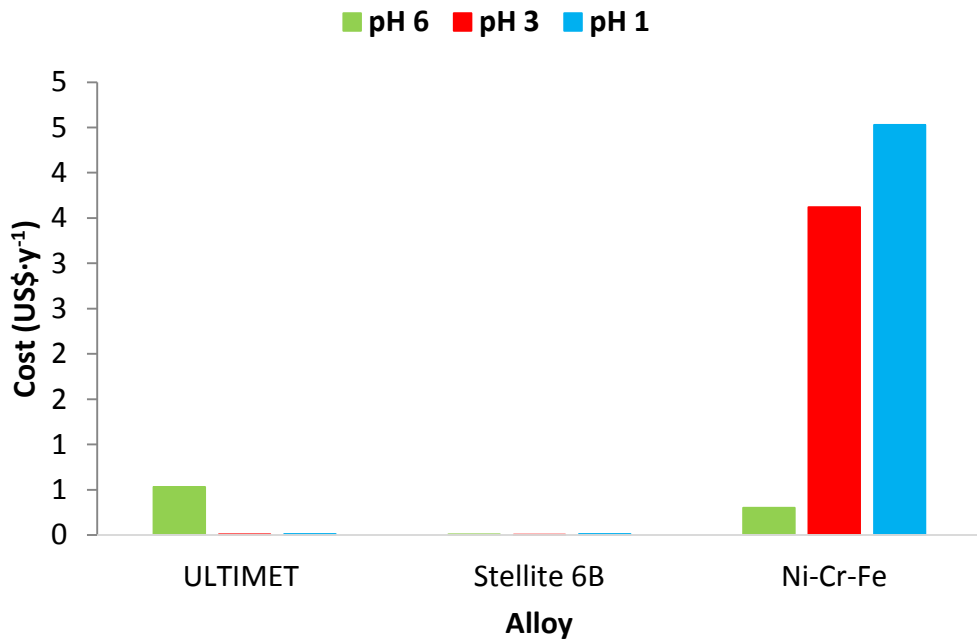
The annual cost ranking (US\$/y) of the coatings (Figure 7.9) due to corrosion at pH 6 was: = Ni-Cr-Fe = Stellite 6 + 0.3 wt% Ru (0.60) > ULTIMET + 0.6 wt% Ru (0.50) > ULTIMET No Ru (0.40) > ULTIMET + 0.3 wt% Ru = Stellite 6 No Ru = Stellite 6 + 0.6% Ru (0.30). This showed Ni-Cr-Fe and Stellite 6 with 0.6 wt% Ru was the most expensive coating (Figure 7.9). Ni-Cr-Fe had the shortest predicted life apart from Stellite 6 with 0.3 wt% Ru. ULTIMET with 0.3 wt% Ru and Stellite 6 with 0.6 wt% Ru had the longest predicted life (Figure 7.10).

At pH 3, the annual cost ranking (US\$/y) of the coatings (Figure 7.9) due to corrosion at was: Ni-Cr-Fe (7.25) > ULTIMET + 0.3 wt% Ru (4.60) > Stellite 6 + 0.3 wt% Ru (3.10) > ULTIMET + 0.6 wt% Ru (2.40) > ULTIMET No Ru (1.70) > Stellite 6 + 0.6 wt% Ru (0.50). From the ranking, the cost of Ni-Cr-Fe was the most expensive coatings, with low predicted life (Figure 7.10). Stellite 6 with 0.6 wt% Ru had the longest expected life and lowest cost.

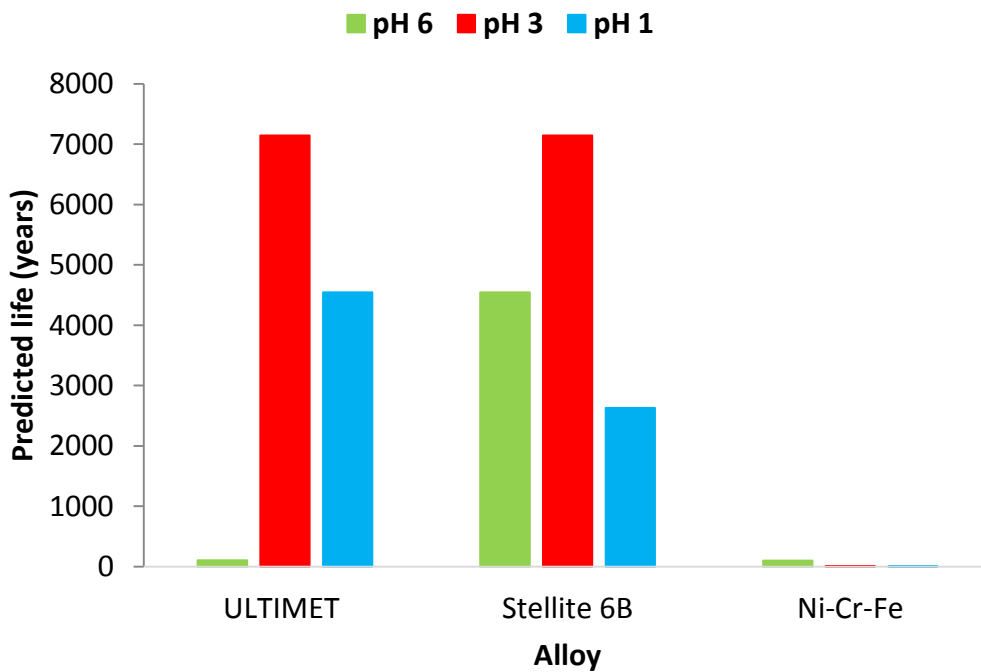
At pH 1, the annual cost ranking (US\$/y) of the coatings (Figure 7.9) due to corrosion at was: ULTIMET No Ru (15.40) > ULTIMET + 0.3 wt% Ru (10.40) > Ni-Cr-Fe (9.06) > Stellite 6 + 0.6 wt% Ru (7.60) > ULTIMET + 0.6 wt% Ru (5.80) > Stellite 6 + 0.3 wt% Ru (3.70). From the ranking, Ni-Cr-Fe appeared to have a lower cost than the other coatings apart from ULTIMET No Ru and ULTIMET + 0.3 wt% Ru. It has the lowest expected life.

The annual cost ranking (US\$/kg) of the coatings (Figure 7.11) due to tribocorrosion at pH 6 was: Ni-Cr-Fe (523.41) > ULTIMET No RU (88.20) > ULTIMET + 0.6 wt% Ru (84.30) > Stellite 6 No Ru (39.60) > Stellite 6 + 0.6 wt% Ru (37.90). This ranking showed Ni-Cr-Fe coating was the most expensive coating per year, and it has a shortest life based on plant experience (Figure 7.12).

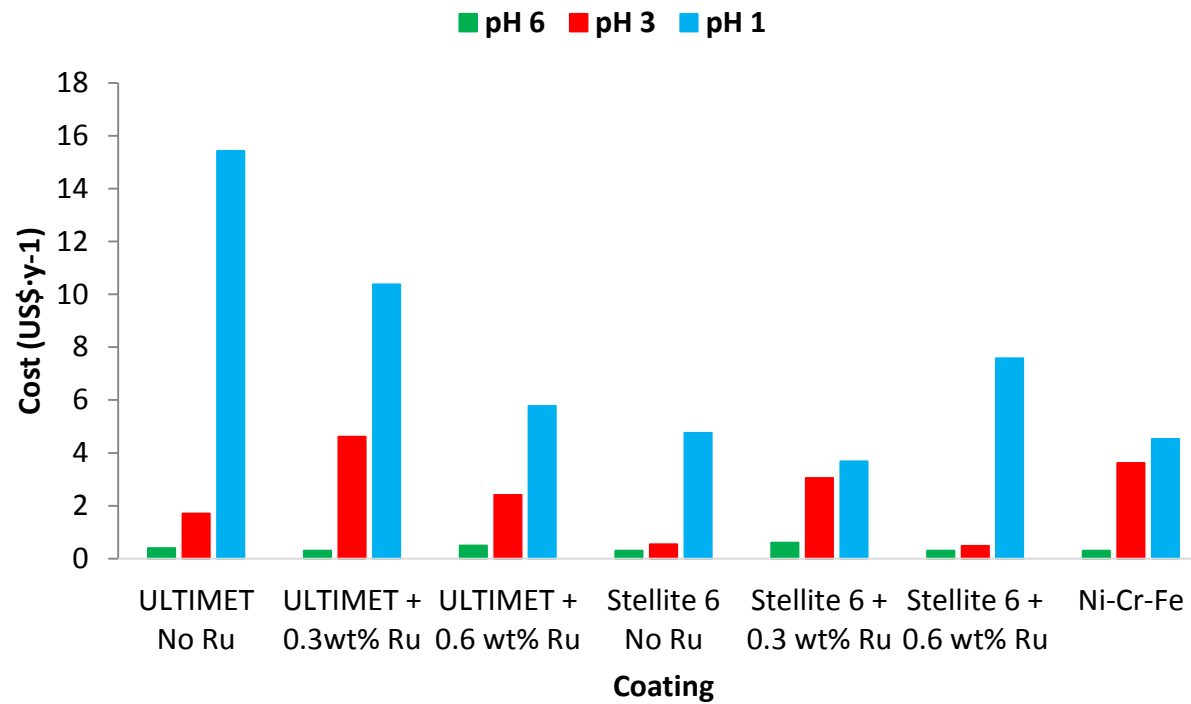




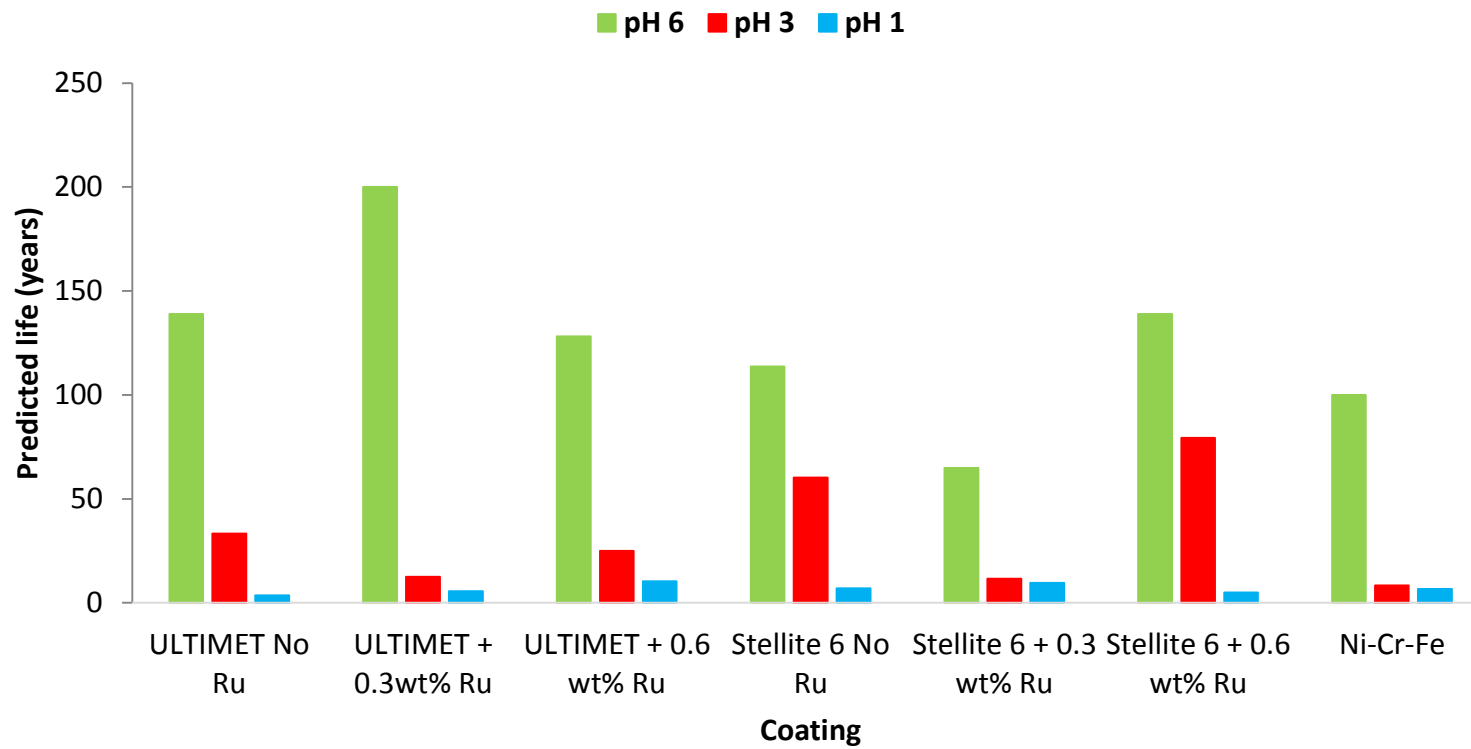
**Figure 7.7.** Cost comparison of alloys due to corrosion in synthetic mine water at pH 6, 3 and 1.



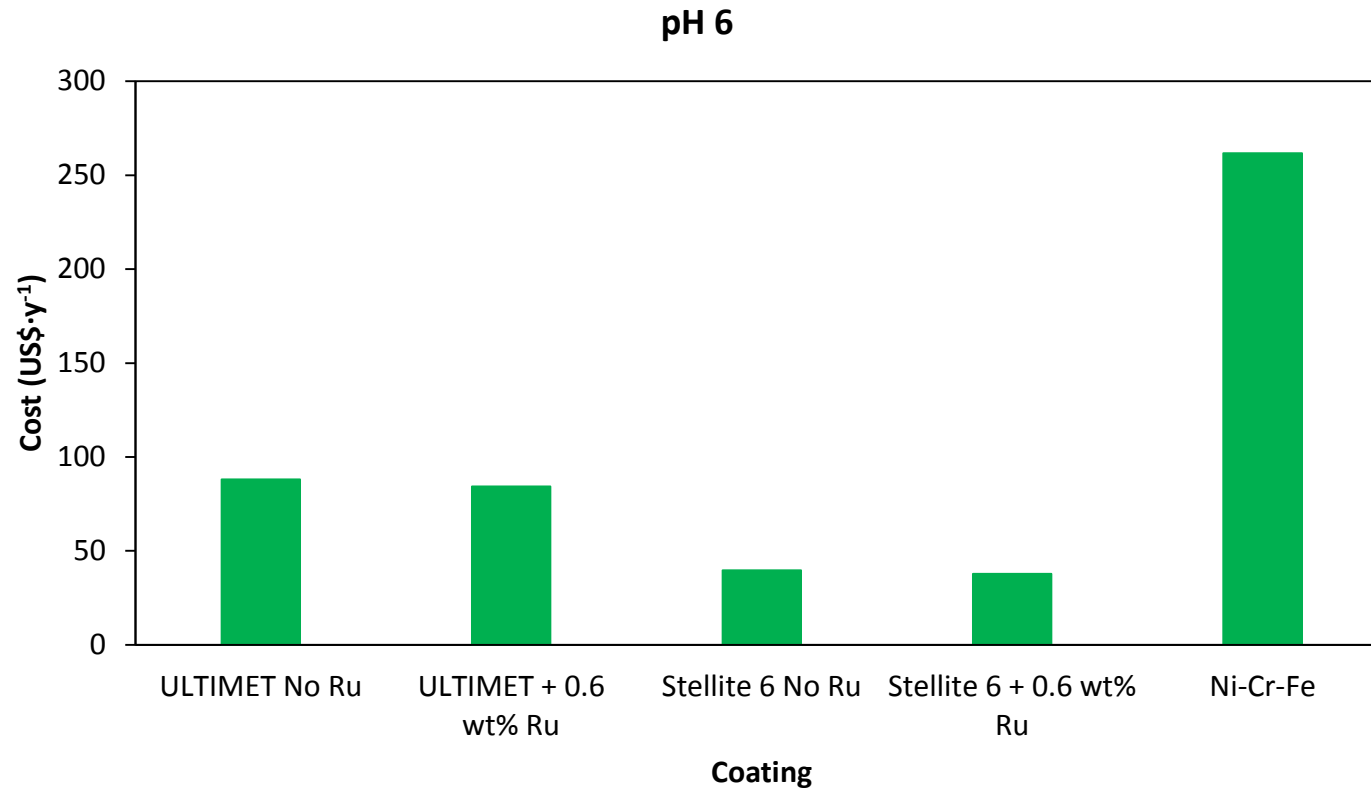
**Figure 7.8.** Prediction of life comparison of alloys due to corrosion in synthetic mine water at pH 6, 3 and 1.



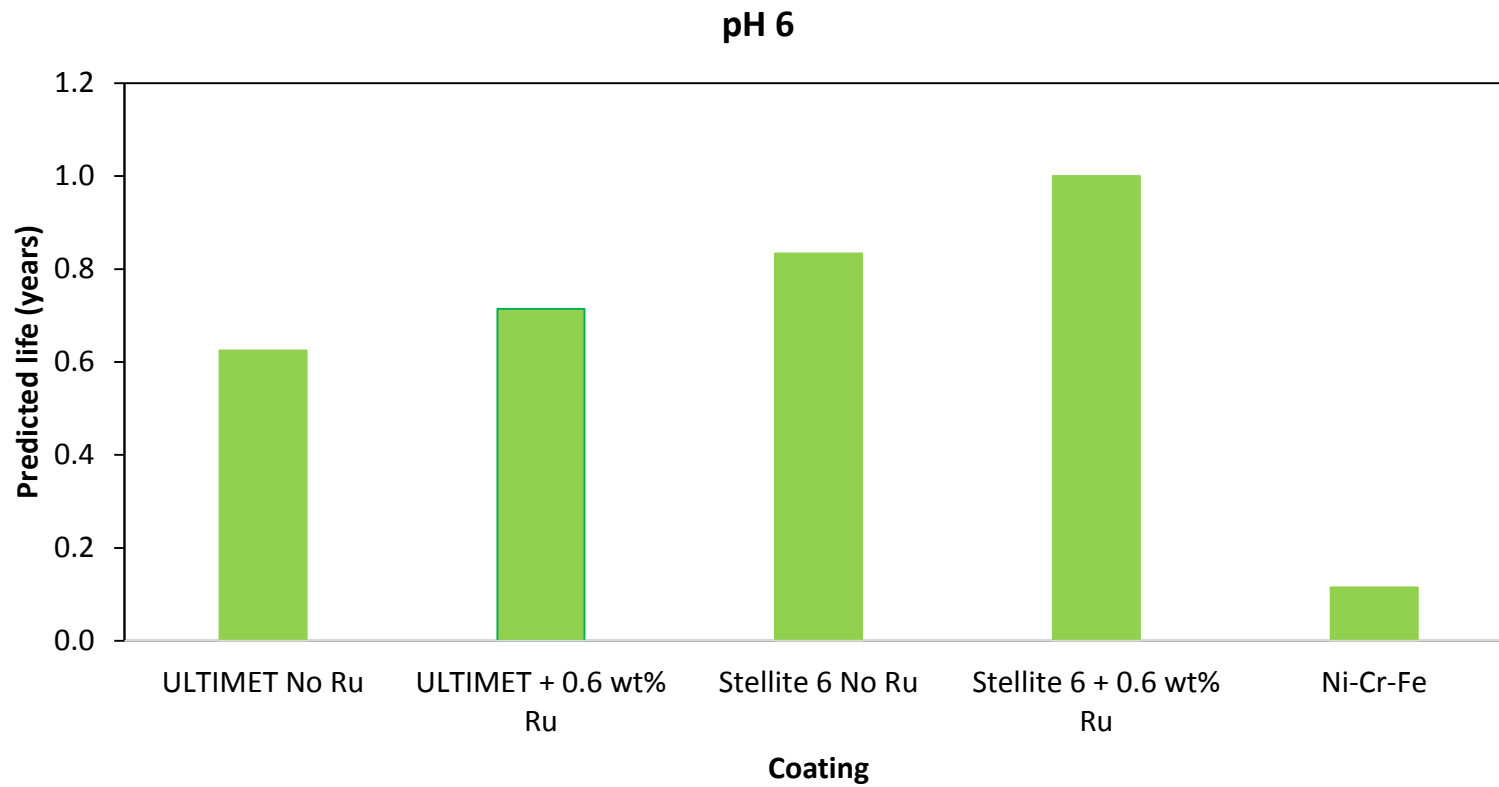
**Figure 7.9.** Cost comparison of coatings with no Ru, nominal 0.3 wt% Ru and nominal 0.6 wt% Ru and Ni-Cr-Fe coating due to corrosion in synthetic mine water at pH 6, 3 and 1.



**Figure 7.10.** Prediction of life comparison of coatings due to corrosion in synthetic mine water at pH 6, 3 and 1.



**Figure 7.11.** Cost comparison of coatings with no Ru, nominal 0.3 wt% Ru and nominal 0.6 wt% Ru and Ni-Cr-Fe coating due to tribocorrosion in synthetic mine water at pH 6.



**Figure 7.12.** Prediction of life comparison of coatings due to tribocorrosion in synthetic mine water at pH 6.

From the cost comparisons, Stellite 6B bulk alloy and the Stellite 6 coatings showed lower costs than the other coatings. If the cost of replacement of shaft sleeves at the Otjihase Underground Mine is US\$ 15 080.00 (R 226 200.00) and the total cost to replace valves by a Stellite 6B material, and shaft sleeve coating by Stellite 6 with 0.6 wt% Ru for a pump, the total cost for this would be US\$ 6 533.35 (R 97 999.80), then the cost saving due to corrosion is US\$ 8 546.68 (R 12 200.20). This means the material costs when using Stellite 6B bulk alloy and Stellite 6 with nominal 0.6 wt% Ru coating will be lower than for Ni-Cr-Fe coating which are being currently used at the Otjihase Underground Mine. Therefore, it is recommended that the shaft sleeve coating be made from Stellite 6 with nominal 0.6 wt% Ru coating and the valve should be made out of Stellite 6B bulk alloy.

# CHAPTER 8: CONCLUSIONS AND RECOMMENDATIONS

---

## 8.1 Conclusions

### 8.1.1 Failure of Otjihase Underground Mine pump systems

1. The first objective of the research was to identify the compositions of the pump components being used in the mine. Optical emission spectrometry and SEM-EDX showed that the sleeve was a medium-carbon steel (AISI 1526 grade), the coating on the shaft sleeve was a nickel-chromium alloy (UNS N06600 grade), and the valve was a ductile (nodular) cast iron (UNS F32800 (A536) grade). Hardness results showed the shaft sleeve coating had the highest hardness.
2. The degradation of the Ni-Cr-Fe coating of the pump sleeve at the Otjihase Underground Mine was caused by a synergetic effect of chemical reactions of mine water slurry with reacting with the steels, and abrasion wear due to the friction between the debris trapped in packing glands and steel surfaces, leaving the underlying mild steel substrate suffered uniform corrosion.
3. The Otjihase Underground Mine water analysis for Conveyor No. 6 pump showed many more suspended particles, higher conductivity and salinity, ion concentrations of alkali and alkaline earth elements, rare earth elements, chlorides, sulphates and nitrates (hence higher acidity), and lower resistivity than the Kuruma, North, Satellite and 22 BOOC water pumps, explaining the higher corrosion.

### 8.1.2 Comparison of the targeted substitute alloys (bulk materials)

1. Stellite 6B ( $368 \pm 13$  HV<sub>3</sub>) and ToughMet 3 ( $368 \pm 14$  HV<sub>3</sub>) had very similar and high hardnesses, while ULTIMET ( $304 \pm 22$  HV<sub>3</sub>) had a slightly lower hardness. Hastelloy G30 had a lowest hardness of  $180 \pm 10$  HV<sub>3</sub>.
2. Stellite 6B had the lowest corrosion current densities in synthetic mine water (pH 6, 3 and 1) at room temperature.
3. ULTIMET, Stellite and Hastelloy G30 had high resistance to localised corrosion, while ToughMet 3 did not.
4. Surface morphologies (studied by SEM) indicated general corrosion with shallow pits and intergranular corrosion for ULTIMET in synthetic mine water. Stellite 6B experienced intergranular corrosion, with carbides inside pits and oxides on the surface at all pH values. ToughMet 3 had severe selective corrosion attack on the copper-rich parts.



5. At high pH, Stellite 6B had a lower corrosion rate, while at lower pH values ULTIMET showed slightly lower, but very similar, corrosion rates to Stellite 6B. Thus, Stellite 6B is better than ULTIMET for applications where corrosion may be experienced at high pH, although at low pH either alloy may be used.
6. ULTIMET had higher wear rates than Stellite 6B at both 5 N and 10 N loads in sliding wear. This showed Stellite 6B had higher resistance to wear.
7. ULTIMET had slip steps on the surface near the wear track with little debris, while Stellite 6B had some of the matrix ploughed out, leaving carbides on the surface and debris in the grooves in sliding wear.

### 8.1.3 Comparison of the spray-coatings

1. Ru additions to ULTIMET and Stellite 6 coatings affected the hardness of the coatings. The ULTIMET coating with nominal 0.3 wt% Ru had a higher hardness than nominal 0.6 wt% Ru and 0 wt% Ru, while increased Ru contents in Stellite 6 coatings increased the hardness. The Ru distribution was poor, and this probably gave the strange results. Cr<sub>2</sub>O<sub>3</sub> had the highest hardness of all the coatings.
2. Cyclic potentiodynamic polarisation measurements in synthetic mine water showed that all coatings displayed active-passive transition behaviour. The least corrosion was found for coatings with nominal 0.3 wt% Ru at pH 6. The corrosion rates of the Cr<sub>2</sub>O<sub>3</sub> were higher than ULTIMET and Stellite 6 coatings, and was probably due to the cracks at the Cr<sub>2</sub>O<sub>3</sub> coating – NiCrAlY bond coating interface.
3. The lack of hysteresis loops on the reverse scans of all the samples tested indicated high resistance to localised corrosion.
4. The sliding abrasive wear rates (*k*) of the coatings and steel substrate were lower at 5 N, and higher at 10 N, as expected. Stellite 6 had the lowest *k* at all loads tested. At 5 N, Stellite 6 with nominal 0.3 wt% Ru had the lowest *k*, while at 10 N, the lowest *k* was for Stellite 6 with nominal 0.6 wt% Ru.
5. The tribocorrosion wear rates for the coatings on mild steel of Stellite 6 with no Ru were lower than for ULTIMET without Ru at all loads. With increased load, the tribocorrosion wear rates also increased for Cr<sub>2</sub>O<sub>3</sub> coatings. Stellite 6 coating with nominal 0.6 wt% Ru showed good tribocorrosion resistance, with the lowest tribocorrosion rates at all loads which was better than the Cr<sub>2</sub>O<sub>3</sub> benchmark coating.
6. The cost comparisons of the best materials showed that the Stellite 6B bulk alloy and the nominal 0.6 wt% Ru Stellite 6 coating had lower costs and longer expected operational time than the other materials.

## 8.2 Recommendations to Otjihase Underground Mine

Based on a good combination of high hardness and high resistance against electrochemical corrosion, tribocorrosion and sliding abrasive wear of the bulk Stellite 6B alloy and the nominal 0.6 wt% Ru Stellite 6 coating, the following recommendations are made for solving tribocorrosion problems at Otjihase Underground Mine:

1. The nominal 0.6 wt% Ru Stellite 6 coating is recommended to coat the shaft sleeve at Otjihase Underground Mine, and it should be evaluated there.
2. The Stellite 6B is recommended for the valve at Otjihase Mine, and it should also be evaluated there.

## 8.3 Recommendations for further study

The following strategy may be implemented in future work to understand and potentially improve the corrosion and wear resistance of the coatings on mild steel:

1. Elemental analysis for ULTIMET and Stellite 6 should be done using techniques other than SEM-EDX analysis, such as inductively plasma optical emission spectrometry (ICP-OES) or electron probe micro-analyser (EPMA, with wavelength-dispersive spectrometry (WDS), to accurately measure C, Ru and O contents, and so more properly understand their effects.
2. Heat treatments of the bulk alloys should be done to improve their microstructures and hence their properties, especially their carbide distributions which could improve their corrosion and wear resistance.
3. Stellite 6 and ULTIMET coatings should be studied further after producing more homogeneous powders by milling their powders with Ru to produce homogeneous distributions of Ru. Higher additions of Ru could be added, i.e. more than nominal 0.6 wt% Ru, although this would be more expensive.
4. Corrosion tests of the bulk Stellite 6B and Stellite 6 coatings should be done in actual Otjihase Mine water, using the most corrosive water available, *i.e.* Conveyor 6 sump in summer.

## REFERENCES

---

1. Mufenda, M. and Ellmies, R. (2009) Characterization of contamination of stream sediments and surface water at Otjihase mine, Namibia, *Communs Geological Survey of Namibia*, 14, 41-55.
2. Weatherly International PLC (2010) Central Operations Executive Summary, [www.weatherlyplc.com/operations/central-operations/](http://www.weatherlyplc.com/operations/central-operations/), Accessed 10 July 2012.
3. Dunn, J.P., Koppula, P.R., Stenger, H.G. and Wachs, I.E. (1998) Oxidation of sulfur dioxide to sulfur trioxide over supported vanadia catalysts, *Applied Catalysis B: Environmental*, 19(2), 103-117.
4. Roy, P. and Sardar, A. (2015) SO<sub>2</sub> Emission control and finding a way out to produce sulphuric acid from industrial SO<sub>2</sub> emission, *Chemical Engineering and Process Technology*, 6(2), 1-7.
5. Schweitzer, P.A. (2010) *Fundamentals of corrosion: mechanisms, causes and preventative methods*, CRC Press, Florida, USA.
6. Yang, L. (2008) *Techniques for corrosion monitoring*, Woodhead Publishing Series in Metals and Surface Engineering, and CRC Press LLC, Texas, USA.
7. Bradford, S.A. (2001) *Corrosion Control*, CASTI Publishing Inc., Edmonton, Canada.
8. Azzia, M., Paquette, M., Szpunar, J.A., Klemberg-Sapieha, J.E. and Martinu, L. (2009) Tribocorrosion behaviour of DLC-coated 316L stainless steel, *Wear*, 267, 860–866.
9. Landolt, D. and Mischler, S. (2011) *Tribocorrosion of Passive Metals and Coatings*, Woodhead Publishing: Elsevier Science, Cambridge, England.
10. Bosch, R.W., Féron, D. and Celis, J.P. (2007) *Electrochemistry in light water reactors*, Woodhead Publishing, Cambridge, England. 222
11. McEwan, J.J. (2004) *Corrosion Control in Southern Africa*, Corrosion Institute of Southern Africa, Johannesburg, South Africa.
12. Zhang D.K., Wang, S.Q., Shen, Y. and Ge, S.R. (2012) Interactive mechanisms of fretting wear and corrosion of steel wires in alkaline corrosion medium, *Proceedings of the Institution of Mechanical Engineers, Part J: Journal of Engineering Tribology*, 226(9), 738-747.
13. Banas, J. and Mazurkiewicz, A. (2000) The effect of copper on passivity and corrosion behaviour of ferritic and ferritic–austenitic stainless steels, *Materials Science and Engineering: A.*, 277(1–2), 183-191.
14. Lin, H.T., Tsai, W.T., Lee, J.T. and Huang, C.S. (1992) The electrochemical and corrosion behavior of austenitic stainless steel containing Cu, *Corrosion Science*, 33(5), 691-697.
15. Oguzie, E.E., Li, J., Liu, Y., Chen, D., Li, Y., Yang, K. and Wang, F. (2010) The effect of Cu addition on the electrochemical corrosion and passivation behavior of stainless steels, *Electrochimica Acta*, 55(17), 5028-5035.

16. Ogura, S., Sugimoto, K. and Sawada, Y. (1976) Effects of Cu, Mo and C on the corrosion of deformed 18Cr8Ni stainless steels in H<sub>2</sub>SO<sub>4</sub>/NaCl solutions, *Corrosion Science*, 16(5), 323-337.
17. Pardo, A., Merino, M.C., Carboneras, M., Coy, A.E. and Arrabal, R. (2007) Pitting corrosion behaviour of austenitic stainless steels with Cu and Sn additions, *Corrosion Science*, 49(2), 510-525.
18. Hong, J.H., Lee, S.H., Kim, J.G. and Yoon, J.B. (2012) Corrosion behaviour of copper containing low alloy steels in sulphuric acid, *Corrosion Science*, 54, 174-182.
19. Fontana, M.G. (1987) *Corrosion Engineering: 3<sup>rd</sup> Edn.*, McGraw-Hill Book Company, New York, USA.
20. Mobin, M. and Shabnam, H. (2010) Corrosion behaviour of mild steel and SS 304L in the presence of dissolved copper, *Journal of Minerals and Materials Characterization and Engineering*, 9(12), 1113-1130.
21. Jirarungsatian, C. and Prateepasen, A. (2010) Pitting and uniform corrosion source recognition using acoustic emission parameters, *Corrosion Science*, 52(1), 187-197.
22. Smith, W.F. and Hashemi, J. (2006) *Foundations of materials science and engineering*, McGraw-Hill, Inc., New York, USA.
23. Kruger, J. and Rhyne, K. (1982) Current understanding of pitting and crevice corrosion and its application to test methods for determining the corrosion susceptibility of nuclear waste metallic containers, *Nuclear and Chemical Waste Management*, 3(4), 205-227.
24. Dundas, H.J. and Bond, A.P. (1978) *Intergranular Corrosion of Stainless Alloys*, ASTM International, Philadelphia, USA.
25. Gellings, P.J. and de Jongh, M.A. (1967) Grain boundary oxidation and the chromium-depletion theory of intercrystalline corrosion of austenitic stainless steels, *Corrosion Science*, 7(7), 413-421.
26. Parkins, R.N. (1982) *Corrosion Process*, Applied Science Publishers Ltd, London, England.
27. Callister, W.D. and Rethwisch, D.G. (2011) *Materials Science and Engineering: An Introduction*, 8th Edn., John Willy and Sons, Inc., New York, USA.
28. Davis, J.R. (2000) *Corrosion: Understanding the basics (06691G)*, ASM International, Ohio, USA.
29. Guthrie J., Battat, B. and Grethlein, C. (2002) Accelerated corrosion testing, *The AMPTIAC Quarterly*, 6(3), 1-5.
30. Denny, A.J. (1996) *Principles and prevention of corrosion: 2 Edn.*, Prentice Hall New York, USA.
31. Corrosionpedia. Potentiodynamic, [www.corrosionpedia.com](http://www.corrosionpedia.com), Accessed November 2014.
32. Princeton Applied Research (1982) Basics of corrosion measurements, Application note Corr-1., [www.princetonappliedresearch.com](http://www.princetonappliedresearch.com), Accessed April 2014.

33. Enos, D.G. and Scribner, L.L. (1997) The potentiodynamic polarisation scan: Technical Report 33, Solartron Instrument, Accessed April 2014.
34. Kelly, R.G., Scully, J.R., David, W., Shoosmith, D.W. and Buchheit, R.G. (2003) Electrochemical Techniques in Corrosion Science and Engineering, Marcel Dekker, Inc., New York, USA.
35. Thompson, N.G., Beavers, J.A. and Durr, C.L. (1992) Potentiodynamic polarization studies on candidate container alloys for the Tuff Repository, Cortest Columbus Technologies, Inc., U.S. Nuclear Regulatory Commission, Columbus, USA.
36. Calle, L.M. and MacDowell, L.G. (2004) Electrochemical evaluation of stainless steels in acidified sodium chloride solutions, NASA Kennedy Space Center and ASRC Aerospace, Florida, USA.
37. Giordano, E.J., Alonso-Falleiros, N., Ferreira, I. and Balancin, O. (2010) Electrochemical behavior of two austenitic stainless steel biomaterials, *Revista Escola de Minas*, 63, 159-166.
38. Roberge, P.R. (2008) *Corrosion Engineering: Principles and Practice: 1<sup>st</sup> Edn.*, McGraw-Hill Companies, Inc., New York, USA.
39. Kumar, H. and Yadav, V. (2013) Corrosion characteristics of mild steel under different atmospheric conditions by vapour phase corrosion inhibitors, *American Journal of Materials Science and Engineering*, 1(3), 34-39.
40. Anejjar, A., Zarrok, H., Hammouti, B. and Ebenso, E.E. (2014) Inhibition of carbon steel corrosion in 1 M HCl medium by potassium thiocyanate, *Journal of the Association of Arab Universities for Basic and Applied Sciences*, 15, 21-27.
41. Sherif, E.S.M., Abdo, H.S. and Almajid, A.A. (2015) Corrosion behavior of cast iron in freely aerated stagnant Arabian Gulf seawater, *Materials*, 8, 2127-2138.
42. Ibrahim, M.A.M., Abd El Rehim, S.S. and Hamza, M.M. (2009) Corrosion behavior of some austenitic stainless steels in chloride environments, *Materials Chemistry and Physics*, 115(1), 80-85.
43. Andijani, I. and Turgoose, S. (1999) Studies on corrosion of carbon steel in deaerated saline solutions in presence of scale inhibitor, *Desalination*, 123(2-3), 223-231.
44. Noor, E.A. and Al-Moubaraki, A.H. (2008) Corrosion behavior of mild steel in hydrochloric acid solutions, *International Journal of Electrochemical Science*. 3(7), 806-818.
45. Mennucci, M.M., Banczek, E.P., Rodrigues, P.R.P. and Costa, I. (2009) Evaluation of benzotriazole as corrosion inhibitor for carbon steel in simulated pore solution, *Cement and Concrete Composites*, 31(6), 418-424.
46. Mobin, M., Malik, A.U. and Andijani, I.N. (2007) The effect of heavy metal ions on the localized corrosion behavior of steels, *Desalination*, 217(1-3), 233-241.
47. Makar, J.M., Desmoyers, R. and MacDonald, S.E. (2001) Failure modes and mechanisms of gray cast iron pipes, *Proceedings of Underground Infrastructure Research: Municipal, Industrial and Environmental Research Applications*, Institute for Research in Construction, Kitchener, Canada.

48. Petersen, R.B. and Melchers, R.E. (2012) Long-term corrosion of cast iron cement lined pipes, Australian Corrosion Association, 23, 1-12.
49. Flowserve Corporation (2001) Graphitic Corrosion, FlowServe Materilas News letter, 2(2), 1-4, [www.flowserve.net/files/Files/Literature/Foundry/newsletters/mn\\_2002\\_12.pdf](http://www.flowserve.net/files/Files/Literature/Foundry/newsletters/mn_2002_12.pdf), Accessed November 2013.
50. Mohebbi, H. and Li, C.Q. (2011) Experimental investigation on corrosion of cast iron pipes, International Journal of Corrosion, 2011, 1-12.
51. Mehra, R. and Soni, A. (2002) Cast iron deterioration with time in various aqueous salt solutions, Bulletin of Materials Science, 25(1), 53-58.
52. Kuzucu, V., Ceylan, M., Çelik, H. and Aksoy, İ. (1998) Phase investigation of a cobalt base alloy containing Cr, Ni, W and C, Journal of Materials Processing Technology, 74(1–3), 137-141.
53. Disegi, J.A., Kennedy, R.L. and Pilliar, R. (1999) Cobalt-base alloys for biomedical applications, ASTM Special Technical Publication: STP 1365, West Conshohocken, Pennsylvania, USA.
54. Yangtao, X., Tiandong, X. and Yanling, H. (2009) Microstructures comparison of Stellite 6 alloy by self- propagating high-temperature synthesis and cast HS111 alloy, Rare Metal Materials and Engineering, 38(8), 1333-1337.
55. Tomlinson, W.J. and Linzell, C.R. (1988) Anodic polarization and corrosion of cemented carbides with cobalt and nickel binders, Journal of Materials Science, 23(3), 914-918.
56. Sacks, N. (2003) The wear and corrosive-wear response of tungsten carbide-cobalt hardmetals under woodcutting and three body abrasion conditions, PhD thesis, Faculty of Engineering, University of Erlangen-Nürnberg, Germany.
57. Frenk, A. and Kurz, W. (1994) Microstructural effects on the sliding wear resistance of a cobalt-based alloy, Wear, 174(1), 81-91.
58. Contu, F., Elsener, B. and Böhni, H. (2005) Corrosion behaviour of CoCrMo implant alloy during fretting in bovine serum, Corrosion Science, 47(8), 1863-1875.
59. Metikoš-Huković, M. and Babić, R. (2007) Passivation and corrosion behaviours of cobalt and cobalt–chromium–molybdenum alloy, Corrosion Science, 49(9), 3570-3579.
60. Badawy, W.A., Al-Kharafi, F. M. and Al-Ajmi, J.R. (2000) Electrochemical behaviour of cobalt in aqueous solutions of different pH, Journal of Applied Electrochemistry, 30(6), 693-704. 229
61. Sarantopoulos, D.M., Beck, K.A., Holsen, R. and Berzins, D.W. (2011) Corrosion of CoCr and NiCr dental alloys alloyed with palladium, The Journal of Prosthetic Dentistry, 105(1), 35-43.
62. Liu, H., Tao, J., Xu, J., Chen, Z. and Gao, Q. (2009) Corrosion and tribological behaviors of chromium oxide coatings prepared by the glow-discharge plasma technique, Surface and Coatings Technology, 204(1–2), 28-36.

63. Pang, X., Gao, K., Yang, H., Qiao, L., Wang, Y. and Volinsky, A. A. (2007) Interfacial microstructure of chromium oxide coatings, *Advanced Engineering Materials*, 9(7), 594-599.
64. Cetinel, H., Celik, E. and Kusoglu, M.I. (2008) Tribological behavior of Cr<sub>2</sub>O<sub>3</sub> coatings as bearing materials, *Journal of Materials Processing Technology*, 196(1–3), 259-265.
65. Toma, D., Brandl, W. and Marginean, G. (2001) Wear and corrosion behaviour of thermally sprayed cermet coatings, *Surface and Coatings Technology*, 138(2–3), 149-158.
66. Li, C.L., Zhao, H.X. and Matsumura, M. (2000) Corrosion properties of materials coated with Cr<sub>2</sub>O<sub>3</sub>/NiCr and with Cr<sub>2</sub>O<sub>3</sub>+NiCr functionally gradient materials, *Materials and Corrosion*, 51(7), 502-510.
67. Dong, Z., Chen, W., Zheng, W. and Guzonas, D. (2012) Corrosion behavior of chromium oxide based ceramics in supercritical water (SCW) environments, *Corrosion Science*, 65, 461-471.
68. Wang, P.Z., Yang, Y.S., Ding, G., Qu, J.X. and Shao, H.S. (1997) Laser cladding coating against erosion-corrosion wear and its application to mining machine parts, *Wear*, 209(1–2), 96-100.
69. Lalvani, S.B., Swisher, J. H. and Pagano, M. A. (1990) A review of chlorine-induced corrosion in underground mines and coal preparation plants, *Fuel Processing Technology*, 25(1), 17-32.
70. White, R.A. and Hagginson, A. (1985) Factors affecting the corrosivity of underground minewater, *Proceedings of Mintek 50: International Conference on Mineral Science and Technology*, Randburg, South Africa.
71. GRUNDFOS A/S Mining. Pumps in metal mining, [www.grundfos.com](http://www.grundfos.com), Accessed May 2013.
72. Carter, A.M.F. (1986) Erosion, corrosion, and the abrasion of material-handling systems in the mining industry, *Journal of the South African Institute of Mining and Metallurgy*, 86(7), 235-242.
73. Ash, S.H., Dierks, H.A., Felegy, E.W., Huston, K.M., Kennedy, D.O., Miller, P.S. and Rosella, J.J. (1955) Corrosive and erosive effects of acid mine waters on metals and alloys for mine pumping equipment and drainage facilities, Bureau of Mines: Bulletin 555, United States Government Printing Office, Washington, USA, 4-44.
74. Flynn, D.J. (2009) *The Nalco Water Handbook*, 3<sup>rd</sup> Edn., McGraw-Hill, Inc., New York, USA.
75. Wu, L.K., Hu, J.M. and Zhang, J.Q. (2012) Electrodeposition of zinc-doped silane films for corrosion protection of mild steels, *Corrosion Science*, 59, 348-351.
76. González, M.B. and Saidman, S.B. (2011) Electrodeposition of polypyrrole on 316L stainless steel for corrosion prevention, *Corrosion Science*, 53(1), 276-282.
77. Romero, R., Martin, F., Ramos-Barrado, J.R. and Leinen, D. (2010) Study of different inorganic oxide thin films as barrier coatings against the corrosion of galvanized steel, *Surface and Coatings Technology*, 204(12–13), 2060-2063.



78. Zeng, Z., Sakoda, N., Tajiri, T. and Kuroda, S. (2008) Structure and corrosion behavior of 316L stainless steel coatings formed by HVOF spraying with and without sealing, *Surface and Coatings Technology*, 203(3–4), 284-290.
79. Kartsonakis, I.A., Balaskas, A.C., Koumoulos, E.P., Charitidis, C.A. and Kordas, G.C. (2012) Incorporation of ceramic nanocontainers into epoxy coatings for the corrosion protection of hot dip galvanized steel, *Corrosion Science*, 57, 30-41.
80. Smith, T. (2005) Phalaborwa Copper Mine: Case history, *Hot Dip Galvanizing Today*, 2(4), 57.
81. Díaz, B., Światowska, J., Maurice, V., Seyeux, A., Härkönen, E., Ritala, M., Tervakangas, S., Kolehmainen, J. and Marcus, P. (2013) Tantalum oxide nanocoatings prepared by atomic layer and filtered cathodic arc deposition for corrosion protection of steel: Comparative surface and electrochemical analysis, *Electrochimica Acta*, 90, 232-245.
82. Fang, L., Xie, L.B., Hu, J., Li, Y. and Zhang, W.T. (2011) Study on the growth and corrosion resistance of manganese phosphate coatings on 30CrMnMoTi alloy steel, *Physics Procedia*, 18, 227-233.
83. Peng, T. and Man, R. (2009) Rare earth and silane as chromate replacers for corrosion protection on galvanized steel, *Journal of Rare Earths*, 27(1), 159-163.
84. Thompson, S.C. (1995) Molybdates: An Alternative to hexavalent chromates in corrosion prevention and control, *Proceedings of the 4<sup>th</sup> Annual Air Force Worldwide Pollution Prevention*, August 14-17, San Antonio, Texas, 50-56.
85. Kalendová, A., Veselý, D. and Stejskal, J. (2008) Organic coatings containing polyaniline and inorganic pigments as corrosion inhibitors, *Progress in Organic Coatings*, 62(1), 105-116.
86. Hu, J., Li, X., Gao, J. and Zhao, Q. (2009) UV aging characterization of epoxy varnish coated steel upon exposure to artificial weathering environment, *Materials and Design*, 30(5), 1542-1547.
87. Potgieter, J.H. (1991) Alloys cathodically modified with noble metals, *Journal of Applied Electrochemistry*, 21(6), 471-482.
88. International Platinum Group Metals Association (IPA): PGM Facts, [www.ipa-news.com](http://www.ipa-news.com), Accessed March 2015.
89. Sherif, E.S., Potgieter, J.H., Comins, J.D., Cornish, L., Olubambi, P.A. and Machio, C.N. (2009) Effects of minor additions of ruthenium on the passivation of duplex stainless-steel corrosion in concentrated hydrochloric acid solutions, *Journal of Applied Electrochemistry*, 39(8), 1385-1392.
90. Banda, S.C.K. and van der Merwe, J. (2014) Effect of small additions of ruthenium on pitting corrosion resistance of LDX2101 duplex stainless steel, *Corrosion Engineering, Science and Technology*, 49(1), 32-38.
91. Reclaru, L., Lüthy, H., Eschler, P-Y, Blatter, A. and Susz, C. (2005) Corrosion behaviour of cobalt–chromium dental alloys doped with precious metals, *Biomaterials*, 26(21), 4358-4365.

92. Potgieter, J.H., Thomson, J., Adams, F.V. and Afolabi, A.S. (2014) Effect of additions of Ru and Pd on the electrochemical behaviour of austenitic stainless steel in organic acids, *International Journal of Electrochemical Science*, 9, 6451-6463.
93. Olaseinde, O.A. (2014) Heat treatment and corrosion behaviour of 2101 duplex stainless steel cathodically modified with ruthenium, PhD thesis, Faculty of Engineering and the Built Environment, University of the Witwatersrand, Johannesburg.
94. Pirso, J., Viljus, M., Juhani, K. and Letunovič, S. (2009) Two-body dry abrasive wear of cermets, *Wear*, 266(1–2), 21-29.
95. Karamiş, M.B., Yildizli, K. and Erođlu, M. (2006) Erosion behavior of hardfaced AISI 1020 steel, *Proceedings of the 5<sup>th</sup> International Conference on Tribology, AITC-AIT*, 1-9.
96. Gohar, R. and Rahnejat, H. (2008) *Fundamentals of Tribology*, Imperial College Press, London, England.
97. Bhushan, B. (2002) *Introduction to Tribology*, John Wiley and Sons Inc., New York, USA.
98. Blau, P.J. (2001) The significance and use of the friction coefficient, *Tribology International*, 34(9), 585-591.
99. Williams, J.A. (2005) *Engineering Tribology*, Cambridge University Press, Cambridge, England.
100. Petrica, M., Badisch, E. and Peinsitt, T. (2013) Abrasive wear mechanisms and their relation to rock properties, *Wear*, 308(1–2), 86-94.
101. Gee, M.G., Gant, A.J., Roebuck, B. and Mingard, K.P. (2014) *Wear of hardmetals*, in *Comprehensive Hard Materials*, Elsevier: Oxford, England.
102. Yust, C.S. (1985) *Tribology and wear*, *International Metals Reviews*, 30(1), 141-154.
103. Zum Gahr, K. H. (1987) *Microstructure and wear of materials*, Elsevier Science Publisher B.V, 10, Amsterdam, The Netherlands.
104. Miller, R.S. (1993) Corrosion in pumps and other damage mechanisms, *Proceedings of the 10<sup>th</sup> International Pump Users Symposium*, Turbomachinery Laboratory, Texas A and M, University System, 111-133.
105. Pirso, J., Viljus, M., Letunovič, S., Juhani, K. and Joost, R. (2011) Three-body abrasive wear of cermets, *Wear*, 271(11–12), 2868-2878.
106. Hurricks, P.L. (1973) Some metallurgical factors controlling the adhesive and abrasive wear resistance of steels: A review, *Wear*, 26(3), 285-304.
107. Industeel ArcelorMittal Group, *Introduction to abrasion phenomenon*, [www.creusabro.com](http://www.creusabro.com), Accessed 25 November 2014.
108. Buttery, T.C. and Archard, J.F. (1970) Grinding and abrasive wear, *Proceedings of the Institution of Mechanical Engineers*, 185(1), 537-551.
109. Popov, V.S. and Nagorny, P.L. (1971) Resistance to abrasive wear of complex-alloyed austenitic alloys, *Metal Science and Heat Treatment*, 13(3), 252-254.

110. Kuiry, S. (2012) Evaluation of wear-corrosion synergy through tribocorrosion studies, Tribology and Mechanical Testing, Bruker Nano Surfaces Division.
111. Sethuramiah, A. (2003) Lubricated wear Science and Technology, in Tribology Series, Elsevier Science B.V, Amsterdam, The Netherlands.
112. Klarstrom, D. and Crook, P. (2001) Cobalt Alloys: Properties and Applications, Encyclopedia of Materials: Science and Technology, 2<sup>nd</sup> Edn., Elsevier: Oxford, England, 1281-1288.
113. Antony, K. (1983) Wear-resistant cobalt-base alloys, Journal of Metals, 35(2), 52-60.
114. Yu, H., Ahmed, R., de Villiers Lovelock, H. and Davies, S. (2007) Tribo-mechanical evaluations of cobalt-based (Stellite 4) alloys manufactured via hiping and casting, Proceedings of the World Congress on Engineering, London, U.K, 1385-1390.
115. Levy, A.V. and Crook, P. (1991) The erosion properties of alloys for the chemical processing industries, Wear, 151(2), 337-350.
116. Zhang, K. and Battiston, L. (2002) Friction and wear characterization of some cobalt- and iron-based superalloys in zinc alloy baths, Wear, 252(3), 332-344.
117. Küçükömeroğlu, T. and Kara, L. (2014) The friction and wear properties of CuZn39Pb3 alloys under atmospheric and vacuum conditions, Wear, 309(1–2), 21-28.
118. De Gee, A.W.J. and Zaat, J.H. (1962) Wear of copper alloys against steel in oxygen and argon, Wear, 5(4), 257-274.
119. Cawley, J., Metcalf, J.E.P., Jones, A.H., Band, T.J. and Skupien, D.S. (2003) A tribological study of cobalt chromium molybdenum alloys used in metal-on-metal resurfacing hip arthroplasty, Wear, 255(7–12), 999-1006.
120. Moore, A.J.W., Tegart, W.J.McG. (1952) Relation between friction and hardness, Proceedings of the Royal Society of London: Series A, Mathematical and Physical Sciences, 212(1111), 452-458.
121. HAYNES International, Corrosion-resistant alloys, [www.haynesintl.com](http://www.haynesintl.com), Accessed April 2013.
122. Ahn, H.S. and Kwon, O.K. (1999) Tribological behaviour of plasma-sprayed chromium oxide coating, Wear, 225–229, 814-824.
123. Negroni, G. (2014) Corrosion and tribocorrosion study of CoCrMo biomedical alloys, MSc Dissertation, Department of Chemistry, Materials and Chemical Engineering “Giulio Natta”, Polytechnic of Milan, Italy.
124. Ponthiaux, P., Wenger, F. and Celis, J.P. (2012) Tribocorrosion: Material behavior under combined conditions of corrosion and mechanical loading, INTECH Open Access Publisher.
125. Mischler, S. (2008) Triboelectrochemical techniques and interpretation methods in tribocorrosion: A comparative evaluation, Tribology International, 41(7), 573-583.
126. Chen, J. and Dong, H (2009) Corrosion and corrosion wear behaviour of plasma carburised Stellite 21 Co–Cr alloy, Tribology - Materials, Surfaces and Interfaces, 3(1), 24-30.

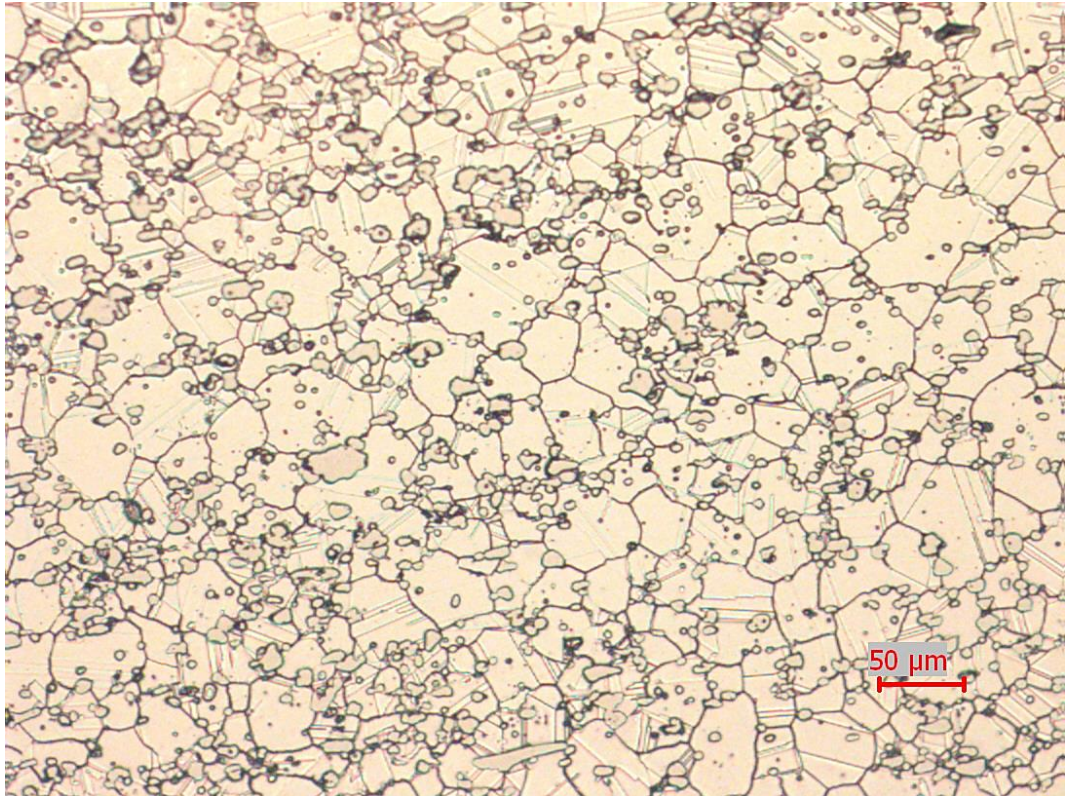
127. Fauchais, P. and Vardelle, A. (2012) Thermal sprayed coatings used against corrosion and corrosive wear, *Advanced Plasma Spray Applications*, University of Limoges, France.
128. American Welding Society (1985) *Thermal Spraying: Practice Theory and Application*, Florida, USA.
129. Schneider, K.E., Belashchenko, V., Dratwinski, M., Siegmann, S. and Zagorski, A. (2006) *Thermal spraying for power generation components*, WILEY-VCH Verlag GmbH and Co., Weinheim, Germany.
130. Davis, J.R. (2004) *Handbook of Thermal Spray Technology*, ASM International, Ohio, USA.
131. Lourens, J. (2012) Increase the operating life of pumps by using thermal spray coatings, [www.thermaspray.co.za](http://www.thermaspray.co.za), accessed May 2015.
132. Oksa, M., Turunen, E., Suhonen, T., Varis, T. and Hannula, S.P. (2011) Optimization and characterization of high velocity oxy-fuel sprayed coatings: Techniques, materials, and applications, *Coatings*, 1, 17-52.
133. Ogunmuyiwa, E.N. (2013) Processing, characterization and tribological assessment of novel WC-VC-Co coatings and alloys, PhD thesis, Faculty of Engineering and the Built Environment, University of the Witwatersrand, Johannesburg, South Africa.
134. Howse, H.J. and van Wyk, P. (1998) The application of thermal spray coatings for combating slurry erosion in centrifugal pumps, *Proceedings of the 6<sup>th</sup> International Tribology Conference of South African Institute of Tribology*, South African Institute of Tribology, Sandton, South Africa.
135. Pawlowski, L. (2008) *The Science and Engineering of Thermal Spray Coatings*, 2nd Edn., John Wiley and Sons, West Sussex, England.
136. Sulzer, Atmospheric plasma spraying (APS) for thermal insulation and improved wear resistance, [www.sulzer.com/en/Products-and-Services](http://www.sulzer.com/en/Products-and-Services), Accessed September 2015.
137. Flame Spray Technologies Ltd, HVOF - High velocity oxygen fuel-HVOF, <http://www.fst.nl/hvof/>, Accessed May 2015.
138. Jegadeeswaran, N., Ramesh, M.R., Prakrathi, S. and Bhat, K.U. (2014) Hot corrosion behaviour of HVOF sprayed Stellite-6 coatings on gas turbine alloys, *Transactions of the Indian Institute of Metals*, 67(1), 87-93.
139. Cramer, S.D. and Covino, B.S. (2005) *ASM Handbook: Corrosion: Materials*, 13B, ASM International, Ohio, USA.
140. Malvern Instruments Ltd, Laser diffraction: particle size distributions from nanometers to millimeters, <http://www.malvern.com/en/products/technology/laser-diffraction/>, Accessed March 2015.
141. Exner, H.E. and Hougardy, H.P. (1988) *Quantitative Image Analysis of Microstructures: A Practical and Assessment of Materials*, DGM Informationsgesellschaft Verlag, Germany.
142. Allen, C. (1991) Corrosion of galvanised steel in synthetic mine waters, *British Corrosion Journal*, 26(2), 93-102.

143. ASM International G5-94 (Re-approved 2004) (2010) Standard reference test methods for making potentiostatic and potentiodynamic anodic polarisation measurements, ASTM International, West Conshohocken, USA.
144. ASM International G102-89 (Re-approved 2010) (2010) Standard practise for calculation of corrosion rates and related information from electrochemical measurements, ASTM International, West Conshohocken, USA.
145. Coffey, G.W., Pederson, L.R., Ponds, D.M., Rieke, P.C. and Thomsen, E.C. (2007) Fabrication and characterization of a novel Luggin capillary reference electrode for use in solid state electrolytes, *Solid State Ionics*, 178(11–12), 827-832.
146. Cornish, L.A., Witcomb, M.J., Coetzee, S.H., Tshawe, W. and Prins, S.N. (2008) Anomalies and pitfalls in phase analyses using BSE, *Proc. Microsc. Soc. South. Afr.*, University of Botswana, Gaborone, 38, 9.
147. Klarstrom, D.L. (1993) Wrought cobalt- base superalloys, *Journal of Materials Engineering and Performance*, 2(4), 523-530.
148. Karassik, I.J., Messina, J.P., Cooper, P. and Heald, C.C. (2000) *Pump Handbook*, 3<sup>rd</sup> Edn., The McGraw-Hill Companies, Inc., New York, USA.
149. Bachus, L. and Custodio, A. (2003) *Know and Understand Centrifugal Pumps*, Elsevier Science, Oxford, England.
150. Girdhar, P., Moniz, O. and Mackay, S. (2005) *Practical Centrifugal Pumps: Design, Operation and Maintenance*, Newnes, Oxford, England.
151. Ilunga, O.K. Private communication: corrosion at the Otjihase Underground Mine, March 2012.
152. Weast, R.C. and Astle, M.J. (1978) *Handbook of Chemistry and Physics*, 59<sup>th</sup> Edn., CRC Press Inc., Florida, USA.
153. Massalski, T.B. (1990) *Binary Alloy Phase Diagrams*, 2<sup>nd</sup> Edn., ASM International: Metals Park, Ohio, USA.
154. Sebastiani, M., Mangione, V., de Felicis, D., Bemporad, E., Carassiti, F., Bemporad, E. and Carassiti, F. (2012) Wear mechanisms and in-service surface modifications of a Stellite 6B Co–Cr alloy, *Wear*, 290-291, 10-17.
155. Zhang, X., Li, Y., Tang, N., Onodera, E. and Chiba, A. (2014) Corrosion behaviour of CoCrMo alloys in 2 wt% sulphuric acid solution, *Electrochimica Acta*, 125, 543-555.
156. Li, W., Brown, B., Young, D. and Nescic, S. (2014) Investigation of pseudo-passivation of mild steel in CO<sub>2</sub> corrosion, *Corrosion*, 70(3), 294-302.
157. Rodríguez-Díaz, R.A., Ramirez-Ledesma, A. L., Aguilar-Mendez, M. A., Uruchurtu Chavarin, J., Hernández Gallegos, M. A. and Juárez-Islas, J. A. (2015) Electrochemical corrosion behavior of a Co20Cr alloy in artificial saliva, *International Journal of Electrochemical Science*, 10(9), 7212-7226.

158. Scheers, P.V. (1992) The effects of flow velocity and pH on the corrosion rate of mild steel in a synthetic minewater, *Journal of the South African Institute of Mining and Metallurgy*, 92(10), 275-281.
159. Prawoto, Y., Ibrahim, K. and Wan Nik, W.B. (2009) Effect of pH and chloride concentration on the corrosion of duplex stainless steel, *The Arabian Journal for Science and Engineering*, 34(2C), 115-127.
160. Smolenska, H. (2010) Cobalt base clad layer resistance on the corrosion under low sulfur pressure solid state phenomena, 165, 173-176.
161. Manuel, R.W. (1947) Effect of Carbide structure on the corrosion resistance of steel, *Corrosion*, 3(9), 415-431.
162. Marimuthu, V. and Kannoorpatti, K. (2016) Corrosion behaviour of high chromium white iron hardfacing alloys in acidic and neutral solutions, *Journal of Bio- and Tribo-Corrosion*. 2(4), 29.
163. Kong, H., Yoon, E.S. and Kwon, O.K. (1995) Self-formation of protective oxide films at dry sliding mild steel surfaces under a medium vacuum, *Wear*, 181, 325-333.
164. Merz, R., Brodyanski, A. and Kopnarski, B. (2015) On the role of oxidation in tribological contacts under environmental conditions, *Conference Papers in Science*, 1-11.
165. Jena, A.K. and Chaturvedi, M.C. (1984) The role of alloying elements in the design of nickel-base superalloys, *Journal of Materials Science*, 19(10), 3121-3139.

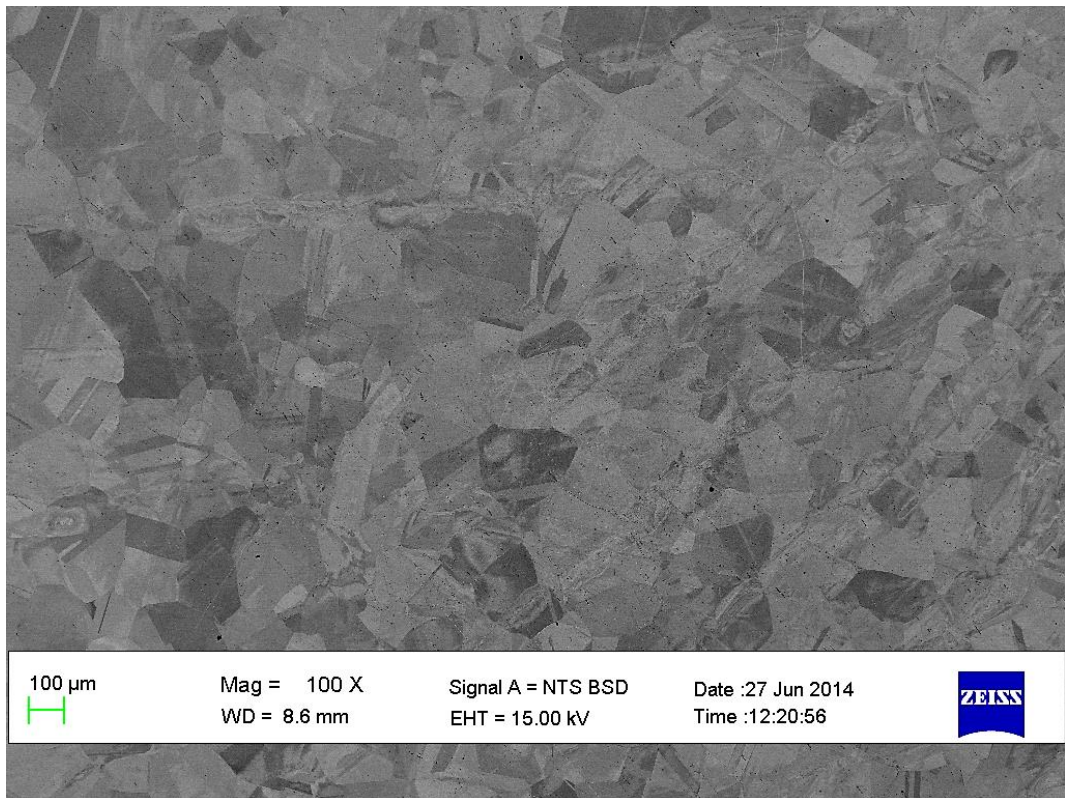
**APPENDIX A: Optical and SEM micrographs of as-received:  
A1) Stellite 6B, and A2) Hastelloy G30.**

---



**Figure A<sub>1</sub>.** Optical micrograph of as-received Stellite 6B, showing equiaxed grains and twinned  $\gamma$  grains in the matrix, with  $\text{Cr}_7\text{C}_3$  (dark) at the grain boundaries.

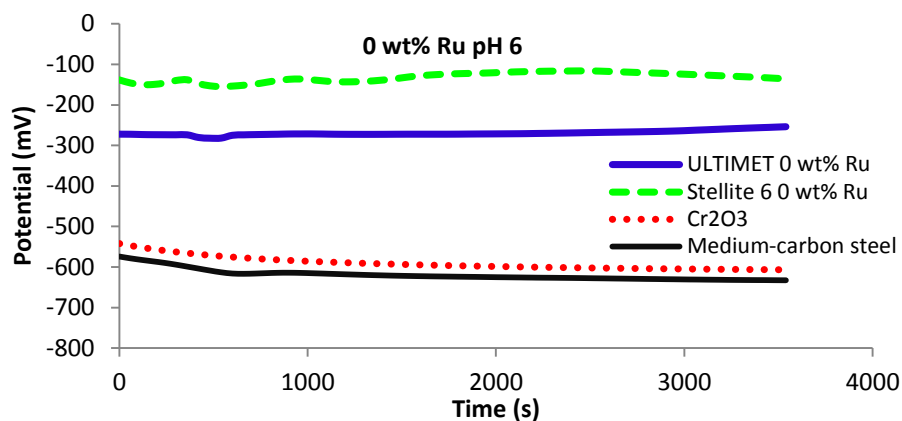




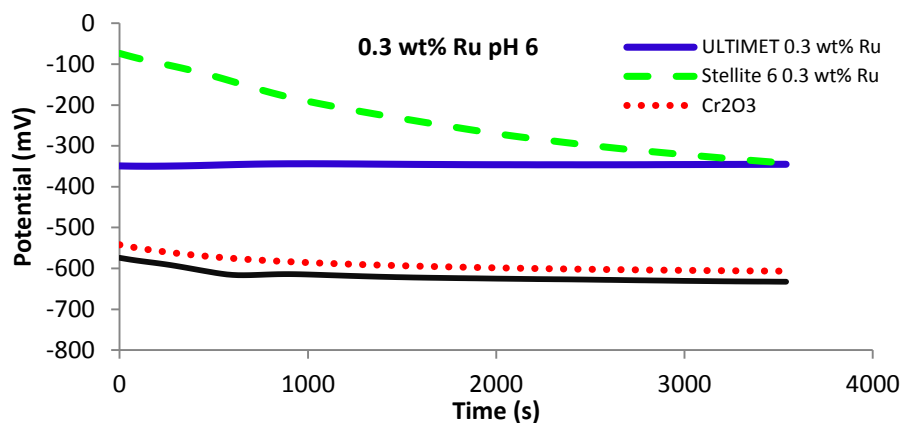
**Figure A<sub>2</sub>.** SEM-BSE micrograph of as-received Hastelloy G30, showing equiaxed grains of different orientations.

## APPENDIX B: OCP of ULTIMET and Stellite 6 coatings, Cr<sub>2</sub>O<sub>3</sub> coating and mild steel substrate in synthetic mine water

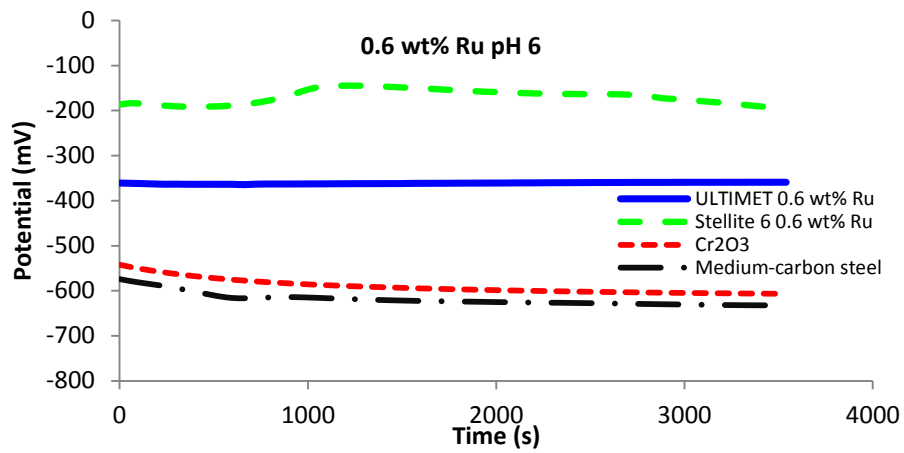
---



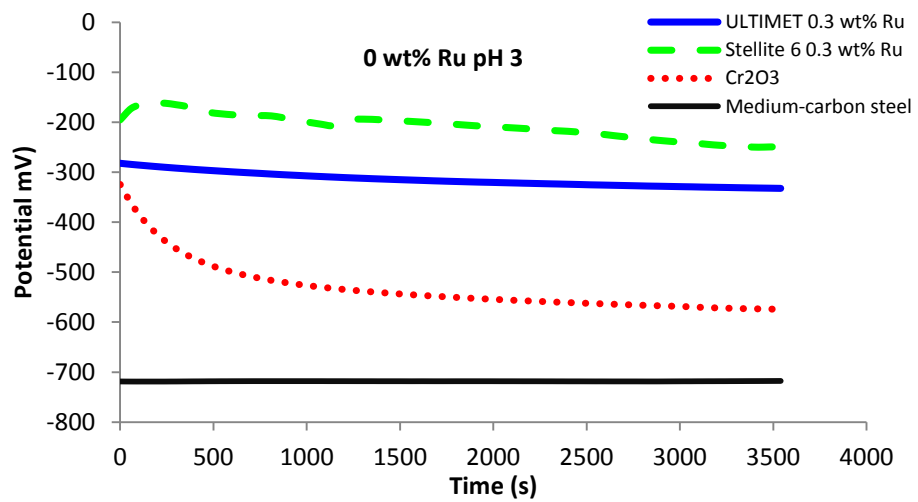
**Figure B1.** OCP of ULTIMET and Stellite 6 coatings with no Ru, Cr<sub>2</sub>O<sub>3</sub> coating and mild steel substrate in synthetic mine water at ambient temperature, pH 6.



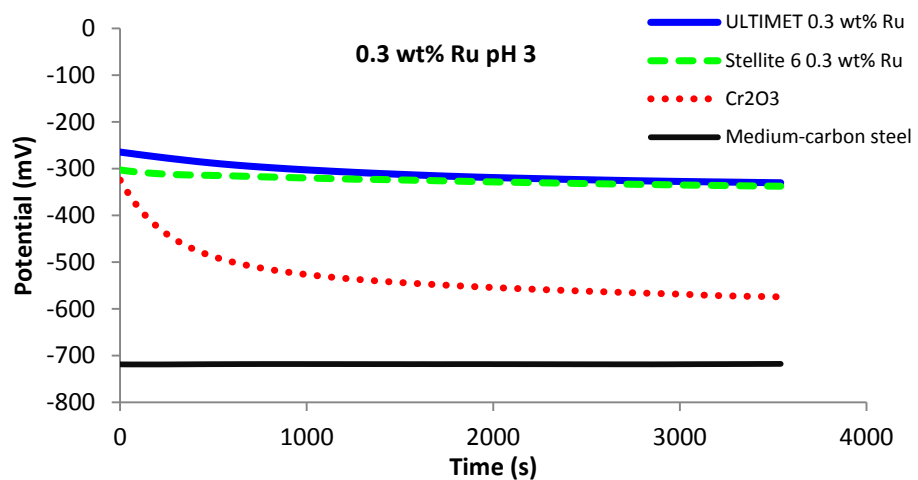
**Figure B2.** OCP of ULTIMET and Stellite 6 coatings with 0.3 wt% Ru, Cr<sub>2</sub>O<sub>3</sub> coating and mild steel substrate in synthetic mine water at ambient temperature, pH 6.



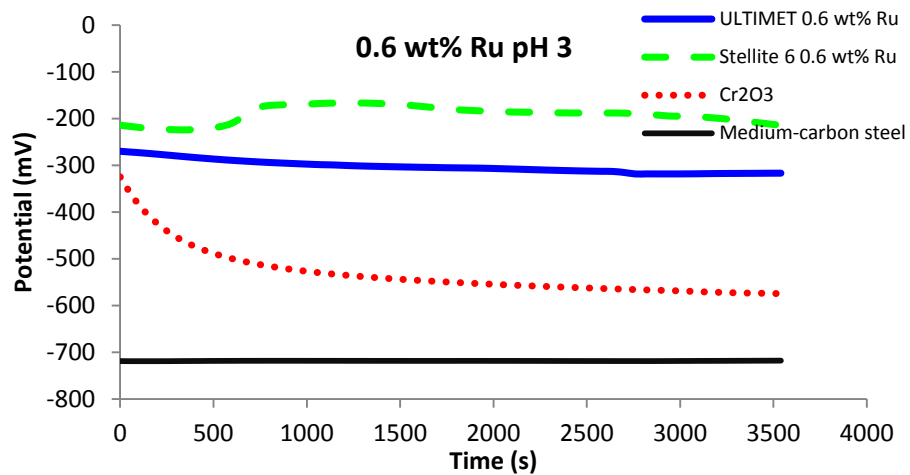
**Figure B3.** OCP of ULTIMET and Stellite 6 coatings with 0.6 wt% Ru, Cr<sub>2</sub>O<sub>3</sub> coating and mild steel substrate in synthetic mine water at ambient temperature, pH 6.



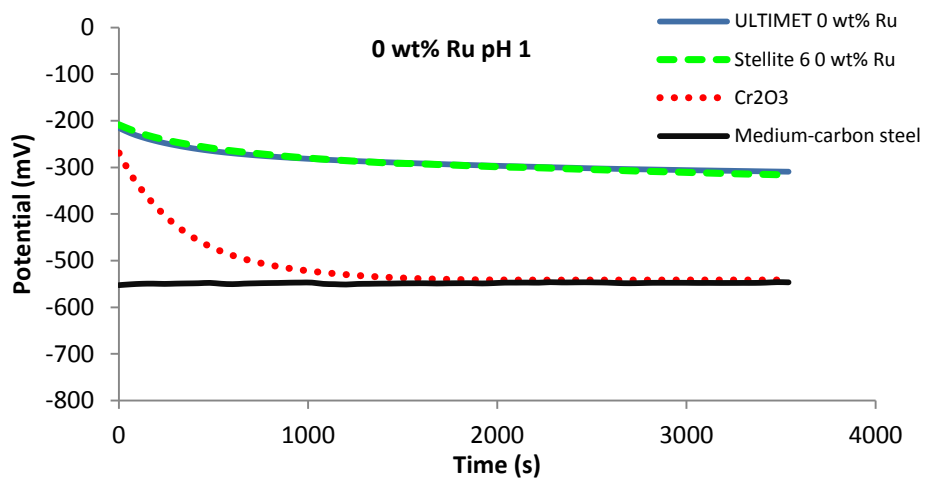
**Figure B4.** OCP of ULTIMET and Stellite 6 coatings with no Ru, Cr<sub>2</sub>O<sub>3</sub> coating and mild steel substrate in synthetic mine water at ambient temperature, pH 3.



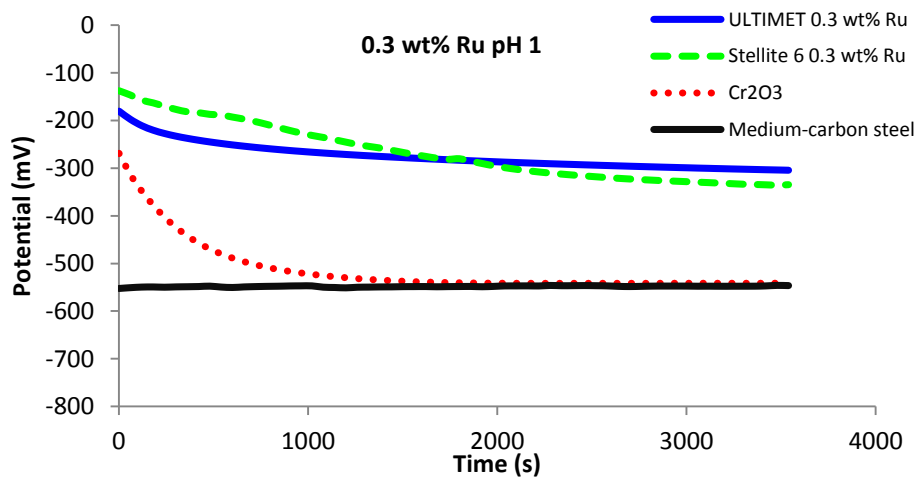
**Figure B5.** OCP of ULTIMET and Stellite 6 coatings with 0.3 wt% Ru, Cr<sub>2</sub>O<sub>3</sub> coating and mild steel substrate in synthetic mine water at ambient temperature, pH 3.



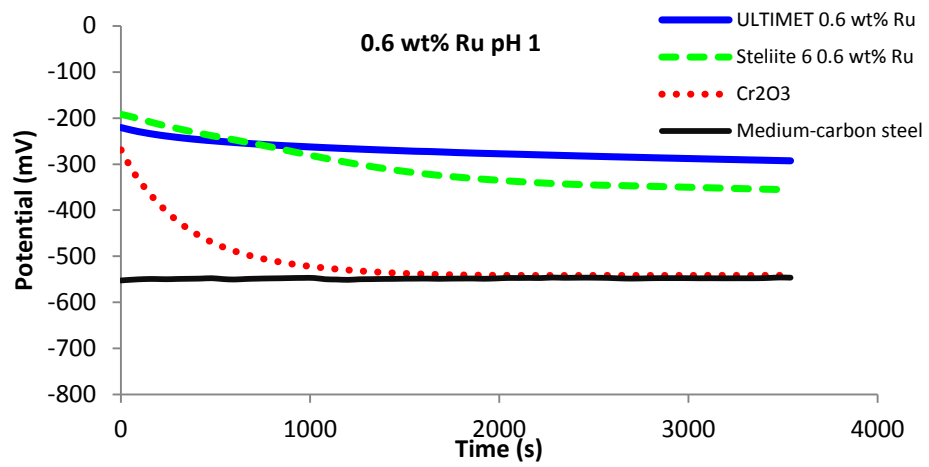
**Figure B6.** OCP of ULTIMET and Stellite 6 coatings with 0.6 wt% Ru, Cr<sub>2</sub>O<sub>3</sub> coatings and mild steel substrate in synthetic mine water at ambient temperature, pH 3.



**Figure B7.** OCP of ULTIMET and Stellite 6 coatings with no Ru, Cr<sub>2</sub>O<sub>3</sub> coatings and mild steel substrate in synthetic mine water at ambient temperature, pH 1.



**Figure B8.** OCP of ULTIMET and Stellite 6 coatings with 0.3 wt% Ru, Cr<sub>2</sub>O<sub>3</sub> coatings and mild steel substrate in synthetic mine water at ambient temperature, pH 1.



**Figure B9.** OCP of ULTIMET and Stellite 6 coatings with 0.6 wt% Ru, Cr<sub>2</sub>O<sub>3</sub> coatings and mild steel substrate in synthetic mine water at ambient temperature, pH 1.

## **APPENDIX C: AWARD**

---

Corrosion Institute of Southern Africa 2<sup>nd</sup> prize, School of Chemical and Metallurgical Engineering Poster Day, University of the Witwatersrand, 8 November 2012.

## APPENDIX D: PUBLICATIONS AND PRESENTATIONS

---

1. **Hango, S.I.**, Cornish, L.A., Chown, L.H., and Shrivastava, S. (2012) Coatings on Steels. 2<sup>nd</sup> African Materials Science & Engineering Network Workshop, Nairobi, 21-24 Mar, p.17.
2. **Hango, S.I.**, Cornish, L.A., Chown, L.H., van der Merwe, J.W. and Kavishe, F.P.L. (2012) Failure of Pump Shaft Sleeves in Highly Corrosive Mine Water at Otjihase Mine. Microscopic Society of Southern Africa Conference Proceedings, Cape Town, vol. 42, p. 97.
3. **Hango, S.I.**, Cornish, L.A., Chown, L.H., van der Merwe, J.W. and Kavishe, F.P.L. (2013) Corrosion of Pump Systems at Otjihase Underground Mine. 5th Cross-Faculty Graduate Symposium Book of Abstracts, University of the Witwatersrand, p. 37, 1-2 August 2013.
4. **Hango, S.I.**, Cornish, L.A., Chown, L.H., van der Merwe, J.W. and Kavishe, F.P.L. (2013) Erosion-Corrosion of Hard Facing Materials Exposed to Mine Water Conditions. 1<sup>st</sup> Annual Conference Book of Abstracts, University of Namibia, p. 25-26 October 2013.
5. **Hango, S.I.**, Cornish, L.A., Chown, L.H., van der Merwe, J.W. and Kavishe, F.P.L. (2014) Corrosion of ULTIMET and STELLITE 6B Alloys in Synthetic Mine Water. 2<sup>nd</sup> Annual Conference Book of Abstracts, University of Namibia, pp. 41-42, 30-31 October 2014.
6. **Hango, S.I.**, Cornish, L.A., Chown, L.H., van der Merwe, J.W. and Kavishe, F.P.L. (2014) Wear Behaviour of ULTIMET and STELLITE 6B Hard Facing Alloys. 6<sup>th</sup> Cross-Faculty Graduate Symposium Book of Abstracts, University of the Witwatersrand, p. 36, 28-29 October 2014.
7. **Hango, S.I.**, Chown, L.H., van der Merwe, J.W., Kavishe, F.P.L. and Cornish, L.A. (2014) Corrosion of Selected Hard Facing Materials Exposed to Mine Water. International Science and Technology Journal of Namibia, vol. 4, pp. 90-105.
8. **Hango, S.I.**, Cornish, L.A., Chown, L.H., van der Merwe, J.W. and Kavishe, F.P.L. (2015) Abrasive Wear Behaviour of Selected Cobalt-Based Hard facing Materials. 3<sup>rd</sup> African Materials Science and Engineering Network Workshop, Johannesburg, South Africa, p. 49, 27-29 May 2015.
9. **Hango, S.I.**, van der Merwe, J.W., Chown, L.H., Kavishe, F.P.L. and Cornish, L.A. (2017) A Study of ULTIMET and Stellite 6 Coatings with Ruthenium on Carbon Steel Substrates. Submitted for the 55th Annual Congress of the Microscopic Society of Southern Africa Conference, Bela-Bela, South Africa.
10. **Hango, S.I.**, van der Merwe, J.W., Chown, L.H., Kavishe, F.P.L. and Cornish, L.A. (2017) Development of Wear and Corrosion Resistant Coatings for Potential Use on Sleeves of Pumps in a Copper Mine. Accepted for the 6<sup>th</sup> Regional Conference of Society of Mining Professors (2018), Johannesburg, South Africa.



## COATINGS ON STEELS: PhD PROPOSAL

S.I. Hango<sup>1,2,3</sup>, L.A. Cornish<sup>1,2,3</sup>, L.H. Chown<sup>1,2,3</sup>, J.W. van der Merwe<sup>1,2,3</sup> and F.P.L. Kavishe<sup>3,4</sup>

<sup>1</sup>School of Chemical & Metallurgical Engineering University of the Witwatersrand, South Africa;  
<sup>2</sup>DST/NRF Centre of Excellence in Strong Materials, University of the Witwatersrand, South Africa

<sup>3</sup>African Materials Science And Engineering Network (A Carnegie-IAS Rise Network);

<sup>4</sup>Faculty of Engineering and Information Technology, University of Namibia

Steels are very important for mining tools, building materials and other components, where high strength, ductility, hardness, toughness, cheapness, machinability and hence corrosion and wear resistance are required<sup>1</sup>. Thus, they are widely used.

Steels are often coated to provide a protective surface covering or a decorative finish. These coatings are designed to prevent rusting or to shield the steels from chemical attack. The coatings can contain chromium, lead, tin, zinc, tungsten or non-metallic materials, such as paints and plastics<sup>2</sup>. However, some problems regarding corrosion and wear behaviour have been observed in some specific applications. These include poor adhesion and high porosity. The texture and cleanness of steel substrates can affect adhesion; the rougher the steel surface, the greater the adhesion<sup>3</sup>. Poor adhesion can cause porosity, which in turn facilitates corrosion<sup>4</sup>.

Cobalt-based alloys are widely used in wear-related applications because of their inherent high strength, corrosion resistance, and retained hardness over a wide temperature range and they can be coaxially laser clad on steels<sup>5</sup>. The hardness of cobalt-based alloys is due to the high hardness of carbides or other intermetallic compounds in the cobalt-rich solid solution. The corrosion resistance of cobalt-based alloys is generally good in many environments, and depends on type, concentration, and temperature of the solution<sup>1,6</sup>.

Much work has been done on coating of mining tools and equipment<sup>3</sup>. However, much is still to be done to improve or introduce new coating materials on steels since they rust and have a short lifetime, especially when they are exposed to intensively aggressive environments.

Due to the fact that steels are extremely useful and widely-used materials, it is therefore very important to select their best coating materials with good adhesion.

Currently, a request for permission to undertake research on steels from a Namibian mine has been approved for possible research samples for this project. The mine has experienced corrosion problems with its steels. After contact with the mine, and requesting samples, the following will be carried out next:

- Identify the kind of steels to be coated
- Identify the coating materials
- Select the best suited technique used in engineering coatings on the selected steel<sup>2</sup>

- Analyse the real components using optical microscopy, Scanning Electron Microscopy (SEM) and X-ray Diffraction (XRD)<sup>1,5</sup>
- The depth profile of the coating materials will be probed by Auger electron spectroscopy (AES). The crystalline structure, texture and residual stress of the coatings will be determined by X-ray diffraction (XRD)<sup>1,7</sup>
- Make samples and simulate the environment
- Analyse for the damaging mechanism, such as dislocations, defects, crystallinity, interface, foreign atom agglomerations, etc. will be revealed by transmission electron microscopy (TEM)<sup>1,7</sup>
- Test for mechanical properties, such tensile strength, compression, shear, buckling, and deep-drawing using Universal Testing Machine; hardness test will be done by the use of Brinell, Rockwell and Vickers Hardness Tester.
- At nanoscale, an atomic force microscopy (AFM) will be used and it will measure the elastic modulus of coatings on steel.
- Fracture toughness will be determined by the area under nanoindentation load-displacement curve.
- Nano-scratching test will also be carried out to assess the critical load that is responsible for coating failure<sup>7</sup>.

The project will be based on an actual application, to ensure that the research will be relevant, and could also benefit Namibia as a problem solving in mining industries.

### References

1. Callister, W.D. Jr. and Rethwisch, D.G. (2010) *Materials Science and Engineering: An Introduction*, 8<sup>th</sup> Edition, John Wiley and Sons, Inc. NY.
2. Grainger, S., *Engineering (1989) Coatings – Design and Application*, Abington Publishing, England.
3. Diaz, M. and Skowronek, W.R, (2002) *Understanding coating adhesion. Tube and Pipe Fabrication* Article <http://www.thefabricator.com/article/tubepipefabrication/understanding-coating-adhesion>
4. Teixeira, C.H.S.B., *et al.* (2011) *Mat. Corr.*, **62**, (9) 853.
5. Antony, K.C., (1983) *JOM* **35**, (2) 52.
6. Hickl, A.J., (1980) *JOM* **32**, (3) 6.
7. Wo, P.C., *et al.* (2012) *Mat. Sc. & Eng., A* **534**, 297.

E-mail: silasithete@yahoo.com



## FAILURE OF PUMP SHAFT SLEEVES IN HIGHLY CORROSIVE MINE WATER AT OTJIHASE MINE

S.I. Hango<sup>1,2,4</sup>, L.A. Cornish<sup>1,2,3</sup>, L.H. Chown<sup>1,2,3</sup>, J.W. van der Merwe<sup>1,2,3</sup> and F.P.L. Kavishe<sup>1,4</sup>

<sup>1</sup>African Materials Science and Engineering Network, <sup>2</sup>School of Chemical and Metallurgical Engineering and <sup>3</sup>DST/NRF Centre of Excellence for Strong Materials, University of the Witwatersrand, Johannesburg and <sup>4</sup>Faculty of Engineering and Information Technology, University of Namibia.

Steels are widely used where excellent oxidation resistance, wear resistance, high strength, ductility, hardness, toughness and low cost are required<sup>1</sup>. However, they can experience corrosion problems when exposed to aggressive environments, and even on stainless steels, the protective passivation film on the surface can be attacked and penetrated, allowing corrosion to occur<sup>2</sup>. This can result in failure of the component, leading to blockage and leakage of pipes due to various corrosion products, frequent maintenance and replacement of parts, and perhaps, even serious injuries.

Steel shaft sleeves are used in Otjihase Mine water pumps, which continuously pump water from underground reservoirs to the surface to prevent flooding of the copper mine in Namibia. This is an investigation of the corrosion behaviour of steel shaft sleeves from Otjihase Mine water pumps, to determine the effect of the mine water on the performance of the pumps and advise on possible preventative methods.

Failed pump samples were obtained from the mine, and inspected. Sections were cut through the pump shaft sleeves and prepared metallographically for optical microscopy and SEM characterization. XRD was also done. Samples of the mine water were collected and chemically analysed by inductively coupled plasma mass (optical emission) spectrometry. The particle sizes in the mine water were measured by a Malvern Mastersizer 2000.

The pump shaft sleeves had been coated (Fig. 1), and the coating had scratches (E) caused by the suspended particles, as well as small pits (P). In places, the coating had been completely removed, and the substrate had experienced general corrosion (G). The mine water was cloudy when collected, and became clearer on standing once fine sediment settled out. Analysis identified large amounts of alkali earth metals and rare earth elements, as well as high levels of total dissolved solids (TDS) of sulphates, nitrates and chlorides, and gases such as oxygen and chlorine. The emission of SO<sub>2</sub> and Cl<sub>2</sub> from vehicles' fuel combustion in the close confines of the mine equipment oxidized in water to H<sub>2</sub>SO<sub>4</sub> and HCl and contributed to the observed corrosion<sup>3</sup>.

The SEM-EDX results showed that the shaft sleeve substrates were medium-carbon steel, which was confirmed by XRD, and the coating was a nickel-chromium alloy of composition: 58.4 Ni, 36.8 Cr, 2.7 Fe and 2.1 Si (wt%). Although designed to protect the medium-carbon steels, the coating was worn by erosion from the solid particles suspended in the mine water (average particle size was ~12.3 μm), and also pitted from the acidic water (Fig. 1). Once the protective

coating was breached, there was serious corrosion of the medium-carbon steel substrate<sup>3</sup>.

Fig. 2 shows the substrate and coating of thickness ~1000 μm, where the attack was much less. There were also some discontinuities at the substrate-coating interface, which were better revealed by optical microscopy, than SEM.

The initial results showed that the protective coatings were removed by both erosion and pitting, and once removed, the underlying medium-carbon steel corroded quickly. Thus, the components experienced very high corrosion rates due to very aggressive mine water with suspended particles. Possible remedies could include a harder coating (against erosion) and a more noble material (against the pitting).

### References

1. Askeland, D.R., Fulay, P.P. and Bhattacharya, D.K. (2010). *Essentials of Materials Science and Engineering*, Second Edition, SI. Toronto. Cengage Learning.
2. Mobin, M. and Shabnam, H. (2010). *J. Min. & Mat. Charact. & Eng.*, 9 (12), 17. Aligarh.
3. McEwan, J.J., (ed) (2004). *Corrosion Control in Southern Africa*. Johannesburg. Corrosion Institute of Southern Africa.



Figure 1. Macrograph of a corroded shaft sleeve sample from Otjihase Mine, showing general (G), pitting (P) and erosion (E) corrosion.

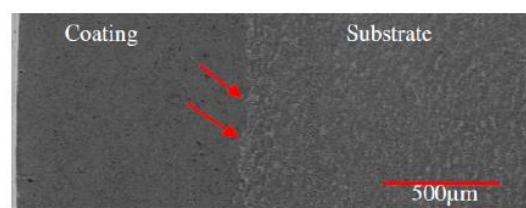


Figure 2. SEM cross-section micrograph of a corroded shaft sleeve sample, showing the thickness of a coating in the unattacked region, and discontinuities at the substrate-coating interface (arrows).

Corresponding author: [silasithete@yahoo.com](mailto:silasithete@yahoo.com)

# Corrosion of Selected Hard Facing Materials Exposed to Mine Water

S.I. Hango<sup>1,2,3,4\*</sup>, L.H. Chown<sup>1,2,3</sup>, J.W. van der Merwe<sup>1,2,3</sup>  
F.P.L. Kavishe<sup>1,4</sup>, L.A. Cornish<sup>1,2,3</sup>

<sup>1</sup>African Materials Science and Engineering Network (AMSEN - A Carnegie-IAS Network).

<sup>2</sup>School of Chemical and Metallurgical Engineering, University of the Witwatersrand, South Africa

<sup>3</sup>DST-NRF Centre of Excellence in Strong Materials, University of the Witwatersrand, South Africa

<sup>4</sup>Faculty of Engineering and Information Technology, University of Namibia, Namibia

Received: 17th February, 2014. Accepted: 22nd September, 2014.

## Abstract

Corrosion damage can cause major failure of mining pumps which could lead to degradation of other mining equipment, as a result of leakage, thus leading to a high rate of replacement and maintenance of pumps and surrounding equipment. Hard facing materials are used to protect moving parts against mechanical and corrosion damage. The corrosion behavior of a corrosion resistant Hastelloy G30 and a hard facing material, a nickel-chromium-iron (Ni-Cr-Fe) alloy (both high chromium nickel-based alloys) exposed to synthetic and acidified mine water were studied using potentiodynamic polarisation. The results showed lower corrosion rates for Hastelloy G30 than for Ni-Cr-Fe. The corrosion rates at pH 6.8, at ambient temperature and 35°C were 0.00011 mm.y<sup>-1</sup> and 0.00035 mm.y<sup>-1</sup> for Hastelloy G30; 0.0016 mm.y<sup>-1</sup> and 0.0017 mm.y<sup>-1</sup> for INCONEL Alloy 600, and at pH 3, at ambient temperature and 35°C corrosion rates were 0.0003 mm.y<sup>-1</sup> and 0.00083 mm.y<sup>-1</sup> for Hastelloy G30; 0.1 mm.y<sup>-1</sup> and 3.2 mm.y<sup>-1</sup> for INCONEL Alloy 600. The microstructures of the alloys before and after corrosion tests were characterised using optical microscopy; X-ray diffraction (XRD), and microhardness measurements were also performed.

**Keywords:** corrosion, synthetic mine water, hard facing.

**ISTJN 2014; 4:90-105.**

\*Corresponding author -E-mail address: shango@unam.na.





## 1 Introduction

Corrosion is a common cause of failure in mining and mineral processing industries, leading to failures of various components, such as pumps, valves, couplings, etc. in acidic and alkaline environments (Yoganandh et al. 2013). The results of corrosion effects usually lead to leakage, high rate of replacement and maintenance. In underground mines, there are  $\text{SO}_4^{2-}$ ,  $\text{Na}^+$ ,  $\text{Ca}^+$ ,  $\text{Mg}^{2+}$  and  $\text{Cl}^-$  in the water with different pH values, and  $\text{CH}_4$ ,  $\text{CO}$ ,  $\text{CO}_2$ , as well as  $\text{H}_2\text{S}$  and  $\text{SO}_2$  in the air. These create an erosive-corrosive environment (Lalvani et al. 1990; Wang et al. 1997; White and Higginson 1985). Carter (1986), Al-Bukhaiti et al. (2007) and Llewellyn et al. (2004) studied factors that affect the corrosion in mining industry and processing plants, such as material properties and pH. They found that steels with less carbon and chromium contents experienced erosive-corrosive and abrasive wear, resulting in ploughing, microcutting, indentation with lips as well as fracture and cracking of carbide phases and fatigue wear.

Hard facing materials protect metal equipment from wear or abrasion (Clark 1985), and are applied as a surface layer on an underlying material, usually low or medium carbon steels (Rodríguez 2003), by depositing a special alloy (the 'hard face') on the substrate, using various welding processes, to improve wear properties and/or dimensions (Berns and Fischer 1986). Hastelloy G30 and INCONEL Alloy 600 hard facing materials are both high-chromium nickel-based alloys, which form a thin passive film when the alloys are immersed in a liquid environment, giving low corrosion rates (Jena and Chaturvedi 1984; Zhang et al. 2012). This makes them useful for improved corrosion resistance in underground mine equipment, especially water pumps and pipes carrying aggressive mine waters. Hastelloy G30 (also known as UNS N06030) is a nickel-based alloy suitable for handling phosphoric, sulphuric and nitric acids, while INCONEL Alloy 600 (also known as UNS N06600) is also a nickel-based alloy with various uses, especially in pump systems operating in highly corrosive environments (HAYNES 2013). This alloy may be hard faced on low or medium carbon steels to protect against mechanical and chemical attack (Rodríguez 2003). The chemical compositions of the two high-chromium nickel-based alloys are given in Table 1 (HAYNES 2013).

This study includes potentiostatic polarisation measurements in synthetic mine water (a simplified underground mining industrial solution), and optical microscopy, X-ray diffraction (XRD) and microhardness measurements.

Table 1: Typical chemical compositions of the test materials (wt%) (HAYNES 2013).

Composition	Sample	
	Hastelloy G30	INCONEL Alloy 600
Ni	Balance	Balance
Co	5.00	0.30
Cr	28.00–31.50	16.60
Mo	4.00–6.00	0.04
W	1.50–4.00	-
Fe	13.00–17.00	4.03
Si	0.80	4.49
Mn	1.50	0.20
Al	-	0.02
C	0.03	0.06
Nb+Ta	0.30–1.50	-
Cu	1.00–2.40	-
P	0.04	-
S	0.02	-
Nb	-	0.01

## 2 Experimental Procedure

The Hastelloy G30 and INCONEL Alloy 600 samples were cut, hot mounted in epoxy resin, ground to 1200 grit, and polished to 1  $\mu\text{m}$  for optical microscopy, hardness measurements and XRD analyses. The Hastelloy specimen was etched electrolytically in 5 g oxalic acid and 95 ml HCl, at 6 V DC for 5 seconds. INCONEL Alloy 600 was etched in equal parts of HCl,  $\text{HNO}_3$  and acetic acid, swabbing for 1 minute at room temperature.

The microstructures were examined before and after the corrosion measurements in a Leica CTR6000 optical microscope. Hardness measurements were performed using an FM-700 Vickers Microhardness tester, with a 2 kg load ( $\text{HV}_2$ ), and five measurements were made with the average being reported.

Samples were prepared metallographically for X-ray diffraction analyses before and after corrosion experiments. A BRUKER D2 PHASER diffractometer was used, with Cobalt 20 radiation at 30 kV and 10 mA. Diffractograms were recorded in a non-spinning regime, at an angle  $2\theta = 20^\circ$  to  $140^\circ$ .

The samples were cold-mounted in epoxy resin, ground to 1200 grit for corrosion measurements, and the exposed areas of the samples to the corrosive environment were measured.

The measurements were carried out in synthetic mine water (pH=6.8) of the composition given in Table 2, at ambient temperature (22°C) and at 35°C in a water bath. The synthetic mine water was prepared from a mixture of salts: magnesium and sodium sulphates, calcium and sodium chlorides into de-ionised water, and acidified with 32% HCl to a pH 3. It was measured for conductivity (using an ORION STAR A212 conductivity meter), total dissolved solids (TDS), salinity, resistivity, pH (using an ORION STAR A211 pH meter), cations ( $\text{Na}^+$ ,  $\text{Ca}^{2+}$  and  $\text{Mg}^{2+}$ ) and anions ( $\text{SO}_4^{2-}$  and  $\text{Cl}^-$ ) using atomic absorption spectroscopy (AAS), inductively coupled plasma optical emission spectroscopy (ICP-OES) at Mintek, Randburg, South Africa.

Table 2: Composition of synthetic mine water solution used in the measurements (Wang et al. 1997; White and Higginson 1985).

Salt	Concentration (mg.L <sup>-1</sup> )
MgSO <sub>4</sub>	198
Na <sub>2</sub> SO <sub>4</sub>	1215
CaCl <sub>2</sub>	1038
NaCl	1379

Potentiodynamic polarization measurements were performed using an Auto Tafel Potentiostat V1.79 and Auto LPR V2.7h software at a scan rate of 0.166 mV.s<sup>-1</sup> after a 30 minute open circuit scan, to stabilise the potential applied, and their electrochemical responses were studied. The corrosion current density ( $i_{corr}$ ) of the samples was obtained from the measured linear polarization resistance (LPR) using the Stern-Geary equation (Kelly et al. 2002):

$$i_{corr} = \frac{1}{2.3R_p} \left( \frac{\beta_a \beta_c}{\beta_a + \beta_c} \right) = \frac{B}{R_p} \quad (1)$$

where  $\beta_a$  = anodic Tafel slope,  $\beta_c$  = cathodic Tafel slope ( $\beta_a = \beta_c = 0.1$ ),  $R_p$  = polarization resistance and,  $B$  = proportionality constant. The corrosion rates in mm.y<sup>-1</sup> were calculated by using Equation 2:

$$\text{Corrosion rate}(CR) = \left( \frac{0.00327 E_w}{\rho} \right) i_{corr} \quad (2)$$

where  $E_w$  = equivalent weight of alloy (g),  $\rho$  = the density of alloy (g.cm<sup>-3</sup>) and  $i_{corr}$  = corrosion current density ( $\mu\text{A.cm}^{-2}$ ).

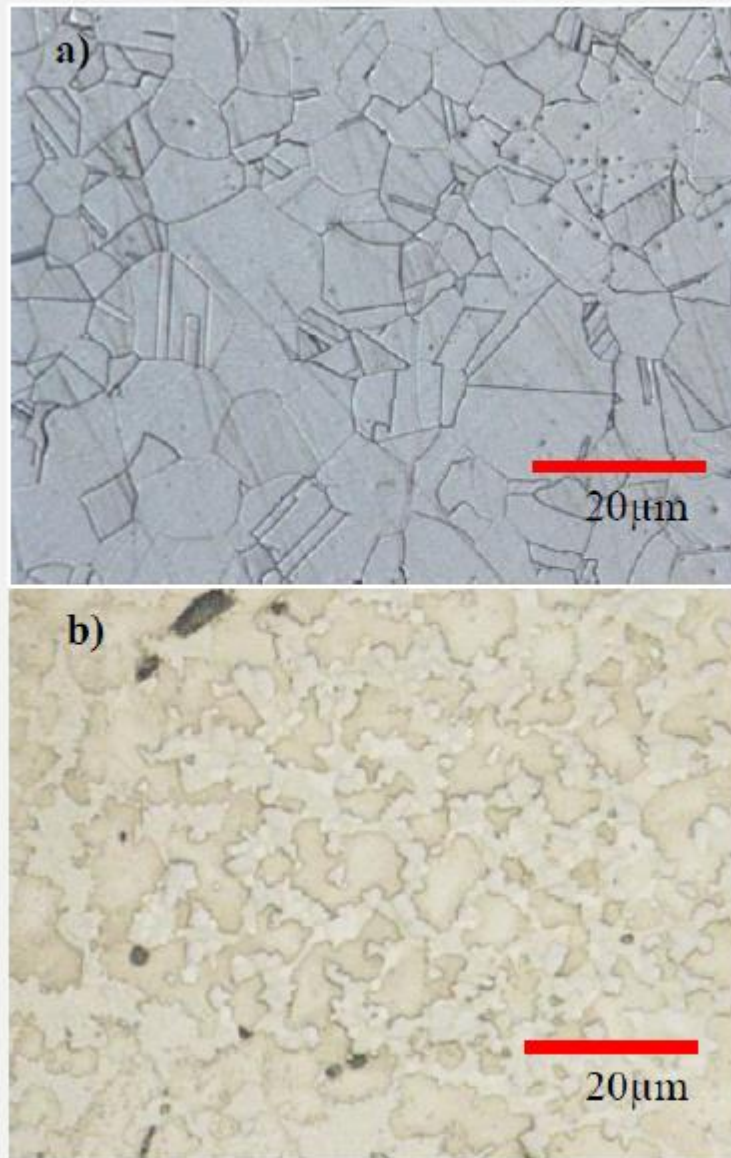


Figure 1: Optical micrographs of: a) Hastelloy G30, showing equiaxed and twinned  $\gamma$ ; and b) INCONEL Alloy 600, showing Ni-Cr (light) and Cr- and Mo-carbides (dark).

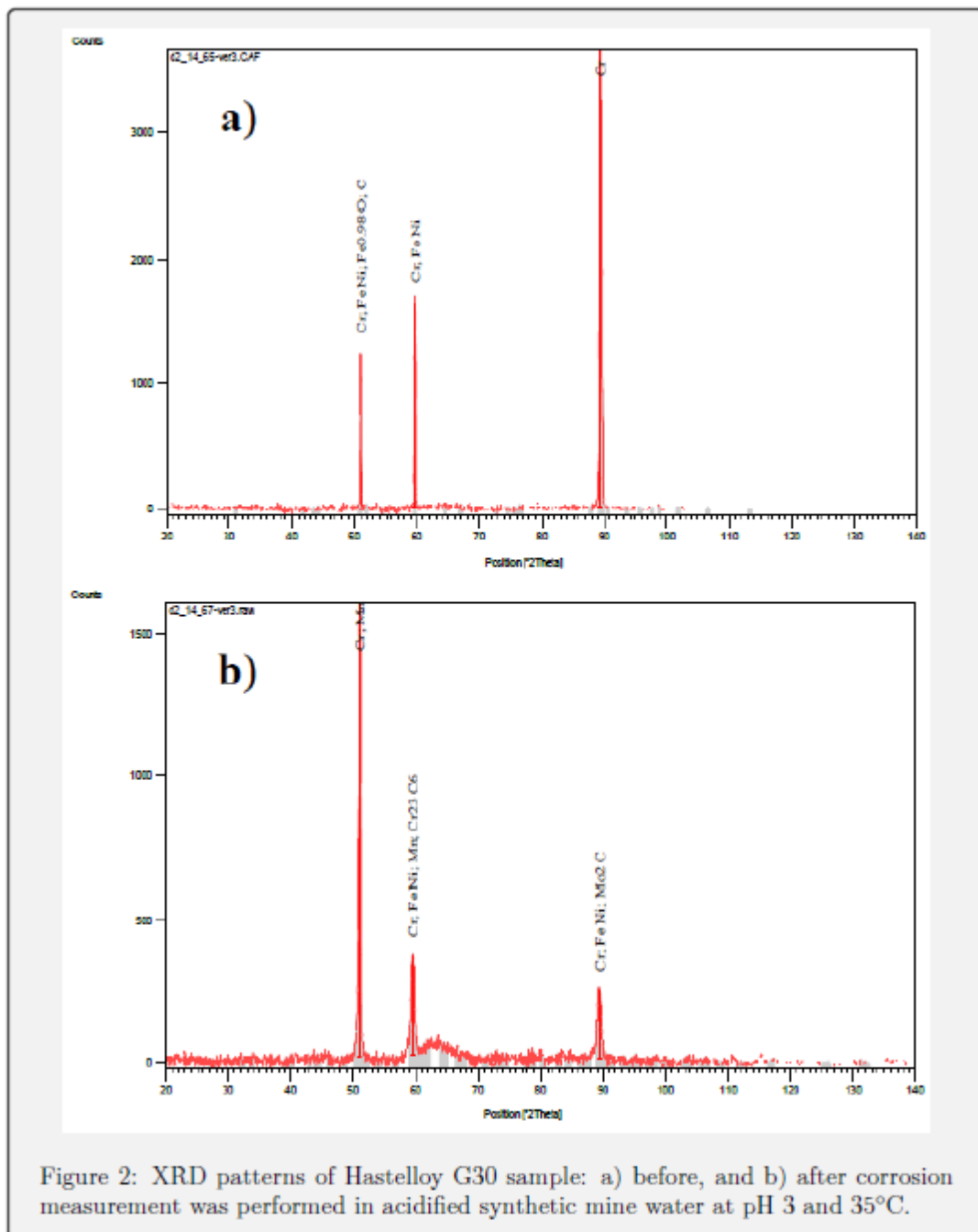


Figure 2: XRD patterns of Hastelloy G30 sample: a) before, and b) after corrosion measurement was performed in acidified synthetic mine water at pH 3 and 35°C.

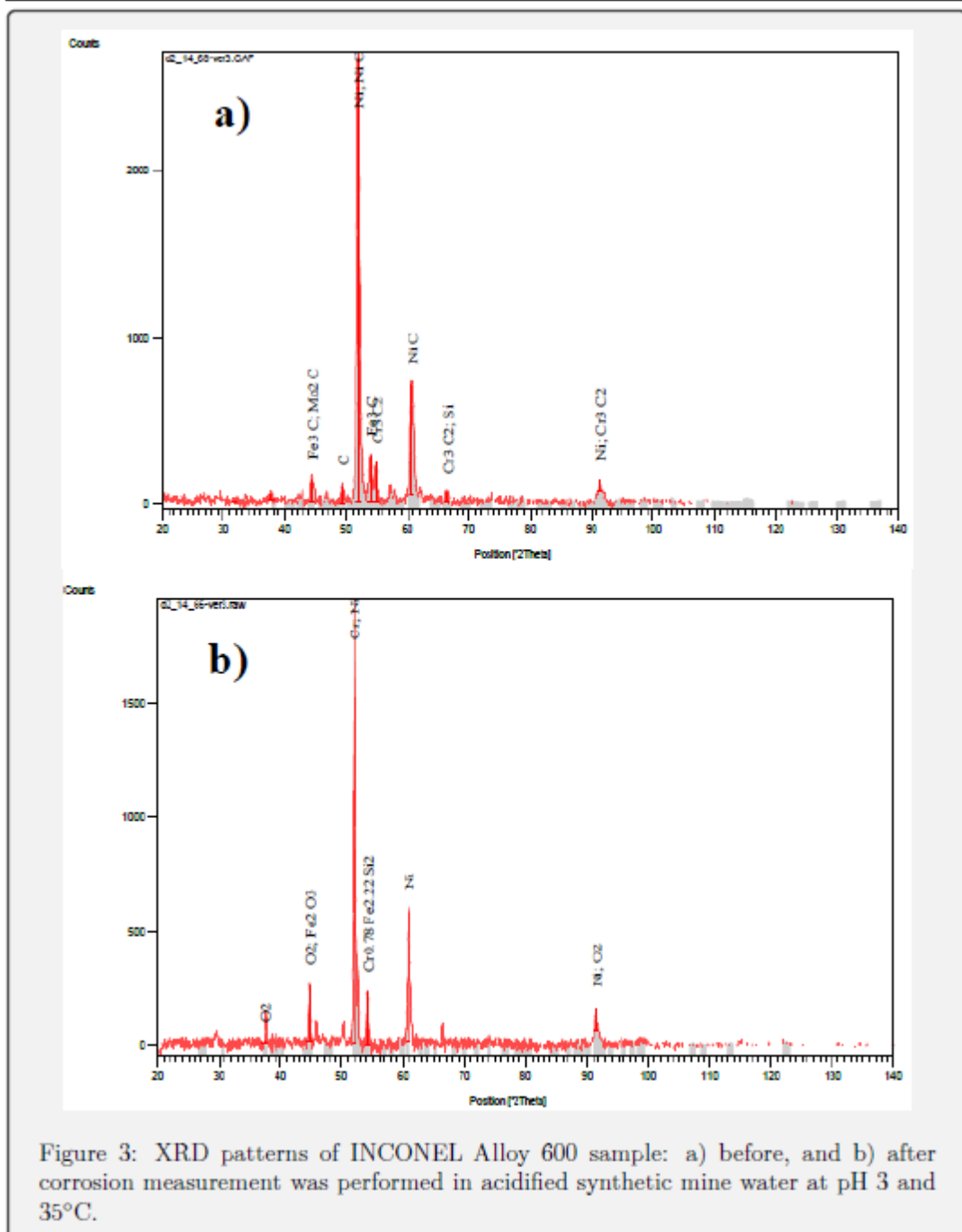


Figure 3: XRD patterns of INCONEL Alloy 600 sample: a) before, and b) after corrosion measurement was performed in acidified synthetic mine water at pH 3 and 35°C.



### 3 Results

#### 3.1 Microstructural and Hardness Characterisation

Optical micrographs of the Hastelloy G30 and INCONEL Alloy 600 before testing are shown in Figure 1. Hastelloy G30 had well defined grain boundaries with equiaxed grains and mechanical twins, while INCONEL Alloy 600 had a two-phase structure, and irregular grain boundaries of Ni-Cr and carbide phases. These were confirmed by XRD analyses. INCONEL Alloy 600 had a hardness of  $652 \pm 36 \text{HV}_2$ , and the Hastelloy G30 hardness was  $176 \pm 6 \text{HV}_2$ .

#### 3.2 XRD Analyses

X-ray diffraction was performed before and after the corrosion measurements in synthetic mine water and are shown in Figures 2-3. The Hastelloy G30 had Ni, Cr, Mn, FeNi,  $\text{Mo}_2\text{C}$ ,  $\text{Cr}_{23}\text{C}_6$  and C before the corrosion tests, and only Cr, Fe, FeNi, NiO,  $\text{Fe}_{0.98}\text{O}$  and C on the surface after corrosion. For INCONEL Alloy 600, the same species as in Hastelloy G30 were detected before corrosion, as well as Si. After corrosion, Cr, Ni,  $\text{O}_2$ ,  $\text{Fe}_2\text{O}_3$  and  $\text{Cr}_{0.78}\text{Fe}_{2.22}\text{Si}_2$  were present.

Table 3: Electrochemical test results of Hastelloy G30 and INCONEL Alloy 600 alloy in synthetic mine water.

Sample	pH	Temperature (°C)	$E_{corr}$ (mV)	$i_{corr}$ ( $\mu\text{A}\cdot\text{cm}^{-2}$ )	Corrosion rate ( $\text{mm}\cdot\text{y}^{-1}$ )
Hastelloy G30	6.8	Ambient	-200	0.011	0.00011
INCONEL Alloy 600			-267	0.17	0.0016
Hastelloy G30		35	-153	0.035	0.00035
INCONEL Alloy 600			-319	0.17	0.0017

#### 3.3 Electrochemical Measurements

Figure 4 shows the corrosion products on the surface of the samples. Hastelloy G30 had a surface film with cracks, and with some corrosion products, while INCONEL Alloy 600 had microcracks in the corrosion products. Figures 5 and 6 show the polarisation curves for both alloys in synthetic and acidified mine water. The corrosion potential ( $E_{corr}$ ) of Hastelloy G30 was higher than that of INCONEL Alloy 600, and a higher corrosion rate

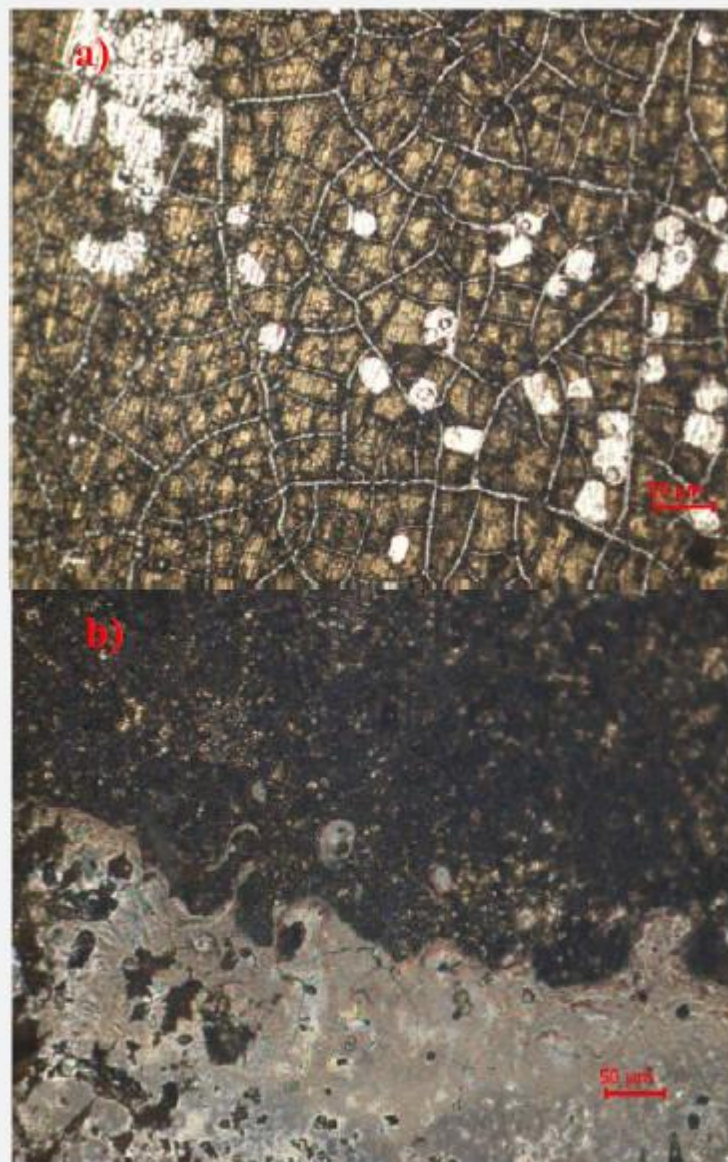
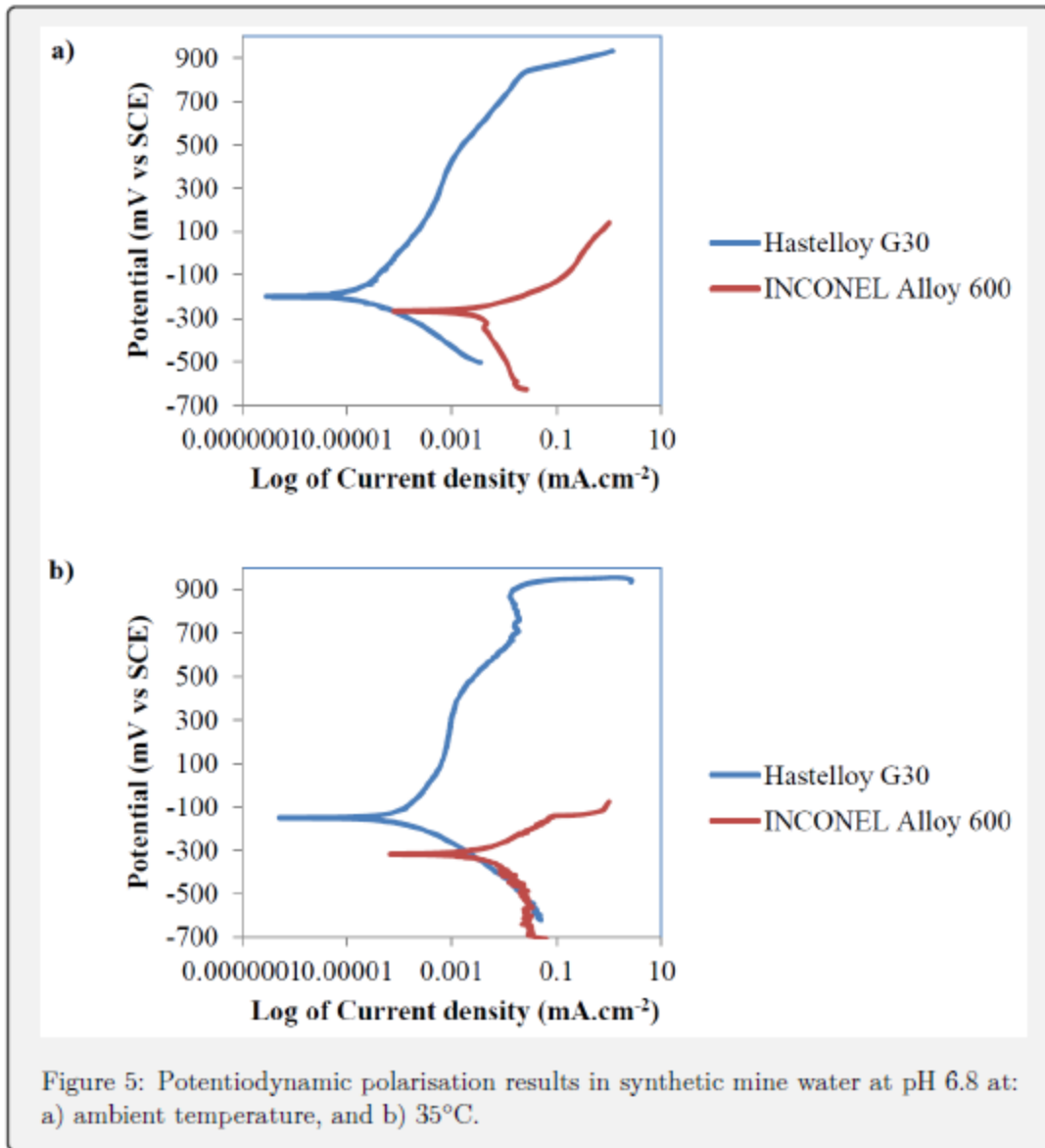


Figure 4: Optical micrographs taken after corrosion measurements in synthetic mine water at pH 3 and 35°C, for: a) Hastelloy G30, showing cracks in the protective film and some white corrosion products; and b) INCONEL Alloy 600, showing microcracks in the corrosion products.



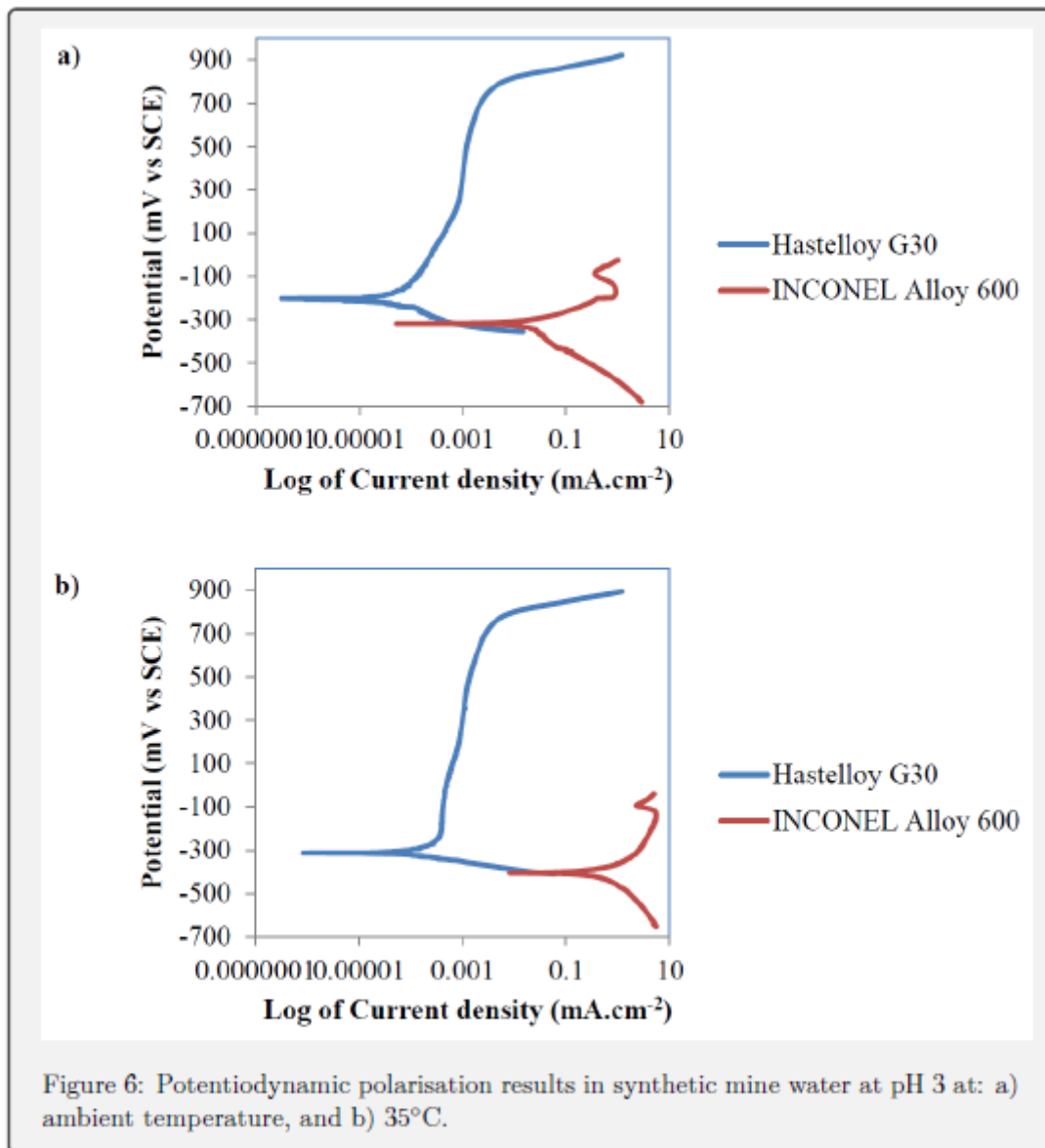


Table 4: Electrochemical test results of Hastelloy G30 and INCONEL Alloy 600 in acidified synthetic mine water.

Sample	pH	Temperature (°C)	$E_{corr}$ (mV)	$i_{corr}$ ( $\mu\text{A}\cdot\text{cm}^{-2}$ )	Corrosion rate ( $\text{mm}\cdot\text{y}^{-1}$ )
Hastelloy G30	3	Ambient	-207	0.033	0.0003
INCONEL Alloy 600			-318	1.1	0.1
Hastelloy G30		35	-312	0.091	0.00083
INCONEL Alloy 600			-405	3.3	3.2

was observed on INCONEL Alloy 600. Hastelloy G30 experienced a slight spontaneous passivation and high breakaway potentials in the solutions tested, with more evidence of pitting in synthetic mine water at 35°C. INCONEL Alloy 600 had no passivation behaviour in all other solutions tested other than in synthetic mine water at pH 3 at 35°C. From these observations, it can be concluded that alloys were more resistant to synthetic mine water than to acidified synthetic mine water. The summary of the electrochemical results is given in Tables 3-4. Table 5 shows properties of synthetic and acidified synthetic mine water.

## 4 Discussion

Optical microscopy showed that Hastelloy G30 had equiaxed and twinned  $\gamma$ , while INCONEL Alloy 600 had Ni-Cr and Cr-Mo-carbide phases, which were confirmed by XRD analyses. The micrographs also showed that the surface layers (consisting of corrosion products) of the INCONEL Alloy 600 were more severely damaged than the Hastelloy G30. This behavior is caused by the presence of  $\text{SO}_4^{2-}$  and  $\text{Cl}^-$  in solution (Li et al. 2001). From the microstructures, it can be concluded that the lower surface damage of the Hastelloy G30 than INCONEL Alloy 600 in all conditions tested was probably due to the higher chromium content in Hastelloy G30, making the surface more resistant to damage by ions in the solutions by forming a more protective film on the surface of Hastelloy G30 (Hayes et al. 2006). Additionally, lower corrosion damage of Hastelloy G30 was also due to its higher Mo and W contents which stabilize the protective film on the surface. The surface layers were probably uniform, and they cracked during drying (Jakupi et al. 2011) when the air reacted with the film formed on the surface of the sample after corrosion measurements in saline environments. XRD patterns showed  $\text{Fe}_2\text{O}_3$ , NiO and  $\text{Fe}_{0.98}\text{O}$  which were corrosion products for both alloys.

Tables 4 and 5 show that the potentiodynamic polarization responses of Hastelloy G30 in synthetic and acidified synthetic mine water at pH 6.8 and 3 had a lower corrosion current



Table 5: Properties of synthetic and acidified synthetic mine water for corrosion measurements.

Properties	Synthetic mine water	Acidified synthetic mine water
Conductivity ( $\mu\text{S.cm}^{-1}$ )	4.9	12.9
TDS (ppt)	2.7	6.4
Salinity (psu)	2.9	7.5
Resistivity (Ohm.cm)	183.5	76.9
pH	6.8	3
$\text{SO}_4^-$ (ppm)	1007	1043
$\text{Na}^+$ (ppm)	928	890
$\text{Ca}^{2+}$ (ppm)	108	111.5
$\text{Cl}^-$ (ppm)	1700	2600
$\text{Mg}^{2+}$ (ppm)	11	12

density ( $i_{corr}$ ) than INCONEL Alloy 600 in all solutions and conditions measured, and hence Hastelloy G30 had a lower corrosion rate than INCONEL Alloy 600. Hastelloy G30 experienced a slight spontaneous passivation and high breakaway potentials in the solutions tested, with more evidence of pitting in synthetic mine water at 35°C. INCONEL Alloy 600 had no passivation behaviour in all other solutions tested, other than in synthetic mine water at pH 3 at 35°C. However, INCONEL Alloy 600 experienced repassivation behaviour after breakaway potential in all conditions tested due to the presence of molybdenum content in the alloy (Hayes et al. 2006).

INCONEL Alloy 600 ( $652 \pm 36\text{HV}_2$ ) was much harder than Hastelloy G30 ( $176 \pm 6\text{HV}_2$ ) because of  $\text{Cr}^-$  and  $\text{Mo}^-$  carbides, which formed in the presence of Si (Pigrova et al. 1980). The hardness values of the samples are important for exposure to erosion-corrosion conditions due to particles in mine water that would cause wear (Wood 2007). The hard face surface can be heat treated without affecting the substrate by laser heat treatment. Bolelli et al. (2008) worked on laser heat treatment of cobalt and nickel alloys, which resulted in fine-grained carbides (improving hardness), and more noble values of corrosion potential and decreased corrosion current density (improving corrosion resistance) by improving inter-lamellar cohesion. INCONEL Alloy 600 is therefore recommended as a hard facing material in mine water conditions, and may be treated similarly to improve its resistance to corrosion and wear.

When the pH of the solution was decreased, the values of conductivity, total dissolved solids (TDS) and salinity increased with a decrease in resistivity. Thus, the acidified synthetic mine water should be more corrosive than synthetic mine water.

The results showed that acidified synthetic mine water had more suspended particles, high conductivity, salinity, and low resistivity and pH as well as high concentration of  $\text{SO}_4^{2-}$ ,

$\text{Ca}^{2+}$ ,  $\text{Cl}^-$  and  $\text{Mg}^{2+}$  than the synthetic mine water, making it to be the most aggressive environment.

## 5 Conclusions

- INCONEL Alloy 600 ( $652 \pm 36\text{HV}_2$ ) was much harder than Hastelloy G30 ( $176 \pm 6\text{HV}_2$ ), making it more suitable to operate effectively in abrasive wear conditions.
- Potentiodynamic polarization responses of Hastelloy G30 sample in synthetic and acidified synthetic mine water at pH 6.8 and 3 showed a lower corrosion current density ( $i_{\text{corr}}$ ) than INCONEL Alloy 600 in all solutions and conditions measured. Hastelloy G30 is more a corrosion resistant material in synthetic mine water than INCONEL Alloy 600.
- When the pH of the solution was decreased, the values of conductivity, total dissolved solids (TDS) and salinity increased with decreased resistivity, hence the acidified synthetic mine water was more corrosive than synthetic mine water.
- INCONEL Alloy 600 is recommended as a hard facing material in mine water conditions.

### Acknowledgements

The authors wish to acknowledge the financial and technical support received from the Carnegie Corporation of New York – through IAS, Department of Science and Technology and National Research Foundation of South Africa and Mintek, South Africa. The authors also wish to thank Multi Alloys, South Africa for the Hastelloy G30 samples.

## References

- [1] Al-Bukhaiti MA, Ahmed SM, Badran FMF, Emara KM. Effect of impingement angle on slurry erosion behaviour and mechanisms of 1017 steel and high-chromium white cast iron. *Wear* 262, 1187-1198 (2007).
- [2] Berns H, Fischer A. Abrasive wear resistance and microstructure of Fe-Cr-C-B hard surfacing weld deposits. *Wear* 112, 163-180 (1986).
- [3] Bolelli G, Lusvardi L, Barletta M. Heat treatment effects on the corrosion resistance of some HVOF-sprayed metal alloy coatings. *Surf. and Coat. Tech.* 202, 4839-4847 (2008).



- [4] Carter AMF. Erosion, corrosion, and abrasion of material handling systems in the mining industry. *J. S. Afr. Inst. Min. Metall.* 86, 235-242 (1986).
- [5] Clark WP. 'High Tech' hardfacing alloys combat corrosion and abrasion of metal parts. *Welding J.* 64, 69-71 (1985).
- [6] Hayes JR, Gray JJ, Szmodis AW, Orme CA. Influence of chromium and molybdenum on the corrosion of nickel-based alloys. *Corrosion* 62, 491-500 (2006).
- [7] HAYNES International. Corrosion-resistant alloys. HAYNES International Website. <http://www.haynesintl.com/cralloys.htm>. Accessed April 2013.
- [8] Jakupi P, Wang F, Noël JJ, Shoesmith DW. Corrosion product analysis on crevice corroded Alloy-22 specimens. *Corr. Sci.* 53, 1670-1679 (2011).
- [9] Jena AK, Chaturvedi MC. The role of alloying elements in the design of nickel-base superalloys. *J. Mat. Sci.* 19, 3121-3139 (1984).
- [10] Kelly RG, Scully JR, Shoesmith D, Buchheit RG. *Electrochemical Techniques in Corrosion Science and Engineering*. Marcel Dekker, Inc. New York, USA (2002).
- [11] Lalvani SB, Swisher JH, Pagano MA. A review of chlorine-induced corrosion in underground mines and coal preparation plants. *Fuel Pr. Tech.* 25, 17-32 (1990).
- [12] Li L, Sagues A. Metallurgical effects on Chloride ion corrosion threshold of Steel in concrete. Technical report to Department of Transportation. University of South Florida. No. WPI 0510806 (2001).
- [13] Llewellyn RJ, Yick SK, Dolman KF. Scouring erosion resistance of metallic materials used in slurry pump service. *Wear* 256, 592-599 (2004).
- [14] Pigrova GD, Korkka SI, Grebtsova TM. Effect of silicon on the phase composition of nickel-base alloys. *Met. Sci. and Heat Treat.* 22, 274-277 (1980).
- [15] Rodríguez J, Guerrero-Mata M, Colás R. Crack propagation in a hard-faced AISI type 304 stainless steel. *Mat. Char.* 51, 95-99 (2003).
- [16] Wang P-Z, Yang Y-S, Ding G, Qu J-X, Shao H-S. Laser cladding coating against erosion-corrosion wear and its application to mining machine parts. *Wear* 209, 96-100 (1997).
- [17] White RA, Higginson A. Factors affecting the corrosivity of underground minewater. *Proc. Mintek 50, Int. Conf. on Min. Sci. and Tech. Sandton, South Africa. 26-30 March 1984* (1985).
- [18] Wood RJK. Tribo-corrosion of coatings: a review. *J. Phys.* 40, 5502-5521 (2007).
- [19] Yoganandh J, Natarajan S, Kumaresh Babu SP. Erosive wear behavior of nickel-based high alloy white cast iron under mining conditions using Orthogonal Array. *J. Mat. Eng. and Perf.* 22, 2534-2541 (2013).

## ABRASIVE WEAR BEHAVIOUR OF SELECTED COBALT-BASED HARDFACING MATERIALS

S.I. Hango<sup>1,2,3</sup>, L.A. Cornish<sup>1,2</sup>, L.H. Chown<sup>1,2</sup>, J.W. van der Merwe<sup>1,2</sup> and F.P.L. Kavishe<sup>1,3</sup>

<sup>1</sup> African Materials Science and Engineering Network (A Carnegie-IAS RISE Network),

<sup>2</sup> School of Chemical and Metallurgical Engineering,

and DST-NRF Centre of Excellence in Strong Materials University of the Witwatersrand,

<sup>3</sup> Faculty of Engineering and Information Technology, University of Namibia, Namibia

Machines that perform in dusty or slurry environments such as mining industry, construction or biomedical applications are exposed to abrasives which enter between the components, or a hard body slides over a soft surface, resulting in abrasive wear<sup>1</sup>. Abrasive wear is a progressive damage, involving material loss on a surface of an engineering material, resulting in leakages, high rates of replacement of worn components or systems, loss in production during downtime for repairing, and maintenance issues. To avoid this, hard facing materials are usually used to protect metal equipment from failing due to abrasion wear<sup>2</sup>, and are applied as a surface layer on an underlying material, usually low or medium carbon steels<sup>3</sup>. Cobalt-based alloys are used as hard facing materials for mining and other processing industries due to their high strength and hardness, and excellent corrosion and wear resistance characteristics<sup>4</sup>.

Two commercial cobalt-based hard facing alloys were used for this study ULTIMET (Co25Cr9Ni5Mo) and Stellite 6B (Co28.8Cr2.6Ni4.5W) alloys were tested for abrasive wear responses at room temperature under unlubricated conditions using a ball-on-disk technique. The chemical compositions of the samples are given in Table 1. The samples were ultrasonically cleaned in ethanol and dried before each test. The tests were performed using a CSM tribometer, using 6 mm diameter 100Cr steel balls. The test parameters were 0.21 m.s<sup>-1</sup> linear speed, 200 m sliding distance, and 10 N applied load were set in the CSM TriboX software for *in situ* measurements. The samples were characterised using SEM with EDX and stereo microscopy before and after wear tests. XRD was used to confirm the phase identifications. Vickers hardness measurements were also done before tests.

The SEM-BSE micrographs of the ULTIMET and Stellite 6B before wear tests are shown in Figures 1 and 2. ULTIMET and Stellite 6B had well defined grain boundaries with equiaxed, mechanically twinned  $\gamma$  grains, which were easier to see in ULTIMET. Table 2 shows EDX analyses of the ULTIMET, and there were similar compositions of the light (L), dark (D) and twinned grains (T) of Figure 1, with Co and Cr as major components in the alloy. These were also found on the grain boundaries, but the analyses of the fine grain boundary precipitates were compromised by the surrounding matrix. They may be  $\gamma$  or Cr<sub>7</sub>C<sub>3</sub><sup>5</sup>.

Table 3 shows EDX analyses of the Stellite 6B, with different compositions of the light major phase with Co and Cr as major components, and the dark grain boundary

phase, Cr<sub>7</sub>C<sub>3</sub>, which was confirmed by XRD. Microhardness tests showed ULTIMET to be softer than Stellite 6B. Their hardnesses were 304±22 HV<sub>3</sub> and 368±13 HV<sub>3</sub> respectively.

The friction behaviour of ULTIMET and Stellite 6B alloys is given in Figure 3. Stellite 6B had a higher  $\mu$  of 0.8±0.1 than 0.6±0.0 for ULTIMET. The wear rate  $k$  for ULTIMET was 1.9×10<sup>-7</sup> mm<sup>3</sup> (N.m)<sup>-1</sup> and Stellite 6B was 9.4×10<sup>-8</sup> mm<sup>3</sup> (N.m)<sup>-1</sup>.

During sliding, the ball ploughed (cut) the surface, producing grooves. The abrasive wear mechanisms for ULTIMET sample against the ball were characterised by cutting damage, grooves, cracks and severe spalling, while for Stellite 6B there was ploughing and grooves. The widest wear track (Figure 4(a)), and thus the highest volume loss occurred on ULTIMET, compared to Stellite 6B sample (Figure 4(b)).

The surface of the ULTIMET (Figure 5) was worn more than the Stellite 6B (Figure 6) sample, meaning Stellite 6B alloy was more resistant to abrasive wear. The worn surfaces showed furrow marks, indicating that the material was removed from the surface during wear. ULTIMET experienced slip bands and slip steps on the surface near the wear track (Figure 5). Stellite 6B had debris collected in the grooves. The matrix phase was ploughed out, leaving carbides on the surface (Figure 6).

The higher hardness value of Stellite 6B than ULTIMET was due to high carbon content, resulting in Cr<sub>7</sub>C<sub>3</sub>, making it more wear resistant. It may be suitable for coating materials operating in corrosion and wear environments.

The financial and technical support from AMSEN, Carnegie-IAS RISE, DST-NRF, S.A., Mr. P. Perel of Multi Alloys, S.A. (free supply of the ULTIMET and Stellite 6B) are gratefully acknowledged.

### References

1. Petrica, M., *et al.* (2013) *Wear*, **308** (1-2), 86-94.
2. Hemmati, I. *et al.* (2013) *Acta Mat.*, **61** (16), 6061-6070.
3. Karamiş, M.B. *et al.* (2006) *Proc. 5th Inter. Conf. on Trib.*, 1-9.
4. Metikoš-Huković, M. and Babić, R. (2007) *Corr. Sci.* **49**, 3570-3579.
5. Klarstrom, D. L. (1993) *J. Mat. Eng. Perf.*, **2**(4), 523-530.





Figure 1. SEM-BSE micrograph of ULTIMET before wear tests, showing equiaxed and twinned  $\gamma$  grains.

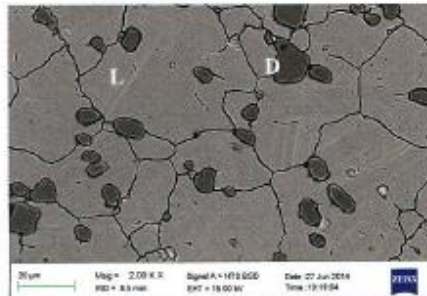


Figure 2. SEM-BSE micrograph of Stellite 6B before wear tests, showing equiaxed and twinned  $\gamma$  grains, with  $Cr_7C_3$  at the grain boundaries.

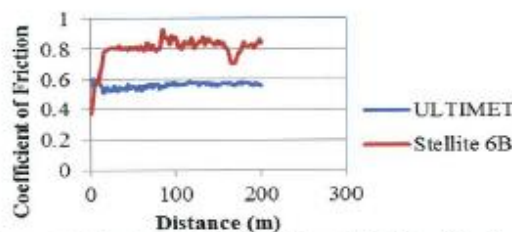


Figure 3. Friction of ULTIMET and Stellite 6B alloys, showing Stellite 6B had a higher  $\mu$  than ULTIMET.

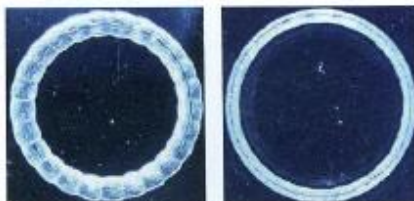


Figure 4. Stereo microscope macrographs of: a) ULTIMET, and b) Stellite 6B after ball-on-disc sliding wear measurements, showing wider wear track on ULTIMET than on Stellite 6B.

Table 1. Chemical compositions of the test alloys.

Sample	Element (wt%)					
	Mn	Fe	Si	C	Nb	N
ULTIMET	0.8	3.0	0.3	0.03	0.01	0.08
Stellite 6B	1.0	2.5	1.3	1.2	-	-



Figure 5. SEM-BSE micrograph of ULTIMET, showing slip bands and slip steps on the surface near the wear track.

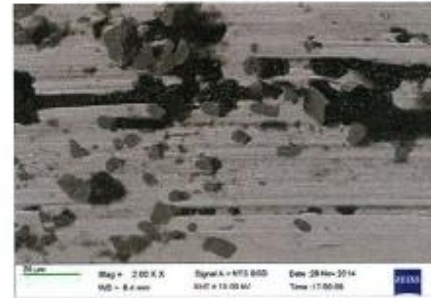


Figure 6. SEM-BSE micrograph of Stellite 6B, showing debris in the grooves, and the matrix phase removed, leaving carbides on the surface.

Table 2. EDX analyses (wt%) of ULTIMET sample of Figure 1.

Element	Overall	Grains	Grain boundary
C	3.5±1.0	2.8±1.0	6.8±2.0
Si	0.3±0.0	0.3±0.1	-
Cr	24.4±0.2	24.7±1.0	23.6±0.4
Mn	0.8±0.1	0.9±0.1	1.0±0.0
Fe	2.8±0.0	2.8±0.1	2.8±0.1
Co	51.9±1.0	52.3±1.0	50±0.3
Ni	8.7±0.1	8.8±0.2	8.4±0.2
Mo	5.4±0	5.1±2.0	5.1±0.3
W	2.1±0.0	2.1±0.1	2.2±0.3
Phase	-	$\gamma$	$Cr_7C_3$

Table 3. EDX analyses (wt%) of Stellite 6B sample of Figure 2.

Element	Overall	Light	Dark
C	7.6±0.0	3.9±1.0	10.6±0.2
O	7.4±1.0	6.5±0.3	-
Si	0.4±0.0	0.5±0.1	-
Cr	29.5±1.0	24.0±0.1	75.3±0.3
Mn	1.5±0.1	1.6±0.1	1.3±0.1
Fe	1.7±0.1	1.9±0.1	0.6±0.0
Co	46.2±0.1	53.7±0.1	9.3±0.1
Ni	1.7±0.1	2.1±0.1	-
Mo	-	0.7±0.4	-
W	4.8±0.1	5.2±0.2	3.1±0.4
Phase	-	$\gamma$	$Cr_7C_3$

Corresponding author: [silas.hango@students.wits.ac.za](mailto:silas.hango@students.wits.ac.za)

## A STUDY OF ULTIMET AND STELLITE 6 COATINGS WITH RUTHENIUM ON CARBON STEEL SUBSTRATES

S.I. Hango<sup>1,2,3</sup>, J.W. van der Merwe<sup>1,2</sup>, L.H. Chown<sup>1,2</sup>, F.P.L. Kavishe<sup>2,3</sup> and L.A. Cornish<sup>1,2</sup>

<sup>1</sup>School of Chemical & Metallurgical Engineering, University of Witwatersrand, Johannesburg, South Africa, DST-NRF Centre of Excellence in Strong Materials, <sup>2</sup>African Materials Science and Engineering Network, and <sup>3</sup>Faculty of Engineering and Information Technology, University of Namibia, Namibia

In the Otjijase Underground Mine, Namibia, water is pumped from natural underground reservoirs to the surface using carbon steel pumps which have their shaft sleeves coated with a Ni-Cr-Fe alloy. The pumps fail very frequently in the highly corrosive mine water, sometimes only lasting a few weeks, flooding the mine. Attempts were made to understand the failure cause, and to recommend more suitable materials.

Preliminary work<sup>1,2</sup> showed that the Ni-Cr-Fe coated, carbon steel shaft sleeves were mechanically worn by particles from the mine water which became trapped with new wear debris in the packing glands of the pumps, producing erosion-corrosion of the pump components. Once the protective coatings on the sleeves were breached, the exposed steel corroded rapidly in the corrosive mine water, resulting in leakages. As well as containing a high amount of total dissolved solids, the mine water pH also varied seasonally, from highly acidic to alkaline. Based on expected corrosion and wear resistance, four hardfacing alloys were identified as possible replacement materials. After corrosion and wear testing<sup>1,3</sup>, ULTIMET and Stellite 6, showed better wear and corrosion properties, and were evaluated as coatings on ASTM A516 steel substrates. Different ruthenium additions were added to the coatings to ascertain whether they would improve corrosion and wear resistance, since Ru has done this for other alloys<sup>4</sup>.

ULTIMET and Stellite 6 powders were each mixed with 0.3 and 0.6 wt% Ru additions, and the powders, also without Ru, were thermally sprayed by high velocity oxy-fuel flame (HVOF) onto the steel substrates. The coatings were characterised using SEM with EDX, and XRD<sup>1</sup>. Corrosion behaviour in synthetic mine water, sliding abrasive wear, and hardness of the coatings and the substrate were determined<sup>1</sup>.

It was expected that the Ru additions would increase the hardness and the corrosion resistance, but the results were variable. An addition of 0.3 wt% Ru gave the highest hardness in the ULTIMET coatings, whereas the Stellite 6 coating with 0.6 wt% Ru had the highest hardness overall. Stellite 6 coatings gave better corrosion and wear resistance than ULTIMET coatings, with no trend for the effect of ruthenium. To analyse this behaviour, the coatings were prepared metallographically, and the poor distribution of ruthenium (e.g. Fig. 1) explained the randomness of the results. Due to ruthenium's much higher melting point, it may not have melted completely during thermal spraying, but it should at least have dissolved. The powder sizes were then measured using a Malvern Mastersizer. ULTIMET and Stellite 6 powders had the expected size distributions, but the Ru powder had a

trimodal distribution. The SEM showed that the Ru powder had agglomerated (Fig. 2).

Although there were improved corrosion and wear properties with added Ru, the randomness of the results was due to the poor Ru distribution caused by agglomeration of the Ru particles. For better effects, the Ru powders should first have been milled separately, then milled with the alloy powders, and not just mixed.

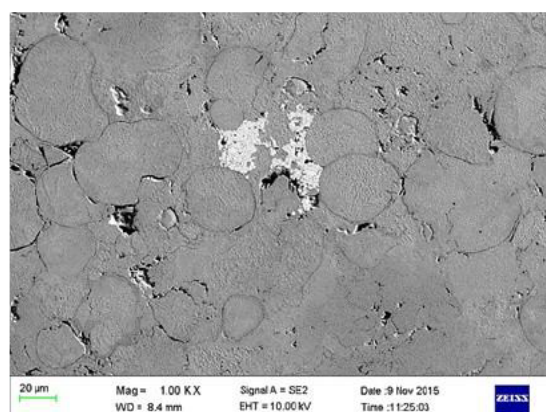


Figure 1. SEM-SE image of Stellite 6 coating with 0.3 wt% Ru, showing the Ru and individual alloy "splats".

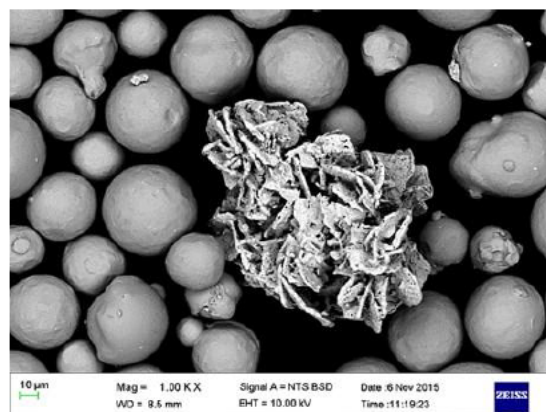


Figure 2. SEM-BSE micrograph of the Stellite 6 powder (spherical particles) and Ru (agglomerated).

### References

1. Hango, S.I., PhD submitted to the University of the Witwatersrand, 2017.
2. Hango, S.I. et al. (2012) Proc. Microsc. Soc. South Afr., 42, 97.
3. Hango, S.I. et al. (2014) Int. Sci. & Technol. J. Namibia (ISTJN), 4, 90.
4. Tomashov, N.D. et al. (1976). Protect. Met., 12(5) 471.

Corresponding author: [Lesley.Cornish@wits.ac.za](mailto:Lesley.Cornish@wits.ac.za)



## DEVELOPMENT OF WEAR AND CORROSION RESISTANT COATINGS FOR POTENTIAL USE ON SLEEVES OF PUMPS IN A COPPER MINE

S.I. Hango<sup>1,2,3</sup>, J.W. van der Merwe<sup>1,2</sup>, L.H. Chown<sup>1,2</sup>, F.P.L. Kavishe<sup>2,3</sup> and L.A. Cornish<sup>1,2</sup>

<sup>1</sup>School of Chemical & Metallurgical Engineering, University of the Witwatersrand, Johannesburg, South Africa, DST- NRF Centre of Excellence in Strong Materials,

<sup>2</sup>African Materials Science and Engineering Network, and

<sup>3</sup>Faculty of Engineering and Information Technology, University of Namibia, Namibia

In the Otjihase Underground Mine, Namibia, where copper is mined, water is pumped from natural underground reservoirs to the surface using pumps. Although the carbon steel pumps have their shaft sleeves coated with a Ni-Cr-Fe alloy, the pumps fail very frequently in the highly corrosive mine water, sometimes only lasting a few weeks. This leads to flooding of parts of the mine. In this work, the causes of the pump failures were determined, and work was done to enable the recommendation of more suitable materials.

The first part of the study<sup>1,2</sup> showed that the carbon steel shaft sleeves coated with Ni-Cr-Fe were abrasively worn by solid particles in the mine water. These particles then became trapped together with wear debris in the packing glands of the pumps, producing erosion-corrosion of the pump components. Once the protective coatings on the sleeves were breached, the exposed steel corroded rapidly in the corrosive mine water, resulting in leakages. As well as containing high amounts of total dissolved solids, the mine water pH also varied from season to season, from highly acidic to alkaline, meaning that a wide variety of conditions were experienced.

Based on the corrosion resistance and wear resistance requirements, four hardfacing alloys were identified as possible replacement materials for coating the sleeves: Hastelloy G30, ULTIMET, Stellite 6B and ToughMet 3. After corrosion and tribology testing<sup>1,3</sup> of the bulk alloys, ULTIMET and Stellite 6 showed better wear and corrosion properties than the other two alloys, and were next evaluated as coatings on ASTM A516 steel substrates. These coatings were thermally sprayed by high velocity oxy-fuel flame (HVOF), which is not an optimal coating process, but at least gave results which could be compared. Small additions of ruthenium have improved corrosion and wear resistance in other alloys.<sup>4,5</sup> Therefore, 0.3 wt% and 0.6 wt% Ru were added to the coatings to assess the effects of ruthenium addition, and these were compared against the coatings without ruthenium.

ULTIMET and Stellite 6 powders with 0, 0.3 or 0.6 wt% Ru were thermally sprayed by HVOF onto ASTM A516 steel substrates. The coatings were characterised using SEM with EDX, and XRD<sup>1</sup>. Corrosion behaviour of the coatings and substrate were determined in synthetic mine water at various pH levels, as well as sliding abrasive wear resistance and hardness<sup>1</sup>.

With the addition of ruthenium to ULTIMET and Stellite the hardness increased. However, in the case of ULTIMET the increase was not linear since the hardness of the 0.3wt% Ru coating was slightly higher than the 0.6wt% Ru coating. The wear resistance of all the coatings improved with the addition of ruthenium except for the 0.3wt% Ru Stellite coating, which had a slightly higher wear rate than the Stellite coating without ruthenium. The corrosion resistance of the coatings were not significantly affected by the addition of ruthenium, and there was no consistent trend. However, the tribocorrosion resistance of both coatings increased with the addition of ruthenium.

It was expected that the Ru additions would improve the corrosion resistance, but the results were variable. The distribution of ruthenium in the coatings were studied metallographically. There was very poor distribution of ruthenium, which was deduced to occur from the agglomeration of the Ru powder.

Although there were improvements in the tribocorrosion resistance of the coatings with added Ru, agglomeration of the Ru particles produced varied results. For more uniform and improved corrosion- and wear resistance, the Ru powder should first have been milled separately, then milled with the coating powder, and not just mixed. Also, the thermal spraying parameters need to be optimised to give better coatings.

#### References

1. HANGO, S.I. 2017. Failure of Pump Systems Operating in Highly Corrosive Mine Water at Otjihase Mine, PhD thesis, submitted to the University of the Witwatersrand.
2. HANGO, S.I., CORNISH, L.A., CHOWN, L.H., VAN DER MERWE, J.W. and KAVISHE, F.P.L. 2012. Failure of pump shaft sleeves in highly corrosive copper solutions at Otjihase Mine, *50th Microscopy Society of Southern Africa Conference Proceedings*, vol. 42, p. 97, Cape Town, 4th – 7th December 2012.
3. HANGO, S.I., CORNISH, L.A., CHOWN, L.H., VAN DER MERWE, J.W. and KAVISHE, F.P.L. 2014. Erosion-Corrosion of hard facing materials exposed to mine water conditions, *International Science and Technology Journal of Namibia (ISTJN)*, vol. 4, pp. 90-105.
4. TOMASHOV, N.D. KAZARIN, V.I. MIKHEEV V.S. and GONCHARENKO, B.A. 1976. Effect of ruthenium in the on the electrochemical and corrosion behaviour of titanium and titanium-nickel alloys in acid chloride solutions, *Protection of Metals*, vol. 12, no. 5, pp. 471-474.
5. SHING, T.L., LUYCKX, S., NORTHROP, I.T. and WOLFF, I. 2004. The effect of ruthenium additions on the hardness, toughness and grain size of WC-Co, *International Journal of Refractory Metals & Hard Materials*, vol. 19, pp. 41-44.